Rotational and Vibrational Spectroscopy and Structure Determination

of Organic Molecules of Astrochemical Relevance

By

Vanessa L. Orr

A dissertation submitted in partial fulfillment of

the requirements for the degree of

Doctor of Philosophy

(Chemistry)

at the

UNIVERSITY OF WISCONSIN-MADISON

2021

Date of final oral examination: 3/26/2021

The dissertation is approved by the following members of the Final Oral Committee:

      Robert J. McMahon, Professor, Chemistry
      R. Claude Woods, Professor, Chemistry
      Etienne Garand, Associate Professor, Chemistry
      Susanna L. Widicus Weaver, Professor, Chemistry and Astronomy

To my family for their unending support, love, and encouragement

Acknowledgments

It feels impossible to try and thank all the important people, who have made my journey to and through graduate school a reality, but I will do my very best. I must begin first and foremost with my parents. My mom and dad have been my strongest supporters and encouragers throughout my entire life, and this would not have been possible without them. Everything I have pursued, from music to chemistry and everything in between, they never let me believe my goals were impossible, and they taught me that with dedication and perseverance I could achieve them. I am especially thankful for all our wonderful conversations on my walks home from work. Though we may have been miles apart you always felt close. I am also thankful for my wonderful brother. I am lucky to have a sibling that, as different as we may be, we have a lot in common as well. I am incredibly thankful to all of them for their support!

Though leaving California had its challenges, part of why I wanted to move to Wisconsin (aside from the excellent research) was because of the network of extended family I have here. Living in the state I grew up visiting as a child has been fantastic. I have to thank in particular Heather and Katelyn and their family, for welcoming me every Thanksgiving, and for all our visits back and forth during my time here.

I must also thank my close friends who have been with me since before this journey began: Alli, Jace, Ivy, Robert, and Annika, and the friends I gained since starting this journey: Alexa, Ariel, Allice, Cara, Amy, and my cohort. To the former, thank you for your 10+ years of friendship and fun. To the later, I am so grateful that our educational paths brought us together and I am glad that we got to be on this adventure called grad school together; you have brought so much joy to my time here.

The journey to graduate school does not happen overnight or by magic, for all of us there was an initial inspiration. My initial affinity for chemistry was sparked by Mr. Hoag in high school. His passion for teaching chemistry combined with my interest in science made it the subject I enjoyed most in high school and led me to pursue chemistry as my major. At California Lutheran University, I majored in chemistry, and my love of the field grew thanks to Dr. Butcher and Dr. Tannaci. I have to thank Dr. T for giving me my first introduction to research and conferences, and for encouraging me to pursue a Ph.D. I have to thank Dr. B for setting me up for success in graduate school by introducing me to physical chemistry, suggesting additional math courses, and selecting me to be a departmental assistant. I am so appreciative to these mentors for their investment in my education.

When I entered graduate school, I gained many new and excellent mentors. I must thank: Dr. Nick Hill and Dr. Brian Esselman for helping me become a better organic chemistry teacher, and for giving me opportunities for leadership. Dr. Cheri Barta for helping me find an intersection of service and science, for entrusting me with much of her job while on maternity leave, and for her overall mentorship and friendship. Dr. Desiree Bates for bringing me onto the Chemistry Opportunities (CHOPs) Team which has allowed me to support diversity initiatives in our department and utilized my desire to plan and coordinate. Dr. Arrietta Clauss for keeping the graduate program running and her insight and collaboration with CHOPs. Thank you to the whole CHOPs Team; working with you has been a privilege and a joy!

Pursing a Ph.D. would be impossible without our research advisors, mentors, and colleagues. Thank you to Prof. Bob McMahon for guiding the research endeavor and for allowing me to follow my passion by supporting my roles in the department (even those that were not specifically research related). Thank you to Prof. Claude Woods for sharing his immense

knowledge about rotational spectroscopy, and for having unending patience and enthusiasm in the process. Also, thank you, Claude, for sharing your stories and for listening to mine. Our conversations have been a significant highlight of my time here. Thank you to Dr. Brian Esselman for your mentorship from early on when I was first learning to fit spectra to now writing my thesis, and for your constant encouragement to "go faster" and "win". A big thanks also to my collaborators: Prof. Kaori Kobayashi at the University of Toyama, Prof. John Stanton at the University of Florida, and Dr. Brant Billinghurst and Dr. Jianbao Zhao at the Canadian Light Source. Thank you to our master glass blower, Tracy Drier, our machine shop team, specifically Steve Myers and Matt Martin, and the electronics team, Bill Goebel and Blaise Thompson; their expertise and efforts have been essential to my research endeavors.

Finally, I must thank my colleagues in the McMahon | Woods Group. To former members, Brent, Stephanie, Ben, Nick, Cara, and Zach, thank you for welcoming me into the group and being fantastic colleagues during my early years of grad school. To the current members, I am so lucky I get to work with friends and the day-to-day life of grad school is made so much brighter when working with you all (which I can definitively say after spending 12 months without seeing you all in-person because of the pandemic). Andrew, Houston, Madison, Maria, Matisha, Sam K., Sam W., and all the undergraduates who have worked with the group, you have each been an important part of my graduate career, and I could write pages on just how important. I cannot wait to see where your careers take each of you. Thanks to you all!

Table of Contents

List of Tables

List of Schemes

List of Figures

Chapter 1: Thesis Overview

Diketene

Thiophene

syn-periplanar

anti-clinal

4-Cyano-1,2-butadiene

Rotational spectroscopy is a gas-phase spectroscopy technique where the data collected is spectra of the transitions between rotational energy levels. It is linked to astrochemistry due to the correlation between rotational transitions measured in a laboratory, and those measured by radio telescopes.[1-2] It is inherently linked to structure determination because the rotational constants are inversely related to the moments of inertia of the molecule, which are dependent on the distribution of mass of the molecule along the principal rotational axes.[3] Within a single millimeter-wave rotational spectrum of a molecule of interest, transitions from the ground vibrational state, many of its excited vibrational states, and often its naturally abundant isotopologues are readily observable. The rotational transitions for these vibrational states and isotopologues are least-squares fit to determine the rotational constants and centrifugal distortion terms that accurately model the spectrum. If there are interactions between vibrational states, coupling terms and the energy gap between the states are incorporated to accurately model the interaction. With the incorporation of high-resolution, rotationally resolved infrared spectra, ro-vibrational transitions can provide the precise vibrational frequency for a given vibrational state. The spectroscopic analysis of a molecule has been greatly facilitated by high-level computational chemistry efforts.

When I arrived at UW-Madison, the collaboration between R. Claude Woods and Robert J. McMahon was well underway, and we are now commonly known as the McMahon | Woods Group. Many major improvements were made to the instrument and are detailed in the theses of Brian J. Esselman (Ph.D. 2012)[4] and Brent K. Amberger (Ph.D. 2015).[5] The group had also developed expertise with Kisiel's AABS suite for the analysis of rotational spectra.[6] The combination of automated data collection and expertise with the analysis software has allowed for much greater efficiency in our collection and analysis of spectra . In his 2015 thesis, Amberger mentioned a number of molecules that were ongoing projects that have now been published

including: benzonitrile,[7] pyrimidine,[8] and formyl azide.[9]   The benzonitrile project was a collaboration with Z. Kisiel and significantly advanced our knowledge of Pickett's SPFIT/SPCAT software which allows for analysis of rotational and ro-vibrational data.[10]   This has led to the treatment of multiple dyads by our group, and others are in progress.[11-13]   This thesis focuses on the rotational spectroscopy in the mm-wave region of three organic molecules: diketene, 4-cyano-1,2-butadiene, and thiophene.   For each molecule we investigate the ground vibrational state, excited vibrational states, and the molecular structure through experiment and computational calculations.

Chapter 2 presents our work on the mm-wave spectrum of diketene.   Initially, we were interested in pyrolyzing diketene into ketene, for subsequent use of ketene in a discharge, with the ultimate goal of producing acylium cation.   Spectroscopy of that ion is an on-going project and a major objective of the group.   The mm-wave spectrum of diketene had not been previously reported.   With the automated broadband scanning feature, we collected the spectrum from 240 – 360 GHz from which the ground state and eight vibrationally excited states were studied.   The investigation of v_{24} = 0, 1, 2, 3, 4 and 5 of the ring-puckering vibrational motion, v_{24}, provided information about the harmonic nature of this vibrational motion.   This work and other recent work in the group[9, 14-15] has expanded our understanding of the trends in the rotational and quartic distortion constants for harmonics contributing to the motivation for their computational estimate for the first time.   Additionally, through collaboration with Ilia A. Guzei, the Department's director of crystallography, we resolved an ambiguity related to the previous X-ray crystal structures of diketene and the subsequent theoretical studies.   Though diketene is liquid at room temperature, we were able to obtain a new crystal structure at −173 °C.   Our updated structure is in excellent agreement with the CCSD(T)/ANO1 optimized structure, resolving the ambiguity.   This work was

published in the *Journal of Physical Chemistry A* in 2016.[16] Chapter 2 also contains update on the group's progress on generating ketene and information about the coupling of $\nu_{24}+\nu_{16}$ and ν_{23} of diketene. As forming diketene in a discharge of ketene is possible, the detailed understanding of its spectrum provided by this work is still relevant to on-going projects.

A unique aspect of our group relative to many rotational spectroscopy groups, is the ability to synthesize molecules or isotopologues of interest. A series of cyanobutadiene isomers of the heterocyclic, aromatic molecule pyridine (C_5H_5N) were synthesized and characterized, and published in 2020.[17] These molecules were targeted for rotational spectroscopy studies due to their relevance to astrochemistry, as many nitriles have strong dipoles and have been detected via radio astronomy.[1-2] These or similar molecules were also recently reported as products in benzene discharges,[18] and have been proposed for searches in the interstellar medium.[19] Chapter 3 details the rotational spectroscopy analysis of 4-cyano-1,2-butadiene, which is the allenyl isomer in the series of butadienes $H_2C=C=CH–CH_2CN$ and which was synthesized by Samuel M. Kougias and Daniel J. Lee. The –CH_2CN group is an internal rotor which gives rise to two stable conformers: *syn-periplanar* (*syn*, C_s) and *anti-clinal* (*anti*, C_1) which are close in relative energy (<1 kcal/mol apart). The *syn* conformer has been successfully treated with a partial-octic, distorted-rotor Hamiltonian. The *anti* conformer exhibits coupling in its ground state and all observed excited vibrational states (ν_{27} = 1, 2, 3, and 4 of ν_{27}, and ν_{26}). All these states have been treated with single-state, partial-octic, distorted-rotor Hamiltonians, by excluding the most obviously perturbed transitions from the fit. Fundamental ν_{27} corresponds to the internal rotation of the –CH_2CN group with respect to the allenyl moiety. The investigation of the coupling between the harmonics of the torsion would greatly benefit from the incorporation of ro-vibrational data for the torsional mode. When this work was presented at the International Symposium on Molecular Spectroscopy in June

2019,[20] we learned about the far-IR beamline at the Canadian Light Source (CLS) in Saskatoon, Canada. We submitted two proposals to the CLS, with the intention of collecting the high-resolution FTIR spectra of 4-cyano-1,2-butadiene to study the torsional mode, and that of HN_3/DN_3 to continue the work presented in Amberger's thesis.[5] We were awarded time for each of them in June 2020, but due to the COVID-19 pandemic we have not yet been able to travel to Canada. We were able to send samples of 4-cyano-1,2-butadiene, and work in collaboration with the beamline scientists at CLS, Brant E. Billinghurst and Jianbao Zhao, to conduct experiments remotely. We also collected high-resolution FTIR spectra of the heterocycles pyrimidine (m-$C_4H_4N_2$), pyridazine (o-$C_4H_4N_2$), and thiazole (c-C_3H_3NS) for other on-going projects in the group. Our work with the CLS is discussed in Appendix A.

Thiophene (C_4H_4S) is the topic of Chapter 4 and Chapter 5. The work on thiophene is in collaboration with Yotaro Ichikawa and Kaori Kobayashi of the University of Toyama, Japan. They have provided us with spectra below 130 GHz, which combined with our spectra from 130 – 360 GHz, gives the spectrum a range from 40 – 360 GHz. This group's previous work on pyrimidine (m-$C_4H_4N_2$) established excellent agreement between the semi-experimental equilibrium (r_e^{SE}) structure from rotational spectroscopy and the high-level *ab intio* structure (r_e), as well as established a method to obtain a best possible theoretical estimate of the structure.[8] Our work on the equilibrium structure determination on thiophene, presented in Chapter 4, employs these same methods to an aromatic, heterocycle containing sulfur. Like all previous structure determinations done in the group,[8, 21-22] the first step to an r_e^{SE} involved obtaining the least-squares fit of the ground state for multiple isotopologues to determine their rotational constants. From the spectrum of the normal isotopologue, all heavy-atom isotopologues (^{34}S, ^{33}S, and ^{13}C) were able to be observed and least-squares fit in their natural abundance. Aatmik R. Patel and Samuel M.

Kougias were able to synthesize every possible deuterium-enriched isotopologue of thiophene. Many heavy atom isotopologues of the deuterated isotopologues were also observable in natural abundance in our deuterated samples. We have measured and least-squares fit the ground state for a total of 26 isotopologues of thiophene (including the normal isotopologue), and 24 are included in our semi-experimental equilibrium (r_e^{SE}) structure determination.

The resultant determinable rotational constants for these isotopologues are then combined with computational corrections (CCSD(T)) for vibration-rotation interactions and electron mass. Then following the method set out in pyrimidine,[8] we established a best possible theoretical structure for comparison to the r_e^{SE} structure. This method first involves optimizing the structure at the CCSD(T) level with multiple basis sets (cc-pCVXZ, where X=D, T, Q, 5) up to the largest achievable, which was quintuple zeta for this size molecule. This CCSD(T)/cc-pCV5Z structure is then corrected to account for extrapolation to the complete basis set limit, residual electron correlation beyond CCSD(T), relativistic effects, and the diagonal Born-Oppenheimer correction. These state-of-the-art calculations were performed in collaboration with John. F. Stanton at the University of Florida. Additionally, we employed a method, developed recently in collaboration with Andrew Owen and Brian Esselman in this group, to analyze the importance of including many isotopologues beyond mono substitution in a structure determination.

In Chapter 5, the analysis of the vibrational states of thiophene is presented. From our combined spectrum from 40 – 360 GHz, we have measured transitions for a surprising 19 excited vibrational states of thiophene ranging in vibrational frequency from 452 to 1163 cm^{-1}. All states are treated with sextic, distorted-rotor Hamiltonians together in a global least-squares fit. None of these excited vibrational states, have been studied previously in the mm-wave region, and the three A_2 symmetry, IR-inactive fundamentals are analyzed for the first time by any high-resolution

spectroscopic method. A number of the other states were previously studied with high-resolution infrared spectroscopy,[23-26] and where possible, we have combined these previously published IR transitions[23, 25] with our mm-wave data. The combination of our mm-wave data, the previous IR transitions, and the coupling terms involved between many of these states has allowed for the precise determination of fundamental frequencies beyond those measured directly by high-resolution IR. In the global fit there are currently three dyads, a triad, and a pentad involving ν_7, ν_{12}, ν_{20}, ν_9, $2\nu_{14}$. This work is ongoing, and Chapter 5 represents the current status of the project.

Finally, Appendix B discusses the updates and modifications made to the mm-wave spectrometer that I was involved in during my thesis work. The previous major reconstruction and updates to the spectrometer and the redesign of its software are detailed in the theses of Brian J. Esselman (Ph.D. 2012)[4] and Brent K. Amberger (Ph.D. 2015).[5] New features and changes to the LabVIEW code by Brian Esselman, with assistance from myself and Maria Zdanovskaia, for the mm-wave spectrometer add a number of new capabilities. The work on the mass spectrometer LabVIEW code, originated by Brian and Josh Shutter, was continued and new features were added by Brian and me, with assistance from Matisha Dorman. This work has re-established our groups capability to collect rotational spectra and mass spectra of ions in a discharge.

Overall, this thesis presents analysis of the rotational spectroscopy and computational chemistry of three moderately sized, organic molecules of astrochemical relevance. In my time, the McMahon | Woods Group has expanded into the analysis of coupled vibrational states, collection and analysis of high-resolution vibrational spectroscopy through collaboration with the CLS and has continued to advance the limits of semi-experimental equilibrium structure determinations.

REFERENCES

1. Endres, C. P.; Schlemmer, S.; Schilke, P.; Stutzki, J.; Müller, H. S. P., The Cologne Database for Molecular Spectroscopy, CDMS, in the Virtual Atomic and Molecular Data Centre, VAMDC. *J. Mol. Spectrosc.* **2016**, *327*, 95-104.

2. Müller, H. S. P.; Thorwirth, S.; Roth, D. A.; Winnewisser, G., The Cologne Database for Molecular Spectroscopy, CDMS. *Astron. Astrophys.* **2001**, *370* (3), L49-L52.

3. Kraitchman, J., Determination of Molecular Structure from Microwave Spectroscopic Data. *Am. J. Phys.* **1953**, *21* (1), 17-24.

4. Esselman, B. J. Computational and Spectroscopic Investigations of Species of Astrochemical Relevance. Ph.D. Thesis, University of Wisconsin-Madison, Madison, WI, 2012.

5. Amberger, B. K. Millimeter-wave Spectroscopy of Highly Nitrogenous Molecules of Potential Astrochemical Interest. Ph.D. Thesis, University of Wisconsin-Madison, Madison, WI, 2015.

6. Kisiel, Z. PROSPE - Programs for ROtational SPEctroscopy. http://info.ifpan.edu.pl/~kisiel/prospe.htm

7. Zdanovskaia, M. A.; Esselman, B. J.; Lau, H. S.; Bates, D. M.; Woods, R. C.; McMahon, R. J.; Kisiel, Z., The 103 – 360 GHz Rotational Spectrum of Benzonitrile, the First Interstellar Benzene Derivative Detected by Radioastronomy. *J. Mol. Spectrosc.* **2018**, *351*, 39-48.

8. Heim, Z. N.; Amberger, B. K.; Esselman, B. J.; Stanton, J. F.; Woods, R. C.; McMahon, R. J., Molecular structure determination: Equilibrium structure of pyrimidine (m-$C_4H_4N_2$) from rotational spectroscopy (r_e^{SE}) and high-level ab initio calculation (r_e) agree within the uncertainty of experimental measurement. *J. Chem. Phys.* **2020**, *152* (10), 104303.

9. Walters, N. A.; Amberger, B. K.; Esselman, B. J.; Woods, R. C.; McMahon, R. J., Millimeter-wave Spectroscopy of syn Formyl Azide ($HC(O)N_3$) in Seven Vibrational States. *J. Mol. Spectrosc.* **2017**, *331*, 71-81.

10. Pickett, H. M., The fitting and prediction of vibration-rotation spectra with spin interactions. *J. Mol. Spectrosc.* **1991**, *148* (2), 371-377.

11. Dorman, P. M.; Esselman, B. J.; Woods, R. C.; McMahon, R. J., An analysis of the rotational ground state and lowest-energy vibrationally excited dyad of 3-cyanopyridine: Low

symmetry reveals rich complexity of perturbations, couplings, and interstate transitions. *J. Mol. Spectrosc.* **2020**, *373*, 111373.

12. Dorman, P. M.; Esselman, B. J.; Park, J. E.; Woods, R. C.; McMahon, R. J., Millimeter-wave spectrum of 4-cyanopyridine in its ground state and lowest-energy vibrationally excited states, ν_{20} and ν_{30}. *J. Mol. Spectrosc.* **2020**, *369*, 111274.

13. Zdanovskaia, M. A.; Esselman, B. J.; Woods, R. C.; McMahon, R. J., The 130–370 GHz Rotational Spectrum of Phenyl Isocyanide (C_6H_5NC). *J. Chem. Phys.* **2019**, *151* (2), 024301.

14. Higgins, P. M.; Esselman, B. J.; Zdanovskaia, M. A.; Woods, R. C.; McMahon, R. J., Millimeter-wave spectroscopy of the chlorine isotopologues of chloropyrazine and twenty-two of their vibrationally excited states. *J. Mol. Spectrosc.* **2019**, *364*, 111179.

15. Esselman, B. J.; Zdanovskaia, M. A.; Woods, R. C.; McMahon, R. J., Millimeter-wave spectroscopy of the chlorine isotopologues of 2-chloropyridine and twenty-three of their vibrationally excited states. *J. Mol. Spectrosc.* **2019**, *365*, 111206.

16. Orr, V. L.; Esselman, B. J.; Dorman, P. M.; Amberger, B. K.; Guzei, I. A.; Woods, R. C.; McMahon, R. J., Millimeter-wave Spectroscopy, X-ray Crystal Structure, and Quantum Chemical Studies of Diketene – Resolving Ambiguities Concerning the Structure of the Ketene Dimer. *J. Phys. Chem. A* **2016**, *120* (39), 7753-7763.

17. Kougias, S. M.; Knezz, S. N.; Owen, A. N.; Sanchez, R. A.; Hyland, G. E.; Lee, D. J.; Patel, A. R.; Esselman, B. J.; Woods, R. C.; McMahon, R. J., Synthesis and Characterization of Cyanobutadiene Isomers—Molecules of Astrochemical Significance. *J. Org. Chem.* **2020**, *85* (9), 5787-5798.

18. McCarthy, M. C.; Lee, K. L. K.; Carroll, P. B.; Porterfield, J. P.; Changala, P. B.; Thorpe, J. H.; Stanton, J. F., Exhaustive Product Analysis of Three Benzene Discharges by Microwave Spectroscopy. *J. Phys. Chem. A* **2020**, *124* (25), 5170-5181.

19. Moreno, R.; Silla, E.; Tunon, I.; Arnau, A., Ab Initio Rotational Constants of the Nitriles Derived from Cyanodiacetylene (HC_4CN). *Astrophys. J.* **1994**, *437*, 532.

20. Orr, V. L.; Esselman, B. J.; Owen, A. N.; Kougias, S. M.; Woods, R. C.; McMahon, R. J. Rotational Spectroscopy of *syn* and *anti-clinal* Penta-3,4-dienenitrile from 130-375 GHz, *International Symposium on Molecular Spectroscopy*, Champaign-Urbana, Illinois, June 17-21, 2019; Champaign-Urbana, Illinois, 2019; RI07.

21. Amberger, B. K.; Esselman, B. J.; Stanton, J. F.; Woods, R. C.; McMahon, R. J., Precise Equilibrium Structure Determination of Hydrazoic Acid (HN$_3$) by Millimeter-wave Spectroscopy. *J. Chem. Phys.* **2015**, *143* (10), 104310.

22. Esselman, B. J.; Amberger, B. K.; Shutter, J. D.; Daane, M. A.; Stanton, J. F.; Woods, R. C.; McMahon, R. J., Rotational spectroscopy of pyridazine and its isotopologs from 235–360 GHz: Equilibrium structure and vibrational satellites. *J. Chem. Phys.* **2013**, *139* (22), 224304.

23. van Wijngaarden, J.; Van Nest, S. J.; van Dijk, C. W.; Tokaryk, D. W., Rovibrational spectrum and analysis of the ν_8 band of thiophene using infrared synchrotron radiation. *J. Mol. Spectrosc.* **2010**, *259* (1), 56-59.

24. van Wijngaarden, J.; Tokaryk, D. W., High resolution synchrotron-based study and analysis of the ν_{14} band of thiophene. *J. Mol. Spectrosc.* **2008**, *251* (1), 365-368.

25. Hegelund, F.; Wugt Larsen, R.; Palmer, M. H., The high-resolution infrared spectrum of thiophene between 600 and 1200cm^{-1}: A spectroscopic and theoretical study of the fundamental bands ν_6, ν_7, ν_{13}, and the *c*-Coriolis interacting dyad ν_5, ν_{19}. *J. Mol. Spectrosc.* **2008**, *247* (1), 100-114.

26. Pankoke, B.; Yamada, K. M. T.; Winnewisser, G., High resolution IR-spectra of furan and thiophene. *Z. Naturforsch., A: Phys. Sci.* **1994**, *48* (12), 1193-202.

Chapter 2: Millimeter-Wave Spectroscopy, X-ray Crystal Structure, and Quantum Chemical Studies of Diketene: Resolving Ambiguities Concerning the Structure of the Ketene Dimer
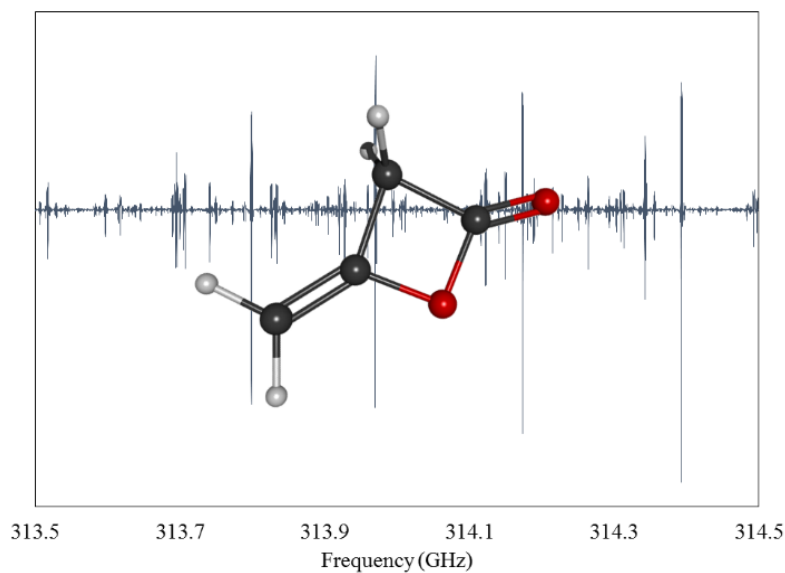
Portions of this work have been published previously:

ABSTRACT

The pure rotational spectrum of diketene has been studied in the millimeter-wave region from ~240 to 360 GHz. For the ground vibrational state and five vibrationally-excited satellites (ν_{24}, $2\nu_{24}$, $3\nu_{24}$, $4\nu_{24}$, and ν_{16}), the observed spectrum allowed for the measurement, assignment, and least-squares fitting a total of more than 10,000 distinct rotational transitions. In each case, the transitions were fit to single-state, complete or near-complete sextic centrifugally-distorted rotor models to near experimental error limits using Kisiel's ASFIT. Additionally, we obtained less satisfactory least-squares fits to single-state centrifugally-distorted rotor models for three additional vibrational states: $\nu_{24}+\nu_{16}$, ν_{23}, and $5\nu_{24}$. The structure of diketene was optimized at the CCSD(T)/ANO1 level, and the vibration-rotation interaction (α_i) values for each normal mode were determined with a CCSD(T)/ANO1 VPT2 anharmonic frequency calculation. These α_i values were helpful in identifying the previously unreported ν_{16} and ν_{23} fundamental states. We obtained a single-crystal X-ray structure of diketene at −173 ℃. The bond distances are increased in precision by more than an order of magnitude compared to those in the 1958 X-ray crystal structure. The improved accuracy of the crystal structure geometry resolves the discrepancy between previous computational and experimental structures. The rotational transition frequencies provided herein should be useful for a mm-wave or terahertz search for diketene in the interstellar medium.

INTRODUCTION

Diketene (**1**, $C_4H_4O_2$, 4-methylene-2-oxetanone) has a rich and interesting history in terms of both structural chemistry and chemical reactivity.[1] Certain ambiguities concerning its structural characterization persist to this day (see below). The dimerization of ketene ($H_2C=C=O$) to form diketene (**1**) is exothermic by 23 kcal/mol[2-4] with an approximate activation energy of $E_a = 31$

kcal/mol.[2] In terms of chemical reactivity, diketene serves as a useful source of ketene upon

vacuum pyrolysis (ca. 550 ℃),[5-7] and the utility of diketene in synthetic organic chemistry has

been widely exploited. Our interest in diketene derives from an interest in the high-resolution gas

phase rotational spectroscopy of diketene, itself, as well as the use of diketene as a pyrolytic

precursor to ketene for the purposes of other chemical and spectroscopic investigations. During

the course of these studies, we became aware of the lingering questions concerning the structure

of diketene, which we decided to address as part of our investigation.

A dimer of ketene was first reported experimentally in 1908.[8] Surprisingly, for such a

simple molecule, the structure of the dimer was unknown and the subject of controversy for 44

years.[1] There were at least five proposed and seriously considered molecular structures of

diketene, one acyclic and four cyclic $C_4H_4O_2$ molecules, as shown in Figure 2.1.[6, 9-11] The first

application of infrared spectroscopy to diketene by Miller and Koch in 1948 suggested a possible

equilibrium between two or three of the proposed structures (**1**, **2**, and **3**, Figure 2.1).[11] The

connectivity of the dimer was not firmly established until the 1950s, when the molecular structure

of diketene (**1**) was determined to be a [2+2] cycloaddition dimer of ketene by single-crystal X-

ray crystallography[12-14] and ^{1}H-NMR spectroscopy.[15] Microwave spectroscopy subsequently
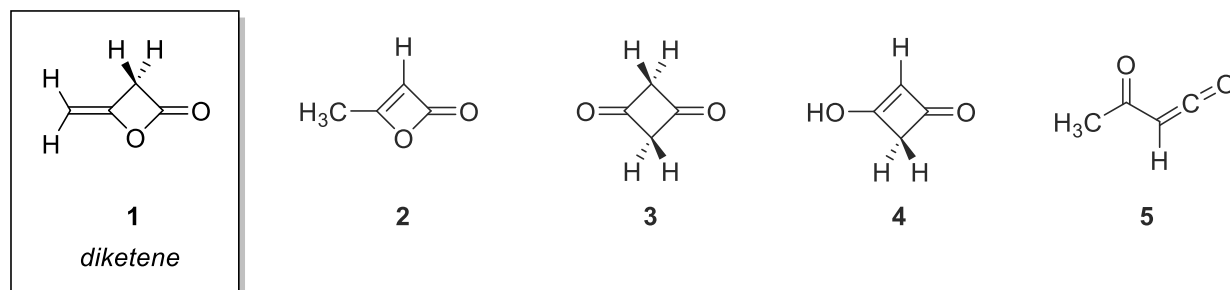
Figure 2.1. Diketene (**1**) and other $C_4H_4O_2$ isomers that have been considered as candidate structures for the dimer of ketene.

provided independent confirmation of the structure of diketene (**1**).[16] Nevertheless, when reliable *ab initio* predictions for the equilibrium structure of diketene (**1**) became available,[17-19] the accuracy of the experimental structure was called into question because of the unusually large discrepancy between computed and experimental values of the vinyl C–O bond distances (1.418 Å CCSD/DZd,[18] 1.47(3) Å X-ray[14]). This led the authors of the computational studies to call for a re-investigation of the experimental structure. In view of these questions concerning the structural data for diketene, we carried out a new single-crystal X-ray diffraction structure determination. Our new data (both experimental and computational) resolve the questions concerning structural parameters for diketene (**1**).

We consider diketene (**1**) to be an intriguing target for astrochemical detection. Ketene *(μ_a = 1.42429 D [20])* is a known molecule in the interstellar medium (ISM) and has been detected in molecular clouds,[21-24] near protostellar cores,[25-26] and extragalactically.[27] Interstellar ketene is postulated to be generated by the reaction of CO with CH_4 on dust-grain surfaces,[25] and this proposal has been supported by laboratory experiments involving the UV laser photolysis of CO-CH_4 ices.[28] If it were observed in the ISM, diketene (**1**) would represent the second molecule containing a four-membered ring and one of the larger organic species (10 atoms) detected.[29-30] Diketene (**1**) has been investigated by microwave spectroscopy up to 30 GHz,[16] as well as by liquid-phase Raman[31-32] and by gas and liquid-phase infrared spectroscopy.[31-35] The original microwave work of Mönnig *et al.*[16] determined the dipole moment *via* the Stark effect ($\mu_a = 2.28 \pm 0.02$ D, $\mu_b = 2.66 \pm 0.02$ D), and the rotational constants of diketene and also those of its two lowest energy vibrational satellites, ν_{24} and $2\nu_{24}$. Since 1967, however, the original microwave study[16] has not been updated. In the current study, we extend the microwave study into the millimeter-wave region and assign and least-squares fit the spectra of diketene and five of its

vibrationally-excited states (ν_{24}, $2\nu_{24}$, $3\nu_{24}$, $4\nu_{24}$, and ν_{16}) to single-state centrifugal distortion/rigid rotor Hamiltonians to within near experimental error. We also obtain least-squares fits of vibrational satellites $\nu_{24}+\nu_{16}$, ν_{23}, and $5\nu_{24}$, but they are less satisfactory, due to lower transition intensities and couplings between states.

COMPUTATIONAL METHODS

A CCSD(T)[36]/ANO1[37] equilibrium structure for diketene (**1**) was obtained using CFOUR[38] with analytic gradients.[39-40] This geometry was utilized to determine the fundamental frequencies, quartic distortion constants, and the vibration-rotation interactions with a 2nd-order vibrational perturbation theory (VPT2) anharmonic frequency calculation by evaluating the cubic force constants using analytical second derivatives at displaced points following the method of Stanton *et al.*[41-42] Output files for all calculations can be found in the Supporting Information of our published *J. Phys. Chem. A* 2016 paper. Diketene was also optimized at the B3LYP[43-44]/6-31G(d)[45] level, for use as an input structure for subsequent Natural Bond Orbital / Natural Resonance Theory (NBO/NRT[46-47]) calculations performed at the same level in Gaussian 09[48] using NBO 6.0[49]. High resolution molecular images were generated using POV-Ray.[50]

EXPERIMENTAL SECTION

Spectroscopy

The millimeter-wave spectrometer utilized for spectral collection has been described previously.[51-52] The diketene sample from BOC Sciences was used without further purification for all rotational spectroscopy studies. The decomposition products and stabilizer were not sufficiently volatile or absorbing to impact our ability to collect the rotational spectrum of diketene. Broadband spectra were collected at room temperature with a diketene pressure of ~ 10-20 mTorr over a frequency range of ~ 240 to 360 GHz. Broadband spectra were analyzed and least squares fit using Kisiel's AABS package[53-54] with ASFIT/ASROT.[55-56] Inertial defects and their standard uncertainties were calculated using Kisiel's PLAN program for each diketene state.

X-Ray Crystallography

The diketene sample was purified for X-ray crystallographic study by a two-stage trap-to-trap distillation. The commercial sample was red-orange in color, but a clear, colorless liquid was obtained upon distillation. Diketene was first cryopumped into a dry ice/acetone trap. The resulting white solid was then cryopumped into a collection flask in liquid nitrogen. Once the sample was warmed, it provided a sufficiently pure liquid sample for crystal growth to occur upon subsequent cooling.

The crystal of freshly distilled diketene was grown by a modified literature technique.[57-58] A thin-walled Lindemann capillary 0.7 mm in diameter was charged with 0.9 μL of diketene placed near the closed tip of the capillary and sealed off at the funnel end. The capillary was mounted on a goniometer head and coaxially aligned with the nozzle of the Oxford Cryostream 700 low temperature device at room temperature. The liquid was supercooled to −18 ℃ and nucleated by

touching the capillary with a cotton swab saturated with liquid nitrogen. The liquid diketene transitioned into a polycrystalline solid that was repeatedly heated and cooled between −8.5 and −11.4 ℃ in order to melt small crystals and preserve the larger ones until only one crystal remained in the liquid. Our purified sample of diketene melted at −10.5 ℃, rather than at the previously reported −6.5 ℃.[12-13] Once a colorless single crystal (2.6 × 0.6 × 0.1 mm) formed, the capillary was carefully cooled to −173 ℃ in order to conduct a single-crystal X-ray diffraction experiment. The X-ray diffraction was carried out in a routine fashion to a resolution of 0.66 Å, as described in the Supporting Information. All atoms were refined independently, the non-hydrogen atoms anisotropically. A complete discussion of the −173 ℃ structure of diketene and its packing features along with the results of its Hirshfeld atom refinement at various levels of theory will be forthcoming in a subsequent publication.

RESULTS AND DISCUSSION

Structure Determination. Our newly obtained X-ray crystal structure and analysis, prompted by the previously-noted discrepancy between the 1952/1958 crystal structure and *ab initio* structures, has largely resolved any structural ambiguity regarding the geometry of diketene (**1**) in the solid and gas phases.[12-14, 17-19] The chemical information file (CIF) for the −173 ℃ structure of diketene has been deposited with the Cambridge Structural Database with refcode CCDC 1487061, and the full report of the X-ray crystallography data is also available in the Supporting Information. Structural parameters from the X-ray crystal structure, along with the CCSD(T)/ANO1 computed structure, are shown in Table 2.1 and Figure 2.2. The current X-ray crystal structure is in very good agreement with the CCSD(T)/ANO1 structure. The *|obs. − calc.|* values for each of the heavy-atom bond distances are ≤ 0.017 Å, with the discrepancy for the problematic C-O bond distance (R_{C2-O5}) being reduced from 0.052 Å [12-14] to 0.017 Å.

Table 2.1. Comparison of Theoretical and Experimental Rotational Constants and Structural Parameters [a]

	μ-wave[16]	1952 X-ray Structure [12-13] C_1	1958 X-ray Structure [14] C_1	2016 X-ray Structure C_1	CCSD / DZd [18] C_s	CCSD(T) / ANO1 C_s
A_0 (MHz)	12141.357(40)				12051	12051
B_0 (MHz)	2781.268(10)				2747	2759
C_0 (MHz)	2296.589(10)				2270	2278
R_{C1-C2}		1.35(6)	1.32(3)	1.3146(11)	1.334	1.325
R_{C2-O5}		1.39(6)	1.47(3)	1.4295(9)	1.418	1.413
R_{C4-O5}		1.40(6)	1.39(3)	1.3849(9)	1.395	1.397
R_{C2-C3}		1.48(6)	1.54(3)	1.5035(10)	1.518	1.509
R_{C3-C4}		1.46(6)	1.51(3)	1.5161(11)	1.536	1.530
R_{C4-O6}		1.24(6)	1.22(3)	1.1914(9)	1.196	1.187
R_{C1-H7}				0.940(14)	1.089	1.081
R_{C1-H8}				0.949(15)	1.088	1.080
R_{C3-H9}				0.955(14)	1.097	1.089
R_{C3-H10}				0.967(12)	1.097	1.089
θ_{C1C2O5}		130(2)	126.9(15)	126.06(7)	126.8	126.6
θ_{C1C2C3}		136(2)	141.6(15)	141.34(7)	140.1	140.1
θ_{C3C2O5}		94(2)	91.3(15)	92.59(5)	93.1	93.3
θ_{C2C3C4}		83(2)	83.0(15)	82.96(5)	82.3	82.6
θ_{C3C4O5}		94.5(2)	95.8(15)	93.85(5)	93.3	93.0
θ_{C3C4O6}		145(2)	140.9(15)	140.08(7)	139.0	139.3
θ_{O5C4O6}		121(2)	123.1(15)	126.07(7)	127.7	127.6
θ_{C2O5C4}		89(2)	90.0(15)	90.56(5)	91.3	91.1
θ_{C2C1H7}				121.0(9)	121.1	120.9
θ_{C2C1H8}				120.5(9)	119.7	119.6
θ_{C2C3H9}				114.9(8)		116.4
$\theta_{C2C3H10}$				115.5(7)		116.4
$\theta_{C1C2C3H9}$				69.4(9)		+66.7
$\theta_{C1C2C3H10}$				−64.2(8)		−66.7

[a] Bond distances (Å), bond angles and dihedral angles (º).

Figure 2.2. a) Single-crystal X-ray structure (C_1) of diketene (**1**), shown with 50 % thermal probability ellipsoids. b) CCSD(T)/ANO1 equilibrium geometry (C_s) of diketene (**1**), depicted with rotational axes and experimental dipole moment vector.[16] Bond distances (Å) are in black and bond angles (º) are in red with standard uncertainties in parenthesis.

In terms of bond angles, the largest difference between the experimental and the predicted value, found for θ_{O5C4O6}, is 1.53º, compared to a difference of 4.5º when the 1958 crystal structure is used. The improved agreement between experiment and theory is attributable to the improvement in the quality of the experimental structure determination, an outcome anticipated by previous investigators.[17-19] The agreement of the CCSD(T)/ANO1 geometry with previous computed structures[17-19] is excellent, exhibiting an expected improvement in accuracy due to the higher level of theory.[59] The original crystallographic work on the structure of the ketene dimer was a tour-de-force in its day;[12-14] the refinement provided by the current study does not diminish the significance of those seminal studies.

The experimental crystal structure and the computed structure (CCSD(T)/ANO1) are not identical, nor should it be expected that they would be identical. The computed structure is planar (C_s), while the experimental structure displays a subtle deviation from planarity, presumably as a consequence of the crystal packing involved in the solid state. Distortions from planarity in four-

membered rings are typically characterized by the 'puckering' or 'butterfly' angle of the ring – in this case the angle between planes defined by C3-C2-O5 and C3-C4-O5. The value of this puckering angle is 2.1° and the manifestation of this distortion is not readily apparent from consideration of the structure depicted in Figure 1.2. Puckering of the ring will also be discussed later, in the context of the vibrational states of diketene (**1**).

In principle, a small molecule such as diketene (**1**) is amenable to gas-phase structure determination by rotational spectroscopy. Low symmetry (C_s), the presence of two oxygen atoms with isotopes of low natural abundance, and high spectral density in the mm-wave region, however, make observation and assignment of isotopologues at natural abundance completely impractical. A gas-phase equilibrium structure determination would likely require the chemical synthesis of at least six heavy-atom and three deuterium isotopologues of diketene (**1**).

Fundamental Vibrations. Using the optimized CCSD(T)/ANO1 geometry, an anharmonic frequency calculation provided fundamental frequencies that are in excellent agreement with experimental values (albeit with a notable exception). As shown in Table 2.2, the agreement is often within a few wavenumbers, validating the quality of the computed geometry and subsequent calculation of the anharmonic force field. An expanded list of predicted and experimental vibrational frequencies, along with a discussion of the problematic fundamental vibration, is available in the Supporting Information. Energies for one, two, and three quantum states were determined computationally; energies for $4\nu_{24}$ and $5\nu_{24}$ are reported as integer multiples of the energy of ν_{24}.

Table 2.2. Experimental and Computed Values for Lowest-Energy Fundamental Vibrations of Diketene (1) [a]

Fundamental	Sym.	Vibrational Motion	gas[34]	gas[32]	solution[32]	Ar matrix[35]	computed[b]	intensity[b]
ν_{20}	A″	C=CH$_2$ wag		838	836	837.3	840	48.7
ν_{13}	A′	in-plane ring stretching		803	803	805.4, 802.7	802	27.4
ν_{21}	A″	C=C twist					718	0.1
ν_{14}	A′	in-plane ring deformation			667		667	0.5
ν_{15}	A′	C=O in-plane bend		525	527	525.1	523	2.9
ν_{22}	A″	C=O out-of-plane bend		506	506	507.3, 505.9	507	1.1
ν_{23}	A″	C=C out-of-plane bend	444	444	443	446.3, 444.8	445	9.5
ν_{16}	A′	C=C in-plane bend	324		325		315	0.7
ν_{24}	A″	ring-puckering	128.8				129	1.0

[a] Frequency (cm^{-1}), intensity (km/mol). [b] CCSD(T)/ANO1 anharmonic VPT2.

Rotational Spectroscopy. The rotational constants of diketene (**1**) determined by Mönnig *et al.*[16] were the starting point of this study for the ground state of diketene and its two lowest energy vibrational satellites (ν_{24} and $2\nu_{24}$). For all the diketene states studied here, a full list of the number and types of transitions observed, measured, and least-squares fit are provided in Table 2.3. These transitions are a combination of R-branch and Q-branch absorptions (of both a- and b-type), which lead to an excellent fit of the quartic and all or most of the sextic centrifugal distortion constants for the states that can be fit by single state models. Each least-squares fit was completed using both the A- and S-reduced Hamiltonians in the I^r representation, which is appropriate for a near-prolate asymmetric top ($\kappa \approx -0.90$ for all states). All measured transitions with an $|obs - calc|$ value > 0.10 MHz, in either the A- or S-reduced fit, were removed from the data sets. In the very transition-rich rotational spectrum, such errors were generally due to accidentally overlapping absorption lines. The S-reduction fits are presented in the manuscript, and the A-reduction fits are available in the Supporting Information. To further validate each least-squares fit, the rotational constants from either the A- and S-reduction were converted to the determinable constants (B'') using Equations 1.1 – 1.6.[60] For the ground state fit, these two methods of generating the determinable constants ($B''^{(A)}$ and $B''^{(S)}$) showed remarkable agreement, differing by 26 Hz, 3.5 Hz, and 4.1 Hz for A'', B'', and C'', respectively. This level of agreement is a clear confirmation that the rotational and quartic distortion constants are very well determined by both reductions. The determinable constants for all vibrational states in this work are available in the Supporting Information.

$$A''^{(A)} = A^{(A)} + 2\Delta_J \tag{1.1}$$

$$B''^{(A)} = B^{(A)} + 2\Delta_J + \Delta_{JK} - 2\delta_J - 2\delta_K \tag{1.2}$$

$$C''^{(A)} = C^{(A)} + 2\Delta_J + \Delta_{JK} + 2\delta_J + 2\delta_K \tag{1.3}$$

$$A''^{(S)} = A^{(S)} + 2D_J + 6d_2 \tag{1.4}$$

$$B''^{(S)} = B^{(S)} + 2D_J + D_{JK} + 2d_1 + 4d_2 \tag{1.5}$$

$$C''^{(S)} = C^{(S)} + 2D_J + D_{JK} - 2d_1 + 4d_2 \tag{1.6}$$

Table 2.3. Number of Observed Rotational Transitions for each Vibrationally-Excited State of Diketene (1) [a]

Transition Type	ground state[b]	ν_{24}[b]	$2\nu_{24}$[b]	ν_{16}	$3\nu_{24}$	$\nu_{24} + \nu_{16}$	ν_{23}	$4\nu_{24}$	$5\nu_{24}$
$^aR_{0,1}$	2222	1932	1518	1346	1419	142	232	683	180
$^bR_{1,1}$	341	325	278	243	223	65	93	145	73
$^bR_{-1,1}$	216	177	155	143	137	66	83	88	75
$^bR_{1,-1}$	151	136	124	78	90	0	1	49	0
$^bR_{3,-1}$	3	1	0	0	1	0	0	0	0
$^bR_{-1,3}$	2	0	0	0	0	0	0	0	0
$^aQ_{0,-1}$	98	74	43	33	29	0	0	0	0
$^aQ_{2,-1}$	97	74	43	30	31	0	0	0	0
$^bQ_{1,-1}$	1278	1016	716	608	601	0	0	274	0
$^bQ_{3,-3}$	12	11	4	6	4	0	0	0	0
Independent Measurements	2700	2199	1654	1449	1438	74	186	661	120

[a] For degenerate sets of lines, each individual transition was included.
[b] Low J transitions were included from Mönnig et al.[16]

The most distinguishable features of the diketene spectra are R-branch band origins consisting of sets of two $^aR_{0,1}$, one $^bR_{1,1}$, and one $^bR_{-1,1}$ type transitions, which appear degenerate for small values of $K_{prolate}$, resulting in lines of particularly high relative intensity. As the degeneracy is lost moving to higher values of $K_{prolate}$, they begin to appear as easily identifiable quartets for several sets of transitions. For the ground state, our spectral region allowed for

observation and fitting of transitions with J' values from 45 to 120 for the R-branch transitions, which we combined with J' values of 2, 3, and 4 from Mönnig *et al.*[16] The Q-branch values of J' range from 62 to 109, which we likewise combined with $J' = 3$ from the previous microwave work.[16] The wide range of transition types and the sheer number of measured transitions allowed for a precise determination of the rotational constants and quartic and sextic distortion terms, except for H_K. The experimental quartic distortion constants were within 1.2 to 4.3 % of those predicted at the CCSD(T)/ANO1 level, with the largest discrepancy in the value of D_K. The value of H_K of the ground state is a smaller by approximately an order of magnitude than any other H_K value. It is the smallest constant value determined for the ground state relative to its estimated uncertainty, but is consistent with the trends of the H_K values for the v_{24} series. Its absolute error is quite similar to the uncertainty of H_K for v_{24}. As a result of our confidence in this value, it was allowed to vary in the least-squares fitting to not artificially impact the other distortion constants. The summary of the spectral parameters from the least-squares fitting for the ground state of diketene and for its vibrational satellites is displayed in Table 2.4. For the ground state, a distribution plot of the J'' and $K_{prolate}''$ of all measured transitions included in the least-squares fit is presented in Figure 2.3 as produced from Kisiel's Automatic Converter (AC) program in the AABS suite.[53-54] The final fit for the ground state included 2700 independent transitions, yielded a σ value of 0.033 MHz, and determined the rotational constants to an estimated uncertainties of 240 Hz, 43 Hz, and 47 Hz for A_0, B_0, and C_0, respectively.

Table 2.4. Rotational and Centrifugal Distortion Constants for Diketene (1) and its Vibrational Satellites,[a] S-Reduction, I[r] Representation

	CCSD(T) / ANO1	diketene, C_s ground state[b]	ν_{24} (A″, 129 cm^{-1})[b]	$2\nu_{24}$ (A′, 258 cm^{-1})[b]	ν_{16} (A′, 315 cm^{-1})
A_v (MHz)	12051	12141.42717 (24)	12020.75853 (31)	11904.30234 (41)	12226.27229 (46)
B_v (MHz)	2759	2781.277396 (43)	2784.529302 (80)	2787.79576 (13)	2781.97391 (14)
C_v (MHz)	2278	2296.590224 (47)	2301.819740 (83)	2307.04237 (14)	2296.13824 (15)
D_J (kHz)	0.140	0.1448857 (80)	0.150070 (20)	0.155193 (38)	0.144049 (40)
D_{JK} (kHz)	1.21	1.195998 (30)	1.149741 (40)	1.101003 (61)	1.184602 (72)
D_K (kHz)	7.16	7.4828 (12)	5.7880 (15)	4.4004 (19)	9.6177 (23)
d_1 (kHz)	−0.0275	−0.0281605 (15)	−0.0279663 (20)	−0.0277209 (42)	−0.0282171 (54)
d_2 (kHz)	−0.00530	−0.00551273 (68)	−0.00502930 (92)	−0.0045852 (14)	−0.0059909 (19)
H_J (Hz)		0.00001237 (42)	0.0000178 (16)	0.0000130 (34)	0.0000177 (36)
H_{JK} (Hz)		−0.0002262 (33)	−0.0002926 (43)	−0.0003549 (61)	−0.0003694 (87)
H_{KJ} (Hz)		0.0009493 (84)	0.004439 (11)	0.006543 (26)	0.000971 (25)
H_K (Hz)		−0.0051 (17)	−0.0740 (21)	−0.1214 (25)	0.0374 (33)
h_1 (Hz)		0.00000446 (11)	0.00000480 (15)	0.00000380 (35)	0.00000615 (47)
h_2 (Hz)		0.000002371 (88)	0.00000211 (11)	0.00000144 (18)	0.00000349 (28)
h_3 (Hz)		0.000000771 (14)	0.000000328 (22)	[−0.000000115][c]	0.000001467 (60)
Δ_i (u Å^2)		−3.2756270 (54)	−3.9812072 (96)	−4.676862 (17)	−2.897961 (18)
κ		−0.902	−0.901	−0.900	−0.902
N_{lines}		2700	2199	1654	1449
σ_{fit}		0.033	0.037	0.036	0.040

	$3\nu_{24}$ (A″, 388 cm^{-1})	$\nu_{24}+\nu_{16}$ (A″, 443 cm^{-1})^d	ν_{23} (A″, 445 cm^{-1})^d	$4\nu_{24}$ (A′, 517 cm^{-1})	$5\nu_{24}$ (A″, 646 cm^{-1})^d
A_v (MHz)	11791.75219 (51)	12100.9 (10)	12110.449 (39)	11682.8790 (11)	11577.513 (48)
B_v (MHz)	2791.07766 (16)	2784.574 (55)	2782.6390 (12)	2794.37538 (28)	2797.6913 (23)
C_v (MHz)	2312.26420 (18)	2300.79979 (53)	2298.1595 (10)	2317.48337 (36)	2322.7172 (11)
D_J (kHz)	0.160628 (47)	0.137335 (65)	0.18574 (33)	0.165828 (86)	0.17360 (40)
D_{JK} (kHz)	1.051826 (79)	1.391 (18)	−2.813 (32)	0.99775 (17)	0.970 (20)
D_K (kHz)	3.2505 (23)	4.83 (73)	65.01 (63)	2.3344 (48)	[1.71]^c
d_1 (kHz)	−0.0274261 (47)	[−0.0280]^f	−0.02931 (13)	−0.0273802 (64)	−0.02753 (14)
d_2 (kHz)	−0.0041709 (18)	[−0.00551]^f	0.00631 (13)	−0.0038626 (35)	−0.003963 (34)
H_J (Hz)	0.0000330 (41)	[0.0000233]^f	0.005384 (51)	0.0000233 (75)	0.000217 (18)
H_{JK} (Hz)	−0.0003439 (79)	[−0.000436]^f	−0.7697 (88)	−0.000202 (22)	[0.000115]^c
H_{KJ} (Hz)	0.007654 (23)	[0.00446]^f	12.68 (23)	−0.00372 (14)	[−0.0510]^c
H_K (Hz)	−0.1333 (29)	[−0.0315]^f	[−0.00518]^e	−0.0334 (56)	[0.317]^c
h_1 (Hz)	0.00000347 (37)	[0.00000651]^f	0.000506 (22)	[0.00000586]^c	[0.0000130]^c
h_2 (Hz)	0.00000140 (23)	[0.00000324]^f	−0.001970 (28)	[0.00000301]^c	[0.00000728]^c
h_3 (Hz)	−0.000000230 (41)	[0.00000102]^f	0.0001129 (60)	[0.000000312]^c	[0.00000184]^c
Δ_i (u Å^2)	−5.363616 (21)	−3.6024 (50)	−3.44345 (18)	−6.041559 (39)	−6.71228 (26)
κ	−0.899	−0.901	−0.901	−0.898	−0.897
N_{lines}	1438	74	186	661	120
σ_{fit}	0.042	0.047	0.044	0.042	0.041

^{a} Fundamental vibrational frequencies calculated at CCSD(T)/ANO1 with anharmonic corrections at VPT2.

^{b} Includes transitions from previous work.[16]

^{c} Fixed in the least-squares fit to the value estimated by extrapolation from the ν_{24} vibrational state series.

^{d} Partially least-squares fit as a single state.

^{e} Fixed to ground state value.

^{f} Predicted from the ground state, ν_{24}, and ν_{16} and held at those values.
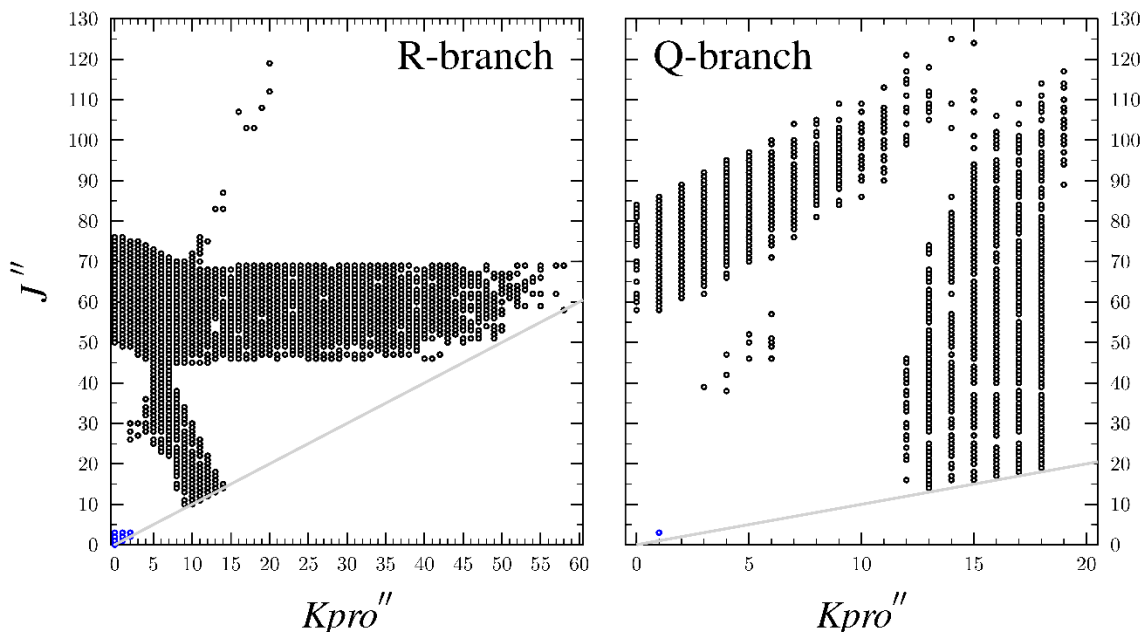
Figure 2.3. Data set distribution plots of *J″* and *K_prolate″* of all transitions for the ground state spectrum of diketene (**1**). Transitions included from Mönnig *et al.*[16] are in blue. Similar plots for other states are provided in the Supporting Information.

Vibration-Rotation Coupling. The computational equilibrium geometry corrected for the vibration-rotation interactions leads to B_0 values that reproduce the previously published and current experimental rotational constants to within 0.74 to 0.81%. This level of agreement is consistent with other coupled-cluster estimates.[61]

The experimental vibration-rotation interaction constants (α_i) for were determined by the change in rotational constant from the ground state to the vibrationally excited state (Table 2.5). The coupled-cluster α_i values for ν_{24} are in excellent agreement (within 1 %) with those experimentally observed. For ν_{16}, the percentage errors are significantly higher for α_B (20 %) and α_C (13 %), primarily due to their small magnitudes, but they still have absolute errors less than 0.2 MHz. The absolute and percentage errors associated with states ν_{24} and ν_{16} are in line with those reported previously using CCSD(T) calculations with similar basis sets.[52, 61-62]

Table 2.5. Experimental and Computed Vibration-Rotation Interaction Constants (α_i) for Diketene (1)

	ν_{24} (A″, 129 cm^{-1})		ν_{16} (A′, 315 cm^{-1})		ν_{23} (A″, 445 cm^{-1})[a]	
	Predicted[b]	Observed[c]	Predicted[b]	Observed[c]	Predicted[b]	Observed[c]
α_A (MHz)	−121	−120.668	85.0	84.845	−25.6	−31.0
α_B (MHz)	3.22	3.252	0.839	0.697	0.597	1.36
α_C (MHz)	5.19	5.229	−0.392	−0.452	0.926	1.56

[a] Values from a partial single-state fit were obtained for ν_{23} despite the impact of coupling to $\nu_{24}+\nu_{16}$. [b] CCSD(T)/ANO1 anharmonic VPT2. [c] Average value of the determinable constants obtained from A-reduction and S-reduction.

The differences between predicted and observed α_i values for ν_{23} are substantially higher (Table 2.5), probably due to the preliminary nature of the fit. Even so, the level of agreement in α_i values, along with the observed relative intensities, is adequate to allow us to confidently assign the identified transitions to ν_{23}.

Computed values (CCSD(T)/ANO1) of the vibration-rotation interaction constants (α_i) were used to predict, and subsequently assign, rotational transitions for the vibrational satellite derived from fundamental ν_{16} (315 cm^{-1}, C=C in-plane bend). Since this state had not been observed in previous microwave work,[16] the predicted changes in rotational constants with respect to the ground state were very important in the initial search for ν_{16}. More than 1600 distinct transitions were eventually measured and least-squares fit to a complete sextic centrifugal distortion/rigid rotor Hamiltonian. As would be expected with no other vibrational states close in energy, a single-state model was sufficient to achieve an excellent fit for all of the measured transitions.

Perturbations are clearly present in the closely lying states of $\nu_{24}+\nu_{16}$ (443 cm^{-1}) and ν_{23} (445 cm^{-1}, the bend of the C=C bond out of the ring plane). This only allowed for a partial least-squares fit for each of these states using a single-state model (Table 2.4). As with ν_{16}, coupled-cluster values of the α_i constants were used to predict, and subsequently assign, transitions for the fundamental ν_{23}. The changes in experimental constants for ν_{24} and ν_{16} relative to the ground state were used to predict constants for the combination state, $\nu_{24}+\nu_{16}$. Based upon these initial predictions, the first few R-branch transitions were unambiguously assigned and least-squares fit for both $\nu_{24}+\nu_{16}$ and ν_{23}.

Vibrational Satellite ν_{24}: Ring-Puckering Mode. The previous experimental work[16] was adequate to predict and assign the spectra of the first two satellites of the nominally ring-puckering mode, ν_{24} and $2\nu_{24}$. Previous computational work estimated that this mode can be characterized as 42% ring puckering, 32 % an out-of-plane bend of the C=C double bond, and 16 % an out-of-plane =CH$_2$ wag.[17] Roughly the same types of R-branch and Q-branch transitions were observed for these states as for the ground state, with previously reported transitions included from Mönnig *et al.*[16] (Table 2.4). Despite fewer transitions that could be successfully identified and measured for these states, excellent fits were obtained using sextic centrifugally distorted Hamiltonians. Combined with the ground state constants, these constants allowed for reliable prediction of all observed ν states of the ν_{24} vibration. In the $\nu_{24} = 2$, 4, and 5 least-squares fits, not all sextic terms could be satisfactorily determined. Values for these distortion terms were extrapolated using a linear or polynomial fit from the values obtained from other ν_{24} states and were fixed (Table 2.4). All transitions of $\nu_{24} = 0$, 1, 2, 3 in our frequency range were well predicted from the single-state models employed, but due to perturbations and/or the small number of transitions measured, this was not the case for $4\nu_{24}$ and $5\nu_{24}$. The band origin frequencies are very regularly spaced (~ 646

MHz) for this series of ν_{24} overtones, which is consistent with the highly harmonic nature of the ring-puckering vibration that has already been observed in the previous infrared analysis.[34] Figure 2.4 shows the progression from the ground state to $5\nu_{24}$ for their $J' = 68 \leftarrow J'' = 67$ band origin transitions in the region of 314 to 319 GHz.
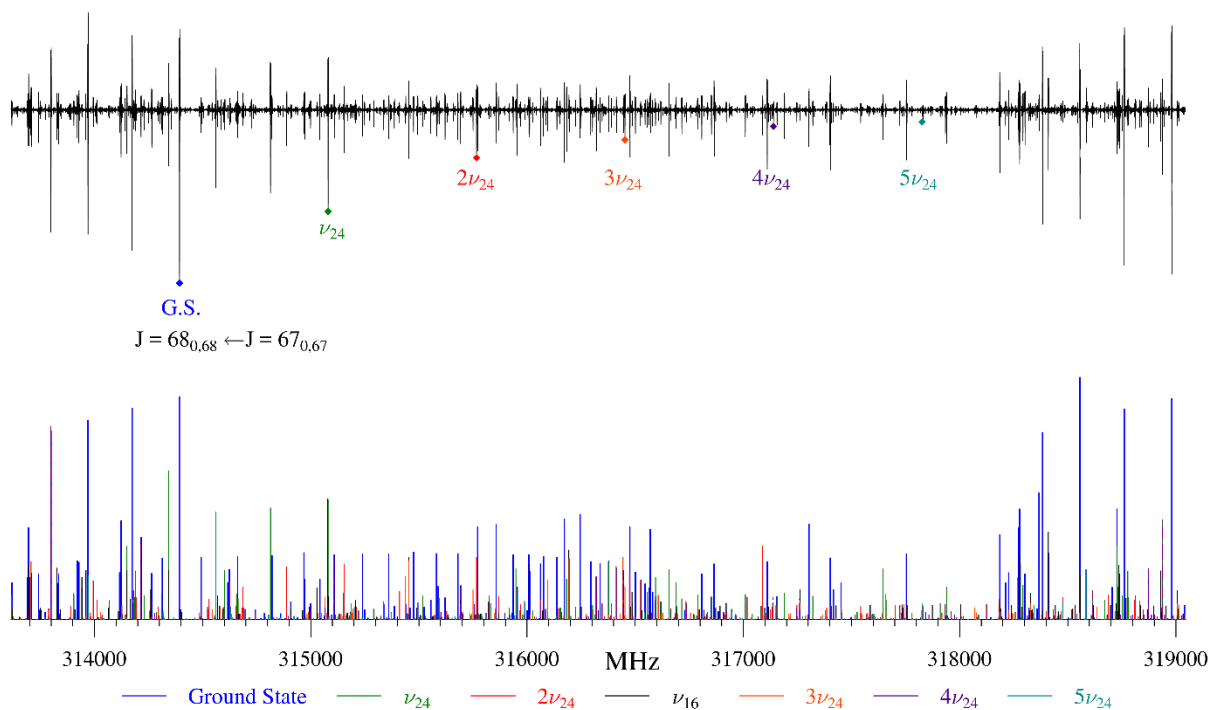
Figure 2.4. Experimental spectrum of diketene (upper) with stick spectrum of each vibrational excited state (lower). Diamond markers denote the $J' = 68 \leftarrow J'' = 67$ band origins for each quantum of ν_{24}.

As can be seen in Figure 2.5a, all of the variations in the rotational constants from $v_{24} = 0$ through $v_{24} = 5$ were monotonic, smooth, and relatively linear, which is another indication of the high degree of harmonicity of this vibration. The changes in each of the rotational constants through $v_{24} = 4$ were fit to a quartic polynomial and extrapolated to $v_{24} = 5$. The extrapolated values of A_0, B_0, and C_0 were in excellent agreement with the experimentally determined values, indicating that the incomplete fit of $5\nu_{24}$ resulted in reliable rotational constants. This linear
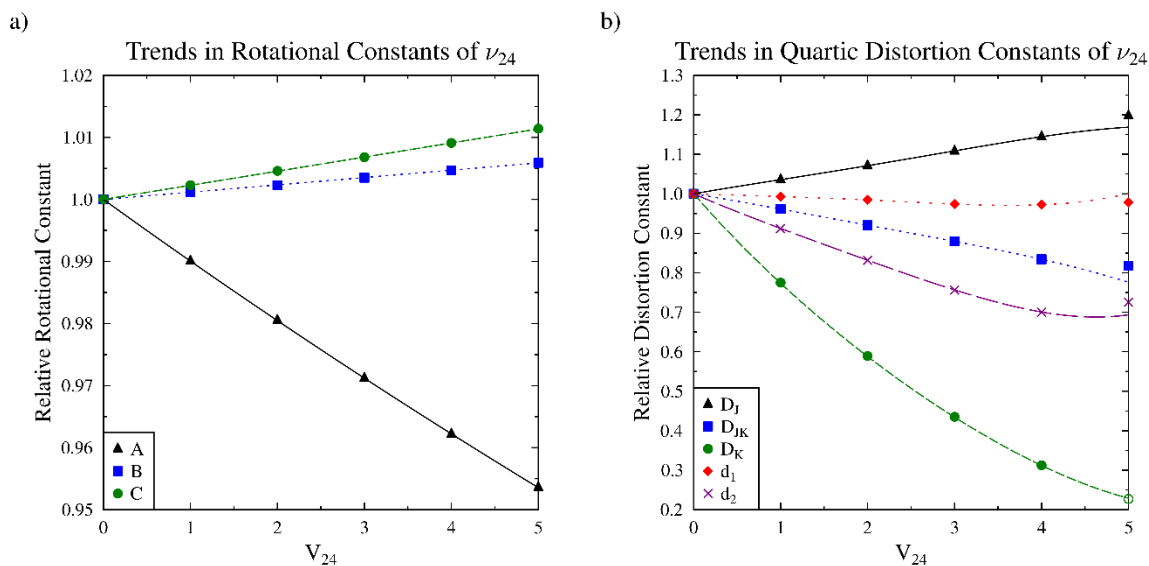
Figure 2.5. (a) Relative determinable rotational constants and (b) relative S-reduction quartic distortion constants, for diketene (**1**) as a function of vibrational excitation (v_{24} = 0, 1, 2, 3, 4, 5). The trend line for each series is a quartic polynomial fit generated from v_{24} = 0, 1, 2, 3, 4 and extrapolated through v_{24} = 5. The value of D_K of $5v_{24}$, represented by an open green circle, was held constant.

behavior has been noted in other ring-containing molecules with highly harmonic ring-puckering modes, such as cyclopent-3-en-1-one (**6**)[63-64] and β-propiolactone (**7**)[65] (Figure 2.6). These smooth changes in the constants are mirrored in the behavior of the quartic distortion terms and provided confirmation of the physical reality of each of the distortion terms for v_{24} = 0 through v_{24} = 4 (Figure 2.5b). This is in stark contrast to the strongly anharmonic character displayed by the quartic distortion terms of the first five ring-puckering vibrations of oxetane measured by high resolution far infrared spectroscopy.[66] The changes of the quartic distortion terms (specifically $\mathit{\Delta}_{JK}$, $\mathit{\Delta}_K$, and δ_K) of oxetane (c-C_3H_6O, **8**) are non-monotonic and show dramatically more complex structure, which has nevertheless been well explained theoretically.[66] Unlike the lower energy states of diketene (v_{24} = 0, 1, 2, and 3) already discussed, only four sextic terms could
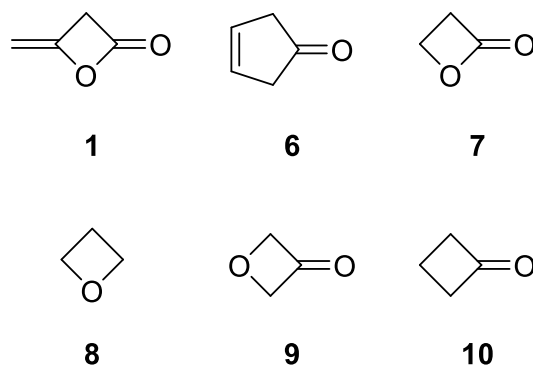
Figure 2.6. Diketene (**1**) and related structures for which ring-puckering vibrational motions are considered.

be determined for $v_{24} = 4$ and only a single sextic term could be determined for $v_{24} = 5$ in their respective least squares fits. These two states are predicted *via* a Boltzmann distribution to have transitions with intensities approximately 8.0 % ($4v_{24}$) and 4.3 % ($5v_{24}$) relative to the identical ground state transition, reducing the number of measurable transitions. In the R-branch series of $4v_{24}$, the transitions could not be measured and least-squares fit in a single-state model beyond $K_{prolate} \sim 25$. The incomplete treatment of the sextic terms due to the lower number of fit transitions, as well as untreated Fermi or Coriolis perturbations to near-energy satellites, can impact the quartic distortion terms in unpredictable ways. It appears, however, that for $4v_{24}$ (517 cm^{-1}) the reduced number of transitions included in the fit and impact of any coupling to v_{22} (507 cm^{-1}) and v_{15} (523 cm^{-1}) has little effect on the quartic distortion terms (Figure 2.5b). Despite the reliability of the $4v_{24}$ rotational and quartic distortion constants, there remains a strong possibility of coupling to v_{22} and/or v_{15}, neither of which have been even partially fit. The low number of transitions assigned and measured for $5v_{24}$ (646 cm^{-1}), due to its transition intensities and possible coupling with $2v_{16}$ (630 cm^{-1}), required that D_K and all of the sextic distortion constants (except H_J) be fixed to extrapolated values in the least-squares fitting. The four remaining $5v_{24}$ quartic

distortion constants from the incomplete fit varied from the extrapolated values by up to 4.4 % (Figure 2.5b).

Because our data set includes numerous instances in which we have measured the same rotational transition for each observed value of ν_{24}, it is possible to utilize these measured intensities (relative to the ground state) to obtain an experimental estimate for the energy of the rotational state, which corresponds to the fundamental frequency of the ν_{24} vibrational mode. The intensities were measured for each of the ν_{24} states (ν_{24} = 0-5) for forty-five such R-branch transition sets. The apparent excitation energy (cm^{-1}) of each vibrational state was estimated from its intensity (relative to the ground state) using Equation 1.7, where c is the speed of light in cm/sec and T is the ambient temperature of 292 K.

$$E_V - E_0(cm^{-1}) = -\frac{k_B T}{hc} ln\left(\frac{I_V}{I_0}\right) \tag{1.7}$$

The mean apparent energy values were plotted versus the vibrational quantum number (Figure 2.7), producing a slope of 123.6 ± 1.5 cm^{-1} (where the uncertainty is at the 95% confidence level from the Student t distribution for four degrees of freedom). The depicted error bars are uncertainties in each apparent energy, which are estimated to be the standard deviations of the mean of the forty-five individual apparent energy values. The slope and its associated uncertainty were determined by a weighted least-squares fitting of the mean of the apparent energy values for each ν_{24} state. This high degree of linearity is another indication of the highly harmonic nature of ν_{24}. The estimated energy of ν_{24} derived from this analysis (123.6 ± 1.5 cm^{-1}; Figure 2.7) is in reasonable agreement with the CCSD(T)/ANO1 predicted value of 129 cm^{-1} (Table 2.2) and the direct gas phase measurement of an absorption peak at 128.8 cm^{-1}.[34] Since the gas phase infrared measurement is not derived from a rotationally-resolved spectrum, the true frequency of the band

origin remains somewhat uncertain, which may account for some portion of the difference between the two experimentally-derived values (123.6 cm^{-1} vs. 128.8 cm^{-1}).
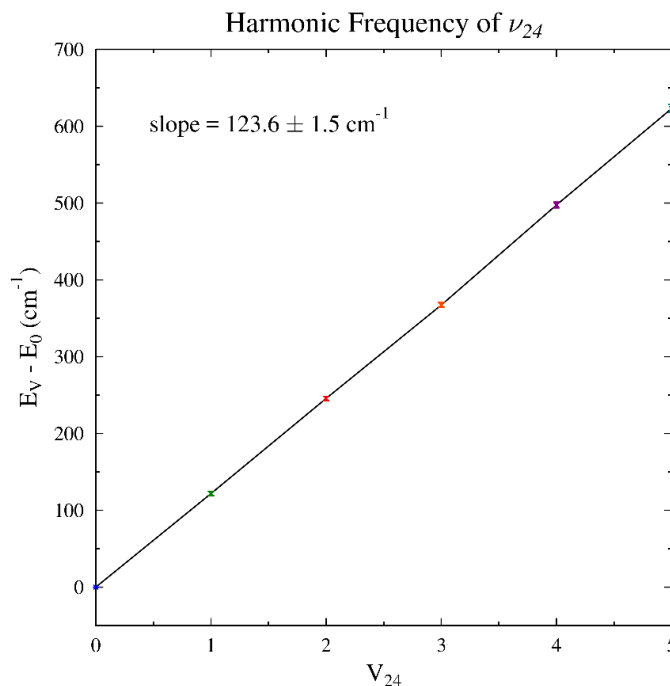
Figure 2.7. Fundamental frequency (cm^{-1}) of ν_{24} vibrational mode of diketene (**1**) derived from measurements of line intensities of rotational transitions from v_{24} = 0, 1, 2, 3, 4, 5.

The highly harmonic nature of the ring-puckering mode of diketene is confirmed by both the regular progression of the rotational and distortion constants as v_{24} changes (Figure 2.5) and the linearity of the vibrational excitation energies estimated from the relative intensities of rotational transitions (Figure 2.7). It is not surprising that a four-membered β-lactone ring, with the conjugation of an ester functional group, would see an increase in rigidity compared to four-membered rings lacking π conjugation. Though π-bonding character within the four-membered ring may not be the only important factor, the relationship between π conjugation, rigidity, and harmonic behavior is consistent with previous reports on the very anharmonic behavior of the ring-puckering mode of oxetan-3-one (**9**)[34] and cyclobutanone (**10**)[67] and harmonic character of the

ring-puckering mode of β-propiolactone (**7**),[65] all shown in Figure 2.6. A Natural Bond Orbital /

Natural Resonance Theory (NBO/NRT) analysis was performed to assess the extent of π

conjugation within the four-membered ring in diketene (**1**), and to estimate the contributions of

the most important resonance structures (Figure 2.8). The highest contributing resonance structure

(**1a**, 65 %) is the conventional depiction of diketene. Important contributors to ring rigidity are

structures **1b** (9 %) and **1d** (5 %), which include a formal π bond within the ring. Further

promoting the planarity and rigidity of diketene is the fact that puckering of the ring would

introduce eclipsing interactions between one of the hydrogens of the CH_2 group in the ring and

both the exocyclic $=CH_2$ group (1,3-allylic strain) and the carbonyl group.
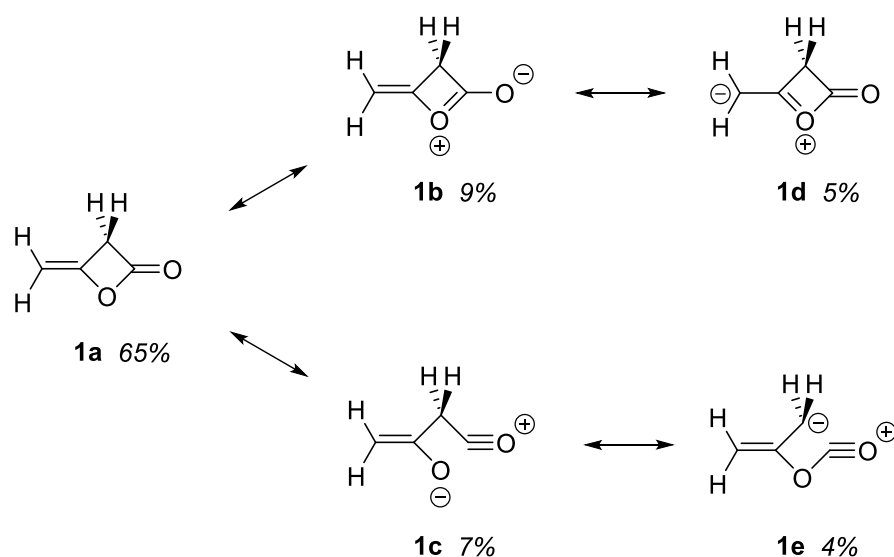
Figure 2.8. Resonance structures and relative contributions for diketene (**1**) computed using Natural Bond Orbital / Natural Resonance Theory (B3LYP/6-31G(d)).

CONCLUSIONS

A long-standing discrepancy between the 1952/1958 X-ray crystal structures and the *ab initio* structures of diketene (**1**) has been resolved. We obtained a new solid-state structure of diketene (**1**) at -173 °C using single-crystal X-ray diffraction. The bond distances are increased in precision by more than an order of magnitude compared to those in the 1958 X-ray crystal structure. The experimental structure exhibits excellent agreement with the equilibrium structure predicted using coupled-cluster theory (CCSD(T)/ANO1). The measured rotational spectrum for diketene (**1**) has been extended from the microwave to the mm-wave region, providing the foundation for an astronomical search for diketene. The precise determination of rotational constants and quartic distortion constants for the ground state of diketene showed excellent agreement with computational predictions. The accuracy of the vibration-rotation interaction (α_i) constants computed at CCSD(T)/ANO1 proved sufficient for the detection of the previously unreported vibrational satellites associated with fundamental modes ν_{16} and ν_{23}. A series of vibrational satellites (ν_{24}, $2\nu_{24}$, $3\nu_{24}$, $4\nu_{24}$, $5\nu_{24}$) have been measured involving the lowest frequency fundamental mode - a ring-puckering mode. These data permit the determination of the fundamental vibrational frequency (123.6 ± 1.5 cm^{-1}) and strongly support the conclusion that the vibrational mode is highly harmonic.

POST 2016 WORK

Previously, we discussed the unsatisfactory treatment of $\nu_{24}+\nu_{16}$ and ν_{23} of diketene. The $\nu_{24}+\nu_{16}$ and ν_{23} states are predicted at 443 and 445 cm^{-1} (Table 2.4, CCSD(T)/ANO1), respectively. State ν_{23} begins to show strong perturbations in the Loomis-Wood plots of its $^{a}R_{0,1}$

series around $K_a^- = 8$ and "disappears" at $K_a^- = 10$, but the series become visible again around K_a^- = 12. State $\nu_{24}+\nu_{16}$ begins to show strong perturbations around $K_a^+ = 6$ before "disappearing" at $K_a^+ = 8$. Some Q-branch series were also assigned, and least-squares fit for each state. Given that the K_a's that interact for ν_{23} are higher than those in $\nu_{24}+\nu_{16}$, this gives an indication that ν_{23} is actually lower in energy than $\nu_{24}+\nu_{16}$, inconsistent with the computed energies. Observable perturbation in the Loomis-Wood plot, inability to predict missing transitions and large statistical uncertainties in the fit indicates that the coupled-state model for the dyad is not properly treating the perturbation yet. No coupling terms or the energy gap are being determined by the fit, they are held fixed (energy gap and Fermi) or held fixed to zero (Coriolis). There is a Fermi coupling term predicted between these states, which can be estimated computationally. The Coriolis terms are not readily available from theoretical predictions because the coupling is between a combination state and a fundamental. The theory for this type of interaction is not yet implemented, and the investigation into this theoretical issue is of fundamental importance to many projects and the broader microwave/mm-wave community. As such, the investigation into this theoretical project been taken on by Andrew N. Owen of our group and John F. Stanton, our collaborator at the University of Florida. With or without initial theoretical predictions or expansion of the frequency range, this project may be feasible given our group's recent success in fitting the mm-wave spectra of coupled dyads.[68-71]

PURSUIT OF THE ACYLIUM ION

The diketene project began because diketene pyrolyzes into ketene ($H_2C=C=O$). In future, we will use ketene in a discharge to attempt formation and the collection of spectra of the acylium

cation ($H_3C-C\equiv O^+$), which would be of great interest to the astrochemical community. We were able to successfully pyrolyze diketene into ketene in our spectrometer using the hot-finger designed by R. Claude Woods and Brent K. Amberger and built by Tracy O. Drier (Figure 2.9). The details of this apparatus are included in Amberger's thesis.[72]
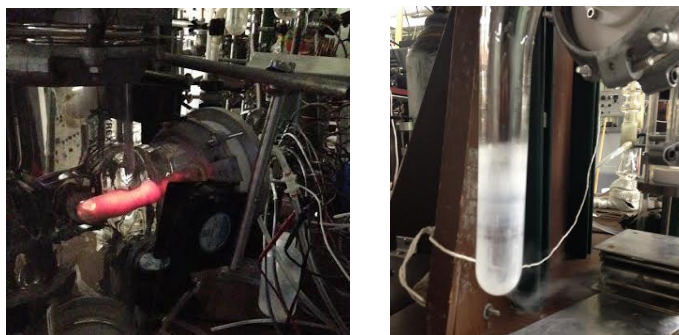
Figure 2.9. The hot-finger at ca. 550 ˚C (left) inside the spectrometer and the glass side-arm trap with ketene and other pyrolysis products (right).

Diketene was not stably stored long-term and is no longer commercially available. While diketene can be synthesized by the procedure by Nakashige, *et al.*,[73] ketene can also be accessed directly via a ketene lamp. Samuel A. Wood constructed a ketene lamp with assistance from Drier and produced a more-than-sufficient amount of ketene from acetone, which is easily available and can be purchased with various isotopic substitutions. The next step in this project is to investigate the discharge of ketene, which we hypothesize will create acylium ion. It is possible that a discharge will also produce diketene, and the work presented in this chapter will certainly allow us to monitor its presence in various discharge conditions, which was one of the original motivations for this project.

ACKNOWLEDGMENTS

SUPPORTING INFORMATION

The Supporting Information is available free of charge on the ACS Publications website at DOI:

10.1021/acs.jpca.6b07610

Description of content of .zip file (Table S1), A-reduction constants (Table S2), determinable constants (Table S3), previous and current rotational constants comparison (Table S4), summary of computational work (Tables S5 and S6), comparison of computational and experimental vibrational frequencies (Table S7), the complete crystallography report (Tables S8-S15, and Figure S10) (PDF)

ASROT/ASFIT output files, CCSD(T)/ANO1 optimization and anharmonic frequency output files, diketene NBO NRT .txt file, diketene.inp file, CIF file (ZIP)

REFERENCES

1. Clemens, R. J., Diketene. *Chem. Rev.* **1986**, *86* (2), 241-318.

2. Chickos, J. S.; Sherwood, D. E.; Jug, K., Mechanism of Thermolysis of Diketene in the Gas Phase. *J. Org. Chem.* **1978**, *43* (6), 1146-1150.

3. Nuttall, R. L.; Laufer, A. H.; Kilday, M. V., The Enthalpy of Formation of Ketene. *J. Chem. Thermodyn.* **1971**, *3* (2), 167-174.

4. Månsson, M.; Nakase, Y.; Sunner, S., The Enthalpies of Combustion and Formation of Diketene. *Acta Chem. Scand.* **1968**, *22* (1), 171-174.

5. Boese, A. B., Diketene - A New Industrial Chemical. *Ind. Eng. Chem.* **1940**, *32* (1), 16-22.

6. Rice, F. O.; Roberts, R., The Structure of Diketene. *J. Am. Chem. Soc.* **1943**, *65* (9), 1677-1681.

7. Andreades, S.; Carlson, H. D., Ketene. *Org. Synth.* **1965**, *45*, 50.

8. Chick, F.; Wilsmore, N. T. M., Acetylketen: A Polymeride of Keten. *J. Chem. Soc., Trans.* **1908**, *93*, 946-950.

9. Angus, W. R.; Leckie, A. H.; Le Fevre, C. G.; Le Fevre, R. J. W.; Wassermann, A., The Constitution of Dimeric Keten. *J. Chem. Soc.* **1935**, 1751-1755.

10. Taufen, H. J.; Murray, M. J., The Structure of Ketene Dimer. *J. Am. Chem. Soc.* **1945**, *67* (5), 754-757.

11. Miller, F. A.; Koch, S. D., Diketene: Infrared Spectrum and Structure. *J. Am. Chem. Soc.* **1948**, *70* (5), 1890-1894.

12. Katz, L.; Lipscomb, W. N., The Crystal and Molecular Structure of Diketene. *Acta Crystallogr.* **1952**, *5* (3), 313-318.

13. Katz, L.; Lipscomb, W. N., The Crystal and Molecular Structure of Diketene. *J. Org. Chem.* **1952**, *17* (4), 515-517.

14. Kay, M. I.; Katz, L., A Refinement of the Crystal Structure of Ketene Dimer. *Acta Crystallogr.* **1958**, *11* (12), 897-898.

15. Bader, A. R.; Gutowsky, H. S.; Williams, G. A.; Yankwich, P. E., The Proton Magnetic Resonance Spectrum and Structure of Diketene. *J. Am. Chem. Soc.* **1956**, *78* (11), 2385-2387.

16. Mönnig, F.; Dreizler, H.; Rudolph, H. D., Rotationsspektrum, Konfiguration, Dipolmoment und Ring-Deformationsschwingung von Diketen. *Z. Naturforsch., A: Phys. Sci.* **1967**, *22*, 1471-1473.

17. Seidl, E. T.; Schaefer, H. F., Diketene and its Cyclic $C_4H_4O_2$ Isomers 1,3-Cyclobutanedione and 2,4-Dimethylene-1,3-dioxetane. *J. Am. Chem. Soc.* **1990**, *112* (4), 1493-1499.

18. Seidl, E. T.; Schaefer, H. F., Molecular Structure of Diketene: A Discrepancy Between Theory and Experiments? *J. Phys. Chem.* **1992**, *96* (2), 657-661.

19. Salzner, U.; Bachrach, S. M., *Ab Initio* Studies of the Dimerization of Ketene and Phosphaketene. *J. Am. Chem. Soc.* **1994**, *116* (15), 6850-6855.

20. Hinze, R.; Zerbe-Foese, H.; Doose, J.; Guarnieri, A., Millimeterwave Spectrum and Dipole Moment in the ν_5, ν_6, and ν_9 Excited States of Ketene: Comparison to *ab Initio* Results for Ketene and Ketene-d_2. *J. Mol. Spectrosc.* **1996**, *176* (1), 133-138.

21. Ohishi, M.; Kawaguchi, K.; Kaifu, N.; Irvine, W.; Minh, Y.; Yamamoto, S.; Saito, S. The *ortho* to *para* Ratio for Ketene in TMC-1, *Atoms, Ions and Molecules: New Results in Spectral Line Astrophysics*, 1991; 387-391.

22. Turner, B. E.; Terzieva, R.; Herbst, E., The Physics and Chemistry of Small Translucent Molecular Clouds. XII. More Complex Species Explainable by Gas-Phase Processes. *Astrophys. J.* **1999**, *518* (2), 699-732.

23. Turner, B., Microwave Detection of Interstellar Ketene. *Astrophys. J.* **1977**, *213*, L75-L79.

24. Johansson, L. E. B.; Andersson, C.; Elldér, J.; Friberg, P.; Hjalmarson, Å.; Höglund, B.; Irvine, W.; Olofsson, H.; Rydbeck, G., Spectral Scan of Orion A and IRC + 10216 from 72 to 91 GHz. *Astron. Astrophys.* **1984**, *130*, 227-256.

25. Ruiterkamp, R.; Charnley, S.; Butner, H.; Huang, H. C.; Rodgers, S.; Kuan, Y. J.; Ehrenfreund, P., Organic Astrochemistry: Observations of Interstellar Ketene. *Astrophys. Space Sci.* **2007**, *310* (3/4), 181-188.

26. Bacmann, A.; Taquet, V.; Faure, A.; Kahane, C.; Ceccarelli, C., Detection of Complex Organic Molecules in a Prestellar Core: A New Challenge for Astrochemical Models. *Astron. Astrophys.* **2012**, *541*, L12.

27. Muller, S.; Beelen, A.; Guélin, M.; Aalto, S.; Black, J. H.; Combes, F.; Curran, S. J.; Theule, P.; Longmore, S. N., Molecules at z = 0.89: A 4-mm-Rest-Frame Absorption-Line Survey toward PKS 1830−211. *Astron. Astrophys.* **2011**, *535*, A103.

28. Maity, S.; Kaiser, R. I.; Jones, B. M., Formation of Ketene (H_2CCO) in Interstellar Analogous Methane (CH_4)-Carbon Monoxide (CO) Ices: A Combined FTIR and Reflectron Time-of-Flight Mass Spectroscopic Study. *Astrophys. J.* **2014**, *789* (1), 36.

29. Müller, H. S. P.; Thorwirth, S.; Roth, D. A.; Winnewisser, G., The Cologne Database for Molecular Spectroscopy, CDMS. *Astron. Astrophys.* **2001**, *370* (3), L49-L52.

30. Müller, H. S. P.; Schlöder, F.; Stutzki, J.; Winnewisser, G., The Cologne Database for Molecular Spectroscopy, CDMS: a Useful Tool for Astronomers and Spectroscopists. *J. Mol. Struct.* **2005**, *742* (1–3), 215-227.

31. Durig, J. R.; Green, W. H.; Hammond, N. C., Raman and Far-Infrared Spectra of Some Four-Membered Ring Molecules. *J. Phys. Chem.* **1966**, *70* (6), 1989-1997.

32. Durig, J. R.; Willis Jr, J. N., The Vibrational Spectra and Structure of Diketene and Diketene-d_4. *Spectrochim. Acta* **1966**, *22* (7), 1299-1313.

33. Miller, F. A.; Carlson, G. L., Diketene: Infrared Spectrum and Structure. II. *J. Am. Chem. Soc.* **1957**, *79* (15), 3995-3997.

34. Carreira, L. A.; Lord, R. C., Far-Infrared Spectra of Ring Compounds. V. Ring-Puckering Potential Functions of Some Oxygen-Containing Molecules. *J. Chem. Phys.* **1969**, *51* (8), 3225-3231.

35. Breda, S.; Reva, I.; Fausto, R., UV-Induced Unimolecular Photochemistry of Diketene Isolated in Cryogenic Inert Matrices. *J. Phys. Chem. A* **2012**, *116* (9), 2131-2140.

36. Pople, J. A.; Head-Gordon, M.; Raghavachari, K., Quadratic Configuration Interaction. A General Technique for Determining Electron Correlation Energies. *J. Chem. Phys.* **1987**, *87* (10), 5968-5975.

37. Almlof, J.; Taylor, P. R., General Contraction of Gaussian Basis Sets. I. Atomic Natural Orbitals for First- and Second-Row Atoms. *J. Chem. Phys.* **1987**, *86* (7), 4070-4077.

38. Stanton, J. F.; Gauss, J.; Harding, M. E.; Szalay, P. G. *CFOUR, Coupled-Cluster Techniques for Computational Chemistry*, v 2.0; Mainz, Germany, 2014.

39. Lee, T. J.; Rendell, A. P., Analytic Gradients for Coupled-Cluster Energies that Include Noniterative Connected Triple Excitations: Application to *cis*- and *trans*-HONO. *J. Chem. Phys.* **1991**, *94* (9), 6229-6236.

40. Scuseria, G. E., Analytic Evaluation of Energy Gradients for the Singles and Doubles Coupled Cluster Method Including Perturbative Triple Excitations: Theory and Applications to FOOF and Cr_2. *J. Chem. Phys.* **1991**, *94* (1), 442-447.

41. Mills, I. M., Vibration-Rotation Structure in Asymmetric- and Symmetric-Top Molecules. In *Molecular Spectroscopy: Modern Research*, Rao, K. N.; Mathews, C. W., Eds. Academic Press: New York, 1972; pp 115-140.

42. Stanton, J. F.; Lopreore, C. L.; Gauss, J., The Equilibrium Structure and Fundamental Vibrational Frequencies of Dioxirane. *J. Chem. Phys.* **1998**, *108* (17), 7190-7196.

43. Becke, A. D., Density-Functional Thermochemistry. III. The Role of Exact Exchange *J. Chem. Phys.* **1993**, *98*, 5648-5652.

44. Lee, C.; Yang, W.; Parr, R. G., Development of the Colle-Salvetti Correlation-Energy Formula into a Functional of the Electron Density. *Phys. Rev. B: Condens. Matter* **1988**, *37* (2), 785-789.

45. Hehre, W. J.; Ditchfield, R.; Pople, J. A., Self—Consistent Molecular Orbital Methods. XII. Further Extensions of Gaussian—Type Basis Sets for Use in Molecular Orbital Studies of Organic Molecules *J. Chem. Phys.* **1972**, *56*, 2257-2261.

46. Glendening, E. D.; Weinhold, F., Natural Resonance Theory: I. General Formalism. *J. Comput. Chem.* **1998**, *19* (6), 593-609.

47. Glendening, E. D.; Weinhold, F., Natural Resonance Theory: II. Natural Bond Order and Valency. *J. Comput. Chem.* **1998**, *19* (6), 610-627.

48. Frisch, M. J.; Trucks, G. W.; Schlegel, H. B.; Scuseria, G. E.; Robb, M. A.; Cheeseman, J. R.; Scalmani, G.; Barone, V.; Mennucci, B.; Petersson, G. A.; Nakatsuji, H.; Caricato, M.; Li, X.; Hratchian, H. P.; Izmaylov, A. F.; Bloino, J.; Zheng, G.; Sonnenberg, J. L.; Hada, M.; Ehara, M.; Toyota, K.; Fukuda, R.; Hasegawa, J.; Ishida, M.; Nakajima, T.; Honda, Y.; Kitao, O.; Nakai, H.; Vreven, T.; Montgomery Jr., J. A.; Peralta, J. E.; Ogliaro, F.; Bearpark, M. J.; Heyd, J.; Brothers, E. N.; Kudin, K. N.; Staroverov, V. N.; Kobayashi, R.; Normand, J.; Raghavachari, K.; Rendell, A. P.; Burant, J. C.; Iyengar, S. S.; Tomasi, J.; Cossi, M.; Rega, N.; Millam, N. J.; Klene, M.; Knox, J. E.; Cross, J. B.; Bakken, V.; Adamo, C.; Jaramillo, J.; Gomperts, R.; Stratmann, R. E.; Yazyev, O.; Austin, A. J.; Cammi, R.; Pomelli, C.; Ochterski, J. W.; Martin, R. L.; Morokuma, K.; Zakrzewski, V. G.; Voth, G. A.; Salvador, P.; Dannenberg, J. J.; Dapprich, S.; Daniels, A. D.; Farkas, Ö.; Foresman, J. B.; Ortiz, J. V.; Cioslowski, J.; Fox, D. J. *Gaussian 09*, Gaussian, Inc.: Wallingford, CT, USA, 2009.

49. Glendening, E. D.; Badenhoop, J. K.; Reed, A. E.; Carpenter, J. E.; Bohmann, J. A.; Morales, C. M.; Landis, C. R.; Weinhold, F. A. *NBO 6.0*, Theoretical Chemistry Institute: University of Wisconsin, Madison, 2013.

50. Cason, C.; Fröhlich, T.; Lipka, C. *Persistence of Vision Raytracer (POV-Ray)*, 3.7; Persistence of Vision Pty. Ltd.: 2013.

51. Amberger, B. K.; Esselman, B. J.; Woods, R. C.; McMahon, R. J., Millimeter-wave Spectroscopy of Carbonyl Diazide, $OC(N_3)_2$. *J. Mol. Spectrosc.* **2014**, *295*, 15-20.

52. Esselman, B. J.; Amberger, B. K.; Shutter, J. D.; Daane, M. A.; Stanton, J. F.; Woods, R. C.; McMahon, R. J., Rotational Spectroscopy of Pyridazine and its Isotopologs from 235-360 GHz: Equilibrium Structure and Vibrational Satellites. *J. Chem. Phys.* **2013**, *139*, 224304.

53. Kisiel, Z., Assignment and Analysis of Complex Rotational Spectra. In *Spectroscopy from Space*, 1 ed.; Demaison, J.; Sarka, K.; Cohen, E. A., Eds. Springer Netherlands: Dordrecht, 2001; pp 91-106.

54. Kisiel, Z. PROSPE - Programs for ROtational SPEctroscopy. http://info.ifpan.edu.pl/~kisiel/prospe.htm

55. Kisiel, Z.; Pszczółkowski, L.; Medvedev, I. R.; Winnewisser, M.; De Lucia, F. C.; Herbst, E., Rotational Spectrum of *trans–trans* Diethyl Ether in the Ground and Three Excited Vibrational States. *J. Mol. Spectrosc.* **2005**, *233* (2), 231-243.

56. Kisiel, Z.; Pszczółkowski, L.; Drouin, B. J.; Brauer, C. S.; Yu, S.; Pearson, J. C.; Medvedev, I. R.; Fortman, S.; Neese, C., Broadband Rotational Spectroscopy of Acrylonitrile: Vibrational Energies from Perturbations. *J. Mol. Spectrosc.* **2012**, *280*, 134-144.

57. Kaufman, H. S.; Fankuchen, I., A Low Temperature Single Crystal X-Ray Diffraction Technique. *Rev. Sci. Instrum.* **1949**, *20* (10), 733-734.

58. Abrahams, S. C.; Collin, R. L.; Lipscomb, W. N.; Reed, T. B., Further Techniques in Single-Crystal X-Ray Diffraction Studies at Low Temperatures. *Rev. Sci. Instrum.* **1950**, *21* (4), 396-397.

59. Bak, K. L.; Gauss, J.; Jørgensen, P.; Olsen, J.; Helgaker, T.; Stanton, J. F., The Accurate Determination of Molecular Equilibrium Structures. *J. Chem. Phys.* **2001**, *114* (15), 6548-6556.

60. Gordy, W.; Cook, R., *Microwave Molecular Spectra*. 3rd. ed.; Wiley Interscience: New York, 1984; Vol. XVIII.

61. Pawłowski, F.; Jørgensen, P.; Olsen, J.; Hegelund, F.; Helgaker, T.; Gauss, J.; Bak, K. L.; Stanton, J. F., Molecular Equilibrium Structures from Experimental Rotational Constants and Calculated Vibration–Rotation Interaction Constants. *J. Chem. Phys.* **2002**, *116* (15), 6482-6496.

62. Amberger, B. K.; Esselman, B. J.; Stanton, J. F.; Woods, R. C.; McMahon, R. J., Precise Equilibrium Structure Determination of Hydrazoic Acid (HN_3) by Millimeter-wave Spectroscopy. *J. Chem. Phys.* **2015**, *143* (10), 104310.

63. Bevan, J. W.; Legon, A. C., Structure and Potential Energy Function of Cyclopent-3-enone. Part 1.-Microwave Spectrum, Ring Planarity, r_s-structure, and Dipole Moment. *J. Chem. Soc., Faraday Trans. 2* **1973**, *69* (0), 902-915.

64. Legon, A. C., Equilibrium Conformations of Four- and Five-Membered Cyclic Molecules in the Gas Phase: Determination and Classification. *Chem. Rev.* **1980**, *80* (3), 231-262.

65. Boone, D. W.; Britt, C. O.; Boggs, J. E., Microwave Spectrum, Dipole Moment, and Ring-Puckering Vibration of β-Propiolactone. *J. Chem. Phys.* **1965**, *43* (4), 1190-1194.

66. Moruzzi, G.; Kunzmann, M.; Winnewisser, B. P.; Winnewisser, M., Ritz Assignment and Watson Fits of the High-Resolution Ring-Puckering Spectrum of Oxetane. *J. Mol. Spectrosc.* **2003**, *219* (1), 152-162.

67. Scharpen, L. H.; Laurie, V. W., Microwave Spectrum, Ring-Puckering Potential Function, Ring Structure, and Dipole Moment of Cyclobutanone. *J. Chem. Phys.* **1968**, *49* (1), 221-228.

68. Zdanovskaia, M. A.; Esselman, B. J.; Lau, H. S.; Bates, D. M.; Woods, R. C.; McMahon, R. J.; Kisiel, Z., The 103 – 360 GHz Rotational Spectrum of Benzonitrile, the First Interstellar Benzene Derivative Detected by Radioastronomy. *J. Mol. Spectrosc.* **2018**, *351*, 39-48.

69. Zdanovskaia, M. A.; Esselman, B. J.; Woods, R. C.; McMahon, R. J., The 130–370 GHz Rotational Spectrum of Phenyl Isocyanide (C_6H_5NC). *J. Chem. Phys.* **2019**, *151* (2), 024301.

70. Dorman, P. M.; Esselman, B. J.; Woods, R. C.; McMahon, R. J., An analysis of the rotational ground state and lowest-energy vibrationally excited dyad of 3-cyanopyridine: Low symmetry reveals rich complexity of perturbations, couplings, and interstate transitions. *J. Mol. Spectrosc.* **2020**, *373*, 111373.

71. Dorman, P. M.; Esselman, B. J.; Park, J. E.; Woods, R. C.; McMahon, R. J., Millimeter-wave spectrum of 4-cyanopyridine in its ground state and lowest-energy vibrationally excited states, ν_{20} and ν_{30}. *J. Mol. Spectrosc.* **2020**, *369*, 111274.

72. Amberger, B. K. Millimeter-wave Spectroscopy of Highly Nitrogenous Molecules of Potential Astrochemical Interest. Ph.D. Thesis, University of Wisconsin-Madison, Madison, WI, 2015.

73. Nakashige, M. L.; Lewis, R. S.; Chain, W. J., Transformation of N,N-dimethylaniline-N-oxides into N-methylindolines by a Tandem Polonovski–Mannich Reaction. *Tetrahedron Lett.* **2015**, *56* (23), 3531-3533.

Chapter 3: Rotational Spectroscopy of *syn* and *anti* 4-Cyano-1,2-butadiene from 130-375 GHz

4-Cyano-1,2-butadiene Coordinate Scan
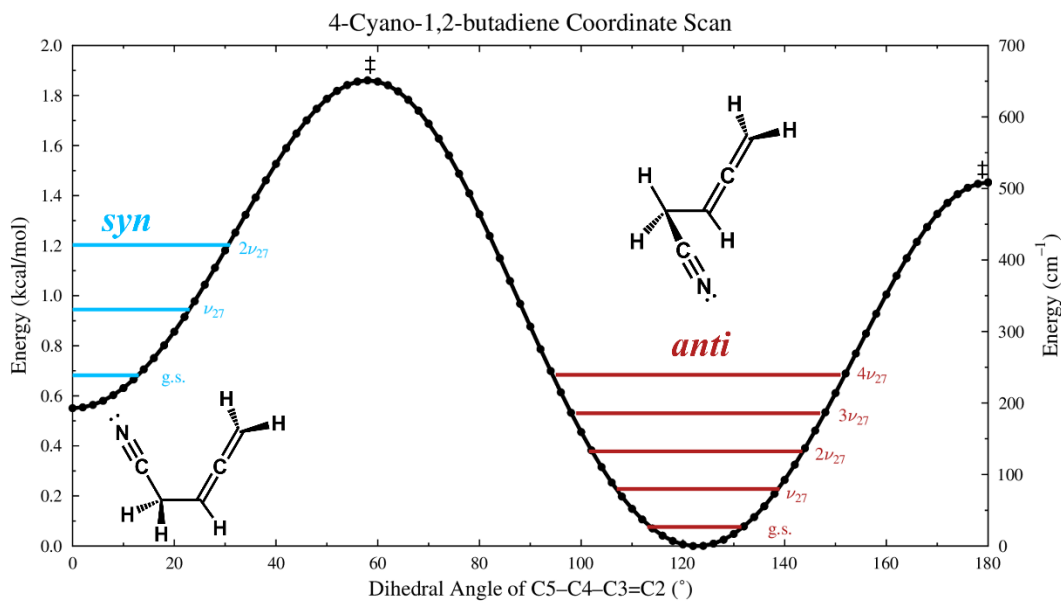
Includes the work of several collaborators:

Brian J. Esselman, Samuel M. Kougias, Daniel J. Lee, Andrew N. Owen,

R. Claude Woods, Robert J. McMahon

of the University of Wisconsin–Madison

Portions of this work have been included in the manuscript:

M.A. Zdanovskaia, P. M. Dorman, V. L. Orr, A. N. Owen, S. M. Kougias, B. J. Esselman, R. C. Woods, R. J. McMahon "Rotational Spectra of Three Cyanobutadiene Isomers (C_5H_5N) of Relevance to Astrochemistry and Other Harsh Reaction Environments"

INTRODUCTION

Many organic molecules containing nitrile groups have been detected in the interstellar medium (ISM)[1] due to a combination of their prevalence in that environment, the availability of laboratory spectra, and their strong dipole moments. Recently, our group synthesized several cyanobutadiene isomers, acyclic isomers of pyridine,[2] which are proposed targets for searches in the ISM.[3] The group has now collected the rotational spectrum of each of them to aid in their future detection in the ISM by radio astronomy. The 4-cyano-1,2-butadiene isomer (also, 1-cyano-2,3-butadiene or penta-3,4-dienenitrile), discussed in this chapter, is the allenyl nitrile ($H_2C=C=CH-CH_2CN$) from this series of cyanobutadienes. The synthesis and spectroscopic properties of this isomer had not been presented in the literature prior to the work by Kougias, *et al.*,[2] and it has not been previously studied by rotational spectroscopy. The products of benzene discharges studied by McCarthy, *et al.* resulted in a number of molecules with an allenyl group,[4] furthering interest in the spectrum of 4-cyano-1,2-butadiene.

The 4-cyano-1,2-butadiene molecule has two low energy conformations, *syn-periplanar* (abbreviated *syn*) and *anti-clinal* (abbreviated *anti*), that are related by the internal rotation of the $-CH_2CN$ group (Figure 3.1). This internal rotation involves an asymmetric frame ($H_2C=C=CH-$) and an asymmetric top ($-CH_2CN$). Rotational spectroscopy has been used as a method to study the various types of internal rotation, whether with a symmetric or an asymmetric top, and with a high or low barrier.[5] One of the seminal works on asymmetric tops with asymmetric frames is the study by Hirota and coworkers of 3-fluoropropene ($CH_2=CH-CH_2-F$)[6] with microwave and far-IR spectroscopy, and with the application of theory from Quade and Lin[7] to model the barrier of rotation (potential function). The low resolution far-IR spectrum was particularly useful in the case of 3-fluoropropene, as multiple hot-bands of the torsional motion were clearly visible in the

spectrum. The assignment of these hot-bands was key to the determination of the shape of the potential well of the *cis* conformation.[6] Now with the advent of synchrotron sources for high-resolution infrared spectroscopy,[8] the far-IR is more accessible for the collection of rotationally-resolved spectra. Herein we present our work to fit the rotational spectrum of the ground state for both conformers and the excited vibrational states for the *anti* conformer from 130 – 375 GHz. Data collection from the Canadian Light Source, both accomplished and projected, will be discussed in Appendix A.
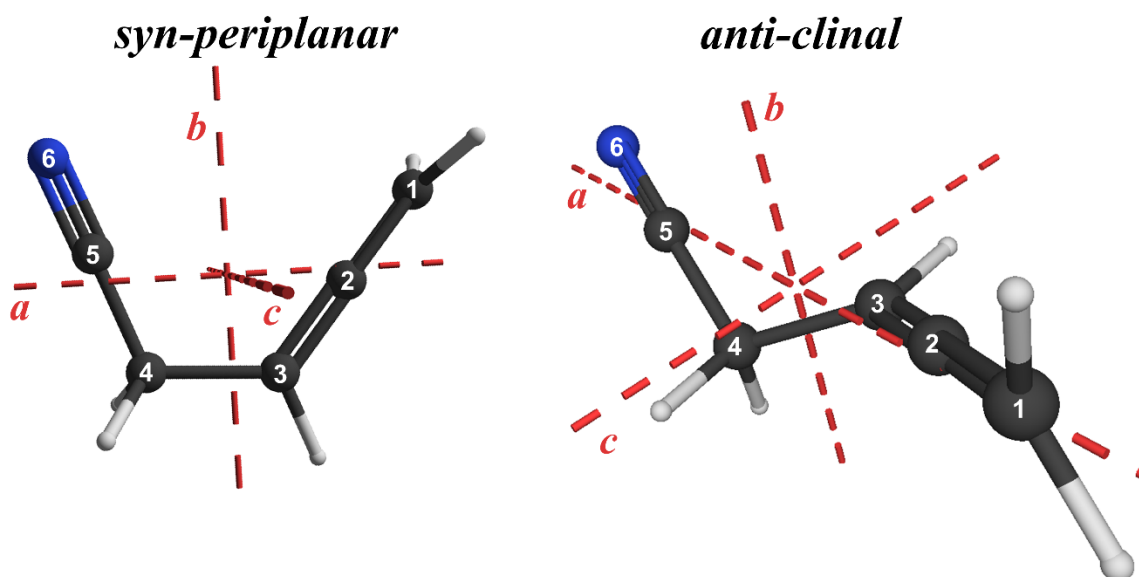
Figure 3.1. The *syn-periplanar* (C_s, left) and *anti* (C_1, right) conformers of 4-cyano-1,2-butadiene (NC−CH_2−CH=C=CH_2) with atoms numbering presented in white.

METHODS

Computational Methods. 4-Cyano-1,2-butadiene has been computationally investigated using the cc-pVTZ basis[9] at the B3LYP[10-11] level of theory with Gaussian 16 Revision B.01.[12] All Gaussian calculations utilized the WebMO interface.[13] Optimizations with the "verytight" convergence criteria and an "ultrafine" integration grid were performed and followed by an anharmonic frequency calculation. The rotational constants, and quartic and sextic centrifugal

distortion constants from these calculations were utilized in the spectral fitting process. The relaxed coordinate scan of the internal rotation was run at the same level of theory. Optimizations of the transition states were also performed with a "verytight" convergence criteria and "ultrafine" integration grid, and standard harmonic frequency calculations were used to confirm their identity as transition states using Gaussian 16, Revision C.01.[14] Optimizations and harmonic frequency calculations of the stable conformers were also performed in CFOUR[15] at the CCSD(T)/cc-pCVTZ level.[16-18]

Rotational Spectroscopy. The millimeter-wave spectrometer used to collect the spectrum in the spectral ranges 130 – 230 and 235 – 375 GHz at pressures between 10 – 13 mTorr has been described previously.[19-20] The sample of 4-cyano-1,2-butadiene was synthesized in the group, as described in detail by Kougias, *et al*.[2] During collection of rotational spectra, the sample flask was cooled with an ice-water bath. The spectrometer absorption chamber was cooled to a temperature ranging from below 0 °C to approximately −50 °C using a recirculating chiller (Thermo Neslab ULT-95). The spectra were combined and visualized using Kisiel's AABS suite of programs.[21-22] The vibrational states presented were initially least-squares fit using a single-state, distorted-rotor Hamiltonian with Kisiel's ASROT/ASFIT programs.[23] The ground state and first fundamental, v_{27}, of the *anti* conformer were also least-squares fit in a two-state fit utilizing Pickett's SPFIT/SPCAT programs.[24]

COMPUTATIONAL RESULTS

Since the rotational spectrum of this molecule had never been collected before, the computational work was very important for the spectral analysis. First, we looked into the relative energies of the two conformers with various levels of theory (Table 3.1). The B3LYP/cc-pVTZ

optimized *anti* conformer has a C2=C3–C4–C5 dihedral angle of 122.7° and the *syn* conformer

has a dihedral of 0.0°. At both the CCSD(T)/cc-pCVTZ+ZPVE and B3LYP/cc-pVTZ+ZPVE

levels the *syn* conformer is higher in energy, by 0.12 and 0.46 kcal/mol (42 and 163 cm^{-1}),

respectively, than the *anti* conformer (Table 3.1). The *anti* 4-cyano-1,2-butadiene conformer has

C_1 symmetry and has dipole moment components $\mu_a = 3.42$ D, $\mu_b = 1.89$ D, $\mu_c = 0.63$ D ($\mu_{total} = $

3.95 D) at the CCSD(T)/cc-pCVTZ level. The *syn* conformer has C_s symmetry and has dipole

moment components $\mu_a = 1.74$ D, $\mu_b = 3.07$ D ($\mu_{total} = 3.53$ D) at the CCSD(T)/cc-pCVTZ level.

Given the similar dipole moments, the *anti* is expected to be more intense in the spectrum, based

on the energy difference and the presence of two enantiomeric *anti* conformers.

Table 3.1. Relative energies (+ZPVE) of the *syn* and *anti* conformers of 4-cyano-1,2-butadiene
and the transition states between conformers

Conformer	CCSD(T) (kcal/mol)	B3LYP (kcal/mol)	B3LYP Dihedral (°)[a]
syn	0.12	0.46	0.0
TS1		1.65	58.0
anti	0.00	0.00	122.7
TS2		1.15	180.0

[a] C2=C3–C4–C5 Dihedral

     The *syn* and *anti* conformers are related by the internal rotation of the −CH$_2$CN asymmetric

top in relation to the –CH=C=CH$_2$ asymmetric frame. To investigate the relationship between

these two conformers with respect to this motion, a relaxed coordinate scan was performed at the

B3LYP/cc-pVTZ level (Figure 3.2). The coordinate scan indicates that the barrier to rotation is

1.86 kcal/mol, and geometry optimization of the transition state gives a relative energy of 1.65

kcal/mol (B3LYP/cc-pVTZ including ZPVE, Table 3.1) relative to the *anti* conformer and a

dihedral angle of 58.0°. There is a smaller barrier between the two enantiomeric *anti* conformers

at 1.15 kcal/mol and a 180° dihedral angle (B3LYP/cc-pVTZ including ZPVE). The coordinate

scan is shown in Figure 3.2 with an overlay of the energy levels (anharmonic approximation) of the corresponding torsional fundamental, ν_{27}, displayed in the potential well for each conformer. The *anti* conformer has a low-energy torsional fundamental, ν_{27}, predicted at 53.2 cm^{-1}. Even its first and second overtones ($\nu_{27} = 2, 3$) are lower in energy than the next fundamental ν_{26}, predicted at 168.8 cm^{-1}. The *syn* conformer, also, has a low-energy torsional fundamental, ν_{27}, predicted at 92 cm^{-1}. The large difference in isomerization energy between the *anti* and *syn* conformers at the CCSD(T) level versus the B3LYP level of theory indicates that the remainder of the potential energy surface may also be quite different from what is shown in Figure 3.2 at other levels of theory. The computational anharmonic frequencies below 250 cm^{-1} are presented in Figure 3.3.
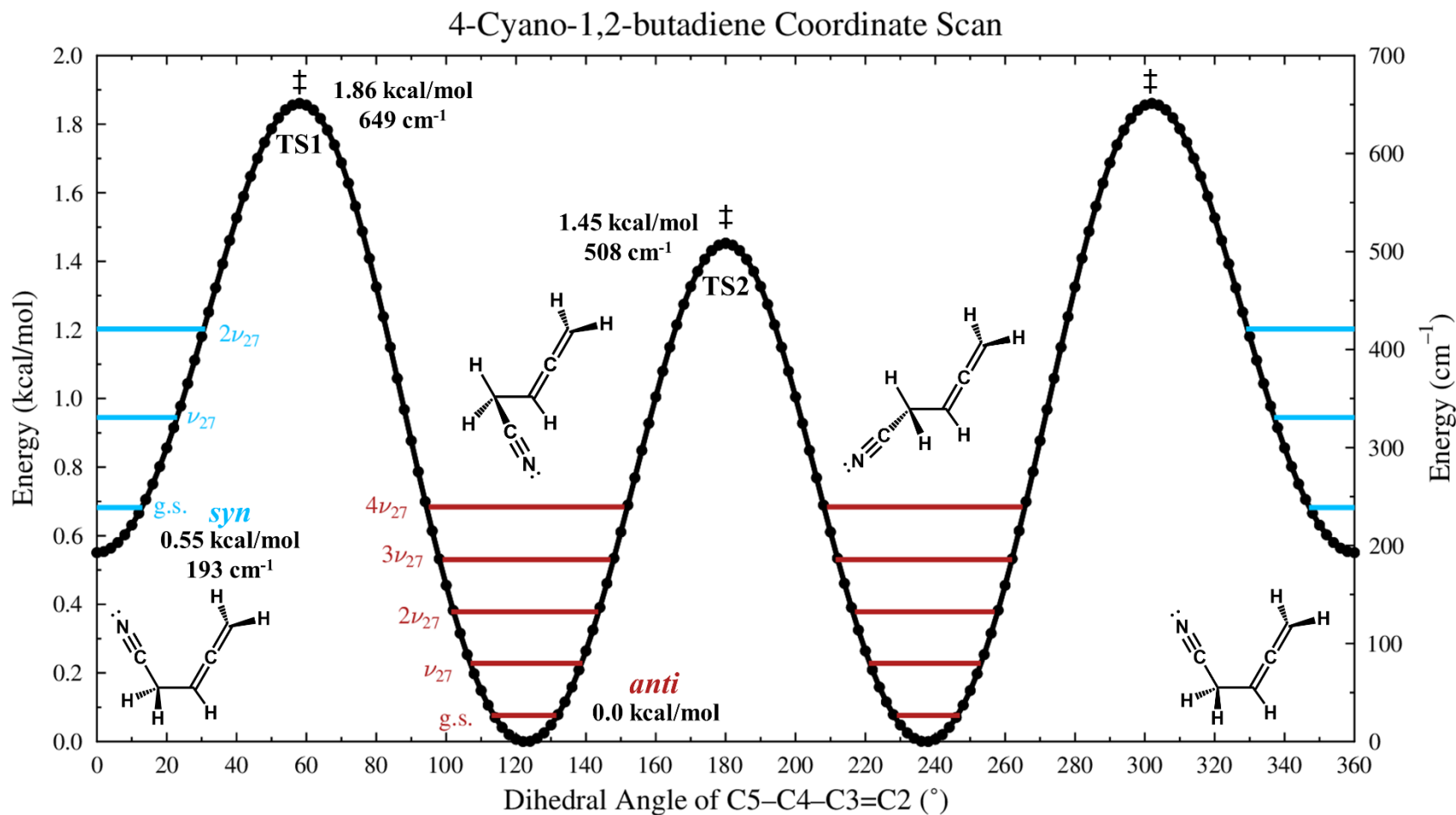
Figure 3.2. Coordinate Scan of the C5–C4–C3=C2 dihedral angle of 4-cyano-1,2-butadiene from the *syn* conformer at 0º through to 360º at the B3LYP/cc-pVTZ level. Energy levels displayed in the potential wells are the ν_{27} harmonics the red are v = 0, 1, 2, 3, 4 for the *anti* conformer, and the energy levels in blue are the v = 0, 1, 2 for the *syn* conformer from the anharmonic frequency calculations at the same level of theory.
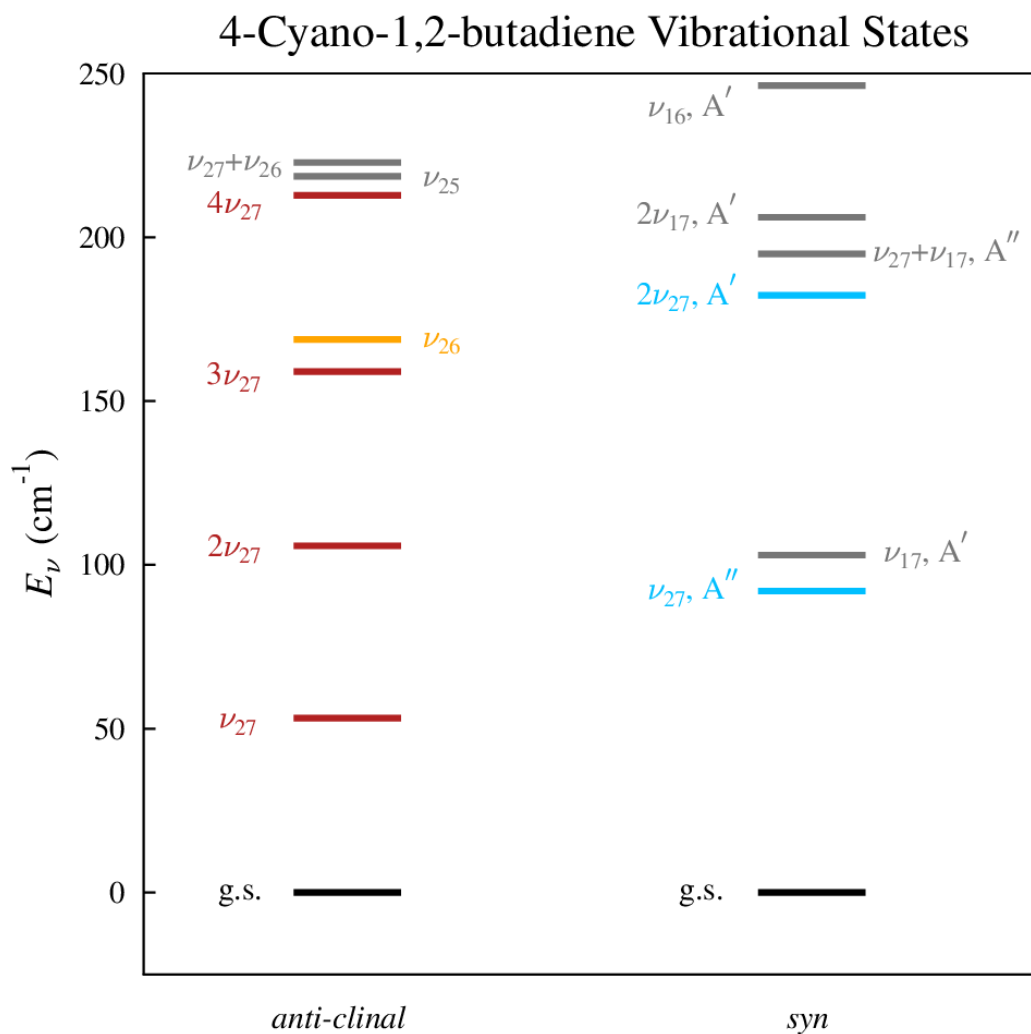
Figure 3.3. The anharmonic frequencies of the vibrational states for the *anti* (left) and *syn* (right) conformations of 4-cyano-1,2-butadiene at the B3LYP/cc-pVTZ level of theory. The ν_{27} harmonics of v = 0, 1, 2, 3, 4 for the *anti* conformer are in red, and the ν_{27} harmonics in blue are the v = 0, 1, 2 for the *syn* conformer, which correspond to the energy levels of the torsional motion shown in Figure 3.2. The rotational spectrum of ν_{26} of the *anti* conformer has been identified, and this state is included here in orange. None of the *syn* excited vibrational states' rotational spectra have been assigned.

SPECTROSCOPIC ANALYSIS

The rotational spectrum of 4-cyano-1,2-butadiene is quite dense. Both conformers and many vibrational states are visible in the spectrum. The transitions of the *anti* conformer dominate the spectrum, as anticipated above. The ^aR-bands begin non-degenerate at low K_a and become K_a degenerate after a few K_a, forming the distinctive band structure that sweeps towards higher frequency. This pattern is clearly shown (in red) by the predicted stick spectrum in the upper portion of Figure 3.4. The prominent bands of the *syn* conformer begin quadruply degenerate (two $^aR_{0,1}$ transitions, $^bR_{1,1}$ $^bR_{1,-1}$, with same J and K_c) at $K_a = 0$, 1 and progress towards lower frequency as K_a increases before turning around and losing degeneracy (shown in Figure 3.4 as the dark blue predicted spectrum).
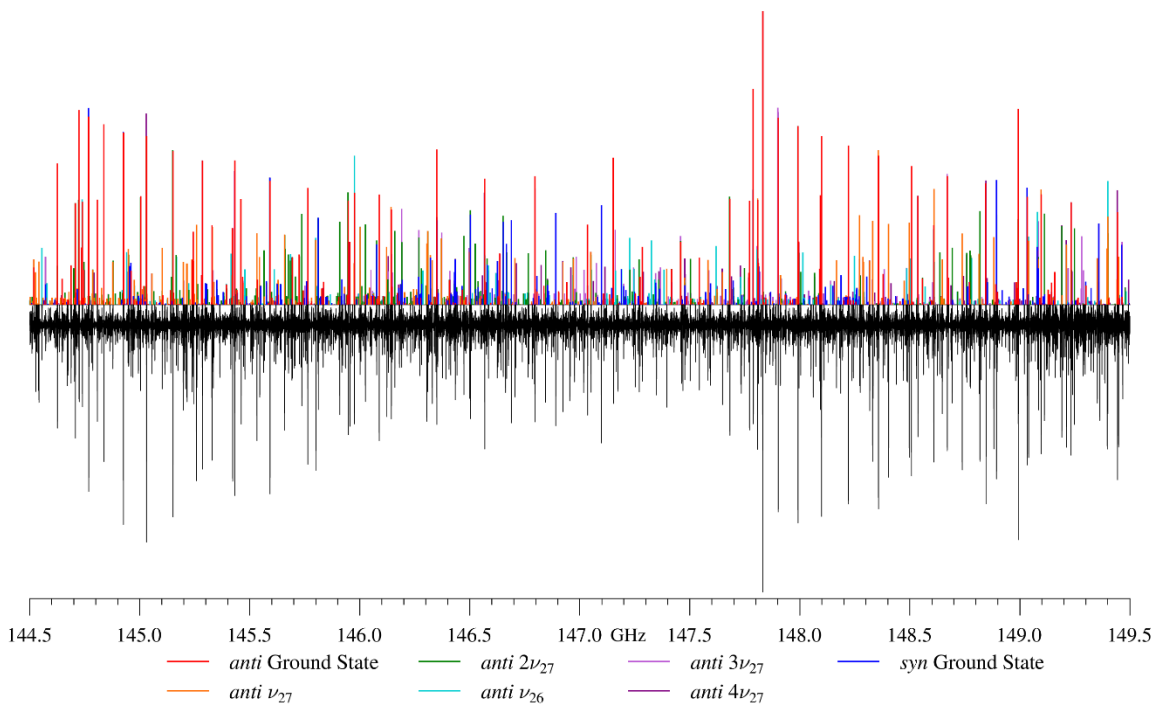
Figure 3.4. The rotational spectrum of 4-cyano-1,2-butadiene (below) and the predicted stick spectrum of the vibrational states (above) from 144.5 to 149.5 GHz. The predicted stick spectrum of the *anti* ground state is shown in red, and the *syn* ground state is shown in dark blue.

The ground state of the *syn* conformer of 4-cyano-1,2-butadiene was fit with a partial-octic, distorted-rotor Hamiltonian in the S-reduction and I^r representation due to the symmetric (C_s) and moderately prolate nature of the molecule. From a least-squares fit of 1037 distinct transitions, all rotational and distortion terms were well determined and are presented in Table 3.2. The computed rotational constant values (B3LYP/cc-pVTZ) are all within 5.2 % of the experimental value, corresponding to differences of about 50 MHz in C_0, 141 MHz in B_0, and 228 MHz in A_0. The best predicted quartic distortion term, D_K, is predicted 5.6% larger than the experimental value, and the least well estimated quartic parameter is d_2, which is 26% smaller than the determined value. For the sextic distortion terms, the discrepancies are even larger, with the poorest predicted values being H_{JK}, which is predicted too large in magnitude by 213%, and H_{KJ}, which is predicted too small by 59%. The fitted H_{JK} value is slightly closer to the predicted value (at 185 %) when the two octic terms are not included, but the error of the fit is larger (0.044 MHz), and a number of lines that fit well in the octic model do not fit well in the sextic only model. The CCSD(T) computed values are much closer to the experimental values; the rotational constants are within 0.7 %, and the quartic distortion constants are within 7.2 %. The sextic distortion terms at the CCSD(T) level are not presented since the anharmonic frequency calculation necessary to generate them was not carried out.

Table 3.2. Spectroscopic constants for the ground vibrational state of *syn* 4-cyano-1,2-butadiene (S-reduction, I^r representation)

	CCSD(T)[a]	B3LYP[b]	Ground State
$A_0^{(S)}$ (MHz)	5964	6195	5967.20194 (49)
$B_0^{(S)}$ (MHz)	2704	2582	2722.54196 (27)
$C_0^{(S)}$ (MHz)	1906	1864	1914.20006 (10)
D_J (kHz)	3.17	2.70	3.278169 (64)
D_{JK} (kHz)	−14.1	−13.5	−14.49228 (47)
D_K (kHz)	21.7	23.4	22.15266 (95)
d_1 (kHz)	−1.25	−1.04	−1.305464 (42)
d_2 (kHz)	−0.0789	−0.0630	−0.084966 (17)
H_J (Hz)		0.0125	0.0110528 (93)
H_{JK} (Hz)		−0.0488	−0.01558 (11)
H_{KJ} (Hz)		−0.0694	−0.16937 (67)
H_K (Hz)		0.270	0.32406 (59)
h_1 (Hz)		0.00664	0.0062750 (75)
h_2 (Hz)		0.000959	0.0011348 (47)
h_3 (Hz)		0.000165	0.0002033 (10)
L_{JJK} (mHz)[c]			−0.000229 (13)
L_{KKJ} (mHz)[c]			0.00305 (35)[c]
N_{lines}			1037
σ (MHz)			0.038
κ	−0.607	−0.669	−0.601
Δ_i (uÅ^2)	−6.576	−6.282	−6.305

[a] CCSD(T)/cc-pCVTZ

[b] B3LYP/cc-pVTZ

[c] All other octic distortion terms held fixed at 0

Table 3.3. Spectroscopic constants for the ground state and vibrationally excited states of *anti* 4-cyano-1,2-butadiene (S-reduction, I^r representation)

	B3LYP/cc-pVTZ	Ground State	ν_{27}	$2\nu_{27}$	$3\nu_{27}$	$4\nu_{27}$
$A_v^{(S)}$ (MHz)	14868	14498.502 (54)	14651.89 (25)	14805.81 (24)	14953.84 (60)	15099.70 (79)
$B_v^{(S)}$ (MHz)	1554	1567.06105 (39)	1574.26340 (49)	1581.42000 (48)	1588.3998 (23)	1595.0438 (36)
$C_v^{(S)}$ (MHz)	1505	1515.78788 (25)	1519.21021 (37)	1522.50843 (39)	1525.64014 (89)	1528.5711 (11)
D_J (kHz)	0.942	1.070797 (41)	1.150472 (45)	1.245264 (46)	1.35714 (29)	1.47176 (70)
D_{JK} (kHz)	−64.6	−73.5256 (34)	−77.7465 (37)	−82.7222 (45)	−88.051 (31)	−91.31 (91)
D_K (kHz)	1414	1612.53 (72)	1696. (17)	1874. (17)	[2147.371][a]	[2513.908][a]
d_1 (kHz)	−0.196	−0.227290 (36)	−0.256616 (47)	−0.291450 (49)	−0.33110 (21)	−0.36661 (24)
d_2 (kHz)	−0.00493	−0.006525 (13)	−0.009896 (19)	−0.014206 (21)	−0.01961 (10)	−0.02573 (36)
H_J (Hz)	0.00431	0.0069724 (42)	0.0079859 (44)	0.0093341 (47)	0.009952 (32)	0.008090 (13)
H_{JK} (Hz)	−0.126	−0.31481 (37)	−0.36026 (31)	−0.42406 (38)	[−0.315][b]	[−0.315][b]
H_{KJ} (Hz)	−12.4	−10.498 (18)	−11.664 (49)	−12.888 (60)	[−10.498][b]	[−10.498][b]
H_K (Hz)	371	397.9 (28)	[397.918][b]	[397.918][b]	[397.918][b]	[397.918][b]
h_1 (Hz)	0.00194	0.0029739 (38)	0.0034622 (48)	0.0041712 (52)	0.004388 (21)	[0.00297][b]
h_2 (Hz)	0.000194	0.0003810 (21)	0.0004926 (28)	0.0006777 (33)	0.000786 (15)	[0.000381][b]
h_3 (Hz)	0.0000121	0.00002859 (60)	0.0000420 (10)	0.0000636 (12)	0.0001128 (39)	[0.0000286][b]
L_J (mHz)		−0.00005092 (15)	−0.00006278 (16)	−0.00008344 (18)	[−0.0000509][b]	[−0.0000509][b]
L_{JJK} (mHz)		0.003273 (13)	0.003896 (15)	0.005411 (17)	−0.0475 (22)	[0.00327][b]
L_{JK} (mHz)		−0.08245 (95)	−0.0698 (13)	−0.0749 (17)	[−0.0825][b]	[−0.0825][b]
L_{KKJ} (mHz)		3.146 (25)	4.81 (18)	7.98 (23)	[3.15][b]	[3.15][b]
L_K (mHz)		[0][c]	[0][b,c]	[0][b,c]	[0][b,c]	[0][b,c]
l_1 (mHz)		−0.00002431 (13)	−0.00002996 (17)	−0.00004233 (19)	[−0.0000243][b]	[−0.0000243][b]
l_2 (mHz)		−0.000004291 (89)	−0.00000508 (11)	−0.00000890 (14)	[−0.00000429][b]	[−0.00000429][b]
l_3 (mHz)		−0.000000731 (40)	−0.000000948 (57)	−0.000001792 (73)	[−0.000000731][b]	[−0.000000731][b]
l_4 (mHz)		[0][c]	[0][b,c]	[0][b,c]	[0][b,c]	[0][b,c]
N_{lines}		788	797	660	129	33
σ (MHz)		0.041	0.044	0.043	0.063	0.073
κ	−0.993	−0.992	−0.992	−0.991	−0.991	−0.990
Δ_i (uÅ^2)	−23.449	−23.948	−22.859	−21.768	−20.708	−19.691

[a] Held constant to extrapolated value

[b] Held constant to ground state value

[c] Held fixed at 0

Table 3.3. cont.

	ν_{26}
$A_v^{(S)}$ (MHz)	[14806.568]
$B_v^{(S)}$ (MHz)	1557.426 (35)
$C_v^{(S)}$ (MHz)	1510.9939 (92)
D_J (kHz)	0.9932 (26)
D_{JK} (kHz)	−100.2 (28)
D_K (kHz)	[1612.54]
d_1 (kHz)	−0.1574 (46)
d_2 (kHz)	0.0306 (41)
H_J (Hz)	0.00809 (17)
H_{JK} (Hz)	3.97 (66)
H_{KJ} (Hz)	[−10.498][b]
H_K (Hz)	[397.918][b]
h_1 (Hz)	[0.00297][b]
h_2 (Hz)	[0.000381][b]
h_3 (Hz)	[0.0000286][b]
L_J (mHz)	[−0.0000509][b]
L_{JJK} (mHz)	[0.00327][b]
L_{JK} (mHz)	[−0.0825][b]
L_{KKJ} (mHz)	[3.15][b]
L_K (mHz)	[0][b,c]
l_1 (mHz)	[−0.0000243][b]
l_2 (mHz)	[−0.00000429][b]
l_3 (mHz)	[−0.000000731][b]
l_4 (mHz)	[0][b,c]
N_{lines}	56
σ (MHz)	0.21
κ	−0.993
Δ_i (uÅ^2)	−24.160

The ground state of *anti* 4-cyano-1,2-butadiene was first treated with an octic, distorted-rotor Hamiltonian in the S-reduction and I^r representation. This conformer is very-nearly prolate based on its κ value of -0.992. It was quickly apparent that the ground state could not be completely fit with a single-state Hamiltonian model and that it showed clear evidence of coupling to its nearest vibrationally excited state (ν_{27}), predicted at 53.2 cm^{-1}. Though this energy gap is somewhat large for coupling between states, for a nearly-prolate molecule with a large A_0 value this coupling phenomenon is not unknown.[25-26] A large A_0 makes the separation between K substates large, which allows for interactions between states to occur at lower K values. As the overtones of ν_{27} inherently have similar energy spacing, further coupling between successive states was expected and became evident upon fitting their spectra. Uncoupled, single-state fits for ν_{27} v = 0, 1, 2, 3, and 4 and ν_{26} are presented in Table 3.3. The single-state fit of the ground state includes R-branch transitions with J' values from 43 to 120 and mainly $K_a < 12$ with a few higher K_a's at low J (< 90) (and a few Q branch transitions with lower J and low K). For ν_{27} the R-branch transition K_a range is from 0 to 13 for J' values ranging from 43 to 118 (no Q branches are measured for this single-state fit). The vibrational state ν_{26} lies close in energy to $3\nu_{27}$, exhibits evidence of coupling, and is likely part of this complex polyad. Overtone $4\nu_{27}$ (currently fit with only 33 transitions), is likely to be further coupled to ν_{25} and $\nu_{27}+\nu_{26}$ which are predicted within 10 cm^{-1}, as well as coupled to $3\nu_{27,}$ $5\nu_{27}$, and ν_{26}.

The overtones of ν_{27}, v = 2, 3, and 4, were predicted from the extrapolation of constants of the ground state and ν_{27} and lower energy harmonics (for v = 3 and 4). This method has proven very effective for the prediction and subsequent assignment of transitions of overtone states in rotational spectra as shown in Chapter 2 for diketene, and in other works.[27-29] The plots of the rotational constants, the quartic and sextic distortion terms, and the inertial defects of the

harmonics of ν_{27} relative to the ground state are presented in Figure 3.5. While the connections between the relative rotational constants appears relatively linear in Figure 3.5 (a), fitting the points to a linear trendline reveals that the R^2 values for each series are not 1, and there is slight curvature in the experimental values compared to the linear trendline. This is consistent with the non-harmonic shape of the potential surface in Figure 3.2. Furthermore, there remains the possibility that the values are perturbed by coupling occurring with nearby states. As a consequence, the relative inertial defect changes (Figure 3.5 b) also deviate from linearity. The relative quartic distortion constants (Figure 3.5 c) do have some regularity but are non-linear (again consistent with a non-harmonic potential). The relative sextic distortion constants are highly non-linear, but are affected by several factors, including additional perturbation of the constants of $v = 3$ and 4 due to the additional interactions of $3\nu_{27}$ with ν_{26} and of $4\nu_{27}$ with $5\nu_{27}$, ν_{25}, and $\nu_{27}+\nu_{26}$. (Figure 3.5 d). Allowing more sextic constants to vary in the $4\nu_{27}$ least-squares fit does lower the overall error of the fit, but the A_v value is less statistically well-determined. Future work on $3\nu_{27}$ and $4\nu_{27}$ may also include extrapolations for the sextic and octic terms that are currently fixed to the ground state values.
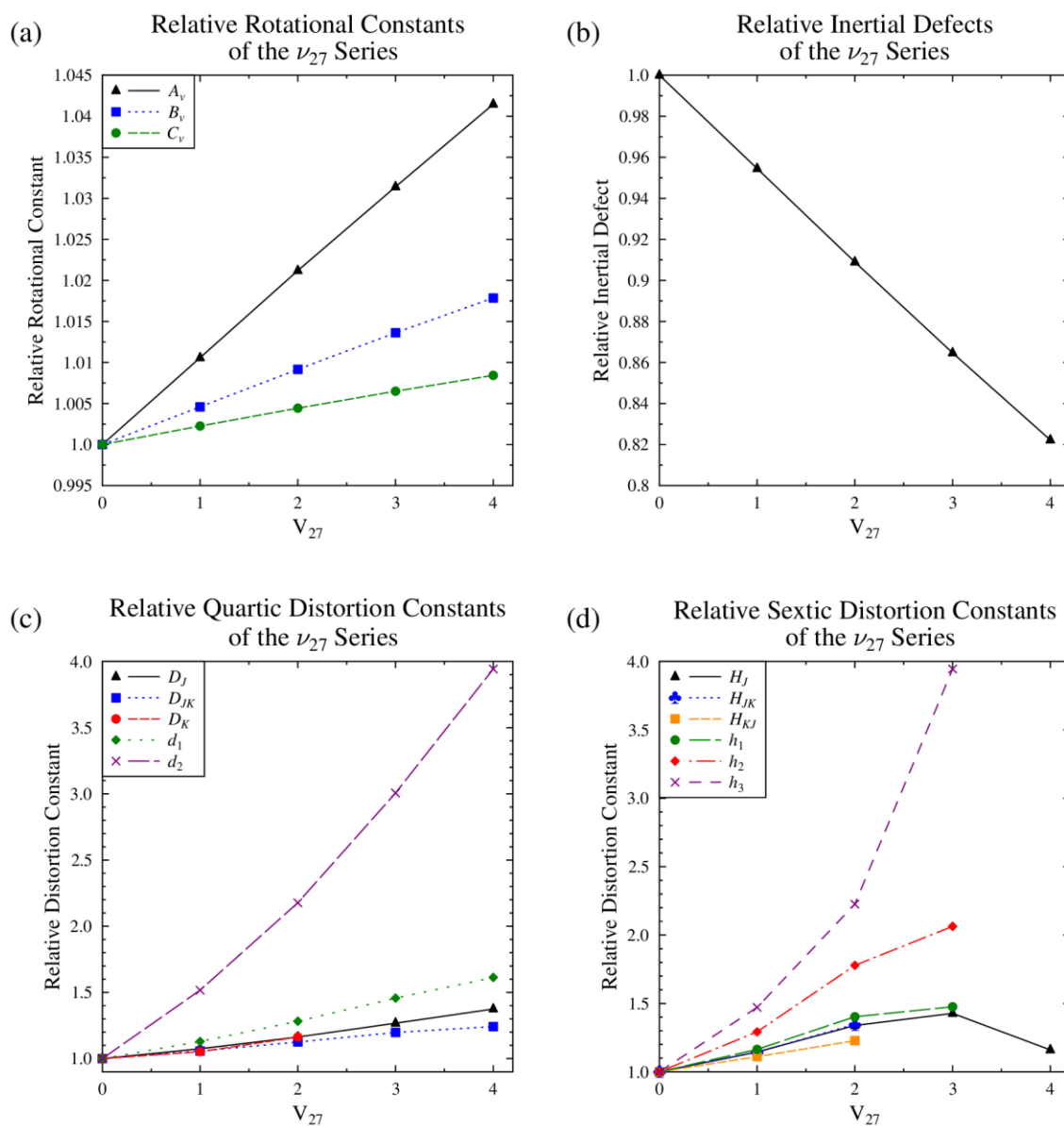
Figure 3.5. (a) Relative rotational constants, (b) relative inertial defects, (c) relative quartic distortion constants, and (d) relative sextic distortion constants of the ν_{27} series of *anti* 4-cyano-1,2-butadiene as a function of the number of quanta of torsional vibrational excitation ($v_{27} = 0, 1, 2, 3, 4$).

Evidence of Coupling

When coupled vibrational states are treated with single-state, distorted-rotor Hamiltonians, they exhibit behavior where some transitions in a series, or occasionally a whole series, will not

be well predicted by a distorted-rotor fit or observed with a simple, straight Loomis-Wood plot. Distinctive evidence of mutual coupling is strongly exhibited in the $^{a}R_{0,1}$ $K_a = 18$ degenerate series in the ground state and the $^{a}R_{0,1}$ $K_a = 14$ degenerate series in v_{27} of the *anti* conformer. The Loomis-Wood plot of $K_a = 18$ in the ground state (Figure 3.6) shows the deviation of the transitions from where they are predicted by the distorted rotor, shows how the energy levels of the transitions at these K_a's are perturbing each other, and shows that they interact most strongly at $J' = 93$. At first there seemed to be large gaps in the Loomis-Wood plots in the middle of the J range 88 to 101 for those K_a's. The measured experimental transitions were determined by first measuring the non-highly perturbed transitions at lower and higher J' (below 88 and above 101). The measured transition from $K_a = 18$ of the ground state was then averaged with the $K_a = 14$ transition in v_{27} with the same J'. This averaged series for low and high J was then modeled and extrapolated for the J's between 88 and 101. To continue measuring transitions between 88 and 101, if the selected transitions were assigned correctly in each state, then their average agreed with the model, allowing for confident identification of these more highly perturbed transitions. Unlike local resonances where a specific one or couple values of J's interact,[20, 30-32] the interaction between these states occurs over many values of J. At the cross-over ($J' = 93$) the two measured transitions are only about ten MHz apart.

This interaction show in Figure 3.6 can be rudimentarily modeled with a simple two state model using equations 3.1 and 3.2. In both equations, E_{14}^{0} is the unperturbed energy level of $K_a = 14$ in v_{27} and E_{18}^{0} is the unperturbed energy level of $K_a = 18$ in the ground state, ΔE_{vib} is energy gap between the unperturbed vibrational states, and $H'_{14,18}$ is the off-diagonal perturbation term. The E_{+} and E_{-} are the energy levels when the resulting quadratic secular equation is solved. How

these equations and the corresponding eigenvalues relate to the predicted and experimental transitions is shown schematically in Figure 3.7 a.

$$E_+ = \frac{(E_{14}^0 + \Delta E_{vib}) + E_{18}^0}{2} + \sqrt{\left(\frac{(E_{14}^0 + \Delta E_{vib}) - E_{18}^0}{2}\right)^2 + {H'}_{14,18}^2} \qquad (3.1)$$

$$E_- = \frac{(E_{14}^0 + \Delta E_{vib}) + E_{18}^0}{2} - \sqrt{\left(\frac{(E_{14}^0 + \Delta E_{vib}) - E_{18}^0}{2}\right)^2 + {H'}_{14,18}^2} \qquad (3.2)$$
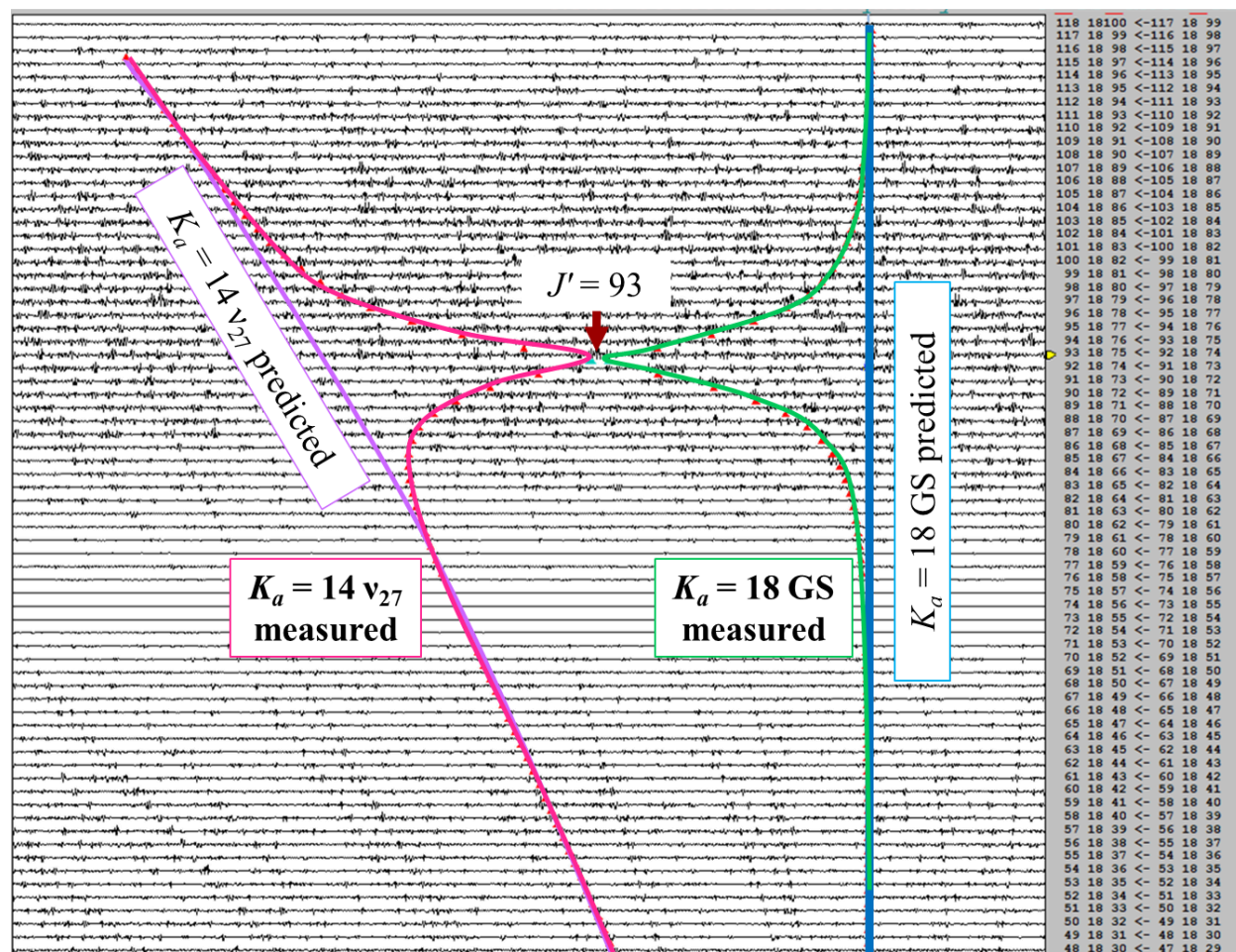
Figure 3.6. A Loomis-Wood plot of K_a =18 of the ground state of *anti* 4-cyano-1,2-butadiene from an effective (uncoupled) fit including decadic distortion constants. The blue line shows where the effective fit predicts the ground state $K_a = 18$ transitions, the purple line is where the effective fit of v_{27} predicts its $K_a = 14$ transitions. The green line is where the transitions in the $K_a = 18$ series are experimentally, and the pink line is where transitions of the v_{27} $K_a = 14$ series are experimentally. The measured experimental transitions are marked by red triangles.
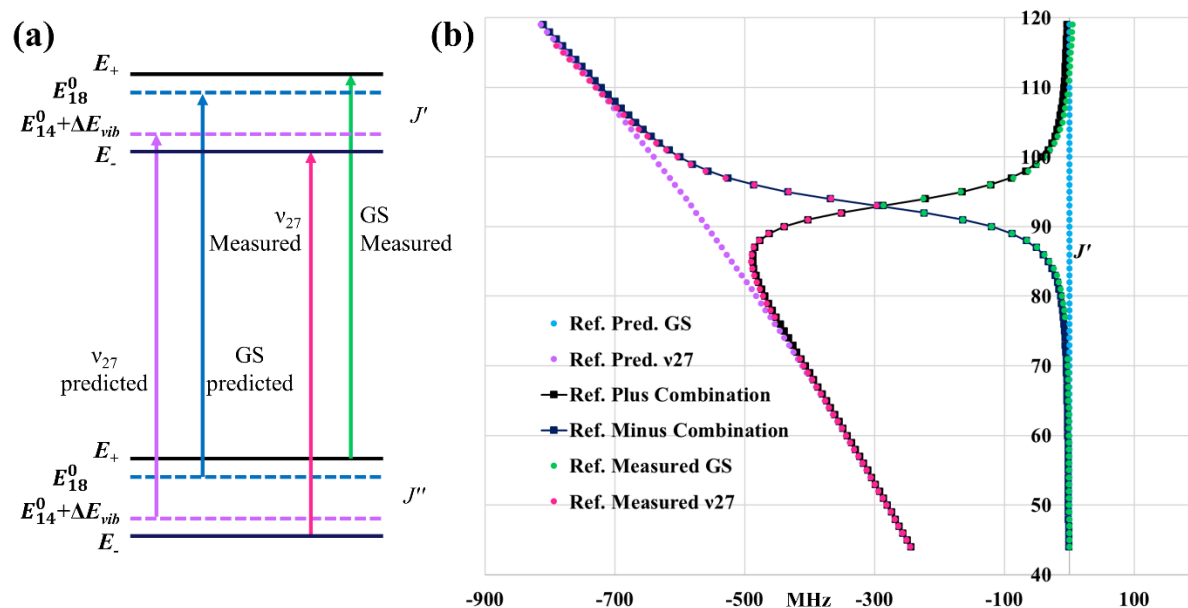
Figure 3.7. (a) Schematic representation of how equations 3.1 and 3.2 relate to the predicted and measured transitions of *anti* 4-cyano-1,2-butadiene $K_a = 18$ in the ground state and $K_a = 14$ in ν_{27}. (b) The measured transition frequencies, predicted transition frequencies, and model of the predicted transitions from E_+ and E_- energy levels with $\Delta E_{GS,27} = 52.025$ (1) cm^{-1} and $H'_{14,18} = 1200$ (50) MHz, all referenced to the predicted ground state $K_a = 18$ to replicate the Loomis-Wood plot.

By modeling the experimental transitions with transition frequencies derived from the E_+ and E_- energy levels (equations 3.1 and 3.2), we determined an energy gap of approximately $\Delta E_{GS,27} = 52.025$ (1) cm^{-1} and $H'_{14,18} = 1200$ (50) MHz. The energy gap and perturbation term values are estimated manually, based on a visual matching of the model to the plotted experimental values (Figure 3.7 b), the error bars are determined by adjusting the values and noting how far they could be adjusted before the model no longer matched the experimental transitions. This energy gap agrees well with the computationally predicted value of $\Delta E_{GS,27} = 53.2$ cm^{-1} (B3LYP/cc-pVTZ, Figure 3.3). The model from equations 3.1 and 3.2 produces a cross-over of the states where the referenced E_+ model transitions follow the low J of the $K_a = 14$ of ν_{27}, crosses at $J' = 93$

and follows $K_a = 18$ of the ground state to higher J's. The inverse of vibrational states is true for E_-. The agreement of the two-state model with the experimental data provides very strong confirmation of the assignments and frequency measurements of the strongly perturbed transition in Figure 3.6, even in the absence of a true overall non-linear least-squares fit of the two states. Determining this energy gap is critical for beginning a coupled fit of the ground state and ν_{27}. During our investigations into phenyl isocyanide,[20] however, it became clear that the vibrational energy gap alone is not what determines where the crossing occurs, and it can be effected by global perturbations due to the Coriolis terms. The above value from the two-state model is probably more well described as the energy separation combining the true vibrational separation and the global Coriolis effects. The fact that the ground state of *anti* 4-cyano-1,2-butadiene is involved in the coupling means the first-order Coriolis terms (G_a, G_b, G_c) are all zero; the higher order Coriolis zeta values cannot yet be obtained computationally in a completely reliable way. Therefore, which terms to use and what to use as initial values for the higher-order terms in the least-squares fits are subject to considerable guess work. We do see a similar strong perturbation displayed in the Loomis-Wood plots of ν_{27} $K_a = 17$ and $2\nu_{27}$ $K_a = 13$. That these K's are somewhat lower than the ground state and fundamental state (18 and 14), indicates that the energy spacing between $\nu_{27} = 1$ and $\nu_{27} = 2$ ($2\nu_{27}$) is slightly smaller than that between 0 and 1, as would be expected from a roughly cosine shaped torsional potential (Figure 3.2). It should be noted that the two-state model, as presented above, implicitly assumes that the off-diagonal perturbing matrix element ($H'_{14,18}$) is independent of J, which is almost certainly not true. It will, however, be expected to vary fairly slowly with J at the high J values germane to Figure 3.7. The actual J dependence will of course depend on which Coriolis term proves to be most important in the final model.

The preliminary spectroscopic constants for the dyad fit are presented in Table 3.4 in the A-reduction and I^r-representation. The K_a's being fit range from 0 to 21 for each state. Not all of the strongly perturbed transitions could be included in the data set of the fit at this preliminary stage. There are still over 200 more transitions measured for each vibrational state compared to their presented effective one-state fits, but the error is over double the experimental error. This dyad fit does not consider that there are additional couplings between these states and higher energy vibrational states, particularly $2\nu_{27}$, to which there is obviously strong coupling, as described above. To fully model the vibrational states in this polyad system, a Hamiltonian that incorporates all the vibrational states, and includes their rotational and distortion constants, and all the appropriate coupling terms between the various states, as well as allowing the energy separations between successive states to vary, will be required. This promises to be a daunting task.

One challenge of a multi-state fit that includes the ground state (in addition to the challenges of determining initial coupling terms from theory) is that the distortion constants for the ground state are not yet well-determined experimentally, so they cannot be confidently used for values that must be held constant in the subsequent higher-energy vibrational states. This is generally part of the approach when fitting a dyad, and deviation from the ground state values is often taken as a strong indication that the distortion constants are absorbing perturbation and are not ready to be varied in the least-squares fit yet.[20, 30-32]

Table 3.4. Dyad fit of the ground state and ν_{27} vibrational state of *anti*-4-cyano-1,2-butadiene (A-reduction., I^r-representation)

	B3LYP/cc-pVTZ	Ground State	ν_{27}
$A_v^{(A)}$ (MHz)	14868	14501.9(20)	14678.1(20)
$B_v^{(A)}$ (MHz)	1554	1566.9810(60)	1574.1871(68)
$C_v^{(A)}$ (MHz)	1505	1515.7432(57)	1519.1673(64)
Δ_J (kHz)	0.951	1.06254(52)	1.14213(57)
Δ_{JK} (kHz)	−64.7	−73.526(20)	−77.721(20)
Δ_K (kHz)	1414	[1413.8][a]	[1413.8][a]
δ_J (kHz)	0.196	0.22047(38)	0.24798(45)
δ_K (kHz)	10.00	[10.0][a]	[10.0][a]
Φ_J (Hz)	0.00470	0.005724(26)	0.006344(29)
Φ_{JK} (Hz)	−0.0302	−0.2985(34)	−0.3438(35)
Φ_{KJ} (Hz)	−12.7	−8.884(27)	−9.269(27)
Φ_K (Hz)	371	[371][a]	[371][a]
ϕ_J (Hz)	0.00196	0.002253(18)	0.002568(22)
ϕ_{JK} (Hz)	0.191	[0.191][a]	[0.191][a]
ϕ_K (Hz)	31.5	[31.5][a]	[31.5][a]
L_{JJK} (mHz)		0.00586(21)	0.00634(22)
ΔE (cm^{-1})		[52.025]	
F_{bc}^{J} (MHz)		0.00271(15)	
F_{bc}^{JJ} (MHz)		−0.0000000086(10)	
σ (MHz)		1.22	1.45
N_{lines}		1140	1007

[a] Held fixed to B3LYP/cc-pVTZ value

An ultimate goal of spectroscopic studies of these conformers would be an experimental determination of the potential energy surface predicted in Figure 3.2. The three critical parameters describing the surface are the isomerization energy and the two barrier heights. The isomerization energy may be determinable from the relative intensities of the transitions of the two conformers and well-predicted (CCSD(T)) computational dipole moments. Information on the barrier heights can be gleaned spectroscopically from the spacing of the vibrational levels in each conformer, and even more directly from tunneling splittings, if those can be observed.[6] The observation of *c*-type transitions would be particularly likely to show effects of tunneling splittings, because the selection rules allow for changes from + to − or − to + symmetry states, so the tunneling splitting will be far more prominent in these transitions than in *a*- and *b*-type transitions (+ to + or − to − selection rules).[6] Thus far, we have not assigned any independent *c*-type transitions or seen evidence of

tunneling splitting in the observed vibrational states. Tunneling splittings increase in magnitude exponentially with the torsional quantum number, so excited states are far more likely to exhibit observable tunneling splitting. The spacing of the vibrational levels in either conformer can in-principle be very exactly determined from a complete polyad perturbation analysis (with considerable difficulty), as described earlier, or more directly from the position of the torsional fundamental and its hot-bands in the infrared spectrum. The possible use of this latter approach has prompted our work with the Canadian Light Source, as discussed in the following section.

CANADIAN LIGHT SOURCE

The work described above was presented at the International Symposium on Molecular Spectroscopy in June 2019 in Urbana-Champaign, Illinois,[33] though the *syn* fit presented here now includes octic terms. At that conference we learned about the Canadian Light Source (CLS), particularly their Far-IR beamline, and we submitted proposals for projects in August 2019 and were initially awarded time in June 2020. Due to the Covid-19 Pandemic, our initially scheduled time in June was not possible, however, we were given time to run experiments remotely with beamline staff Brant Billinghurst and Jianbao Zhao in August and September 2020, and February 2021. This work is discussed further in Appendix A of this thesis.

FUTURE WORK

Experimental work at the Canadian Light Source is ongoing for 4-cyano-1,2-butadiene. In the case of 4-cyano-1,2-butadiene *anti* coupled fit, based on the effective fits it is likely that the Hamiltonian for each vibrational state will require octic distortion constants, which presents a challenge since they cannot be predicted and cannot be experimentally determined without

simultaneously treating the coupling. The theory needs to continue developing to enable the prediction of the octic distortion terms to facilitate the coupled fitting involving the ground state. Theoretical work on predicting coupling terms between the ground state and fundamentals, and between fundamentals and overtones or fundamentals and combination states also requires further development before a fully informed coupled fit of the *anti* vibrational states can be approached. If fewer variables are complete unknowns when beginning a dyad or polyad fit, the prospect of a successful fit will be improved. Finally, we need to delve further into the incorporation of internal-rotation terms into the Hamiltonian to model the barrier and to improve the prediction of the tunneling splitting, as employed previously for 3-fluoropropene.[6]

ACKNOWLEDGMENTS

REFERENCES

1. Müller, H. S. P.; Schlöder, F.; Stutzki, J.; Winnewisser, G., The Cologne Database for Molecular Spectroscopy, CDMS: a Useful Tool for Astronomers and Spectroscopists. *J. Mol. Struct.* **2005**, *742* (1–3), 215-227.

2. Kougias, S. M.; Knezz, S. N.; Owen, A. N.; Sanchez, R. A.; Hyland, G. E.; Lee, D. J.; Patel, A. R.; Esselman, B. J.; Woods, R. C.; McMahon, R. J., Synthesis and Characterization of Cyanobutadiene Isomers—Molecules of Astrochemical Significance. *J. Org. Chem.* **2020**, *85* (9), 5787-5798.

3. Moreno, R.; Silla, E.; Tunon, I.; Arnau, A., Ab Initio Rotational Constants of the Nitriles Derived from Cyanodiacetylene (HC_4CN). *Astrophys. J.* **1994**, *437*, 532.

4. McCarthy, M. C.; Lee, K. L. K.; Carroll, P. B.; Porterfield, J. P.; Changala, P. B.; Thorpe, J. H.; Stanton, J. F., Exhaustive Product Analysis of Three Benzene Discharges by Microwave Spectroscopy. *J. Phys. Chem. A* **2020**, *124* (25), 5170-5181.

5. Lin, C. C.; Swalen, J. D., Internal Rotation and Microwave Spectroscopy. *Rev. Mod. Phys.* **1959**, *31* (4), 841-892.

6. Meakin, P.; Harris, D. O.; Hirota, E., Barriers to Internal Rotation in Asymmetric Molecules: 3-Fluoropropene. *J. Chem. Phys.* **1969**, *51* (9), 3775-3788.

7. Quade, C. R.; Lin, C. C., Internal Rotation in Completely Asymmetric Molecules. I. A General Theory and Analysis of the Microwave Rotational Spectrum of CH_2DCOH, CD_2HCOH, and $CHOOCH_2D$. *J. Chem. Phys.* **1963**, *38* (2), 540-550.

8. McKellar, A. R. W., High-resolution infrared spectroscopy with synchrotron sources. *J. Mol. Spectrosc.* **2010**, *262* (1), 1-10.

9. Dunning, T. H., Gaussian basis sets for use in correlated molecular calculations. I. The atoms boron through neon and hydrogen. *J. Chem. Phys.* **1989**, *90* (2), 1007-1023.

10. Becke, A. D., Density-functional thermochemistry. III. The role of exact exchange. *J. Chem. Phys.* **1993**, *98* (7), 5648-5652.

11. Lee, C.; Yang, W.; Parr, R. G., Development of the Colle-Salvetti correlation-energy formula into a functional of the electron density. *Phys. Rev. B* **1988**, *37* (2), 785-789.

12. Frisch, M. J.; Trucks, G. W.; Schlegel, H. B.; Scuseria, G. E.; Robb, M. A.; Cheeseman, J. R.; Scalmani, G.; Barone, V.; Petersson, G. A.; Nakatsuji, H.; Li, X.; Caricato, M.; Marenich, A. V.; Bloino, J.;

Janesko, B. G.; Gomperts, R.; Mennucci, B.; Hratchian, H. P.; Ortiz, J. V.; Izmaylov, A. F.; Sonnenberg, J. L.; Williams-Young, D.; Ding, F.; Lipparini, F.; Egidi, F.; Goings, J.; Peng, B.; Petrone, A.; Henderson, T.; Ranasinghe, D.; Zakrzewski, V. G.; Gao, J.; Rega, N.; Zheng, G.; Liang, W.; Hada, M.; Ehara, M.; Toyota, K.; Fukuda, R.; Hasegawa, J.; Ishida, M.; Nakajima, T.; Honda, Y.; Kitao, O.; Nakai, H.; Vreven, T.; Throssell, K.; Montgomery, J. A., Jr.; Peralta, J. E.; Ogliaro, F.; Bearpark, M. J.; Heyd, J. J.; Brothers, E. N.; Kudin, K. N.; Staroverov, V. N.; Keith, T. A.; Kobayashi, R.; Normand, J.; Raghavachari, K.; Rendell, A. P.; Burant, J. C.; Iyengar, S. S.; Tomasi, J.; Cossi, M.; Millam, J. M.; Klene, M.; Adamo, C.; Cammi, R.; Ochterski, J. W.; Martin, R. L.; Morokuma, K.; Farkas, O.; Foresman, J. B.; Fox, D. J. Gaussian 16, Revision B.01, Gaussian, Inc., Wallingford CT, 2016.

13. Schmidt, J.; Polik, W., WebMO Enterprise. *WebMO LLC, Holland, MI USA* **2013**.

14. Gaussian 16, Revision C.01, Frisch, M. J.; Trucks, G. W.; Schlegel, H. B.; Scuseria, G. E.; Robb, M. A.; Cheeseman, J. R.; Scalmani, G.; Barone, V.; Petersson, G. A.; Nakatsuji, H.; Li, X.; Caricato, M.; Marenich, A. V.; Bloino, J.; Janesko, B. G.; Gomperts, R.; Mennucci, B.; Hratchian, H. P.; Ortiz, J. V.; Izmaylov, A. F.; Sonnenberg, J. L.; Williams-Young, D.; Ding, F.; Lipparini, F.; Egidi, F.; Goings, J.; Peng, B.; Petrone, A.; Henderson, T.; Ranasinghe, D.; Zakrzewski, V. G.; Gao, J.; Rega, N.; Zheng, G.; Liang, W.; Hada, M.; Ehara, M.; Toyota, K.; Fukuda, R.; Hasegawa, J.; Ishida, M.; Nakajima, T.; Honda, Y.; Kitao, O.; Nakai, H.; Vreven, T.; Throssell, K.; Montgomery, J. A., Jr.; Peralta, J. E.; Ogliaro, F.; Bearpark, M. J.; Heyd, J. J.; Brothers, E. N.; Kudin, K. N.; Staroverov, V. N.; Keith, T. A.; Kobayashi, R.; Normand, J.; Raghavachari, K.; Rendell, A. P.; Burant, J. C.; Iyengar, S. S.; Tomasi, J.; Cossi, M.; Millam, J. M.; Klene, M.; Adamo, C.; Cammi, R.; Ochterski, J. W.; Martin, R. L.; Morokuma, K.; Farkas, O.; Foresman, J. B.; Fox, D. J. Gaussian, Inc., Wallingford CT, 2019.

15. Fausto, R.; Teixeira-Dias, J. J. C.; Ramos, M. N., Relative stability, potential barrier and intensity parameters of the trans and cis isomers of fluoroacetyl fluoride: An ab initio study. *Spectrochim. Acta. A* **1988**, *44* (1), 47-52.

16. Pople, J. A.; Head-Gordon, M.; Raghavachari, K., Quadratic Configuration Interaction. A General Technique for Determining Electron Correlation Energies. *J. Chem. Phys.* **1987**, *87* (10), 5968-5975.

17. Woon, D. E.; Dunning, T. H., Gaussian basis sets for use in correlated molecular calculations. V. Core-valence basis sets for boron through neon. *J. Chem. Phys.* **1995**, *103* (11), 4572.

18. Mills, I. M., Vibration-Rotation Structure in Asymmetric- and Symmetric-Top Molecules. In *Molecular Spectroscopy: Modern Research*, Rao, K. N.; Mathews, C. W., Eds. Academic Press: New York, 1972; Vol. 1, pp 115-140.

19. Esselman, B. J.; Amberger, B. K.; Shutter, J. D.; Daane, M. A.; Stanton, J. F.; Woods, R. C.; McMahon, R. J., Rotational spectroscopy of pyridazine and its isotopologs from 235–360 GHz: Equilibrium structure and vibrational satellites. *J. Chem. Phys.* **2013**, *139* (22), 224304.

20. Zdanovskaia, M. A.; Esselman, B. J.; Woods, R. C.; McMahon, R. J., The 130–370 GHz Rotational Spectrum of Phenyl Isocyanide (C_6H_5NC). *J. Chem. Phys.* **2019**, *151* (2), 024301.

21. Kisiel, Z., Assignment and Analysis of Complex Rotational Spectra. In *Spectroscopy from Space*, Demaison, J.; Sarka, K.; Cohen, E. A., Eds. Springer Netherlands: Dordrecht, 2001; pp 91-106.

22. Kisiel, Z.; Pszczółkowski, L.; Medvedev, I. R.; Winnewisser, M.; De Lucia, F. C.; Herbst, E., Rotational spectrum of trans–trans diethyl ether in the ground and three excited vibrational states. *J. Mol. Spectrosc.* **2005**, *233* (2), 231-243.

23. Kisiel, Z. PROSPE - Programs for ROtational SPEctroscopy. http://info.ifpan.edu.pl/~kisiel/prospe.htm

24. Pickett, H. M., The fitting and prediction of vibration-rotation spectra with spin interactions. *J. Mol. Spectrosc.* **1991**, *148* (2), 371-377.

25. Amberger, B. K. Millimeter-wave Spectroscopy of Highly Nitrogenous Molecules of Potential Astrochemical Interest. Ph.D. Thesis, University of Wisconsin-Madison, Madison, WI, 2015.

26. Vávra, K.; Kania, P.; Koucký, J.; Kisiel, Z.; Urban, Š., Rotational spectra of hydrazoic acid. *J. Mol. Spectrosc.* **2017**, *337*, 27-31.

27. Orr, V. L.; Esselman, B. J.; Dorman, P. M.; Amberger, B. K.; Guzei, I. A.; Woods, R. C.; McMahon, R. J., Millimeter-wave Spectroscopy, X-ray Crystal Structure, and Quantum Chemical Studies of Diketene – Resolving Ambiguities Concerning the Structure of the Ketene Dimer. *J. Phys. Chem. A* **2016**, *120* (39), 7753-7763.

28. Higgins, P. M.; Esselman, B. J.; Zdanovskaia, M. A.; Woods, R. C.; McMahon, R. J., Millimeter-wave spectroscopy of the chlorine isotopologues of chloropyrazine and twenty-two of their vibrationally excited states. *J. Mol. Spectrosc.* **2019**, *364*, 111179.

29. Esselman, B. J.; Zdanovskaia, M. A.; Woods, R. C.; McMahon, R. J., Millimeter-wave spectroscopy of the chlorine isotopologues of 2-chloropyridine and twenty-three of their vibrationally excited states. *J. Mol. Spectrosc.* **2019**, *365*, 111206.

30. Dorman, P. M.; Esselman, B. J.; Woods, R. C.; McMahon, R. J., An analysis of the rotational ground state and lowest-energy vibrationally excited dyad of 3-cyanopyridine: Low symmetry reveals rich complexity of perturbations, couplings, and interstate transitions. *J. Mol. Spectrosc.* **2020**, *373*, 111373.

31. Dorman, P. M.; Esselman, B. J.; Park, J. E.; Woods, R. C.; McMahon, R. J., Millimeter-wave spectrum of 4-cyanopyridine in its ground state and lowest-energy vibrationally excited states, ν_{20} and ν_{30}. *J. Mol. Spectrosc.* **2020**, *369*, 111274.

32. Zdanovskaia, M. A.; Esselman, B. J.; Lau, H. S.; Bates, D. M.; Woods, R. C.; McMahon, R. J.; Kisiel, Z., The 103 – 360 GHz Rotational Spectrum of Benzonitrile, the First Interstellar Benzene Derivative Detected by Radioastronomy. *J. Mol. Spectrosc.* **2018**, *351*, 39-48.

33. Orr, V. L.; Esselman, B. J.; Owen, A. N.; Kougias, S. M.; Woods, R. C.; McMahon, R. J. Rotational Spectroscopy of *syn* and *anti-clinal* Penta-3,4-dienenitrile from 130-375 GHz, *International Symposium on Molecular Spectroscopy*, Champaign-Urbana, Illinois, June 17-21, 2019; Champaign-Urbana, Illinois, 2019; RI07.

Chapter 4: Precise equilibrium structure determination of thiophene (C₄H₄S) by rotational spectroscopy – structure of a five-membered heterocycle containing a second-row atom
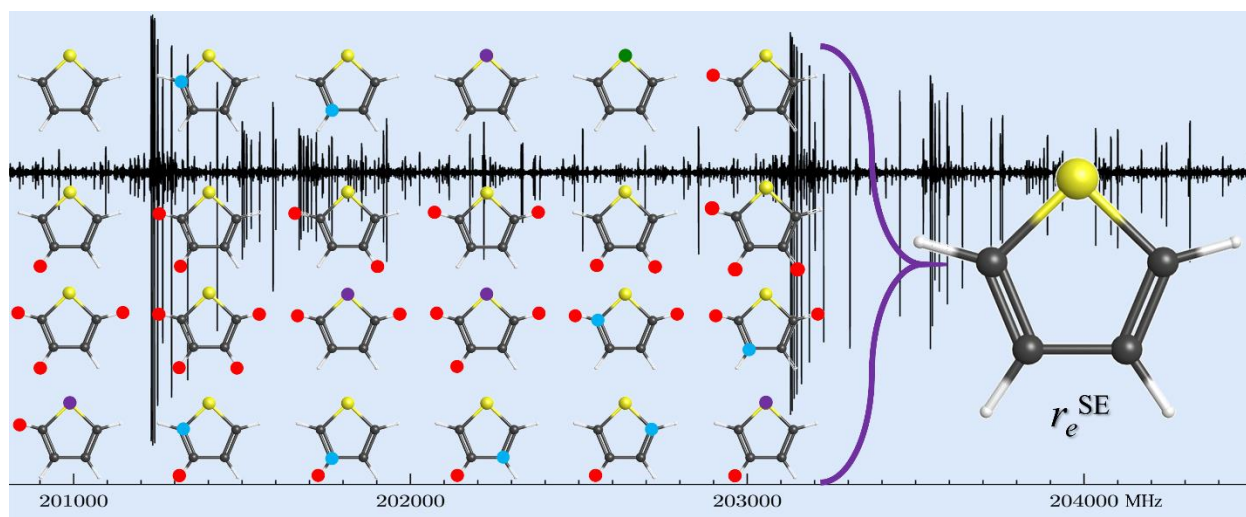
Includes the work of several collaborators:

Brian J. Esselman, Aatmik R. Patel, Samuel M. Kougias, Andrew N. Owen

R. Claude Woods, Robert J. McMahon

University of Wisconsin-Madison

Yotaro Ichikawa and Kaori Kobayashi

University of Toyama, Japan

John F. Stanton

University of Florida

ABSTRACT

The rotational spectrum of thiophene (c-C_4H_4S) has been collected from $8 - 360$ GHz. Samples of varying deuterium-enrichment were synthesized to yield all possible deuterium-substituted isotopologues of thiophene. A total of 26 isotopologues have been measured and least-squares fit using A- and S-reduced distorted rotor Hamiltonians in the I^r representation. The resultant rotational constants (A_0, B_0, C_0) from each reduction were converted to determinable constants (A'', B'', C''). Computed vibrational and electron mass corrections (CCSD(T)/cc-pCVTZ) were applied to the determinable constants to obtain semi-experimental equilibrium rotational constants (A_e, B_e, C_e) for 24 isotopologues. A precise semi-experimental equilibrium (r_e^{SE}) structure has been achieved from a least-squares fit of the equilibrium moments of inertia. The combination of the expanded isotopologue rotational spectroscopy data with high-level computational work establishes a precise r_e^{SE} structure for a heterocycle containing a second-row atom. The CCSD(T)/cc-pCV5Z structure has been obtained and corrected for the extrapolation to the complete basis set, electron correlation beyond CCSD(T), relativistic effects, and the diagonal Born-Oppenheimer correction The precise r_e^{SE} structure is compared to the resulting "best theoretical estimate" structure.

INTRODUCTION

In a recent structure determination of pyrimidine, our group was able to achieve a very satisfying level of agreement between the semi-experimental equilibrium (r_e^{SE}) parameters and the highest practical level of theoretical calculation available to us: differences no more than 0.0004 Å in bond distances and no more than 0.01° in the bond angles employed.[1] That occurrence naturally made us consider the question of whether or not that level of agreement was possible in

parallel treatments of other similarly sized molecules, in particular ones that contained a second-row atom. The present study of thiophene was therefore undertaken with the primary goal of beginning to answer that question. To do so we have again utilized very well-determined rotational constants for a highly redundant set of isotopologues (24), combined with high-level computational vibration-rotation and electron mass corrections, to produce an r_e^{SE} structure. On the theoretical side we have again pushed the coupled cluster calculations to a quintuple zeta basis set and correlated both the core and valence electrons. Furthermore, as for pyrimidine, we corrected this to what we call a "best theoretical estimate" (BTE) structure by adding corrections to address, (1) an approximate extrapolation to a complete basis set, (2) residual electron correlation beyond CCSD(T), (3) relativistic effects, and (4) the diagonal Born-Oppenheimer correction.[1] In answer to the above posed rhetorical question, we have found that for several of the structural parameters the BTE values do indeed fall within the narrow 2σ statistical limits of the r_e^{SE} results, and the corresponding residuals are comparably small to those found in the pyrimidine case. For some other parameters, however, that is not the case. The possible origin of those cases of less exact agreement will be explored in some detail below.

The five-membered, aromatic ring of thiophene (C_4H_4S, Figure 4.1, C_{2v}) is a fundamental molecular building block and is prevalent in pharmaceuticals[2] and organic electronics.[3-4] Thiophenes can be found naturally on Earth and have been detected on Mars.[5-6] Thiophene itself has been proposed to be present in the interstellar medium,[7] and unsaturated carbon chain molecules containing sulfur have been detected.[8-9] The rotational and vibrational spectroscopy of thiophene have been of interest for over a century. The first infrared absorption spectra of thiophene was reported in 1905 by Coblentz,[10] and other Raman and infrared studies were reported in the 1930's and 40's.[11-14] In 1965, a low-resolution infrared study of liquid and vapor phase

thiophene and all its deuterio isotopologues (mono- through tetra-deuterio, except [2,4-^{2}H]-thiophene) was published including assignment of their fundamental vibrations.[15] The vibrational assignments of thiophene were later reaffirmed,[16] and the rotationally resolved IR spectrum of the ν_{13} band of thiophene was reported by G. Winnewisser and co-workers.[17] The rotationally resolved IR spectrum of thiophene has subsequently been analyzed for ν_{14}, ν_8, ν_7 (400 – 750 cm^{-1}),[18-19] and ν_{13}, ν_7, ν_6, ν_5, and ν_{19} (600 – 1200 cm^{-1}).[20] These studies provided the rotational and centrifugal distortion constants for each of these vibrationally excited states, along with their precise vibrational frequencies. More recently, Raman and resonance Raman spectra of neat thiophene and thiophene solvated in various solvents (cyclohexane, dimethyl sulfoxide, and methanol) have also been reported.[21-22] The fundamental vibrational frequencies of thiophene are presented in Chapter 5 of this thesis.

The dipole moment of thiophene, 0.55 ± 0.01 D determined by the Stark effect,[23] permits observation by rotational spectroscopy. Bak *et al*. provided the rotational constants for thiophene and four deuterated isotopologues,[24] and the ^{34}S and the two ^{13}C isotopologues based upon microwave spectral data from 12 – 30 GHz.[25] Using Kraitchman's equations,[26] they determined the first substitution structure of thiophene (r_s) from the parent and five mono-substituted isotopologues.[25] This early microwave data was combined with electron diffraction and liquid-crystal NMR data to determine the r_α structure (ED+MW+LCNMR).[27] Later the microwave, electron diffraction, and vibrational spectroscopy were combined with computational methods to find a mixed-method, semi-experimental equilibrium structure (r_e^{SE}).[28] The work of Bak *et al*.[24-25] was used to determine a subsequent semi-experimental equilibrium structure (r_e^{SE}) with corrections for vibration-rotation interactions and the electron-mass distributions from DFT methods.[29-30] Though not utilized in the previous thiophene structure determinations, additional

rotational transitions of the normal isotopologue of thiophene have been observed in later works,[31-34] as well as transitions for the ^{33}S and ^{34}S isotopologues.[34] In this work, we have greatly extended the data set to include a total of 26 isotopologues, of which 24 were included in the determination of the semi-experimental equilibrium structure (r_e^{SE}) of thiophene. We have systematically investigated the extent to which additional isotopologues are valuable in reducing the statistical errors of the r_e^{SE} structural parameters.
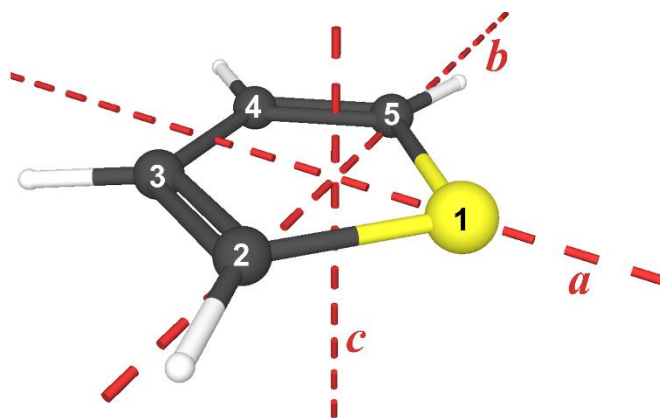
Figure. 4.1. Thiophene (C_4H_4S, $\mu_a = 0.55$ D) with its principal axes and numerical atom designations.

METHODS

Spectroscopy Methods

Rotational spectra of thiophene were collected using two different spectrometers and combined into a single broadband spectrum. The spectrum of thiophene was collected at the University of Toyama between 40 to 121.5 GHz at sample pressures of 30 – 50 mTorr using instrumentation described previously.[35-36] A select number of transitions were collected between 8 – 18 GHz with a FT-MW spectrometer, based on the design of McJunkins and Brown,[37] with a chirp pulse of 50 – 150 or 50 – 200 MHz, at pressures at 9 – 13 mTorr, with 10,000 to 50,000 pulse acquisitions. The broadband spectra of thiophene and its deuterium-containing isotopologues were

collected at the University of Wisconsin-Madison from 130 – 230 and 235 – 360 GHz with a pressure of 5 mTorr using instrumentation described previously.[38-39] The spectrum of tetradeuterio thiophene was collected only from 130 – 230 GHz. Programs from Kisiel's Assignment and Analysis of Broadband Spectra (AABS) software package,[40-42] including ASFIT and ASROT,[43-44] were used to visualize spectra and combine spectra into a single broadband spectrum at each stage of isotopic enrichment, obtain least-squares fits for each isotopologue, generate predicted stick spectra, and create data distribution plots. Measured transitions for each isotopologue were least-squares fit in the I^r representation and the A- and S-reductions, the ground state of the normal isotopologue has been fit in both reductions in the III^r representation, as well.

Computational Methods

The B3LYP calculations were performed using Gaussian 16[45-46] with the WebMO interface.[47] The optimized geometries were calculated at the B3LYP/6-311G+(2d,p) level utilizing a "verytight" convergence criteria and an "ultrafine" integration grid. An anharmonic frequency calculation was performed to obtain the centrifugal distortion constants for the normal isotopologue. The thiolium cations were optimized in the method above and the Natural Population Analysis and the Natural Bond Orbital(NBO)/Natural Resonance Theory(NRT) Analysis were performed with NBO 7.0.8.[48]

All CCSD(T) calculations were performed using CFOUR.[49] Geometry optimizations were performed at the CCSD(T) level with the cc-pCVXZ basis set where X = D, T, Q, and 5. The structure computed at CCSD(T)/cc-pCVTZ was subsequently used for a second-order vibrational perturbation (VPT2) anharmonic frequency calculation by evaluating the cubic force constants using analytical second derivatives at displaced points.[50-52] The VPT2 calculation was used to obtain anharmonic frequencies for each isotopologue and also provided vibration-rotation (α_i)

interactions, along with quartic and sextic distortion terms, (in both the A- and S-reduction, in the I^r representation). The structure computed at the CCSD(T)/cc-pCVTZ level was also used for magnetic calculations to obtain the electron mass corrections to the rotational constants.[53] Additional computational corrections to the CCSD(T)/cc-pCV5Z structure are used to determine the best theoretical structure. These corrections were performed following the method prescribed in Heim, *et al.*[1] and are specified in subsequent text. The xrefit module of CFOUR was utilized to obtain the least-squares fit r_e^{SE} structure.

SYNTHESIS OF DEUTERIO THIOPHENES

In a manner analogous to the incorporation of deuterium in other 5-membered ring heteroaromatic compounds and previous efforts on thiophene itself,[54-57] deuterio isotopologues of thiophene were prepared. The acid-catalyzed reaction involved refluxing thiophene (10 mL), D_2O (20 mL), and fuming sulfuric acid (7 mL) at 100 °C for five days (Scheme 4.1 a). The duration of reflux can be varied to control the level of deuterium-hydrogen exchange. The five-day reaction time resulted in detectable quantities of every possible deuterium-containing isotopologue of the normal isotopologue of thiophene, which is ideal for rotational spectroscopy, due to the ability to obtain the broadband spectra of all isotopologues in a single experiment. This synthetic method results in a great reduction of overall experimental time with an acceptable loss of transitions due to overlapping signals from multiple species. To promote more complete deuteration of thiophene the same reaction was conducted with refluxing extended over two weeks, with the addition of more H_2SO_4 and D_2O after seven days. This procedure yielded a small sample with mostly tetra-deuterio thiophene which also allowed for the assignment of transitions for the [2,3,4,5-^{2}H, ^{34}S] isotopologue. While the extended time for reflux andl replenishing the deuterium source did

increase the amount of deuterium incorporation, this method is not sufficient for obtaining a sample that has only (or even nearly all of) the tetra-deuterio isotopologue present.
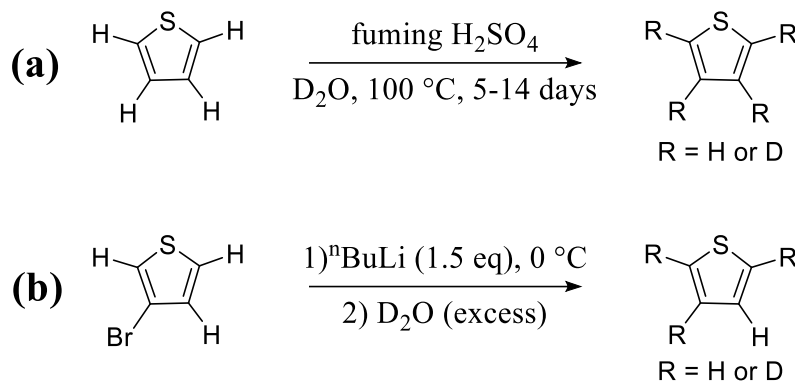
Scheme 4.1. Synthesis of deuterated isotopologues of thiophene.

The deuterium-hydrogen exchange reactions proceed via deuteriation / deprotonation at each carbon atom in the ring (Scheme 4.1 a). The preference for D/H exchange at C2 over C3 is consistent with the relative energies of the thiolium cation intermediates (Figure 4.2). The 9.1 kcal/mol energy difference (B3LYP/6-311G+(2d,p)+ZPVE) is rationalized by delocalization of positive charge over more atoms via π conjugation when the H/D$^+$ is attached to C2, as is shown in the accompanying resonance structures. A similar stabilization is not afforded when the H/D$^+$ attaches to C3. This is clear from the highest contributing resonance structures from the Natural Resonance Theory analysis and the Natural Population Analysis charges of each thiolium displayed in Figure 4.2. The differential rate of exchange leads to the dominance of [2-^{2}H]-, [2,5-^{2}H]-, and [2,3,5-^{2}H]-thiophene in the rotational spectrum of the deuterium-enriched sample (after 5 days reflux), while the lowest-abundance thiophene-d_x species in the spectrum is [3,4-^{2}H]-thiophene (excluding heavy-atom sulfur or carbon isotopologues).

3*H*-thiolium, 9.1 kcal/mol

56%

2*H*-thiolium, 0.0 kcal/mol

46%   21%
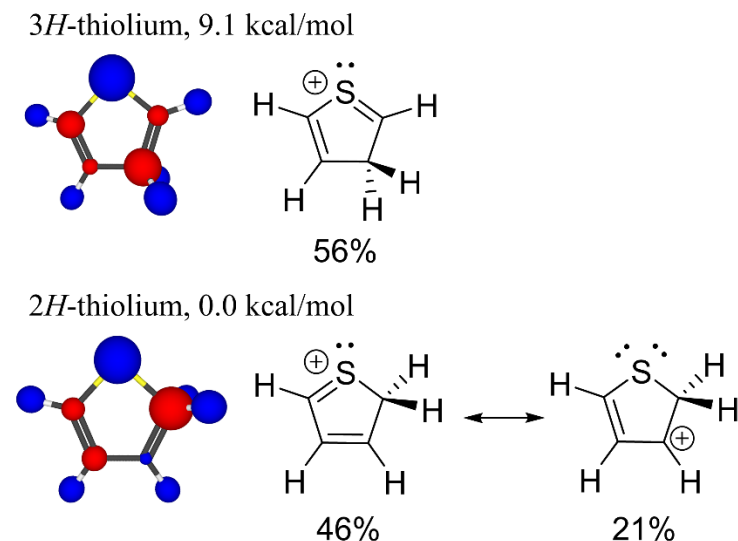
Figure 4.2. 2*H*-Thiolium and 3*H*-thiolium with their relative energies (B3LYP/6-311G+(2d,p)+ZPVE), the National Population Analysis charges as spheres corresponding to local charge (blue for positive and red for negative), and relevant resonance structures from the Natural Resonance Theory analysis.

Since the [3-^{2}H]-thiophene isotopologue cannot be prepared in high abundance using acid-catalyzed H/D exchange, an alternate route was adapted.[58] A sample of [3-^{2}H]-thiophene was generated from 3-bromothiophene by lithium-halogen exchange, followed by quenching with D_2O (Scheme 4.1 b). The resultant sample was primarily [3-^{2}H]-thiophene, but the reaction did contain some [2-^{2}H]-thiophene, along with other combinations of di- and tri-deuterio substituted isotopologues (though in substantially smaller amounts than generated by acid-catalyzed H/D exchange reaction). The rearranged and poly-deuteriated thiophenes, presumably result from the base-catalyzed H/D exchange in the strongly basic conditions. The reaction described in Scheme 4.1b not only allowed for the assignment of more transitions for the [3-^{2}H] isotopologue, but also permitted the observation of sulfur and carbon heavy-atom isotopologues of [3-^{2}H] thiophene.

ANALYSIS OF ROTATIONAL SPECTRA

Normal Isotopologue, ground vibrational state

The rotational spectrum of the ground vibrational state of the normal isotopologue of thiophene has been greatly expanded from previous works (5-40 GHz)[24, 31-34] to include 40-360 GHz, along with some additional transitions between 8 and 17 GHz. The spectrum of thiophene, which includes the normal isotopologue and four heavy-atom isotopologues at natural abundance, is shown in Figure 4.3. The distinct bands in the spectrum are due to $^aR_{0,1}$ transitions that are K_c degenerate and decrease in J as they simultaneously increase in K_a. As K_a continues to increase these transitions generally lose degeneracy around $K_a = 10$ and then become K_a degenerate around $K_a = 20$. With the inclusion of transitions previously reported,[31-32, 34] the data set contains of 3270 transitions with a J'' range from 1 to 93 and K_a'' range from 0 to 38; this is depicted in a data set distribution plot in Figure 4.4. Successful least-squares fitting of this large data set requires a full sextic, distorted-rotor Hamiltonian (A- and S- reduction, I^r and III^r representation all employed). The experimental κ value ($\kappa = (2B-A-C)/(A-C)$) of –0.0917 indicates the highly asymmetric, barely prolate nature of thiophene and suggests the I^r representation to be somewhat more appropriate. The III^r representation has been commonly used in previous studies of thiophene, despite it being more appropriate to oblate asymmetric tops. To allow for comparison with previous work, the A-reduced, I^r and III^r spectroscopic constants from this work are presented in Table 4.1 along with computational values and previously determined values from high-resolution IR studies.[18, 20] With the exception of H_K in the S-reduction, all quartic and sextic constants were satisfactorily determined in both representations and in both reductions with least-squares fit σ values of 0.022 MHz. The computed and experimental spectroscopic constants display excellent agreement. Compared to the experimentally determined A-reduced, I^r-representation

spectroscopic constants, the computed rotational constants (CCSD(T)/cc-pCVTZ) are within 0.8%, the quartic distortion constants are within 2%, and the sextic constants are within 10 % This agreement provides excellent indication that the experimental constants (A-reduction, I^r) are physically meaningful. Constants from the S-reduced I^r and III^r representation least squares fits are presented in the supplementary material at the end of this chapter in Table S4.1.
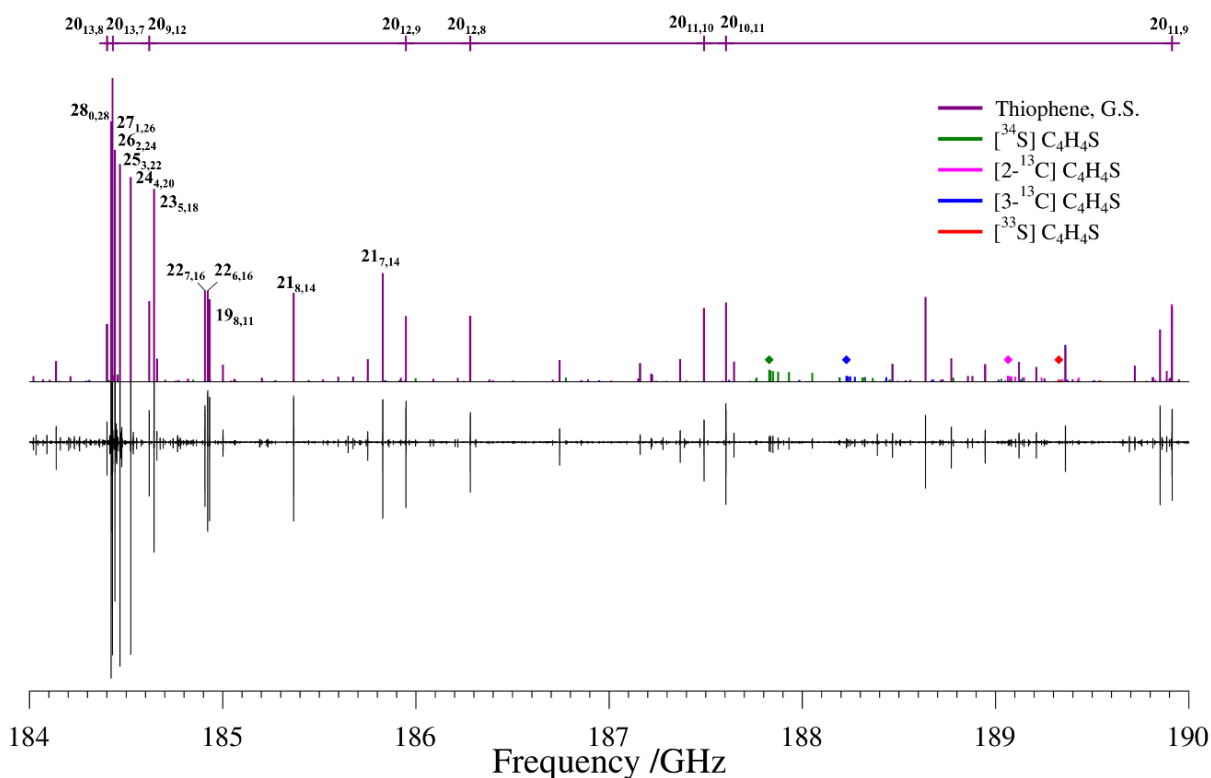
Figure 4.3. Rotational spectrum of thiophene (below) and predicted stick spectra (above) for the vibrational ground states (G.S.) of the normal (purple), [^{34}S] (green), [2-^{13}C] (pink), [3-^{13}C] (blue), and [^{33}S] (red) isotopologues of thiophene from 184 to 190 GHz. The $J' = 29$, $K_a' = 0^+,1^-$ degenerate transition for each heavy atom isotopologue is denoted with a diamond marker in the respective color. Major transitions for the normal isotopologue are indicated explicitly at the top of the figure.
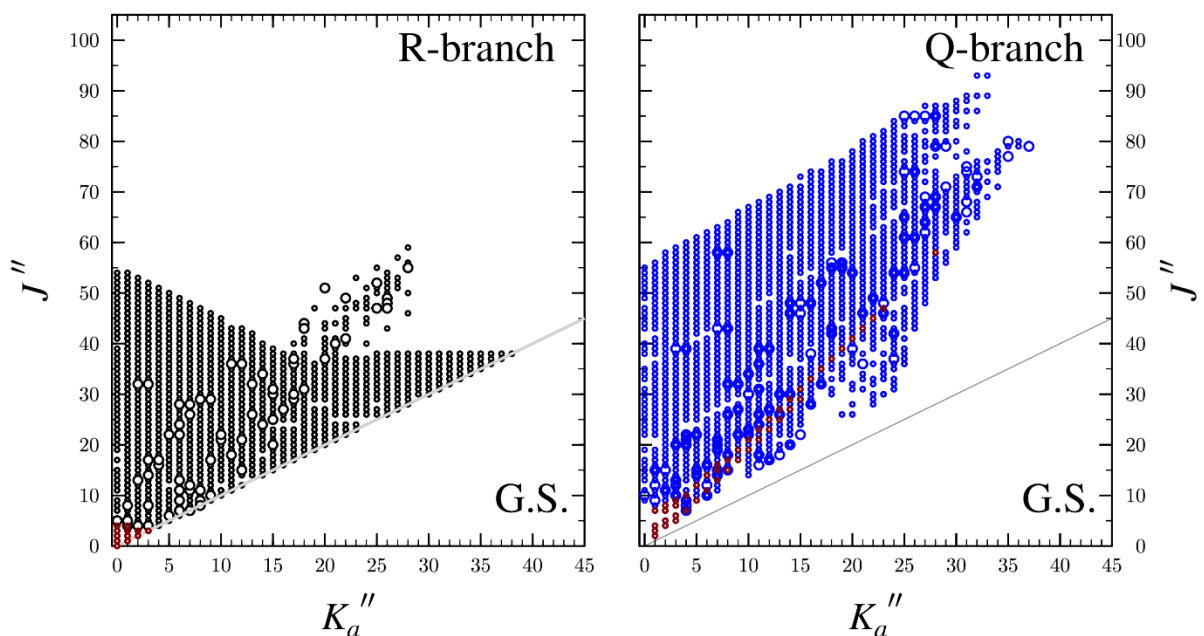
Figure 4.4. Data distribution plots for the vibrational ground state of the normal isotopologue of thiophene. Transitions from the current work are displayed for the R-branch (black) and Q-branch (blue). Transitions included from previous works are displayed in red.[31-32, 34] All transitions have frequencies within twice their experimental error, and the circle size is related to $(f_{obs.} - f_{calc.})/\sigma$.

Table 4.1. Computed and experimental spectroscopic constants for thiophene (A-reduced Hamiltonian, I^r and III^r representations)

| | CCSD(T)/ cc-pCVTZ | Experimental | | B3LYP/ 6-311G+(2d,p)[b] | Experimental | |
		Rotational	IR[20]		Rotational	IR[18]
Representation	I^r	I^r	I^r	III^r	III^r	III^r
$A_0^{(A)}$ (MHz)	7999	8041.594988 (44)	8041.643 (13)[c]	7967	8041.594596 (44)	8041.59567 (25)[c]
$B_0^{(A)}$ (MHz)	5376	5418.264739 (36)	5418.2015 (33)[c]	5367	5418.265640 (36)	5418.26578 (11)[c]
$C_0^{(A)}$ (MHz)	3213	3235.779214 (39)	3235.7763 (36)[c]	3205	3235.778713 (39)	3235.77871 (10)[c]
Δ_J (kHz)	0.823	0.837865 (26)	0.829 (24)[c]	2.15	2.176349 (46)	2.1782 (14)[c]
Δ_{JK} (kHz)	−0.269	−0.272860 (41)	−0.25 (11)[c]	−4.14	−4.28832 (15)	−4.299 (54)[c]
Δ_K (kHz)	2.32	2.32648 (10)	2.32 (10)[c]	2.21	2.32654 (11)	2.3372 (42)[c]
δ_J (kHz)	0.306	0.3116429 (36)	0.307 (12)[c]	0.358	0.357595 (20)	0.35942 (69)[c]
δ_K (kHz)	0.901	0.917685 (27)	0.909 (81)[c]	−1.25	−1.36759 (11)	−1.3766 (45)[c]
Φ_J (Hz)	0.000294	0.0002990 (53)		0.000978	0.000967 (41)	
Φ_{JK} (Hz)	−0.000984	−0.000951 (14)		−0.00548	−0.00559 (30)	
Φ_{KJ} (Hz)	−0.00133	−0.001477 (44)		0.00761	0.00730 (54)	
Φ_K (Hz)	0.00345	0.00342 (11)		−0.00280	−0.00268 (28)	
ϕ_J (Hz)	0.000151	0.00015371 (80)		0.000207	0.000180 (20)	
ϕ_{JK} (Hz)	−0.0000937	−0.0000859 (99)		−0.00340	−0.00320 (17)	
ϕ_K (Hz)	0.00311	0.003184 (21)		0.00123	0.00100 (23)	
$N_{\text{lines MW}}$		3270[a]	6		3270[a]	25
$N_{\text{lines IR}}$		0	3971		0	10,725[d]
σ (MHz)		0.022			0.022	
κ [e]	−0.0965	−0.0917	−0.0918	−0.0920	−0.0917	−0.0917
Δ_i (uÅ^2) [f]	0.0764	0.0657991 (20)	0.06523(21)	0.0776	0.0658357 (20)	0.0658465(56)

[a] Includes transitions from previous literature[31-32, 34]

[b] Values converted from a left-handed coordinate system.

[c] Converted from cm^{-1}

[d] Total transitions

[e] $\kappa = (2B-A-C)/(A-C)$

[f] $\Delta_i = I_c-I_b-I_a$

Heavy-atom isotopologues: [2-^{13}C], [3-^{13}C], [^{34}S], and [^{33}S]-thiophene

Clearly visible in the spectrum at natural abundance are two sulfur isotopologues ([^{34}S] and [^{33}S]) and two ^{13}C-isotopologues ([2-^{13}C] and [3-^{13}C]) of thiophene. Transitions for each of these isotopologues from 40 – 360 GHz were combined with transitions from previous literature (when within 2σ of their experimental error).[25, 34] For the ^{13}C-isotopologues (2.2 % of the intensity of the normal isotopologue), measurement of over 960 distinct transitions for each enabled an A-reduced, sextic, distorted-rotor Hamiltonian least-squares fit in the I^r representation. The 1262 distinct transitions of the [^{34}S] isotopologue (4.3 % natural abundance) were least-squares fit to a sextic, A-reduced, distorted-rotor Hamiltonian. A total 258 transitions were measured, assigned, and least-squares fit to a sextic, distorted-rotor Hamiltonian for the much less abundant [^{33}S] isotopologue (0.75% natural abundance). No sextic-distortion constants were able to be determined for the [^{33}S] isotopologue, unlike for the other three heavy-atom isotopologues which each have some sextic-distortion constants determined. The spectroscopic constants for all rare thiophene isotopologues are presented in Table 4.2 in the A-reduction and I^r representation. All isotopologues have also been fit with a sextic, distorted-rotor Hamiltonian in the S-reduction and I^r representation, which are presented in the supplementary material, Table S4.2 at the end of this chapter. Distortion constants that were not able to be experimentally determined were fixed to the predicted values (CCSD(T)/cc-pCVTZ). The ^{36}S-isotopologue was searched for but not identified due to its low natural abundance (0.01%).

Table 4.2. Spectroscopic constants for isotopologues of thiophene (A-reduced Hamiltonian, I^r representation)^a

Isotopologue	[2-^{13}C]^b	[3-^{13}C]^b	[^{34}S]^b	[^{33}S]^b
$A_0^{(A)}$ (MHz)	7852.77424 (26)	7981.27962 (33)	8041.71455 (21)	8041.6507 (20)
$B_0^{(A)}$ (MHz)	5418.407449 (78)	5319.307988 (88)	5274.186641 (69)	5344.29964 (59)
$C_0^{(A)}$ (MHz)	3204.805018 (85)	3190.617322 (86)	3183.841609 (66)	3209.25676 (13)
Δ_J (kHz)	0.835505 (60)	0.805679 (59)	0.806860 (45)	0.82167 (16)
Δ_{JK} (kHz)	−0.31289 (13)	−0.22714 (23)	−0.24552 (14)	−0.25877 (66)
Δ_K (kHz)	2.26493 (49)	2.25970 (62)	2.32989 (59)	2.3162 (33)
δ_J (kHz)	0.313211 (17)	0.298434 (18)	0.297522 (21)	0.304256 (86)
δ_K (kHz)	0.872765 (80)	0.90851 (11)	0.918853 (91)	0.91756 (39)
Φ_J (Hz)	0.000301 (14)	0.000283 (14)	0.000267 (14)	[0.000286]
Φ_{JK} (Hz)	[−0.001037]	[−0.000862]	[−0.000933]	[−0.000958]
Φ_{KJ} (Hz)	[−0.00115]	−0.00158 (27)	−0.00148 (18)	[−0.00135]
Φ_K (Hz)	[0.00327]	[0.00336]	0.00425 (55)	[0.00345]
ϕ_J (Hz)	[0.000150]	[0.000142]	0.0001356 (77)	[0.000146]
ϕ_{JK} (Hz)	[−0.000131]	[−0.0000510]	[−0.0000781]	[−0.0000857]
ϕ_K (Hz)	[0.00290]	[0.00304]	0.00323 (11)	[0.00313]
N_{lines}	965	983	1262	258
σ (MHz)	0.030	0.029	0.024	0.029
κ	−0.0475	−0.111	−0.139	−0.116
Δ_i (uÅ^2)	0.0666391 (49)	0.0664073 (53)	0.0665535 (39)	0.066099 (20)

^{a} Brackets around a tabulated number indicate that it is held constant at the value predicted by the VPT2 calculation.

^{b} Includes previously reported transitions.[24-25, 34]

^{c} Shaded column indicates isotopologue is not included in structure determination

Table 4.2. cont.

Isotopologue	[2-²H][b]	[3-²H][b]	[2,3-²H]	[2,4-²H]	[2,5-²H]	[3,4-²H]
$A_0^{(A)}$ (MHz)	7437.19652 (21)	7855.99700 (11)	7277.00063 (26)	7288.38296 (28)	6903.42586 (12)	7616.559 (16)
$B_0^{(A)}$ (MHz)	5413.723448 (86)	5138.231795 (65)	5137.629189 (93)	5124.659383 (99)	5410.700126 (70)	4914.6804 (78)
$C_0^{(A)}$ (MHz)	3131.813807 (83)	3105.221251 (71)	3010.348883 (87)	3007.829941 (85)	3032.129303 (70)	2986.05326 (18)
Δ_J (kHz)	0.821125 (56)	0.723059 (43)	0.712885 (52)	0.700284 (50)	0.808168 (44)	0.63872 (28)
Δ_{JK} (kHz)	−0.39209 (25)	−0.13110 (10)	−0.26516 (30)	−0.19014 (12)	−0.52442 (16)	[−0.0691]
Δ_K (kHz)	1.96671 (54)	2.10650 (28)	1.78077 (46)	1.75073 (57)	1.71013 (27)	[1.90]
δ_J (kHz)	0.313560 (25)	0.265110 (11)	0.268996 (25)	0.262854 (24)	0.316189 (17)	0.23246 (14)
δ_K (kHz)	0.77380 (11)	0.855322 (33)	0.725660 (69)	0.739362 (80)	0.639781 (31)	0.7771 (12)
Φ_J (Hz)	0.000295 (15)	0.0002232 (90)	0.000204 (18)	0.000203 (13)	0.000299 (10)	[0.000182]
Φ_{JK} (Hz)	−0.001034 (92)	−0.000548 (38)	−0.00058 (12)	[−0.000408]	−0.000945 (56)	[−0.000484]
Φ_{KJ} (Hz)	[−0.00100]	−0.001723 (75)	[−0.00113]	[−0.00159]	[−0.000556]	[−0.00122]
Φ_K (Hz)	0.00261 (41)	0.00328 (17)	[0.00249]	0.00285 (44)	0.00182 (12)	[0.00266]
ϕ_J (Hz)	0.0001470 (73)	0.0001133 (20)	0.0001002 (88)	0.0001100 (70)	0.0001448 (44)	[0.0000930]
ϕ_{JK} (Hz)	−0.000145 (54)	[0.0000235]	[−0.0000396]	[0.0000445]	[−0.000190]	[0.0000163]
ϕ_K (Hz)	0.00225 (10)	0.002657 (43)	0.00209 (13)	0.00176 (11)	0.001864 (59)	[0.00233]
N_{lines}	1350	1880	1187	1171	1651	203
σ (MHz)	0.028	0.029	0.030	0.030	0.027	0.038
κ	0.0600	−0.1441	−0.0028	−0.0110	0.2288	−0.1670
Δ_i (uÅ²)	0.0650745 (50)	0.0644224 (41)	0.0636014 (58)	0.0636974 (58)	0.0640103 (43)	0.06332 (22)

Table 4.2. cont.

Isotopologue	[2,3,4-²H]	[2,3,5-²H]	[2,3,4,5-²H]	[2,5-²H, ³⁴S]	[2,3,5-²H, ³⁴S]	[2,3,4,5-²H, ³⁴S][c]
$A_0^{(A)}$ (MHz)	7072.27535 (33)	6775.84910 (11)	6587.73131 (19)	6903.5341 (10)	6773.39898 (92)	6588.36 (32)
$B_0^{(A)}$ (MHz)	4909.47072 (10)	5124.450510 (68)	4905.809457 (85)	5268.34457 (31)	4992.25536 (32)	4777.73 (18)
$C_0^{(A)}$ (MHz)	2896.800008 (93)	2916.730636 (65)	2810.896934 (76)	2986.90563 (30)	2872.96809 (23)	2768.4911 (18)
Δ_J (kHz)	0.626846 (51)	0.691920 (37)	0.616403 (40)	0.77885 (13)	0.66822 (12)	0.5868 (72)
Δ_{JK} (kHz)	−0.17023 (13)	−0.326595 (52)	−0.276113 (77)	−0.48356 (37)	−0.3157 (14)	[−0.249]
Δ_K (kHz)	1.60894 (60)	1.50979 (26)	1.38878 (23)	1.7033 (14)	1.5416 (44)	[1.38]
δ_J (kHz)	0.234462 (24)	0.266601 (14)	0.236286 (18)	0.302489 (59)	0.255759 (61)	0.2220 (38)
δ_K (kHz)	0.671460 (99)	0.620324 (28)	0.568327 (49)	0.64991 (23)	0.61845 (89)	0.566 (17)
Φ_J (Hz)	0.000190 (14)	0.0002117 (75)	0.0001862 (84)	0.000304 (27)	0.000178 (16)	[0.000166]
Φ_{JK} (Hz)	[−0.000475]	[−0.000501]	[−0.000511]	[−0.000953]	[−0.000500]	[−0.000484]
Φ_{KJ} (Hz)	[−0.000995]	[−0.00109]	[−0.000706]	[−0.000619]	[−0.00106]	[−0.000724]
Φ_K (Hz)	0.00211 (49)	0.00206 (12)	[0.00169]	[0.00211]	[0.00207]	[0.00169]
ϕ_J (Hz)	0.0001007 (74)	0.0001017 (33)	0.0000875 (41)	[0.000137]	[0.000100]	[0.0000849]
ϕ_{JK} (Hz)	[−0.0000099]	[−0.0000244]	[−0.0000498]	[−0.000170]	[−0.0000266]	[−0.0000425]
ϕ_K (Hz)	0.00183 (13)	0.001532 (41)	0.001444 (76)	[0.00179]	[0.00152]	[0.00135]
N_{lines}	1049	1672	1349	420	458	39
σ (MHz)	0.032	0.027	0.031	0.042	0.039	0.039
κ	−0.0360	0.1442	0.1093	0.1650	0.0867	0.0520
Δ_i (uÅ²)	0.0623391 (69)	0.0625507 (43)	0.0611735 (57)	0.064866 (21)	0.063403 (19)	0.0609 (56)

TABLE 4.2. cont.

Isotopologue	[2,5-^{2}H, 2-^{13}C]	[2,5-^{2}H, 3-^{13}C]	[2-^{2}H, ^{34}S]	[3-^{2}H, 2-^{13}C]	[3-^{2}H, 3-^{13}C]	[3-^{2}H, 4-^{13}C]
$A_0^{(A)}$ (MHz)	6763.951 (25)	6860.084 (23)	7436.867 (16)	7681.748 (50)	7816.982 (61)	7775.957 (57)
$B_0^{(A)}$ (MHz)	5410.779 (17)	5310.446 (15)	5270.6988 (92)	5137.726 (24)	5045.950 (27)	5060.890 (25)
$C_0^{(A)}$ (MHz)	3004.92844 (26)	2992.15721 (26)	3083.34006 (19)	3077.42962 (28)	3065.28593 (28)	3064.43948 (27)
Δ_J (kHz)	0.80594 (48)	0.77532 (42)	0.79181 (27)	0.72086 (53)	0.69553 (59)	0.69958 (62)
Δ_{JK} (kHz)	[–0.556]	[–0.467]	[–0.356]	[–0.166]	[–0.0888]	[–0.107]
Δ_K (kHz)	[1.68]	[1.65]	[1.96]	[2.04]	[2.05]	[2.04]
δ_J (kHz)	0.31705 (24)	0.30220 (21)	0.30004 (13)	0.26642 (26)	0.25353 (29)	0.25592 (31)
δ_K (kHz)	0.6059 (13)	0.6377 (12)	0.7825 (10)	0.8170 (22)	0.8478 (26)	0.8385 (25)
Φ_J (Hz)	[0.000283]	[0.000266]	[0.000271]	[0.000220]	[0.000207]	[0.000213]
Φ_{JK} (Hz)	[–0.00106]	[–0.000885]	[–0.000908]	[–0.000609]	[–0.000440]	[–0.000551]
Φ_{KJ} (Hz)	[–0.000402]	[–0.000682]	[–0.00104]	[–0.00142]	[–0.00175]	[–0.00146]
Φ_K (Hz)	[0.00196]	[0.00207]	[0.00274]	[0.00304]	[0.00320]	[0.00301]
ϕ_J (Hz)	[0.000145]	[0.000136]	[0.000139]	[0.000113]	[0.000106]	[0.000109]
ϕ_{JK} (Hz)	[–0.000222]	[–0.000144]	[–0.000114]	[–0.0000105]	[0.0000666]	[0.0000225]
ϕ_K (Hz)	[0.00167]	[0.00172]	[0.00235]	[0.00250]	[0.00263]	[0.00262]
N_{lines}	165	174	237	133	112	113
σ (MHz)	0.044	0.045	0.039	0.046	0.041	0.041
κ	0.2800	0.1987	0.0049	–0.1051	–0.1663	–0.1525
Δ_i (uÅ^2)	0.06458 (42)	0.06477 (38)	0.06582 (23)	0.06529 (64)	0.06494 (75)	0.06506 (69)

Table 4.2. cont.

Isotopologue	[3-^{2}H, 5-^{13}C]	[3-^{2}H, ^{34}S]	[3-^{2}H, ^{33}S][c]
$A_0^{(A)}$ (MHz)	7671.948 (41)	7854.54066 (70)	7854.84 (47)
$B_0^{(A)}$ (MHz)	5138.104 (20)	5003.23141 (20)	5069.12 (20)
$C_0^{(A)}$ (MHz)	3075.99186 (24)	3055.16443 (14)	3079.66147 (44)
Δ_J (kHz)	0.71761 (45)	0.69720 (10)	0.7052 (18)
Δ_{JK} (kHz)	[–0.154]	–0.11470 (37)	[–0.120]
Δ_K (kHz)	[2.03]	2.1141 (12)	[2.10]
δ_J (kHz)	0.26488 (22)	0.253401 (56)	0.25694 (93)
δ_K (kHz)	0.8111 (18)	0.85353 (24)	0.8361 (76)
Φ_J (Hz)	[0.000219]	0.000239 (33)	[0.000215]
Φ_{JK} (Hz)	[–0.000569]	[–0.000543]	[–0.000551]
Φ_{KJ} (Hz)	[–0.00154]	–0.00177 (46)	[–0.00160]
Φ_K (Hz)	[0.00310]	[0.00318]	[0.00320]
ϕ_J (Hz)	[0.000112]	0.000114 (18)	[0.000110]
ϕ_{JK} (Hz)	[0.0000076]	[0.0000254]	[0.0000244]
ϕ_K (Hz)	[0.00248]	[0.00271]	[0.00269]
N_{lines}	143	664	57
σ (MHz)	0.040	0.035	0.045
κ	–0.1026	–0.1882	–0.1667
Δ_i (uÅ^2)	0.06525 (52)	0.065146 (10)	0.0649 (56)

Deuterium-Enriched Isotopologues

Our work significantly expands the number of deuterium-enriched isotopologues measured and least-squares fit. Previously, rotational transitions of both mono-deuterio-, one di-deuterio ([3,4-^{2}H])-, and tetra-deuteriothiophene isotopologues were reported.[24] The synthesis outlined in Scheme 4.1a, after 5 days of reflux, resulted in a sample containing all possible mono-, di-, tri-, and tetra-deuterio isotopologues. A number of the ^{34}S and ^{13}C variants of these deuterium-enriched isotopologues were also observed at their natural abundances. In total, transitions for 15 isotopologues of thiophene, including the four previously reported, were measured from this sample. For each isotopologue, rotational transitions were least-squares fit to a sextic, distorted rotor Hamiltonian in the A- and S-reductions and the I^r representation (A-reduction Table 4.2, S-reduction in supplementary material Table S4.2). The deuterio isotopologues follow a similar spectral pattern to the normal isotopologue, with strong ^{a}R$_{0,1}$ bands; a portion of the spectrum of the deuterium-containing isotopologues is displayed in Figure 4.5. The band structure of thiophene is such that the spacing between bands and the transitions within the bands allows for clear visibility of each of the various isotopologues. The [2,3,4,5-^{2}H, ^{34}S] species was observed in the original 5-day deuterium enriched sample, though most of the measured transitions come from the sample of primarily tetra-deuterio thiophene (14 day sample). The small amount of sample and presence of other isotopologues in this sample resulted in only a limited number of transitions measured for [2,3,4,5-^{2}H, ^{34}S] being assigned, and the spectroscopic constants were not satisfactorily determined. Transitions from previous microwave work[24] of the [2-^{2}H] and [3-^{2}H] isotopologues that agreed within 2σ of their error were included in their respective data sets.
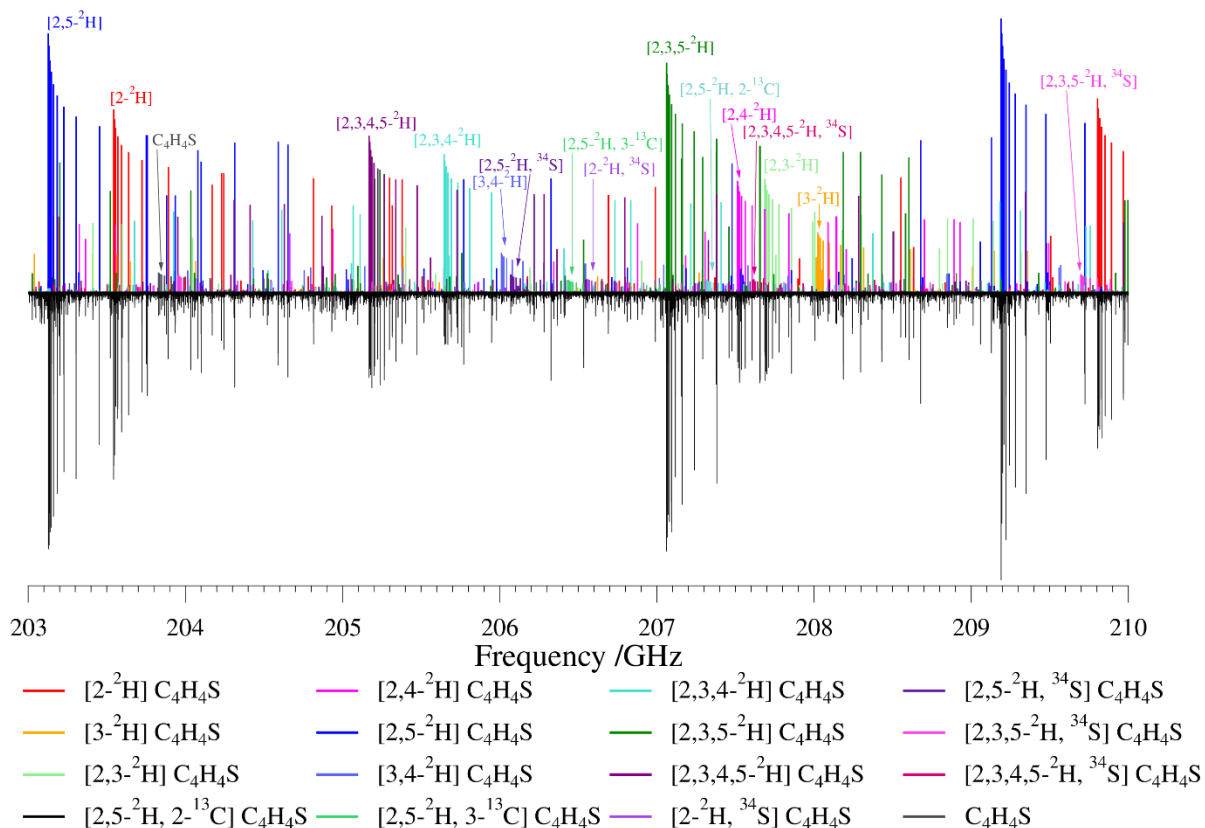
Figure 4.5. Rotational spectrum of deuterium-enriched thiophene (below) and the predicted stick spectra (above) for the vibrational ground states (G.S.) of isotopologues of thiophene from 203 to 210 GHz.

From the primarily [3-^{2}H] sample, from the reaction in Scheme 4.1 b, the [3-^{2}H, ^{34}S] isotopologue was the most naturally abundant heavy-atom isotopologue in this sample, and its enhanced intensity allowed for the measurement of 664 distinct transitions. The presence of deuterium at the 3-position breaks the C_{2v} symmetry, which results in four unique mono-^{13}C isotopologues (1.1 % the intensity of the [3-^{2}H] isotopologue). Over 100 transitions were measured and least-squares fit for each of these [3-^{2}H] ^{13}C isotopologues. The incomplete specificity of the reaction resulted in deuteration at the 2 and 5 positions, as well, and provided additional transitions for the [2-^{2}H, ^{34}S] isotopologue. The ^{33}S is the least naturally abundant isotope and only 57 transitions for [3-^{2}H, ^{33}S] were able to be included in its least-squares fit. Like

with the [2,3,4,5-^{2}H, ^{34}S] isotopologue, the small number of transitions and relatively large error in A_0 and B_0 means the spectroscopic constants of [3-^{2}H, ^{33}S] are not confidently determined. Therefore, neither of these isotopologues were included in the determination of the structure.

STRUCTURE DETERMINATION

The semi-experimental equilibrium structural parameters (r_e^{SE}) of thiophene were determined by least-squares fit of the equilibrium moments of inertia. The experimental A- and S-reduced rotational constants (B_0) of 24 isotopologues provide 72 moments of inertia to determine eight structural parameters (due to the C_{2v} symmetry of thiophene). The B_0 constants were converted to their determinable constants (B'') to remove effects of centrifugal distortion using equations S4.1 – S4.6 in the supplementary material, and then averaged.[59] The averaged B'' constants from the A- and S- reduction were further corrected to their equilibrium rotational constants by applying the computational vibration-rotation corrections (half the sum of the vibration-rotation interactions, α_i) and the computational electron-mass corrections as described in Eq. 4.1.[1, 30] The electron-mass corrections are obtained from the diagonal elements of the electronic contribution to the rotational g-tensor, $g^{\beta\beta}$, multiplied by the electron-proton mass ratio (m_e/M_P) and the computed equilibrium rotational constant ($B^\beta_{CCSD(T)}$), where $\beta = a$, b, or c.[1, 30]

$$B_e^\beta = B''^\beta + \frac{1}{2}\sum_i \alpha_i^\beta - \frac{m_e}{M_P}g^{\beta\beta}B^\beta_{CCSD(T)} \qquad 4.1$$

The deviation in the experimentally determined inertial defect ($\Delta_i = I_c - I_a - I_b$) from the ideal inertial defect value of zero for a planar molecule is much reduced by the inclusion of these computational corrections. The effect of each of the corrections on the inertial defect is shown in Table 4.3 for each isotopologue. Table 4.3 includes the Δ_i r_0, the inertial defects from only the

experimental B'' values relating to an r_0 structure, the $\Delta_i\,r_e^{SE}$ (vib. corr. only), inertial defects from the B'' plus the vibration-rotation corrections only (the electronic-mass corrections are not included), and the $\Delta_i\,r_e^{SE}$, inertial defects calculated from the B'' with the vibration-rotation and electron mass corrections applied. The averages (μ) of these respective inertial defects, as well as the individual values for each isotopologue, indicate that both the vibrational and electronic corrections are needed to bring the Δ_i closer to the ideal value of zero and obtain the best possible equilibrium constants (B_e). It is further clear that even in the final column of this table the inertial defects are highly systematic and fairly constant. The low sample standard deviations (s) strongly indicate the high level of precision in the equilibrium moments of inertia used to calculate $\Delta_i\,r_e^{SE}$ and that the remaining deviations from zero are due to an as yet unidentified systematic effect. Any random errors in the rotational constants (including in the vibration-rotation corrections) larger than a few tens of kHz would cause the value of s to be greater than what is observed. The ratio μ/s in the last column is about 7. It is also notable that all the shifts due to the electron mass correction are +0.01030 or +0.01031, even though the corresponding shifts in the individual rotational constants vary with isotopologue. The constancy in this shift is of course reflected in the standard deviation being the same in the two corresponding columns.

The averaged B'' values and computational corrections for each isotopologue are submitted to the *xrefit* module in CFOUR[49] which least-squares fits the semi-experimental equilibrium moments of inertia and determines the structural parameters. The r_e^{SE} structural parameters are presented in Figure 4.6a and in Table 4.4, alongside the computed structural parameters (CCSD(T)/cc-pCV5Z) and experimental structural parameters determined previously.[25, 27-28, 30] Figure 4.6b presents the number of isotopologues with substitution(s) at the designated position used in least-squares fit of the structure from 24 isotopologues. (For example, the three at the C2

position indicates that its substitution is present in three isotopologues: [2-^{13}C], [2,5-^{2}H, 2-^{13}C], and [3-^{2}H, 2-^{13}C]. The structural parameters are presented graphically in Figure 4.7.

Table 4.3. Inertial defects (Δ_i in uÅ^2) of thiophene with and without vibration-rotation and electron mass corrections

Isotopologue	Δ_i r_0	Δ_i r_e^{SE} (vib. corr. only)	Δ_i r_e^{SE}
Normal	0.06561	−0.00902	0.00128
[2-^{13}C]	0.06645	−0.00900	0.00130
[3-^{13}C]	0.06621	−0.00901	0.00129
[^{34}S]	0.06636	−0.00898	0.00132
[^{33}S]	0.06591	−0.00908	0.00122
[2-^{2}H]	0.06490	−0.00921	0.00109
[3-^{2}H]	0.06423	−0.00903	0.00128
[2,3-^{2}H]	0.06342	−0.00919	0.00112
[2,4-^{2}H]	0.06351	−0.00922	0.00109
[2,5-^{2}H]	0.06385	−0.00938	0.00093
[3,4-^{2}H]	0.06313	−0.00889	0.00142
[2,3,4-^{2}H]	0.06216	−0.00917	0.00114
[2,3,5-^{2}H]	0.06238	−0.00937	0.00094
[2,3,4,5-^{2}H]	0.06101	−0.00933	0.00098
[2,5-^{2}H, ^{34}S]	0.06470	−0.00934	0.00096
[2,3,5-^{2}H, ^{34}S]	0.06323	−0.00930	0.00100
[2,5-^{2}H, 2-^{13}C]	0.06443	−0.00940	0.00091
[2,5-^{2}H, 3-^{13}C]	0.06460	−0.00918	0.00113
[2-^{2}H, ^{34}S]	0.06565	−0.00923	0.00108
[3-^{2}H, 2-^{13}C]	0.06510	−0.00888	0.00143
[3-^{2}H, 3-^{13}C]	0.06476	−0.00899	0.00131
[3-^{2}H, 4-^{13}C]	0.06487	−0.00900	0.00130
[3-^{2}H, 5-^{13}C]	0.06506	−0.00905	0.00126
[3-^{2}H, ^{34}S]	0.06495	−0.00900	0.00131
Average (μ)	0.06444	−0.00914	0.00117
Std. Dev. (s)	0.00139	0.00016	0.00016

Table 4.4. Experimental and computational structural parameters of thiophene

	$r_e^{\text{SE a,b}}$	$r_e^{\text{ c}}$	$r_e^{\text{SE d}}$	r_s	r_e	r_α
	this work millimeter-wave	this work computational	ref. [30] microwave	ref. [25] microwave	ref. [28] e	ref. [27] f
$R_{\text{S1-C2}}$ (Å)	1.71049 (18)	1.70944	1.7126 (5)	1.7140 (14)	1.704 (2)	1.7136 (11)
$R_{\text{C2-C3}}$ (Å)	1.36564 (31)	1.36632	1.3622 (8)	1.3696 (17)	1.372 (3)	1.3783 (15)
$R_{\text{C2-H}}$ (Å)	1.07714 (17)	1.07633	1.0771 (5)	1.0776 (15)	1.085 (5)	1.0688 (6)
$R_{\text{C3-H}}$ (Å)	1.07856 (14)	1.07860	1.0794 (3)	1.0805 (14)	1.088	1.0812 (11)
½ $A_{\text{C2-S1-C5}}$ (°)	46.024 (7)	46.051	45.94 (2)	46.09 (5)	46.2 (1)	46.28 (4)
$A_{\text{S1-C2-C3}}$ (°)	111.608 (16)	111.596	111.66 (3)	111.49 (24)	111.6	111.34 (7)
$A_{\text{S1-C2-H}}$ (°)	120.065 (28)	120.286	120.11 (10)	119.89 (82)	119.9 (3)	120.24 (8)
$A_{\text{C2-C3-H}}$ (°)	123.414 (23)	123.416	123.46 (7)	123.25 (7)	123.4	123.56 (8)
$A_{\text{C2-S1-C5}}$ (°)	92.047 (15)	92.101	91.88 (4)	92.17 (10)	92.4 (2)	92.56 (8)
$N_{\text{isotopologues}}$	24		8	6		

[a] Error reported is 2σ
[b] Vibrational and electronic correction at CCSD(T)/cc-pCVTZ level
[c] CCSD(T)/cc-pCV5Z
[d] Vibration-rotation coupling and electronic correction at B2PLYP/VTZ
[e] Combined electron diffraction, microwave, vibrational, computational
[f] Combined electron diffraction, microwave, liquid-crystal NMR
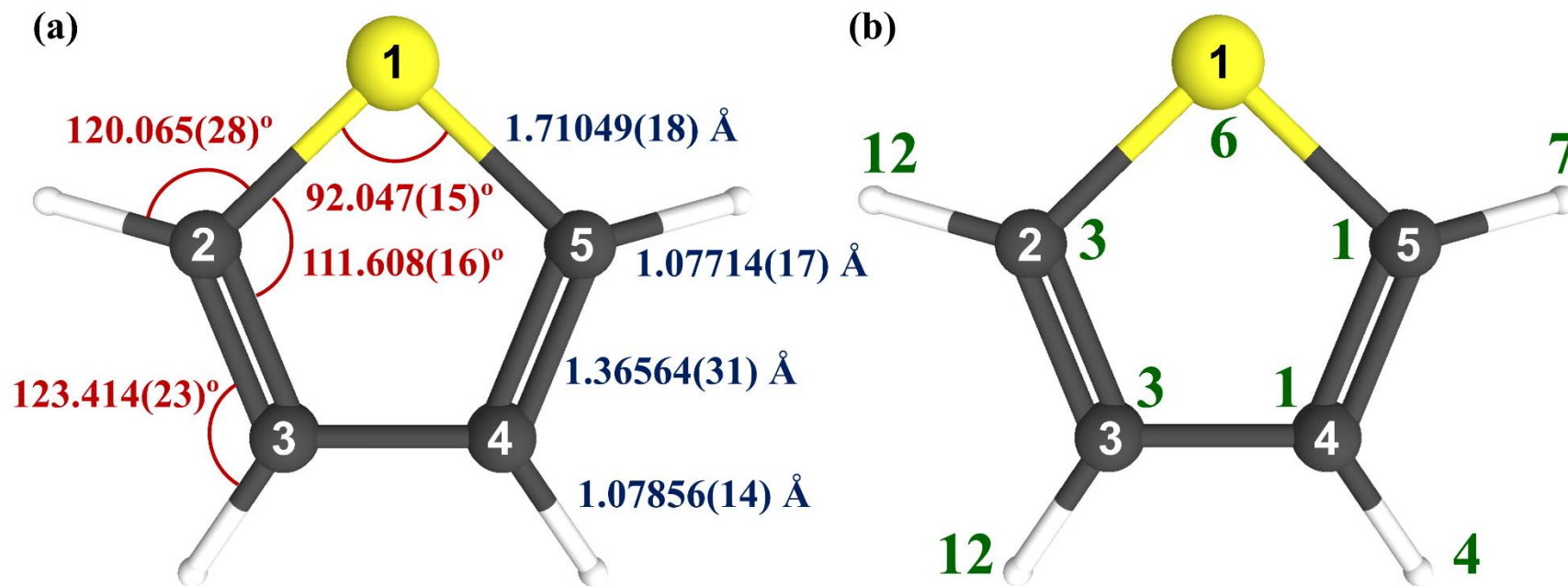
Figure 4.6. (a) Semi-experimental equilibrium structure (r_e^{SE}) of thiophene and (b) number of isotopic substitutions at each position included in the structure determined from the least-squares fit of 24 isotopologues.

To provide the best comparison to the semi-experimental equilibrium structure, four computational corrections to the CCSD(T)/cc-pCV5Z structure have been implemented to address residual error in the computational structure.

1. Residual basis set effects beyond cc-pCV5Z.

2. Residual electron correlation effects beyond the CCSD(T) treatment.

3. Effects of scalar (mass-velocity and Darwin) relativistic effects

4. The diagonal Born-Oppenheimer correction (DBOC)

These four corrections are obtained in a manner similar to pyrimidine[1] using equations 4.2 through 4.8.

1. To estimate the correction needed to approach the infinite basis set limit, equilibrium structural parameters obtained with the cc-pCVXZ (X = T, Q, and 5) basis sets were extrapolated using the empirical exponential formula[60] (equation 4.2)

$$R(x) = R(\infty) + Ae^{-Bx} \tag{4.2}$$

R(x) are the values of the parameters obtained using the largest three basis sets (x = 3, 4, and 5), and R(∞) is the desired basis set limit estimate. Using these three basis sets equation 4.2 can be expressed as equation 4.3.

$$R(\infty) = -\frac{R(4)^2 - R(3)R(5)}{R(3) + R(5) - 2R(4)} \tag{4.3}$$

The correction to the structure due to a finite basis set is then estimated by equation 4.4.

$$\Delta R(\text{basis}) = R(\infty) - R(\text{CCSD(T)/cc-pCV5Z}) \tag{4.4}$$

2. Residual correlation effects are assessed by doing geometry optimizations at the CCSDT(Q) level[61] and then estimating the correlation correction in equation 4.5.

$$\Delta R(\text{cor}) = R(\text{CCSDT(Q)}) - R(\text{CCSD(T)}) \tag{4.5}$$

Due to the expense of calculations at the CCSDT(Q) level, the cc-pVDZ basis in the frozen-core approximation is used for these calculations.

3. The relativistic corrections are obtained by subtraction of the parameters with a standard non-relativistic calculation from the equilibrium structure obtained with the X2C-1e variant of coupled-cluster theory,[62-64] as in equation 4.6.

$$\Delta R(\text{rel}) = R(\text{CCSD(T)/cc-pCVTZ})_{SFX2C\text{-}1e} - R(\text{CCSD(T)/cc-pCVTZ})_{NR} \tag{4.6}$$

4. The diagonal Born-Oppenheimer correction (DBOC)[65-66] is obtained from equation 4.7.

$$\Delta R(\text{DBOC}) = R(\text{SCF/cc-pVTZ})_{DBOC} - R(\text{SCF/cc-pVTZ})_{NR} \tag{4.7}$$

Here the first value is obtained by minimizing the DBOC-corrected SCF energy with respect to nuclear positions, and the latter is again the traditional calculation.

The sum of these corrections is used to obtain the best equilibrium structural parameters, given by equation 4.8.

$$\Delta R(\text{best}) = \Delta R(\text{basis}) + \Delta R(\text{cor}) + \Delta R(\text{rel}) + \Delta R(\text{DBOC}) \tag{4.8}$$

The values of each correction, ΔR(best), are applied to the structural parameters determined by CCSD(T)/cc-pCV5Z and are presented in Table 4.5 and Figure 4.7. We will refer to them as the "best theoretical estimate" (BTE) parameters.
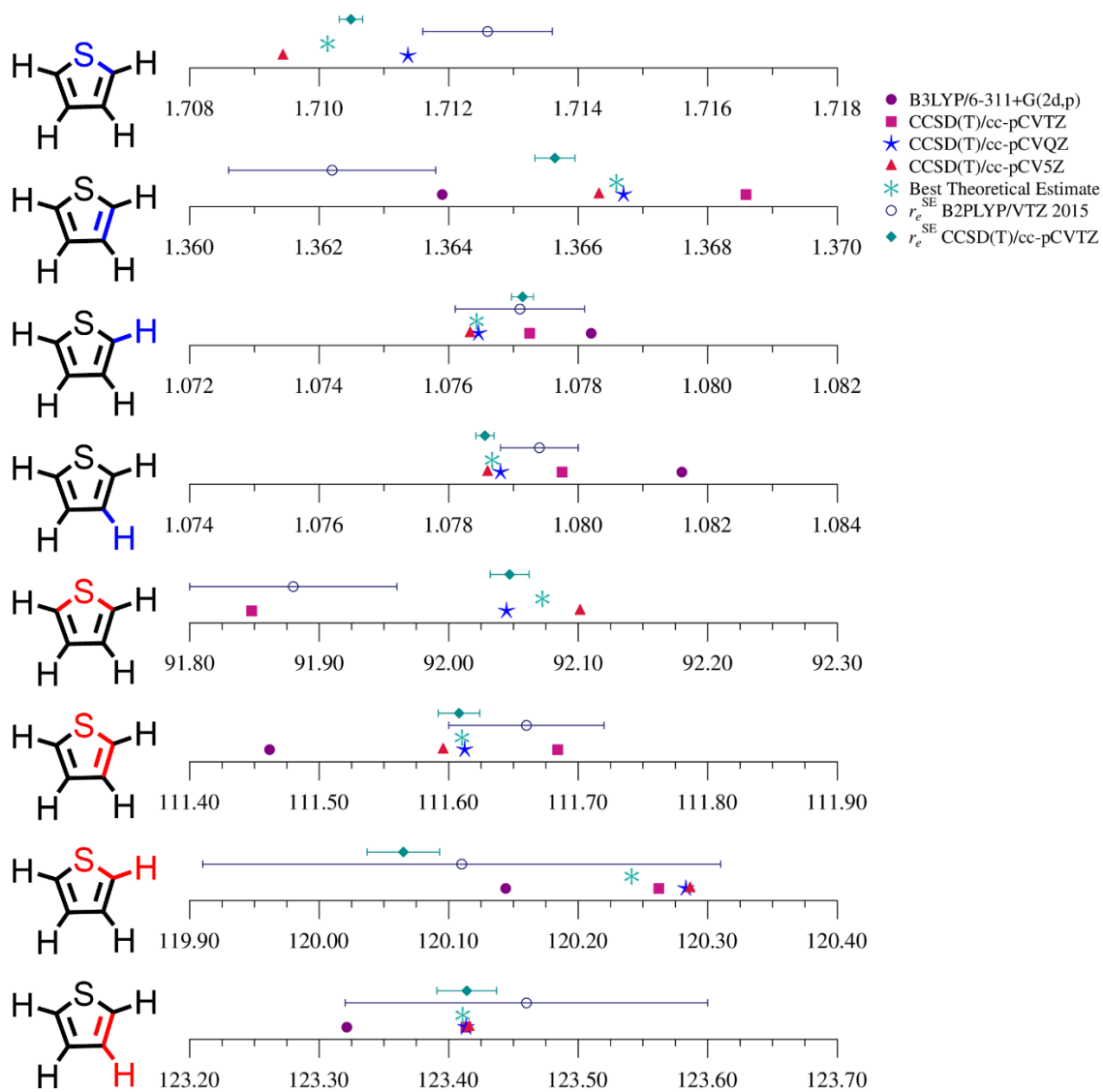
Figure 4.7. Graphical comparison of the thiophene structural parameters with bond distances in angstroms (Å, blue) and angles in degrees (°, red). All errors shown are 2σ.

Table 4.5. Parameters and corrections for the best theoretical estimate of the equilibrium structure of thiophene

	Basis set correction (Eq. 4.4)	Correlation correction (Eq.4.5)	Relativity correction (Eq. 4.6)	DBOC (Eq. 4.7)	Sum of corrections (Eq. 4.8)	CCSD(T)/ cc-pCV5Z	Best theoretical estimate	$r_e^{\text{SE a}}$
$R_{\text{S1-C2}}$ (Å)	−0.000756	0.001481	−0.000052	0.000009	0.000682	1.70944	1.71013	1.71049 (18)
$R_{\text{C2-C3}}$ (Å)	−0.000093	0.000705	−0.000355	0.000012	0.000269	1.36632	1.36659	1.36564 (31)
$R_{\text{C2-H}}$ (Å)	−0.000026	0.000090	−0.000100	0.000135	0.000099	1.07633	1.07643	1.07714 (17)
$R_{\text{C3-H}}$ (Å)	−0.000055	0.000103	−0.000111	0.000130	0.000067	1.07860	1.07867	1.07856 (14)
½ $A_{\text{C2-S1-C5}}$ (°)	0.011523	−0.015291	−0.011943	0.001172	−0.014540	46.051	46.036	46.024 (7)
$A_{\text{S1-C2-C3}}$ (°)	−0.005025	0.005053	0.015810	−0.001276	0.014561	111.596	111.610	111.608 (16)
$A_{\text{S1-C2-H}}$ (°)	0.000635	−0.015990	−0.031264	0.001444	−0.045175	120.286	120.241	120.065 (28)
$A_{\text{C2-C3-H}}$ (°)	−0.002507	−0.005022	0.003706	−0.001211	−0.005033	123.416	123.411	123.414 (23)
$A_{\text{C2-S1-C5}}$ (°)	0.023045	−0.030583	−0.023887	0.002345	−0.029079	92.101	92.072	92.047 (15)

[a] Error reported is 2σ

DISCUSSION

In the r_e^{SE} structure the largest computed statistical (2σ) bond distance uncertainty is in $R_{C2\text{-}C3}$ (0.00031 Å), and the largest bond angle uncertainty is in $A_{S1\text{-}C2\text{-}H}$ (0.028°). Exactly how reliable these error estimates are, however, is a more subtle question. Comparing the current r_e^{SE} to the previously published r_e^{SE} structure (Table 4.4), which applied vibrational and electronic corrections computed using DFT methods[30] to the rotational constants of eight isotopologues,[25] none of the previous parameters fall within the 2σ error bars of our current r_e^{SE} structure except for the $R_{C2\text{-}H}$ distance. For most parameters, the earlier r_e^{SE} structure[30] is not in close agreement with our BTE structure either. The differences between the two r_e^{SE} structures is presumably due to a combination of the incorporation of the precisely determined moments of inertia for more isotopologues and to the higher-level computational treatment.

The large number of isotopologues incorporated in our current studies poses some new challenges with respect to analysis and interpretation of data. We therefore developed a new method to analyze the contribution and importance of each isotopologue to the r_e^{SE} structure determination. A traditional substitution structure (r_s) from a Kraitchman analysis[26] relies on single isotopic substitution, which is sufficient to determine the structure. Originally this calculation employed ground state constants (B_0), but it can also be applied to equilibrium rotational constants. That possibility does demonstrate that there is, at least in principle, sufficient information content in the value of the rotational constants for the normal form and the singly substituted forms to locate every atom in the molecule. We have found, however, that the use of multiply substituted isotopologues does provide useful additional structural information. The structural parameters become highly over-determined, and the experimental uncertainty can be pushed well below the value achievable with smaller data sets, *i.e.*, single substitutions. The

analysis of isotopologue incorporation was performed with an iterative analysis, where we began

with the normal isotopologue and five mono-substituted isotopologues ([2-^{13}C], [3-^{13}C], [^{34}S], [2-^{2}H], [3-^{2}H]) as the "core set" and then added each of the multiply substituted isotopologues, one-at-a-time, to the least-squares fit of the structure in *xrefit*. The value of the square root of the sum

of the squared relative errors was determined for each isotopologue addition, which we call the

r_e^{SE} *Uncertainty* (Eq. 4.9),

$$r_e^{SE} Uncertainty = \sqrt{\sum_p \left(\frac{\sigma_p}{P}\right)^2}$$
(4.9)

where P is each structural parameter determined by *xrefit* and σ_p is the respective (1σ) error of

each parameter. The isotopologue that results in the lowest value of the r_e^{SE} *Uncertainty* for the

extended set is then incorporated into the structure determination for a total of seven isotopologues.

The procedure repeats again with testing each remaining isotopologue, and incorporating the one

that gives the smallest r_e^{SE} *Uncertainty* into the fit, for a new total of eight isotopologues. This

procedure repeats until all 24 isotopologues are incorporated. As this iterative process could be

time-consuming, a program, *xrefiteration,* has been written to automate it. The code will be

discussed in more detail in a publication on the improved semi-experimental equilibrium structure

determination of pyridazine.[67] The resultant r_e^{SE} *Uncertainty* values from each iteration are plotted

in Figure 4.8, along with the r_e^{SE} *Uncertainty* for just the bond distances and just the angles.

Upon examination of the *xrefiteration* results, we observe that the addition of the [2,3-^{2}H]

and [2,4-^{2}H] isotopologues (the last two) causes the r_e^{SE} *Uncertainty* with 24 isotopologues to

increase to nearly the same as the r_e^{SE} *Uncertainty* with 12 isotopologues. We also ran *xrefit* with

no computational corrections giving an r_0 structure and with vibrational corrections only (no

electronic corrections) providing an r_e^{SE} (vib. corr. only) structure. These structures, as well as an

r_e^{SE} without the last two isotopologues ([2,3-^{2}H] and [2,4-^{2}H]), labeled r_e^{SE} (r_{22}), are compared to

the r_e^{SE} structure in Table 4.6. Despite the modest increase in the errors obtained by including the

last two isotopologues, the r_e^{SE} structural parameters themselves are hardly changed at all. In all

the structures presented in Table 4.6, the largest error in the bonds occurs for $R_{C2\text{-}C3}$ and the largest

statistical error in the angles occurs for $A_{S1\text{-}C2\text{-}H}$. In comparing the r_e^{SE} (vib. corr. only) structure

to the r_e^{SE} structure, we note that, while the error in the parameters is dramatically smaller in the

r_e^{SE} structure, the values of each of the parameters in these two structures are nearly identical. The

reduction in the error bars is not surprising, given that the electron mass corrections reduce the

inertial defects by an order of magnitude (Table 4.3), because sets of moments of inertia exhibiting

non-zero inertial defects can never be perfectly fit to planar model of a molecule.
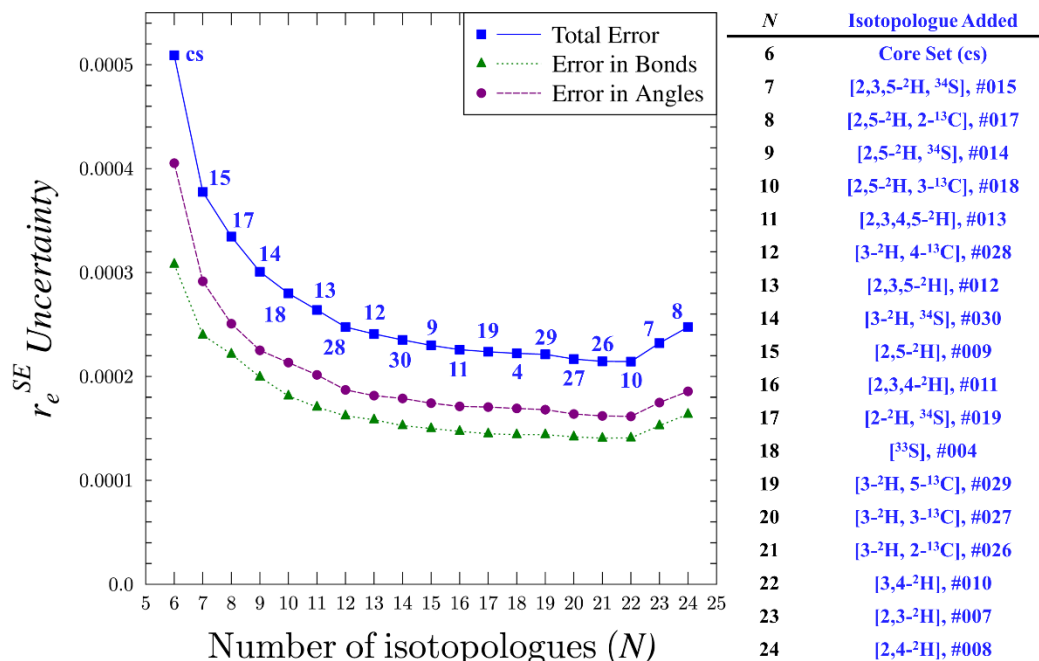
Figure 4.8. Plot of the r_e^{SE} *Uncertainty* v. the number of isotopologues (N) incorporated in the structure determination. The total error (r_e^{SE} *Uncertainty*), the error in bonds (r_e^{SE} *Uncertainty* in bonds parameters) and the error in angles (r_e^{SE} *Uncertainty* in the angle parameters) are presented. The numbers at each data point correspond to the isotopologue numbering scheme, which is presented explicitly in the accompanying table.

Table 4.6. Comparison of thiophene structural parameters[a]

	r_e^{SE}	r_0	r_e^{SE} (vib. corr. only)	r_e^{SE} (r_{22})
$R_{S1\text{-}C2}$ (Å)	1.71049 (18)	1.7173 (67)	1.71049 (96)	1.71051 (16)
$R_{C2\text{-}C3}$ (Å)	1.36564 (31)	1.369 (12)	1.36565 (165)	1.36562 (27)
$R_{C2\text{-}H}$ (Å)	1.07714 (17)	1.0766 (65)	1.07715 (92)	1.07722 (15)
$R_{C3\text{-}8}$ (Å)	1.07856 (14)	1.0773 (53)	1.07857 (76)	1.07856 (12)
½ $A_{C2\text{-}S1\text{-}C5}$ (°)	46.024 (7)	46.05 (27)	46.024 (39)	46.023 (6)
$A_{S1\text{-}C2\text{-}C3}$ (°)	111.608 (16)	111.59 (61)	111.607 (87)	111.608 (14)
$A_{S1\text{-}C2\text{-}H}$ (°)	120.065 (28)	119.6 (1.0)	120.066 (148)	120.048 (25)
$A_{C2\text{-}C3\text{-}H}$ (°)	123.414 (23)	123.48 (87)	123.414 (124)	123.414 (20)
$A_{C2\text{-}S1\text{-}C5}$ (°)	92.047 (15)	92.10 (55)	92.047 (78)	92.047 (13)
$N_{isotopologues}$	24	24	24	22[b]

[a] All uncertainties are 2σ

[b] [2,3-^{2}H] and [2,4-^{2}H] not included

Comparison of the various corrections terms in Table 4.5 to equivalent data for pyrimidine shows that the former are somewhat larger, but not by a great deal. This leads us to suspect that the BTE results in thiophene might exhibit an accuracy very close to what was obtained for pyrimidine. Referring to the last two columns of Table 4.5 or to Figure 4.7 we observe that for several structural parameters the BTE values are within the 2σ error bars of the results, or nearly so, and the corresponding residuals (δ) are similar in magnitude to those of pyrimidine: (2σ, δ)= (0.00018, 0.00036) for R_{S1-C2}, (0.00014, −0.00011) for R_{C3-H}, (0.016, −0.002) for $A_{S1-C2-C3}$, (0.023, 0.003) for $A_{C2-C3-H}$, and (0.015, −0.025) for $A_{C2-S1-C5}$. On the contrary, for two of the bond distances and especially for one of the angles the corresponding BTE values are well outside the error bars of the r_e^{SE} results, and the residuals are substantially bigger than any of the residuals found in pyrimidine: (0.00031, −0.00095) for R_{C2-C3}, (0.00017, 0.00071) for R_{C2-H}, and (0.028, −0.176) for $A_{S1-C2-H}$. It is easily seen that all the offending parameters involve C2 and the H atom on that carbon. We suspect that this problem arises because these two atoms lie close to the b principal axis, a classically problematic issue in using moments of inertia to determine structures. The uncertainties in atom coordinates are typically magnified when those atoms lie near any principal axis, but not on it. Sometimes the principal axes can be substantially rotated by isotopic substitution to move such atoms away from the axis and greatly mitigate this problem. Not much rotation can occur in thiophene, however, because the heavy sulfur atom must always be very near the a axis. In a planar molecule the atom a-axis coordinates determine I_b and the b-axis coordinates determine I_a. An atom being near the b axis will hinder determination of its a-axis coordinate and conversely.

To obtain a better understanding of the origin of the structural errors in thiophene we have expressed the various structure types in a new coordinate system shown in Table 4.7. We use

rectangular coordinates aligned with the symmetry axis, but with the S atom at the origin. There are 4 unique a-axis coordinates and 4 unique b-axis coordinates. We find that the agreement between BTE and r_e^{SE} for all the b-axis coordinates is excellent. The a-axis coordinate residuals for C3 and H3 are fairly small (especially considering that the values themselves are large), but the a-axis coordinate residuals for C2 (0.00052 Å) and H2 (−0.00263 Å) are clearly where the problem lies. Since there is little reason to believe the BTE value of the a-axis coordinates would be less accurate than those of the b-axis coordinates, it seems reasonable that any accuracy problems in the present thiophene r_e^{SE} determination trace back to the nearness of the C2 and H2 atoms to the b principal axis, for which we have not found a satisfactory way to correct. Excluding that issue the present work does appear to confirm that agreement between r_e^{SE} and BTE structure can be about as good for a molecule containing a second-row atom as for one which does not.

Table 4.7. Thiophene rectangular coordinates with the sulfur atom centered at the origin (0,0)[a]

	r_e^{SE}		CCSD(T)/cc-pCV5Z		Best Theoretical Estimate	
	a	*b*	*a*	*b*	*a*	*b*
S	0.00000	0.00000	0.00000	0.00000	0.00000	0.00000
C2	−1.18770	1.23092	−1.18639	1.23072	−1.18718	1.23091
C5	−1.18770	−1.23092	−1.18639	−1.23072	−1.18718	−1.23091
C3	−2.45058	0.71120	−2.45004	0.71108	−2.45108	0.71117
C4	−2.45058	−0.71120	−2.45004	−0.71108	−2.45108	−0.71117
H2	−0.89155	2.26655	−0.89397	2.26657	−0.89418	2.26670
H5	−0.89155	−2.26655	−0.89397	−2.26657	−0.89418	−2.26670
H3	−3.34246	1.31770	−3.34181	1.31780	−3.34285	1.31803
H4	−3.34246	−1.31770	−3.34181	−1.31780	−3.34285	−1.31803

[a] a-axis and b-axis coordinates in Å

ACKNOWLEDGMENTS

REFERENCES

1. Heim, Z. N.; Amberger, B. K.; Esselman, B. J.; Stanton, J. F.; Woods, R. C.; McMahon, R. J., Molecular structure determination: Equilibrium structure of pyrimidine (m-$C_4H_4N_2$) from rotational spectroscopy (r_e^{SE}) and high-level ab initio calculation (r_e) agree within the uncertainty of experimental measurement. *J. Chem. Phys.* **2020**, *152* (10), 104303.

2. Singh, A.; Singh, G.; Bedi, P. M. S., Thiophene derivatives: A potent multitargeted pharmacological scaffold. *J. Heterocycl. Chem.* **2020**, *57* (7), 2658-2703.

3. Amna, B.; Siddiqi, H. M.; Hassan, A.; Ozturk, T., Recent developments in the synthesis of regioregular thiophene-based conjugated polymers for electronic and optoelectronic applications using nickel and palladium-based catalytic systems. *RSC Advances* **2020**, *10* (8), 4322-4396.

4. Barbarella, G.; Melucci, M.; Sotgiu, G., The Versatile Thiophene: An Overview of Recent Research on Thiophene-Based Materials. *Adv. Mater.* **2005**, *17* (13), 1581-1593.

5. Heinz, J.; Schulze-Makuch, D., Thiophenes on Mars: Biotic or Abiotic Origin? *Astrobiology* **2020**, *20* (4), 552-561.

6. Eigenbrode, J. L.; Summons, R. E.; Steele, A.; Freissinet, C.; Millan, M.; Navarro-González, R.; Sutter, B.; McAdam, A. C.; Franz, H. B.; Glavin, D. P.; Archer, P. D.; Mahaffy, P. R.; Conrad, P. G.; Hurowitz, J. A.; Grotzinger, J. P.; Gupta, S.; Ming, D. W.; Sumner, D. Y.; Szopa, C.; Malespin, C.; Buch, A.; Coll, P., Organic matter preserved in 3-billion-year-old mudstones at Gale crater, Mars. *Science* **2018**, *360* (6393), 1096.

7. Lattelais, M.; Ellinger, Y.; Matrane, A.; Guillemin, J. C., Looking for heteroaromatic rings and related isomers as interstellar candidates. *Phys. Chem. Chem. Phys.* **2010**, *12* (16), 4165-4171.

8. Agúndez, M.; Cernicharo, J.; Guélin, M., New molecules in IRC +10216: confirmation of C_5S and tentative identification of MgCCH, NCCP, and SiH_3CN. *Astron. Astrophys.* **2014**, *570*.

9. Cernicharo, J.; Guelin, M.; Hein, H.; Kahane, C., Sulfur in IRC +10216. *Astron. Astrophys.* **1987**, *181*, L9-L12.

10. Coblentz, W. W., *Investigations of Infrared Spectra Part 1 - Infra-Red Absorption Spectra*. Carnegie Institution of Washington: 1905.

11. Thompson, H. W.; Temple, R. B., The infra-red spectra of furan and thiophen. *Trans. Faraday Soc.* **1945**, *41*, 27-34.

12. Barnes, R.; Liddel, U.; Williams, V., Infrared Spectroscopy. Industrial Applications. *Ind. Eng. Chem. Anal. Ed.* **1943**, *15* (11), 659-709.

13. Barnes, R. B.; Brattain, R. R., The Near Infrared Spectrum of Benzene-d_6. *J. Chem. Phys.* **1935**, *3* (8), 446-449.

14. Bonino, G. B.; Manzoni-Ansidei, R., The Raman Spectra of Thiophenes and Furans and a few of their derivatives. *Z. Physik. Chem.* **1934**, *B25*, 327-347.

15. Rico, M.; Orza, J. M.; Morcillo, J., Fundamental vibrations of thiophene and its deuterated derivatives. *Spectrochim. Acta* **1965**, *21* (4), 689-719.

16. Klots, T. D.; Chirico, R. D.; Steele, W. V., Complete vapor phase assignment for the fundamental vibrations of furan, pyrrole and thiophene. *Spectrochim. Acta A* **1994**, *50* (4), 765-795.

17. Pankoke, B.; Yamada, K. M. T.; Winnewisser, G., High resolution IR-spectra of furan and thiophene. *Z. Naturforsch., A: Phys. Sci.* **1994**, *48* (12), 1193-202.

18. van Wijngaarden, J.; Van Nest, S. J.; van Dijk, C. W.; Tokaryk, D. W., Rovibrational spectrum and analysis of the ν_8 band of thiophene using infrared synchrotron radiation. *J. Mol. Spectrosc.* **2010**, *259* (1), 56-59.

19. van Wijngaarden, J.; Tokaryk, D. W., High resolution synchrotron-based study and analysis of the ν_{14} band of thiophene. *J. Mol. Spectrosc.* **2008**, *251* (1), 365-368.

20. Hegelund, F.; Wugt Larsen, R.; Palmer, M. H., The high-resolution infrared spectrum of thiophene between 600 and 1200 cm^{-1}: A spectroscopic and theoretical study of the fundamental bands ν_6, ν_7, ν_{13}, and the *c*-Coriolis interacting dyad ν_5, ν_{19}. *J. Mol. Spectrosc.* **2008**, *247* (1), 100-114.

21. Wu, X.-F.; Zheng, X.; Wang, H.-G.; Zhao, Y.-Y.; Guan, X.; Phillips, D. L.; Chen, X.; Fang, W., A resonance Raman spectroscopic and CASSCF investigation of the Franck–Condon region structural dynamics and conical intersections of thiophene. *J. Chem. Phys.* **2010**, *133* (13), 134507.

22. Singh, D. K.; Srivastava, S. K.; Ojha, A. K.; Asthana, B. P., Vibrational study of thiophene and its solvation in two polar solvents, DMSO and methanol by Raman spectroscopy combined with ab initio and DFT calculations. *J. Mol. Struct.* **2008**, *892* (1), 384-391.

23. Ogata, T.; Kozima, K., Microwave spectrum, barrier height to internal rotation of methyl group of 3-methylthiophene, and dipole moments of 3-methylthiophene and thiophene. *J. Mol. Spectrosc.* **1972**, *42* (1), 38-46.

24. Bak, B.; Christensen, D.; Rastrup-Andersen, J.; Tannenbaum, E., Microwave Spectra of Thiophene, 2- and 3-Monodeutero, 3,3′-Dideutero, and Tetradeuterothiophene. Structure of the Thiophene Molecule. *J. Chem. Phys.* **1956**, *25* (5), 892-896.

25. Bak, B.; Christensen, D.; Hansen-Nygaard, L.; Rastrup-Andersen, J., The structure of thiophene. *J. Mol. Spectrosc.* **1961**, *7* (1), 58-63.

26. Kraitchman, J., Determination of Molecular Structure from Microwave Spectroscopic Data. *Am. J. Phys.* **1953**, *21* (1), 17-24.

27. Liescheski, P. B.; Rankin, D. W. H., Determination of the r_a structure of thiophene by combined analysis of electron diffraction, liquid crystal NMR and rotational data. *J. Mol. Struct.* **1988**, *178*, 227-241.

28. Kochikov, I. V.; Tarasov, Y. I.; Spiridonov, V. P.; Kuramshina, G. M.; Rankin, D. W. H.; Saakjan, A. S.; Yagola, A. G., The equilibrium structure of thiophene by the combined use of electron diffraction, vibrational spectroscopy and microwave spectroscopy guided by theoretical calculations. *J. Mol. Struct.* **2001**, *567-568*, 29-40.

29. Piccardo, M.; Penocchio, E.; Puzzarini, C.; Biczysko, M.; Barone, V., Semi-Experimental Equilibrium Structure Determinations by Employing B3LYP/SNSD Anharmonic Force Fields: Validation and Application to Semirigid Organic Molecules. *J. Phys. Chem. A* **2015**, *119*, 2058-2082.

30. Penocchio, E.; Piccardo, M.; Barone, V., Semiexperimental Equilibrium Structures for Building Blocks of Organic and Biological Molecules: The B2PLYP Route. *J. Chem. Theory Comput.* **2015**, *11* (10), 4689-4707.

31. White, W. F. *Microwave Spectra of Some Sulfur and Nitrogen Compounds*; NASA: Hampton, VA, 1974; pp 99-100.

32. Pozdeev, N. M.; Gunderova, L. N., Microwave spectra of thiophane and thiophene. *Khim. Seraorg. Soedin., Soderzh. Neftyakh Nefteprod.* **1972**, *9*, 101-6.

33. Pozdeev, N. M.; Panikovskaya, L. I.; Lisovskaya, L. N.; Mamleev, A. K. Rotation constants and dipole moment of thiophene, *Primen. Mol. Spektrosk. Khim., Sb. Dokl. Sib. Soveshch., 3rd, Krasnoyarsk, USSR*, 1966; 26-7.

34. Kretschmer, U.; Stahl, W.; Dreizler, H., The Rotational Spectra of the [32]S-, [33]S-, and [34]S-Isotopomers of Thiophene. *Z. Naturforsch., A: Phys. Sci.* **1993**, *48* (5-6), 733-736.

35. Kobayashi, K.; Takamura, K.; Sakai, Y.; Tsunekawa, S.; Odashima, H.; Ohashi, N., The Microwave Spectroscopy of Methyl Formate in the Second Torsional Excited State. *Astrophys. J., Suppl. Ser.* **2013**, *205* (1), 9.

36. Fukuyama, Y.; Odashima, H.; Takagi, K.; Tsunekawa, S., The Microwave Spectrum of Propionitrile (C_2H_5CN) in the Frequency Range from 8 to 200 GHz. *Astrophys. J., Suppl. Ser.* **1996**, *104*, 329.

37. McJunkins, A.; Brown, G. G., An Inexpensive Room-Temperature Chirped-Pulse Fourier Transform Microwave (RT-CP-FTMW) Spectrometer. *J. Undergrad. Chem. Res.* **2011**, *10* (4), 158-161.

38. Esselman, B. J.; Amberger, B. K.; Shutter, J. D.; Daane, M. A.; Stanton, J. F.; Woods, R. C.; McMahon, R. J., Rotational spectroscopy of pyridazine and its isotopologs from 235–360 GHz: Equilibrium structure and vibrational satellites. *J. Chem. Phys.* **2013**, *139* (22), 224304.

39. Zdanovskaia, M. A.; Esselman, B. J.; Woods, R. C.; McMahon, R. J., The 130–370 GHz Rotational Spectrum of Phenyl Isocyanide (C_6H_5NC). *J. Chem. Phys.* **2019**, *151* (2), 024301.

40. Kisiel, Z., Assignment and Analysis of Complex Rotational Spectra. In *Spectroscopy from Space*, Demaison, J.; Sarka, K.; Cohen, E. A., Eds. Springer Netherlands: Dordrecht, 2001; pp 91-106.

41. Kisiel, Z.; Pszczółkowski, L.; Drouin, B. J.; Brauer, C. S.; Yu, S.; Pearson, J. C.; Medvedev, I. R.; Fortman, S.; Neese, C., Broadband rotational spectroscopy of acrylonitrile: Vibrational energies from perturbations. *J. Mol. Spectrosc.* **2012**, *280*, 134-144.

42. Kisiel, Z.; Białkowska-Jaworska, E.; Pszczółkowski, L., The Millimeter-Wave Rotational Spectrum of Fluorobenzene. *J. Mol. Spectrosc.* **2005**, *232* (1), 47-54.

43. Kisiel, Z. PROSPE - Programs for ROtational SPEctroscopy. http://info.ifpan.edu.pl/~kisiel/prospe.htm

44. Kisiel, Z.; Białkowska-Jaworska, E., Sextic centrifugal distortion in fluorobenzene and phenylacetylene from cm-wave rotational spectroscopy. *J. Mol. Spectrosc.* **2019**, *359*, 16-21.

45. Gaussian 16, Revision B.01, Frisch, M. J.; Trucks, G. W.; Schlegel, H. B.; Scuseria, G. E.; Robb, M. A.; Cheeseman, J. R.; Scalmani, G.; Barone, V.; Petersson, G. A.; Nakatsuji, H.; Li, X.; Caricato, M.; Marenich, A. V.; Bloino, J.; Janesko, B. G.; Gomperts, R.; Mennucci, B.; Hratchian, H. P.; Ortiz, J. V.; Izmaylov, A. F.; Sonnenberg, J. L.; Williams-Young, D.; Ding, F.; Lipparini, F.; Egidi, F.; Goings, J.; Peng, B.; Petrone, A.; Henderson, T.; Ranasinghe, D.; Zakrzewski, V. G.; Gao, J.; Rega, N.; Zheng, G.; Liang, W.; Hada, M.; Ehara, M.; Toyota, K.; Fukuda, R.; Hasegawa, J.; Ishida, M.; Nakajima, T.; Honda, Y.; Kitao, O.; Nakai, H.; Vreven, T.; Throssell, K.; Montgomery, J. A., Jr.; Peralta, J. E.; Ogliaro, F.; Bearpark, M. J.; Heyd, J. J.; Brothers, E. N.; Kudin, K. N.; Staroverov, V. N.; Keith, T. A.; Kobayashi, R.; Normand, J.; Raghavachari, K.; Rendell, A. P.; Burant, J. C.; Iyengar, S. S.; Tomasi, J.; Cossi, M.; Millam, J. M.; Klene, M.; Adamo, C.; Cammi, R.; Ochterski, J. W.; Martin, R. L.; Morokuma, K.; Farkas, O.; Foresman, J. B.; Fox, D. J. Gaussian, Inc., Wallingford CT, 2016.

46. Gaussian 16, Revision C.01, Frisch, M. J.; Trucks, G. W.; Schlegel, H. B.; Scuseria, G. E.; Robb, M. A.; Cheeseman, J. R.; Scalmani, G.; Barone, V.; Petersson, G. A.; Nakatsuji, H.; Li, X.; Caricato, M.; Marenich, A. V.; Bloino, J.; Janesko, B. G.; Gomperts, R.; Mennucci, B.; Hratchian, H. P.; Ortiz, J. V.; Izmaylov, A. F.; Sonnenberg, J. L.; Williams-Young, D.; Ding, F.; Lipparini, F.; Egidi, F.; Goings, J.; Peng, B.; Petrone, A.; Henderson, T.; Ranasinghe, D.; Zakrzewski, V. G.; Gao, J.; Rega, N.; Zheng, G.; Liang, W.; Hada, M.; Ehara, M.; Toyota, K.; Fukuda, R.; Hasegawa, J.; Ishida, M.; Nakajima, T.; Honda, Y.; Kitao, O.; Nakai, H.; Vreven, T.; Throssell, K.; Montgomery, J. A., Jr.; Peralta, J. E.; Ogliaro, F.; Bearpark, M. J.; Heyd, J. J.; Brothers, E. N.; Kudin, K. N.; Staroverov, V. N.; Keith, T. A.; Kobayashi, R.; Normand, J.; Raghavachari, K.; Rendell, A. P.; Burant, J. C.; Iyengar, S. S.; Tomasi, J.; Cossi, M.; Millam, J. M.; Klene, M.; Adamo, C.; Cammi, R.; Ochterski, J. W.; Martin, R. L.; Morokuma, K.; Farkas, O.; Foresman, J. B.; Fox, D. J. Gaussian, Inc., Wallingford CT, 2019.

47. Schmidt, J.; Polik, W., WebMO Enterprise. *WebMO LLC, Holland, MI USA* **2013**.

48. NBO 7.0.8 (11-Feb-2020) NBO 7.0. E. D. Glendening, J. K. Badenhoop, A. E. Reed, J. E. Carpenter, J. A. Bohmann, C. M. Morales, P. Karafiloglou, C. R. Landis, and F. Weinhold, Theoretical Chemistry Institute, University of Wisconsin, Madison, WI (2018).

49. J. F. Stanton, J. Gauss, M. E. Harding, and P. G. Szalay, CFOUR, Coupled-Cluster Techniques for Computational Chemistry, with contributions from A. A. Auer, R. J. Bartlett, U. Benedikt, C. Berger, D. E. Bernholdt, Y. J. Bomble, L. Cheng, O. Christiansen, M. Heckert, O. Heun, C. Huber, T.-C. Jagau, D. Jonsson, J. Jusélius, K. Klein, W. J. Lauderdale, F. Lipparini, D. A. Matthews, T. Metzroth, L. A. Mück, D. P. O'Neill, D. R. Price, E. Prochnow, C. Puzzarini, K. Ruud, F. Schiffmann, W. Schwalbach, C. Simmons, S. Stopkowicz, A. Tajti, J. Vázquez, F. Wang, J. D. Watts, and the integral packages MOLECULE (J. Almlöf and P. R. Taylor), PROPS (P. R. Taylor), ABACUS (T. Helgaker, H. J. Aa. Jensen, P. Jørgensen, and J. Olsen), and ECP routines by A. V. Mitin and C. van Wüllen, http://www.cfour.de.

50.   Mills, I. M., Vibration-Rotation Structure in Asymmetric- and Symmetric-Top Molecules. In *Molecular Spectroscopy: Modern Research*, Rao, K. N.; Mathews, C. W., Eds. Academic Press: New York, 1972; Vol. 1, pp 115-140.

51.   Schneider, W.; Thiel, W., Anharmonic Force Fields from Analytic Second Derivatives: Method and Application to Methyl Bromide. *Chem. Phys. Lett.* **1989**, *157* (4), 367-373.

52.   Stanton, J. F.; Lopreore, C. L.; Gauss, J., The equilibrium structure and fundamental vibrational frequencies of dioxirane. *J. Chem. Phys.* **1998**, *108* (17), 7190-7196.

53.   Flygare, W. H., Magnetic interactions in molecules and an analysis of molecular electronic charge distribution from magnetic parameters. *Chem. Rev.* **1974**, *74* (6), 653-687.

54.   Lin, S.; Herbert, D. E.; Velian, A.; Day, M. W.; Agapie, T., Dipalladium(I) Terphenyl Diphosphine Complexes as Models for Two-Site Adsorption and Activation of Organic Molecules. *J. Am. Chem. Soc.* **2013**, *135* (42), 15830-15840.

55.   Leis, H. J.; Fauler, G.; Windischhofer, W., Stable isotope labeled target compounds: preparation and use as internal standards in quantitative mass spectrometry. *Curr. Org. Chem.* **1998**, *2* (2), 131-144.

56.   Burton, A. G.; Forsythe, P. P.; Johnson, C. D.; Katritzky, A. R., The kinetics and mechanism of the electrophilic substitution of heteroaromatic compounds. Part XXVII. The nitration and hydrogen exchange of 1,3,5-trimethylpyrazole, 3,5-dimethylisoxazole, and 3,5-dimethylisothiazole. *J. Chem. Soc. B* **1971**, 2365-2371.

57.   Roussel, P.; Metzger, J., Synthesis and infrared spectral study of the deuteriothiazoles. *Bull. Soc. Chim. Fr.* **1962**, 2075-2078.

58.   Alonso, B.; Ocejo, M.; Carrillo, L.; Vicario, J. L.; Reyes, E.; Uria, U., Using Heteroaryl-lithium Reagents as Hydroxycarbonyl Anion Equivalents in Conjugate Addition Reactions with (S,S)-(+)-Pseudoephedrine as Chiral Auxiliary; Enantioselective Synthesis of 3-Substituted Pyrrolidines. *J. Org. Chem.* **2013**, *78* (2), 614-627.

59.   Gordy, W.; Cook, R., *Microwave Molecular Spectra*. 3rd. ed.; Wiley Interscience: New York, 1984; Vol. XVIII.

60.   Puzzarini, C.; Bloino, J.; Tasinato, N.; Barone, V., Accuracy and Interpretability: The Devil and the Holy Grail. New Routes across Old Boundaries in Computational Spectroscopy. *Chem. Rev.* **2019**, *119* (13), 8131-8191.

61.   Bomble, Y. J.; Stanton, J. F.; Kállay, M.; Gauss, J., Coupled-cluster methods including noniterative corrections for quadruple excitations. *J. Chem. Phys.* **2005**, *123* (5), 054101.

62. Cheng, L.; Gauss, J., Analytic energy gradients for the spin-free exact two-component theory using an exact block diagonalization for the one-electron Dirac Hamiltonian. *J. Chem. Phys.* **2011**, *135* (8), 084114.

63. Liu, W.; Peng, D., Exact two-component Hamiltonians revisited. *J. Chem. Phys.* **2009**, *131* (3), 031104.

64. Dyall, K. G., Interfacing relativistic and nonrelativistic methods. II. Investigation of a low-order approximation. *J. Chem. Phys.* **1998**, *109* (11), 4201-4208.

65. Handy, N. C.; Yamaguchi, Y.; Schaefer, H. F., The diagonal correction to the Born–Oppenheimer approximation: Its effect on the singlet–triplet splitting of CH_2 and other molecular effects. *J. Chem. Phys.* **1986**, *84* (8), 4481-4484.

66. Born, M.; Huang, K., *Dynamical Theory of Crystal Lattices*. Oxford University Press: New York, 1956.

67. Owen, A. N.; Zdanovskaia, M. A.; Esselman, B. J.; Stanton, J. F.; Woods, R. C.; McMahon, R. J., Improved Semi-Experimental Equilibrium Structure Determination and Theoretical Prediction of Pyridazine (*o*-$C_4H_4N_2$). *Manuscript in preparation*.

Table S4.1. Computed and experimental spectroscopic constants for thiophene (S-reduced Hamiltonian, I^r and III^r representations)

	CCSD(T)/ cc-pCVTZ	Experimental Rotational	B3LYP/ 6-311G+(2d, p)[c]	Experimental Rotational
Representation	I^r	I^r	III^r	III^r
$A_0^{(S)}$ (MHz)	7999	8041.595658 (44)	7967	8041.596797 (44)
$B_0^{(S)}$ (MHz)	5376	5418.262629 (36)	5367	5418.262388 (36)
$C_0^{(S)}$ (MHz)	3214	3235.780781 (39)	3205	3235.780008 (39)
D_J (kHz)	0.692	0.703074 (26)	1.915	1.919636 (31)
D_{JK} (kHz)	0.515	0.535835 (27)	−2.729	−2.748122 (30)
D_K (kHz)	1.667	1.652637 (67)	1.030	1.043067 (21)
d_1 (kHz)	−0.306	−0.3116416 (36)	−0.358	−0.357588 (19)
d_2 (kHz)	−0.065	−0.0673942 (18)	−0.118	−0.128344 (10)
H_J (Hz)	0.000218	0.0002125 (54)	0.000456	0.000483 (14)
H_{JK} (Hz)	−0.00172	−0.001668 (10)	−0.00199	−0.002106 (21)
H_{KJ} (Hz)	0.00225	0.002158 (32)	0.00275	0.002883 (16)
H_K (Hz)	0.000672	[0.000672][a]	−0.00122	−0.0012686 (96)
h_1 (Hz)	0.000129	0.00013105 (73)	0.000191	0.000161 (17)
h_2 (Hz)	0.0000381	0.00004305 (56)	0.000261	0.000236 (12)
h_3 (Hz)	0.0000216	0.00002252 (14)	0.0000159	0.0000139 (27)
N_{lines}		3270[b]		3270[b]
σ (MHz)		0.022		0.022
κ	−0.0965	−0.917	−0.0920	−0.0917
Δ_i (uÅ^2)	0.0763	0.0656923 (20)	0.0776	0.0657344 (20)

[a] Held constant to CCSD(T)/cc-pCVTZ value.
[b] Includes transitions from previous literature[31-32, 34]
[c] Values converted from a left-handed coordinate system.

Table S4.2. Spectroscopic constants for isotopologues of thiophene (S-reduced Hamiltonian, I^r representation)[a]

Isotopologue	[2-^{13}C][b]	[3-^{13}C][b]	[^{34}S][b]	[^{33}S][b]
$A_0^{(S)}$ (MHz)	7852.77554 (31)	7981.28038 (34)	8041.71507 (20)	8041.6515 (20)
$B_0^{(S)}$ (MHz)	5418.40562 (10)	5319.305933 (98)	5274.184579 (69)	5344.29761 (59)
$C_0^{(S)}$ (MHz)	3204.806550 (87)	3190.618898 (88)	3183.843198 (67)	3209.25834 (13)
D_J (kHz)	0.699151 (61)	0.675952 (59)	0.680947 (46)	0.69162 (14)
D_{JK} (kHz)	0.50644 (37)	0.55134 (32)	0.51005 (19)	0.52162 (77)
D_K (kHz)	1.58322 (56)	1.61109 (65)	1.69958 (45)	1.6659 (33)
d_1 (kHz)	–0.313237 (19)	–0.298436 (19)	–0.297537 (19)	–0.304257 (86)
d_2 (kHz)	–0.068193 (11)	–0.0648635 (97)	–0.0629687 (79)	–0.065028 (28)
H_J (Hz)	0.000218 (14)	0.000203 (14)	0.000197 (12)	[0.000212]
H_{JK} (Hz)	–0.00154 (18)	–0.00148 (15)	[–0.00166]	[–0.00169]
H_{KJ} (Hz)	0.00303 (51)	0.00179 (36)	0.00209 (20)	[0.00218]
H_K (Hz)	[0.000597]	[0.000672]	[0.000759]	[0.000716]
h_1 (Hz)	[0.000128]	[0.000121]	0.0001220 (61)	[0.000126]
h_2 (Hz)	[0.0000360]	[0.0000386]	0.0000414 (25)	[0.0000367]
h_3 (Hz)	[0.0000221]	[0.0000203]	0.00002108 (86)	[0.0000205]
N_{lines}	965	983	1262	258
σ (MHz)	0.030	0.029	0.024	0.029
κ	–0.0475	–0.111	–0.139	–0.116
Δ_i (uÅ^2)	0.0665430 (53)	0.0662984 (55)	0.0664410 (39)	0.065992 (20)

[a] Brackets around a tabulated number indicate that it is held constant at the value predicted by the VPT2 calculation.

[b] Includes previously reported transitions.[24-25, 34]

[c] Shaded column indicates isotopologue is not included in structure determination

Table S4.2. cont.

Isotopologue	[2-²H][b]	[3-²H][b]	[2,3-²H]	[2,4-²H]	[2,5-²H]	[3,4-²H]
$A_0^{(S)}$ (MHz)	7437.19729 (20)	7855.99758 (11)	7277.00130 (27)	7288.38317 (21)	6903.42658 (12)	7616.557 (16)
$B_0^{(S)}$ (MHz)	5413.721571 (84)	5138.229854 (63)	5137.627501 (97)	5124.657587 (77)	5410.698544 (68)	4914.6794 (78)
$C_0^{(S)}$ (MHz)	3131.815069 (83)	3105.222733 (72)	3010.350104 (87)	3007.831223 (83)	3032.130273 (70)	2986.05460 (18)
D_J (kHz)	0.681599 (56)	0.606648 (43)	0.592435 (59)	0.578844 (46)	0.666346 (46)	0.53795 (23)
D_{JK} (kHz)	0.44481 (26)	0.56738 (10)	0.45748 (34)	0.538407 (90)	0.32619 (15)	[0.531]
D_K (kHz)	1.26981 (35)	1.52438 (13)	1.17863 (53)	1.14275 (32)	1.00164 (15)	[1.40]
d_1 (kHz)	–0.313542 (24)	–0.265109 (10)	–0.268999 (28)	–0.262829 (14)	–0.316194 (18)	–0.23302 (18)
d_2 (kHz)	–0.0697451 (78)	–0.0582064 (36)	–0.060220 (10)	–0.0607188 (32)	–0.0709025 (42)	–0.050945 (68)
H_J (Hz)	0.000225 (17)	0.0001465 (92)	0.000142 (21)	0.0001209 (96)	0.000236 (10)	[0.000123]
H_{JK} (Hz)	–0.00182 (18)	–0.001063 (43)	–0.00110 (18)	[–0.000752]	–0.001619 (44)	[–0.000972]
H_{KJ} (Hz)	0.00247 (37)	0.00117 (10)	0.00143 (38)	[0.000762]	0.002274 (91)	[0.00129]
H_K (Hz)	[0.000387]	[0.000920]	[0.000530]	[0.000791]	[0.000116]	[0.000696]
h_1 (Hz)	0.0001224 (73)	0.0000964 (20)	0.000084 (10)	[0.0000878]	0.0001222 (46)	[0.0000794]
h_2 (Hz)	0.0000329 (50)	0.0000385 (12)	0.0000307 (52)	[0.0000401]	[0.0000309]	[0.0000293]
h_3 (Hz)	0.0000219 (10)	0.00001676 (26)	0.0000181 (12)	[0.0000168]	0.00002505 (58)	[0.0000136]
N_{lines}	1350	1880	1187	1171	1651	203
σ (MHz)	0.028	0.029	0.030	0.030	0.027	0.038
κ	0.0600	–0.1441	–0.0028	–0.0110	0.2288	–0.1670
Δ_i (uÅ²)	0.0649842 (49)	0.0643123 (41)	0.0635073 (58)	0.0635933 (53)	0.0639373 (43)	0.06322 (22)

Table S4.2. cont.

Isotopologue	[2,3,4-²H]	[2,3,5-²H]	[2,3,4,5-²H]	[2,5-²H, ³⁴S]	[2,3,5-²H, ³⁴S]	[2,3,4,5-²H, ³⁴S][c]
$A_0^{(S)}$ (MHz)	7072.27605 (33)	6775.84957 (12)	6587.73179 (20)	6903.5350 (11)	6773.39956 (92)	6588.36 (32)
$B_0^{(S)}$ (MHz)	4909.46919 (10)	5124.449058 (64)	4905.808107 (85)	5268.34308 (37)	4992.25390 (32)	4777.72 (18)
$C_0^{(S)}$ (MHz)	2896.801160 (94)	2916.731610 (66)	2810.897843 (77)	2986.90670 (30)	2872.96911 (23)	2768.4921 (18)
D_J (kHz)	0.520247 (60)	0.567721 (40)	0.507404 (48)	0.64538 (15)	0.55289 (13)	0.4870 (65)
D_{JK} (kHz)	0.46951 (35)	0.41849 (19)	0.37771 (25)	0.31768 (78)	0.3762 (24)	[0.348]
D_K (kHz)	1.07591 (53)	0.88863 (18)	0.84381 (29)	1.0354 (14)	0.9648 (52)	[0.882]
d_1 (kHz)	–0.234458 (26)	–0.266630 (16)	–0.236303 (23)	–0.302494 (66)	–0.255757 (61)	–0.2225 (45)
d_2 (kHz)	–0.0532931 (94)	–0.0621192 (50)	–0.0545074 (35)	–0.066729 (35)	–0.057659 (83)	–0.0503 (12)
H_J (Hz)	0.000123 (19)	0.000151 (12)	0.000144 (17)	0.000237 (30)	0.000111 (16)	[0.000116]
H_{JK} (Hz)	–0.00080 (11)	–0.000862 (70)	–0.000906 (94)	–0.00127 (36)	[–0.000792]	[–0.000780]
H_{KJ} (Hz)	0.00123 (28)	[0.000857]	[0.00105]	[0.00185]	[0.000895]	[0.00101]
H_K (Hz)	[0.000472]	[0.000474]	[0.000270]	[0.000173]	[0.000473]	[0.000301]
h_1 (Hz)	0.0000821 (97)	0.0000936 (52)	0.0000802 (86)	[0.000116]	[0.0000843]	[0.0000717]
h_2 (Hz)	[0.0000292]	0.0000379 (16)	[0.0000270]	[0.0000292]	[0.0000328]	[0.0000249]
h_3 (Hz)	0.0000159 (14)	0.00001790 (55)	0.00001552 (66)	[0.0000210]	[0.0000158]	[0.0000131]
N_{lines}	1049	1672	1349	420	458	39
σ (MHz)	0.032	0.027	0.031	0.042	0.039	0.039
κ	–0.0360	0.1442	0.1093	0.1650	0.0867	0.0520
Δ_i (uÅ²)	0.0622446 (70)	0.0624700 (44)	0.0610925 (58)	0.064788 (22)	0.063317 (19)	0.0608 (56)

Table S4.2. cont.

Isotopologue	[2,5-^{2}H, 2-^{13}C]	[2,5-^{2}H, 3-^{13}C]	[2-^{2}H, ^{34}S]	[3-^{2}H, 2-^{13}C]	[3-^{2}H, 3-^{13}C]	[3-^{2}H, 4-^{13}C]
$A_0^{(S)}$ (MHz)	6763.947 (25)	6860.081 (23)	7436.863 (16)	7681.747 (50)	7816.981 (61)	7775.956 (56)
$B_0^{(S)}$ (MHz)	5410.781 (17)	5310.447 (15)	5270.7000 (92)	5137.725 (24)	5045.949 (27)	5060.889 (25)
$C_0^{(S)}$ (MHz)	3004.92939 (26)	2992.15823 (26)	3083.34137 (19)	3077.43102 (28)	3065.28740(28)	3064.44094 (27)
D_J (kHz)	0.66744 (43)	0.64197 (37)	0.66389 (23)	0.60549 (44)	0.58584(48)	0.58884 (51)
D_{JK} (kHz)	[0.271]	[0.329]	[0.404]	[0.520]	[0.563]	[0.552]
D_K (kHz)	[0.996]	[0.989]	[1.33]	[1.47]	[1.51]	[1.49]
d_1 (kHz)	–0.31845 (33)	–0.30329 (28)	–0.30128 (18)	–0.26733 (34)	–0.25428 (37)	–0.25668 (39)
d_2 (kHz)	–0.07065 (11)	–0.06776 (10)	–0.065200 (70)	–0.05859 (13)	–0.05559 (14)	–0.05613 (14)
H_J (Hz)	[0.000229]	[0.000200]	[0.000203]	[0.000151]	[0.000134]	[0.000144]
H_{JK} (Hz)	[–0.00154]	[–0.00131]	[–0.00148]	[–0.00114]	[–0.000949]	[–0.00109]
H_{KJ} (Hz)	[0.00203]	[0.00171]	[0.00189]	[0.00139]	[0.00105]	[0.00139]
H_K (Hz)	[0.0000682]	[0.000166]	[0.000450]	[0.000827]	[0.000979]	[0.000771]
h_1 (Hz)	[0.000121]	[0.000114]	[0.000119]	[0.0000959]	[0.0000904]	[0.0000931]
h_2 (Hz)	[0.0000273]	[0.0000329]	[0.0000340]	[0.0000346]	[0.0000368]	[0.0000346]
h_3 (Hz)	[0.0000236]	[0.0000216]	[0.0000203]	[0.0000169]	[0.0000155]	[0.0000159]
N_{lines}	165	174	237	133	112	113
σ (MHz)	0.044	0.045	0.039	0.046	0.041	0.041
κ	0.2800	0.1987	0.0049	–0.1051	–0.1663	–0.1525
Δ_i (uÅ^2)	0.06452 (41)	0.06470 (38)	0.06573 (23)	0.06519 (64)	0.06483 (75)	0.06495 (69)

Table S4.2. cont.

Isotopologue	[3-²H, 5-¹³C]	[3-²H, ³⁴S]	[3-²H, ³³S]ᶜ
$A_0^{(S)}$ (MHz)	7671.947 (41)	7854.54126 (65)	7854.84 (47)
$B_0^{(S)}$ (MHz)	5138.103 (19)	5003.22949 (16)	5069.12 (20)
$C_0^{(S)}$ (MHz)	3075.99325 (24)	3055.16594 (14)	3079.66292 (44)
D_J (kHz)	0.60206 (37)	0.588513 (76)	0.5958 (15)
D_{JK} (kHz)	[0.534]	0.53756 (46)	[0.534]
D_K (kHz)	[1.46]	1.5705 (12)	[1.56]
d_1 (kHz)	–0.26554 (28)	–0.253387 (27)	–0.2571 (11)
d_2 (kHz)	–0.05844 (11)	–0.054331 (10)	–0.05493 (42)
H_J (Hz)	[0.000147]	0.000157 (17)	[0.000146]
H_{JK} (Hz)	[–0.00108]	–0.00103 (16)	[–0.001103]
H_{KJ} (Hz)	[0.00124]	[0.00126]	[0.00128]
H_K (Hz)	[0.000901]	[0.000964]	[0.000942]
h_1 (Hz)	[0.0000953]	[0.0000922]	[0.0000943]
h_2 (Hz)	[0.0000360]	[0.0000330]	[0.0000345]
h_3 (Hz)	[0.0000168]	[0.0000150]	[0.0000157]
N_{lines}	143	664	57
σ (MHz)	0.040	0.035	0.045
κ	–0.1026	–0.1882	–0.1667
Δ_i (uÅ²)	0.06515 (52)	0.0650305 (99)	0.0648 (56)

Equations for the determinable constants[59]

$$A_0'' = A_0^{(A)} + 2\Delta_{\mathrm{J}} \qquad (S4.1)$$

$$B_0'' = B_0^{(A)} + 2\Delta_{\mathrm{J}} + \Delta_{\mathrm{JK}} - 2\delta_J - 2\delta_K \qquad (S4.2)$$

$$C_0'' = C_0^{(A)} + 2\Delta_{\mathrm{J}} + \Delta_{\mathrm{JK}} + 2\delta_J + 2\delta_K \qquad (S4.3)$$

$$A_0'' = A_0^{(S)} + 2D_{\mathrm{J}} + 6d_2 \qquad (S4.4)$$

$$B_0'' = B_0^{(S)} + 2D_J + D_{JK} + 2d_1 + 4d_2 \qquad (S4.5)$$

$$C_0'' = C_0^{(S)} + 2D_J + D_{JK} - 2d_1 + 4d_2 \qquad (S4.6)$$

Chapter 5: Combined Millimeter-wave and Infrared Spectroscopic Analysis of the Excited Vibrational States of Thiophene (C₄H₄S)
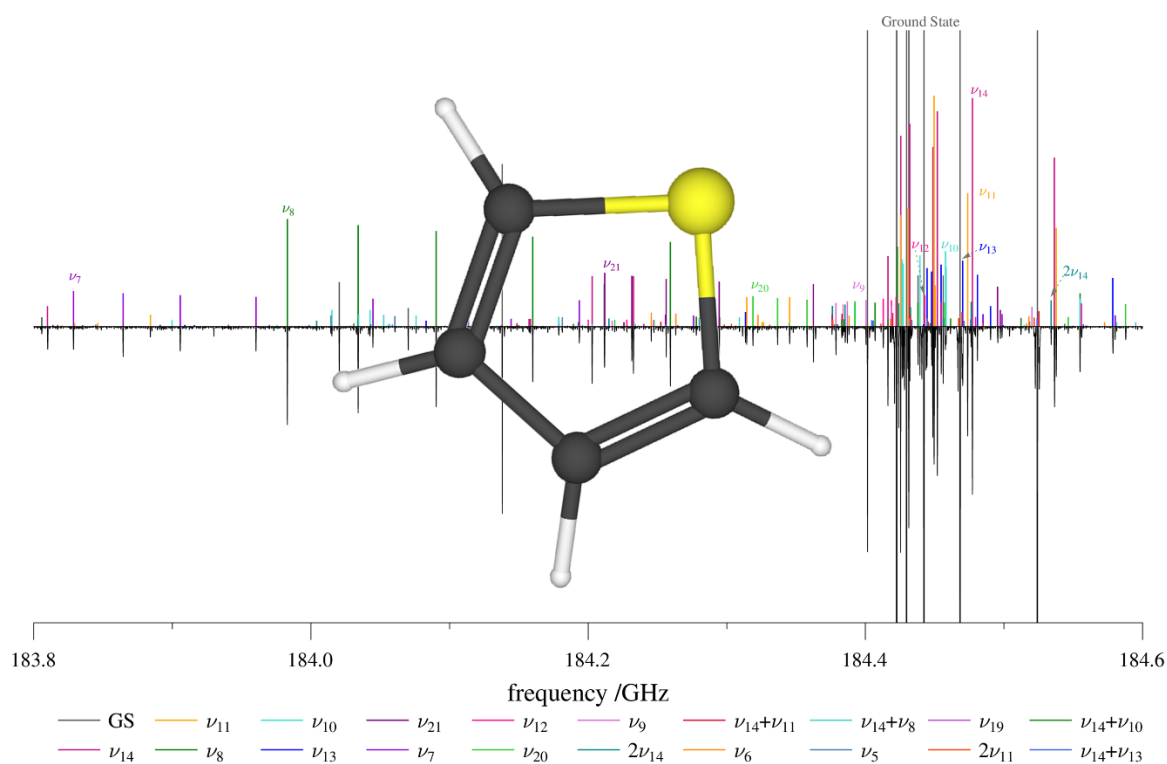
Includes the work of several collaborators:

Brian J. Esselman, R. Claude Woods, Robert J. McMahon

University of Wisconsin-Madison

Yotaro Ichikawa and Kaori Kobayashi

University of Toyama, Japan

ABSTRACT

The rotational spectra from 40 to 360 GHz of 19 excited vibrational states of thiophene (C_4H_4S, C_{2v}, $\mu_a = 0.55 \pm 0.01$ D) below 1163 cm^{-1} are presented for the first time. For ν_{14}, ν_8, ν_{13}, ν_7, ν_6, ν_5, ν_{19}, where published high-resolution IR data are available, these measurements have been incorporated into a global least-squares fit involving the ground state. Rotational constants for twelve of these states are reported for the first time, including the three A_2 symmetry states that are not visible by IR spectroscopy. Thus far, a total of 13,840 distinct pure-rotational transitions and 19 nominal interstate transitions have been measured, assigned, and least-squares fit to A-reduced, sextic distorted-rotor Hamiltonians in I^r representation. Many vibrational states are treated as interacting states using Coriolis coupling terms. An analysis of a pentad of Coriolis-coupled states (ν_7, ν_{12}, ν_{20}, ν_9, and $2\nu_{14}$) between 840 and 904 cm^{-1} has been performed. Above 904 cm^{-1}, transitions have been assigned for $\nu_{14}+\nu_{11}$, ν_6, $\nu_{14}+\nu_8$, ν_5, ν_{19}, $2\nu_{11}$, $\nu_{14}+\nu_{10}$, $\nu_{14}+\nu_{13}$, by starting with extrapolated constants (overtones and combination states) or from previously determined constants from high-resolution IR of the fundamentals. This Chapter presents the current state of this ongoing research project.

INTRODUCTION

Thiophene (C_4H_4S, C_{2v}, Figure 5.1) is a sulfur-containing heterocycle with a relatively small dipole moment along the a-axis ($\mu_a = 0.55 \pm 0.01$ D).[1] The original microwave study of thiophene by Bak et $al.$[2-3] determined a substitution structure from the spectroscopic constants of six isotopologues. Subsequent studies expanded the frequency range and refined the dipole moment and rotational constants.[1, 4-6] The nuclear quadrupole coupling constants for the [^{33}S]-isotopologue were determined by Kretschmer, et $al.$ from their analysis of the three most abundant

sulfur isotopologues of thiophene ([^{32}S], [^{33}S], and [^{34}S]).[7] During the course of our semi-experimental equilibrium structure determination of thiophene presented in Chapter 4, it was apparent that many vibrational states were also present at favorable relative intensities for investigation. While the ro-vibrational spectra of some of these vibrational states have been studied by high-resolution IR,[8-11] the vibrationally excited states of thiophene have not been studied by pure rotational spectroscopy.

The vibrational spectrum of thiophene was initially reported[12] in 1905 and has been well studied since using Raman,[13-16] low-resolution IR,[14, 17-21] and high-resolution IR[8-11] spectroscopy (Table 5.1). Analysis of the rotationally resolved IR transitions of ν_{13} resulted a determination of the rotational and several quartic centrifugal distortion constants for both ν_{13} and the ground state, as well as a precise vibrational frequency for ν_{13}.[11] Analysis of the infrared spectrum from 600 to 1200 cm^{-1} provided rotational and quartic spectroscopic constants for fundamentals ν_6, ν_7, ν_{13}, ν_5 and ν_{19}.[10] Subsequent analysis of the infrared spectrum from 400 to 750 cm^{-1} determined spectroscopic constants and frequencies for the ν_{14}, ν_8, and ν_7 fundamentals.[8-9] The spectroscopic constants from these previous studies provided an excellent starting point for the assignment of the mm-wave spectra of the vibrational satellites in this work. The computational and experimentally measured fundamental frequencies for the vibrational states of thiophene are listed in Table 5.1. The combination states and overtones investigated in this work are also included in Table 5.1. The energy levels of the vibrational states from the ground state to 1260 cm^{-1} are shown graphically in Figure 5.2.
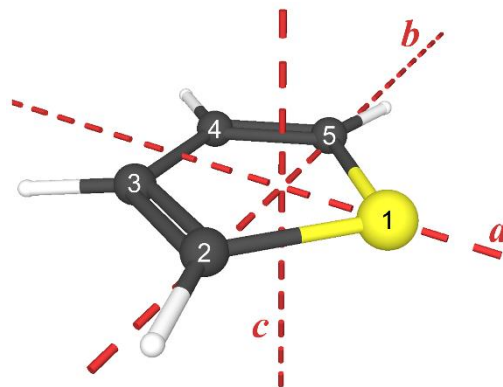
Figure 5.1. Thiophene structure with principal inertial axes and numerical atom positions.

Table 5.1. Thiophene Vibrational Modes (cm^{-1})

mode	Sym.	B3LYP[a]	CCSD(T)[b]	Vapor Phase[c]	This Work
ν_1	A_1	3122	3130	3125.6	
ν_2	A_1	3084	3100	3097.0	
ν_3	A_1	1403	1410	1409.7	
ν_4	A_1	1365	1370	1364	
ν_5	A_1	1091	1082	1081.54328 (5)[e,10]	1081.544113 (47)
ν_6	A_1	1033	1034	1036.43440 (5)[e,10]	1036.434222 (33)
ν_7	A_1	820	834	840.0094537 (64)[8]	840.0107647 (97)
ν_8	A_1	606	605	608.6679444 (49)[8]	608.6679415 (83)
ν_9	A_2	902	898	900	900.01243 (80)
ν_{10}	A_2	675	682	683.5	
ν_{11}	A_2	570	563	564.4	
ν_{12}	B_1	862	867	866[d]	865.98970 (50)
ν_{13}	B_1	709	715	712.10378 (3)[10]	712.103743 (22)
ν_{14}	B_1	454	450	452.4144843 (54)[8]	452.4144840 (97)
ν_{15}	B_2	3120	3127	*unobserved*[d]	
ν_{16}	B_2	3072	3087	3087[d]	
ν_{17}	B_2	1511	1512	1510[d]	
ν_{18}	B_2	1253	1253	1255.8[d]	
ν_{19}	B_2	1090	1085	1083.96911 (6)[e,10]	1083.968984 (43)
ν_{20}	B_2	864	864	872.8[d]	873.31026 (50)
ν_{21}	B_2	733	750	753.5[d]	753.4942 (65)
$\nu_{14}+\nu_{13}$	A_1	1162	1163	1162.5	
$2\nu_{11}$	A_1	1140	1127	1128.5	
$2\nu_{14}$	A_1	907	899	904	903.76750 (80)
$\nu_{14}+\nu_8$	B_1	1060	1055	*unobserved*	
$\nu_{14}+\nu_{10}$	B_2	1129	1132	*unobserved*	
$\nu_{14}+\nu_{11}$	B_2	1023	1012	*unobserved*	

[a] Fundamental frequency B3LYP/6-311G+(2d,p)
[b] Fundamental frequency CCSD(T)/cc-pCVTZ
[c] Reference 14 unless otherwise noted.
[d] Mode reassigned to symmetry elements of the group by computational conventions.[10]
[e] values from a coupled dyad with c-Coriolis term included
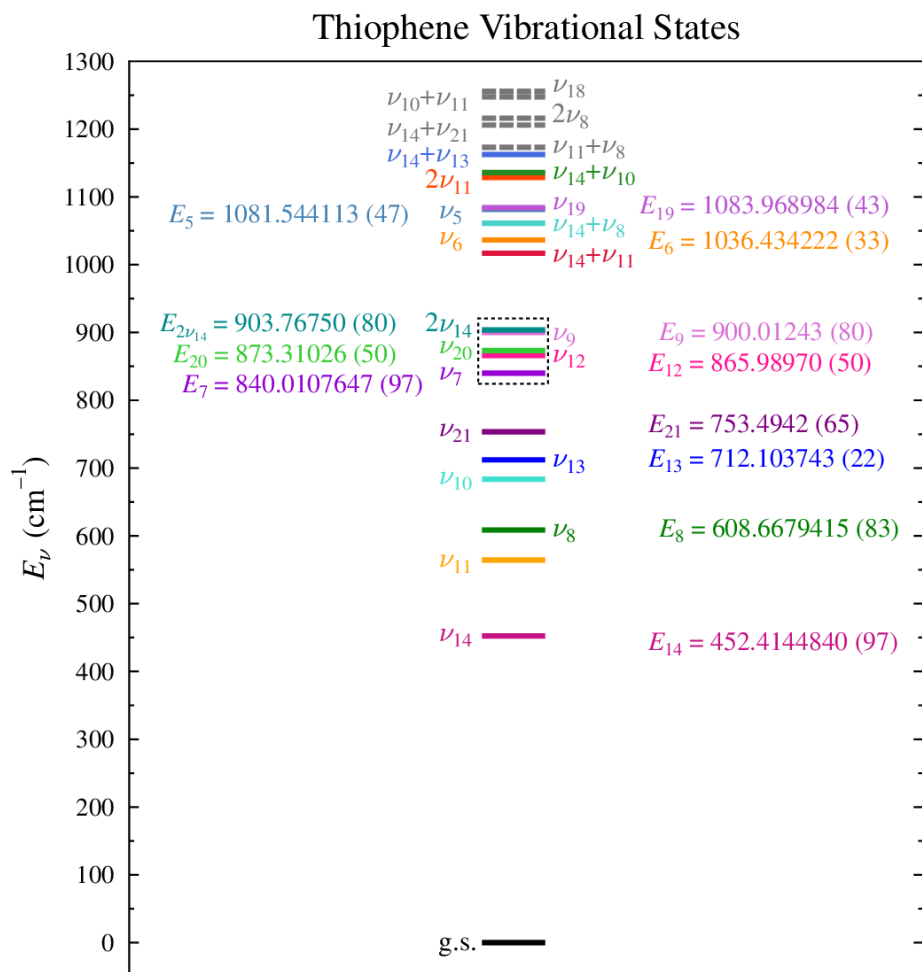
Figure 5.2. The vibrational state manifold of thiophene below 1260 cm^{-1}. Noted energy values in cm^{-1} are determined from this study with previously measured high-resolution IR data[8, 10] or through their coupling interactions. Unspecified fundamentals or combination states are the vapor phase experimental data presented in Table 5.1. Combination states listed as *unobserved* in Table 5.1 are included as the sum of their component fundamental frequencies. The pentad of states is noted by the dashed black box. States with dashed lines in grey have not yet been identified in the mm-wave region.

EXPERIMENTAL METHODS

The spectra for this work were obtained from rotational spectrometers at the University of Toyama[22-23] and the University of Wisconsin–Madison[24-25] (both described previously) using commercially available thiophene at 5 – 50 mTorr at room temperature as described in Chapter 4

of this thesis. The separate spectral segments were combined into a single broadband spectrum using Kisiel's Assignment and Analysis of Broadband Spectra (AABS) suite.[26-27] The measured rotational transitions have an estimated uncertainty of 0.05 MHz, the IR transitions from van Wijngaarden *et al.*[8] have an estimated uncertainty of 0.00032 cm^{-1} (9.6 MHz), and the IR transitions from Hegelund *et al.* have an estimated uncertainty of 0.001 cm^{-1} (30 MHz).[10] Transitions for all vibrational states were least-squares fit to sextic, disorted-rotor Hamiltonian models in the A-reduction and I^r representation using Pickett's SPFIT/SPCAT,[28] which allowed for simultaneous fitting of all vibrational states and the inclusion of previous high-resolution infrared transitions.[8, 10] Coriolis-coupling was employed for many states, and is detailed for each state below. Kisiel's ASCP_L and SVIEW_L were utilized for visualization of spectra and transition measurement along with AC and PIFORM for analysis.[29]

COMPUTATIONAL METHODS

Geometry optimization and subsequent anharmonic frequency calculation of thiophene at the B3LYP/6-311G+(2d,p) level was carried out with Gaussian 16 software[30] with the WebMO interface[31] utilizing an "ultrafine" integration grid and a "verytight" convergence criteria. An optimization was also completed at CCSD(T)[32]/cc-pCVTZ.[33-35] Vibration-rotation interactions were computed at the same level with a second-order vibrational perturbation theory (VPT2) anharmonic frequency calculation by evaluating the cubic force constants, using analytical second derivatives at displaced points[36-38] in CFOUR.[39] These calculations provided vibrational frequencies, vibration-rotation interaction constants, and Coriolis zeta constants.

VIBRATIONAL STATE ANALYSIS

The rotational spectrum of thiophene is dominated by the ground state, but as shown in the segment of the spectrum from 183.8 to 184.6 GHz, Figure 5.3, several vibrationally excited states are sufficiently populated for a relatively straightforward assignment and least-squares fitting of transitions. Previously published high-resolution infrared transitions were included in our data set for ν_{14}, ν_8, and ν_7 from van Wijngaarden, *et al.*,[8] and for ν_{13}, ν_6, ν_5, and ν_{19} from Hegelund *et al.*[10]

Ground State, C_{2v}

The ground vibrational state spectrum and spectral analysis of thiophene has been expanded, relative to previous literature, as described in Chapter 4 of this thesis. The distinct bands in the spectrum are due to $^aR_{0,1}$ transitions that are K_c degenerate and progress to higher frequency as they decrease in J and increase in K_a. The transitions generally lose K_c degeneracy around $K_a = 10$, and become K_a degenerate around $K_a = 20$ depending on J. With the inclusion of previously reported transitions,[4, 6-7] the data set contains of over 3000 pure-rotational transitions with a range of J range from 1 to 93 and K_a range from 0 to 38. Least-squares fitting of the moderately large data set requires a sextic, distorted-rotor Hamiltonian in A-reduction and I^r representation. With an experimental κ value ($\kappa = (2B-A-C)/(A-C)$) of -0.0917, the I^r representation is more appropriate due to the slightly prolate nature of thiophene. While the ground state spectroscopic constants have been presented in Chapter 4, the simultaneous fitting of all of the vibrational states allowed for additional rotational transitions that are blended with transitions from other vibrational states to be included in the least-squares fit. All sextic constants were satisfactorily determined and the least-squares fit has a satisfactory σ value of 0.023 MHz, well within the standard error of frequency measurement (0.050 MHz). There is generally great

agreement between the computed and experimental spectroscopic constants. The CCSD(T) values predicted for A_0, B_0, C_0 are within 0.8% of the experimental values and the quartic distortion constants agree within 2%. The computational sextic constants are within 31 % of the values determined, which is a larger discrepancy than for those determined for the least-squares fit presented in Chapter 4 where the computational agrees within 10% of the experimental value. This variance in the sextic constants is possibly due to the incorporation of IR transitions whose upper state is coupled and not yet well modeled, leading to fluctuation in these constants dependent on the treatment of those IR transitions, since all states are being least-squares fit simultaneously. Sextic distortion terms that cannot be currently determined for excited vibrational states are held to a previous ground state value. When the analysis of the spectra is complete the sextic constants for the pure-rotational fit and the global fit should be closer in agreement.
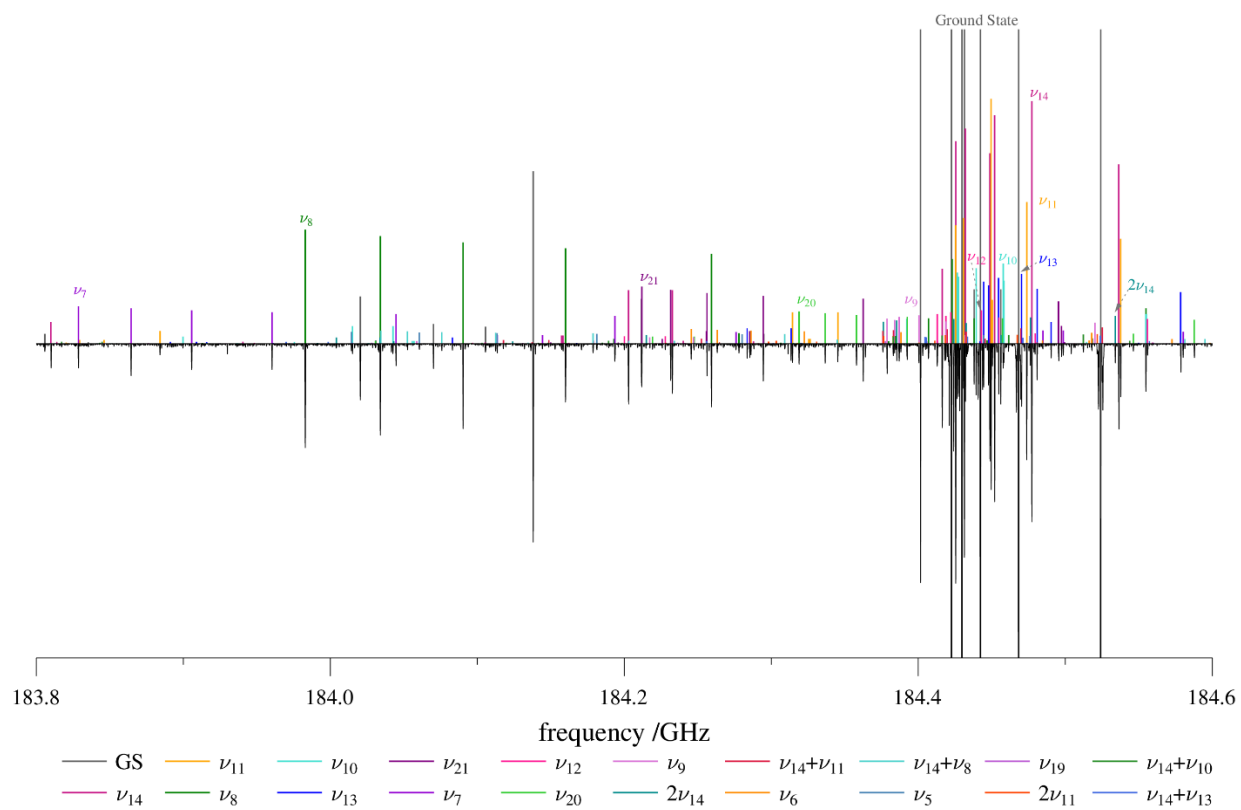
Figure 5.3. Experimental rotational spectrum of thiophene (below) and the predicted spectrum of the vibrational states (above) from 183.8 to 184.6 GHz. States with fundamental frequencies below 904 cm^{-1} are labeled at their $K_a = 0$ transition.

Table 5.2. Spectroscopic constants for vibrational states of thiophene between 0.0 and 609 cm^{-1} (A-reduction, I^r representation)

	Ground State	ν_{14}, B_1	ν_{11}, A_2	ν_8, A_1
Freq. (cm^{-1})	0.0	452.4144840 (97)	[564.4][14]	608.6679415 (83)
$A_v^{(A)}$ (MHz)	8041.59495 (12)	8020.38459 (32)	8022.865 (91)	8041.049 (91)
$B_v^{(A)}$ (MHz)	5418.264712 (92)	5409.57745 (15)	5412.51928 (19)	5421.83671 (21)
$C_v^{(A)}$ (MHz)	3235.779261 (97)	3237.02558 (13)	3236.94295 (20)	3227.66865 (21)
Δ_J (kHz)	0.837887 (55)	0.831927 (78)	0.836805 (47)	0.84962 (11)
Δ_{JK} (kHz)	−0.273393 (94)	−0.19438 (32)	−0.28271 (51)	−0.30184 (52)
Δ_K (kHz)	2.32778 (22)	2.2116 (10)	2.2527 (23)	2.4295 (21)
δ_J (kHz)	0.311618 (10)	0.308162 (30)	0.310666 (21)	0.317328 (31)
δ_K (kHz)	0.917615 (73)	0.88632 (11)	0.8994 (12)	0.9496 (12)
Φ_J (Hz)	0.000306 (10)	0.000317 (16)	[0.000321]^a	0.000282 (26)
Φ_{JK} (Hz)	−0.001083 (38)	−0.00091 (10)	[−0.00103]^a	[−0.00103]^a
Φ_{KJ} (Hz)	−0.00181 (11)	[−0.00172]^a	[−0.00172]^a	[−0.00172]^a
Φ_K (Hz)	0.00502 (19)	0.00395 (60)	[0.00448]^a	[0.00448]^a
ϕ_J (Hz)	0.0001484 (22)	0.0001514 (64)	[0.000150]^a	[0.000150]^a
ϕ_{JK} (Hz)	−0.000116 (25)	[−0.000107]^a	[−0.000107]^a	[−0.000107]^a
ϕ_K (Hz)	0.003025 (57)	0.00230 (19)	[0.00308]^a	[0.00308]^a
$\nu_{11} \leftrightarrow \nu_8\ G_a$ (MHz)			−3150 (19)	
$N_{lines\ MMW}$	3301^b	1622	1237	1154
N_{lines} IR	15505^c	1915^d		2972^d
σ_{MMW} (MHz)	0.023	0.036	0.043	0.033
σ_{IR} (cm^{-1})	0.0027^e	0.0000591		0.0000977
κ^f	−0.0917	−0.0916	−0.0908	−0.0883
Δ_i (uÅ^2)^g	0.0658	−0.310	−0.236	0.515

^{a} Held constant to ground state value

^{b} Includes transitions from references 4, 6-7

^{c} Total IR transitions, includes transitions from references 8, 10

^{d} Transitions from reference 8

^{e} Overall error of all IR states

^{f} $\kappa = (2B−A−C)/(A−C)$

^{g} $\Delta_i = I_c−I_b−I_a$

ν_{14} (B_1, 452.4 cm^{-1})

The lowest-energy fundamental ν_{14} (B_1) is a symmetric, ring-folding motion. In contrast to the ground-state spectrum, the spectrum of ν_{14} begins at low K_a by progressing toward lower frequency as K_a increases, then exhibits a turn-around and progresses toward higher frequency as K_a continues to increase. The small change in C_{14} from C_0 means these low K_a transitions are interspersed amongst the ground state $^aR_{0,1}$ branch of low K_a transitions (Figure 5.3). This state has a precise fundamental frequency of 452.4144840 (97) cm^{-1} determined by the least-squares fit of over 1600 a-type R and Q pure rotational transitions with 1915 high resolution IR transitions.[8] From this combined data set, all quartic and four sextic centrifugal distortion constants were determined. The Φ_{KJ} and ϕ_{JK} sextic centrifugal distortion constants were not satisfactorily determined and were held constant at their corresponding ground-state values. Table 5.3 presents the vibration-rotation constants ($B_0 - B_\nu$) for ν_{14} and all other fundamental vibrational states investigated in this work. The agreement between the experimental and CCSD(T)/cc-pCVTZ values for this state is excellent, 0.14% for $A_0 - A_{14}$, 4.1% for $B_0 - B_{14}$, and 0.51% for $C_0 - C_{14}$. The B3LYP values are also in good agreement, 3.9% for $A_0 - A_{14}$, 2.9% for $B_0 - B_{14}$, 4.5% for $C_0 - C_{14}$. This agreement makes the assignment of ν_{14} unambiguous and, if constants from the previous high-resolution IR were not available, would have provided sufficient information to begin transition assignment.

Table 5.3. Vibration-rotation interaction constants of thiophene fundamentals

State, Sym.	ν_{14}, B_1	ν_{11}, A_2	ν_8, A_1	ν_{10}, A_2	ν_{13}, B_1	ν_{21}, B_2	ν_7, A_1
Freq. (cm^{-1})[a]	452.4	564.4[14]	608.7	683.5[14]	712.1	753.5	840.0
				Experimental			
$A_0 - A_v$ (MHz)	21.21036 (34)	18.730 (91)	0.546 (91)	4.63405 (49)	11.41 (18)	2.31 (18)	7.39616 (97)
$B_0 - B_v$ (MHz)	8.68726 (18)	5.74543 (21)	−3.57200 (23)	12.575 (11)	5.50452 (37)	3.125 (11)	5.4326 (63)
$C_0 - C_v$ (MHz)	−1.24632 (16)	−1.16369 (22)	8.11061 (23)	−0.84273 (15)	−1.03058 (38)	3.80693 (32)	7.256 (37)
				CCSD(T)/cc-pCVTZ			
$A_0 - A_v$ (MHz)	21.24	26.68	−7.75	4.17	16.11	−2.94	9.88
$B_0 - B_v$ (MHz)	8.33	5.49	−3.68	12.96	5.40	1.79	6.10
$C_0 - C_v$ (MHz)	−1.24	−1.16	7.86	−0.91	−1.03	3.73	10.57
				B3LYP/6-311G+(2d,p)			
$A_0 - A_v$ (MHz)	22.03	26.87	−6.35	4.09	17.52	−4.82	7.22
$B_0 - B_v$ (MHz)	8.94	5.47	−3.19	12.54	5.17	6.00	6.02
$C_0 - C_v$ (MHz)	−1.19	−1.13	9.22	−0.96	−1.12	3.46	10.04

State, Sym.	ν_{12}, B_1	ν_{20}, B_2	ν_9, A_2	ν_6, A_1	ν_5, A_1	ν_{19}, B_2
Freq. (cm^{-1})[a]	866.0	873.3	900.0	1036.4	1081.5	1084.0
			Experimental			
$A_0 - A_v$ (MHz)	9.3774 (21)	−8.6530 (24)	18.0749 (25)	9.7791 (57)	−7.591 (14)	−2.3552 (22)
$B_0 - B_v$ (MHz)	8.3278 (63)	3.412 (35)	7.820 (35)	−2.5964 (21)	−7.1924 (69)	−7.4263 (30)
$C_0 - C_v$ (MHz)	−0.52916 (26)	5.513 (37)	0.21197 (33)	3.19731 (33)	−0.19 (13)	0.26 (13)
			CCSD(T)/cc-pCVTZ			
$A_0 - A_v$ (MHz)	−11.49	11.56	15.06	8.74	−6.87	−2.75
$B_0 - B_v$ (MHz)	4.59	7.49	6.89	−2.54	−7.73	−7.69
$C_0 - C_v$ (MHz)	2.12	−0.58	0.13	3.17	8.39	−8.51
			B3LYP/6-311G+(2d,p)			
$A_0 - A_v$ (MHz)	9.02	−9.22	15.66	9.91	−7.04	−2.83
$B_0 - B_v$ (MHz)	6.92	1.08	6.72	−2.85	−7.25	−7.58
$C_0 - C_v$ (MHz)	−0.73	1.95	0.04	3.42	0.12	−0.29

[a] Frequency rounded to the nearest tenth of a wavenumber (cm^{-1}) as determined in this work unless cited

Dyad, ν_{11} (A_2, 564.4 cm^{-1}) and ν_8 (A_1, 608.7 cm^{-1})

By symmetry, fundamental band ν_{11} (A_2, 564.4 cm$^{-1, 14}$) has no IR intensity and its rotational constants have not been measured and reported previously by rotational spectroscopy. This mode corresponds to the asymmetric ring-puckering in which all C-atoms have large alternating out-of-pane motions. Like ν_{14}, the ν_{11} $^aR_{0,1}$ transitions initially progress to lower frequency at low K_a and exhibit a turn-around before progressing to higher frequency. This state is coupled to ν_8 (A_1, 608.6679444 (49) cm^{-1}),[8] which corresponds to the ring-breathing motion involving the symmetric bending of the C−S−C bonds. Unlike ν_{14} and ν_{11}, the low K_a transitions of ν_8 do not begin near the main ground state $^aR_{0,1}$ band, but rather begin lower in frequency due to the relatively large value of $C_0 - C_8$ (8.11061 (23) MHz). The smaller value of C_8 also means that as J increases, the distance between the $K_a = 0^+,1^-$ degenerate transitions and the ground state $K_a = 0^+,1^-$ transitions increases. Additionally, the separation between K_a's in the band-head is larger than in the ground state as indicated by the larger inertial defect ($\Delta_i = 0.515$ uÅ^2). The ν_{11} and ν_8 states are coupled by a G_a Coriolis-coupling coefficient. The combined fit of over 1100 distinct mm-wave transitions for each vibrational state and 2972 IR transitions from ref. 8 for ν_8 allowed for the determination of the rotational constants, the quartic centrifugal distortion terms, a G_a coefficient of −3150 (19) MHz and the ν_8 frequency of 608.6679415 (83) cm^{-1}, with the energy of ν_{11} energy fixed at the literature value of 564.4 cm^{-1}.[14] The inclusion of the G_a coefficient causes a deviation in the experimental vibration-rotation interaction values for the A_v rotational constant compared to the computationally predicted values. The averages, however, of the computational vibration-rotation interactions ($A_0 - (A_8+A_{11})/2$) for these states are 9.5 MHz (CCSD(T)) and 10.3 MHz (B3LYP) which do agree with the experimental average of 9.64 (13) MHz. The fitting of additional transitions may better determine these constants. The computed

vibration-rotation interaction values for $B_0 - B_v$ and $C_0 - C_v$ presented in Table 5.3 are in good agreement with their experimental values (within 4.4% CCSD(T) for both states, and with B3LYP they are within 14% for v_8 and 4.8% for v_{11}). While our determined frequency differs slightly from the previously published value,[8] the deviation is well within the combined reported errors of each of the values.

Triad v_{10} (A_2, 683.5 cm^{-1}), v_{13} (B_1, 712.1 cm^{-1}), and v_{21} (B_2, 753.5 cm^{-1})

Fundamental v_{10} (683.5 cm$^{-1,14}$), like v_{11}, has no IR intensity due to its A_2 symmetry. The vibrational motion for this state involves the asymmetric, large-amplitude C–H wagging motions while maintaining a C_2 symmetry axis. Like v_{14} and v_{11}, the low K_a transitions of v_{10}, are within the $^aR_{0,1}$ band of the ground state, and the transitions progress to lower frequency for a few K_a values before turning around and progressing toward higher frequency (Figure 5.3). The measurement and least-squares fit of 978 distinct transitions allowed for the determination of the rotational, the quartic centrifugal distortion constants for this state for the first time (Table 5.4). Fundamental v_{13} (B_1, 712.10378 (3) cm^{-1})[10] involves the symmetrical out-of-plane bending of the C−H bonds. The spectrum of this state behaves similarly to v_{14}, v_{11}, and v_{10}, again consistent with their negative inertial defects. A least-squares fit was achieved from 855 pure rotational transitions and 4315 previously reported high-resolution IR transitions.[10] This allowed for the determination of the rotational constants, the quartic centrifugal distortion constants, and a resultant fundamental frequency of 712.103743 (22) cm^{-1}. The v_{21} fundamental (B_2, 753.5 cm^{-1})[14] has a low predicted IR intensity and was not reported in the previous high-resolution IR study.[10] The v_{21} mode corresponds to the in-plane, asymmetric C−S stretching. In the spectrum of v_{21}, at low K_a the $^aR_{0,1}$

transitions progress to higher frequency as K_a increases, similar to ν_8. From the least-squares fit of 874 distinct transitions the rotational and quartic centrifugal distortion constants were determined. These three states are coupled to each other by two Coriolis terms, a G_b between ν_{10} and ν_{21} and a G_a between ν_{13} and ν_{21}. At this point in the analysis, the $G_{b10,21}$ term is 398 (28) MHz and the $G_{a13,21}$ term is −2090 (54) MHz with the ν_{10} energy fixed at the previously determined literature value of 683.5 cm^{-1},[14] the ν_{13} frequency is 712.103743 (22) cm^{-1}, as stated previously, and the ν_{21} frequency is 753.4942 (65) cm^{-1} in the present least squares fit. The sextic centrifugal-distortion constants were held constant to ground-state values for all three vibrational states in this triad. The spectroscopic constants and determined fundamental frequencies of these states are presented in Table 5.4.

Of the states in this triad, the vibration-rotation interaction terms for ν_{21} agree the least-well with the computationally predicted values (Table 5.3). While the other two states, ν_{10} and ν_{13} have computed $A_0 - A_\nu$ values that are within 12% and 53%, respectively, for both levels of theory presented, the $A_0 - A_{21}$ value is of the wrong sign and differs by up to 308% at the B3LYP level (227% from CCSD(T)). As noted for the interaction between ν_{11} and ν_8, the computational average vibration-rotation interactions $(A_0 - (A_{13}+A_{21})/2)$ for these states are 6.6 MHz (CCSD(T)) and 6.4 MHz (B3LYP) which do agree with the experimental average of 6.86 (25) MHz. This indicates influence from the incorporation of a G_a term between ν_{13} and ν_{21}. The $C_0 - C_\nu$ values for these three states, however, are within 14% or well below for both levels of theory presented. The predicted $B_0 - B_\nu$ for ν_{10} and ν_{13} are within 6.1 % for both levels of theory, though for ν_{21} there is less agreement. This suggests that despite the inclusion of coupling terms, this triad system is not yet well treated with the current Hamiltonian model, and further transition assignment and a

refinement of the coupling treatment is needed. There is also some indication of small local resonances in Loomis-Wood plots, which prompted the coupled state treatment, and these resonances are not yet well described by the model. The Coriolis parameters are thus currently primarily dependent on the global perturbation.

Table 5.4. Spectroscopic constants of the ν_{10}, ν_{13}, ν_{21} triad of thiophene vibrational states (A-reduction, I^r representation)

	ν_{10}, A_2	ν_{13}, B_1	ν_{21}, B_2
Freq. (cm^{-1})	[683.5][a]	712.103743 (22)	753.4942 (65)
$A_v^{(A)}$ (MHz)	8036.96090 (47)	8030.18 (18)	8039.28 (18)
$B_v^{(A)}$ (MHz)	5405.690 (11)	5412.76019 (36)	5415.140 (11)
$C_v^{(A)}$ (MHz)	3236.62199 (12)	3236.80984 (37)	3231.97233 (30)
Δ_J (kHz)	0.814577 (65)	0.832451 (59)	0.874727 (83)
Δ_{JK} (kHz)	−0.13294 (29)	−0.3125 (15)	−0.3347 (13)
Δ_K (kHz)	2.21519 (87)	2.3281 (27)	2.4012 (31)
δ_J (kHz)	0.299820 (32)	0.308627 (30)	0.328568 (39)
δ_K (kHz)	0.86490 (16)	0.8505 (23)	1.0589 (22)
Φ_J (Hz)	[0.000321][b]	[0.000321][b]	[0.000321][b]
Φ_{JK} (Hz)	[−0.00103][b]	[−0.00103][b]	[−0.00103][b]
Φ_{KJ} (Hz)	[−0.00172][b]	[−0.00172][b]	[−0.00172][b]
Φ_K (Hz)	[0.00448][b]	[0.00448][b]	[0.00448][b]
ϕ_J (Hz)	[0.000150][b]	[0.000150][b]	[0.000150][b]
ϕ_{JK} (Hz)	[−0.000107][b]	[−0.000107][b]	[−0.000107][b]
ϕ_K (Hz)	[0.00308][b]	[0.00308][b]	[0.00308][b]
$\nu_{10} \leftrightarrow \nu_{21}$ G_b (MHz)	398 (28)		
$\nu_{13} \leftrightarrow \nu_{21}$ G_a (MHz)		−2090 (54)	
$N_{lines\ MMW}$	978	855	874
$N_{lines\ IR}$		4315[c]	
σ_{MMW} (MHz)	0.046	0.051	0.035
σ_{IR} (cm^{-1})		0.00079	
κ	−0.0963	−0.0921	−0.0917
Δ_i (uÅ^2)	−0.228	−0.168	0.178

[a] Held constant to literature value[14]
[b] Held constant to ground state value
[c] Transitions from reference [10]

Pentad of ν_7, ν_{12}, ν_{20}, ν_9, $2\nu_{14}$

Fundamental ν_7 (A_1, 840.0094537 (64) cm^{-1})[8] is a ring-breathing motion involving in-plane wagging of the C2=C3 bonds. The spectrum of ν_7, behaves similarly to ν_8 and ν_{21}. The $^aR_{0,1}$ bands for ν_7 begin lower in frequency than the ν_8 $^aR_{0,1}$ bands. From our 841 mm-wave transitions and with the addition of 1947 high-resolution IR transitions from literature,[8] we were able to determine the rotational and quartic distortion constants and a vibrational frequency of 840.0107647 (97) cm^{-1}. This value is quite different from the previously determined value using the same IR transitions with a difference of 0.0013 cm^{-1},[8] which is likely due and the incorporation of a Fermi term (W) between ν_7 and $2\nu_{14}$, as well as the incomplete treatment of the pentad with its various coupling interactions. The spectroscopic constants of ν_7 along with the other states in the pentad, ν_{12}, ν_{20}, ν_9, $2\nu_{14}$, are presented in Table 5.5. The states ν_{12}, ν_{20}, ν_9, $2\nu_{14}$ have the symmetries B_1, B_2, A_2, and A_1, respectively. Coriolis-coupling terms include a G_b term between ν_7 and ν_{12} determined at 803.1 (3.0) MHz, a G_c term between ν_7 and ν_{20} at 1857.0 (10.0), and a G_a term between ν_7 and ν_9 which is held constant at the B3LYP predicted value of -1837 MHz.

The next higher two states in the pentad are ν_{12} (B_1, 866 cm^{-1})[14] and ν_{20} (B_2, 872.8 cm^{-1}),[14] which are strongly coupled through an a-type Coriolis interaction. Mode ν_{12} is the symmetrical H−C2=C3−H torsion. The ν_{20} vibrational motion is an in-plane, asymmetric C2=C3–C4 bend. The values of the coupling terms are $G_{a12,20} = 594.92$ (32) MHz and $G_a{}^K{}_{12,20} = -0.005178$ (29) MHz. Precise values of the vibrational frequencies of ν_{12} and ν_{20} are able to be determined due to the relationship with ν_7, resulting in values of 865.98970 (50) cm^{-1} for ν_{12} and 873.31026 (50) cm^{-1} for ν_{20}. The corresponding energy gap between the states is 7.32056 (71) cm^{-1}. This fairly small energy gap, in conjunction with a significant G_a term, yields very large resonances with ΔK_a

$= 0$ between ν_{12} and ν_{20}, as shown in Figure 5.4. Many of these interactions are strong enough that nominal interstate transitions, rotational transitions between one vibrational state and another, are observable.[24, 26, 40-41] We measured and assigned 19 nominal interstate transitions thus far. Their corresponding intrastate resonance transitions are substantially weakened relative to the other transitions in their series. Their intensity has transferred to the nominal interstate transitions, so that the overall intensity of the four interacting transitions (two intrastate and two nominal interstate) is conserved. The SPCAT spectral prediction software reliably predicts this intensity change. We note that the vibration-rotation interactions between the levels of theory presented seem inconsistent based on the mode assignments for these two states and will investigate this further as we continue the analysis of the pentad.

Table 5.5. Spectroscopic constants for ν_7, ν_{12}, ν_{20}, ν_9, and $2\nu_{14}$ pentad of thiophene vibrational states (A-reduction, I^r representation)

	ν_7, A_1	ν_{12}, B_1	ν_{20}, B_2	ν_9, A_2	$2\nu_{14}$, A_1
Freq. (cm^{-1})	840.0107647 (97)	865.98970 (50)	873.31026 (50)	900.01243 (80)	903.76750 (80)
$A_v^{(A)}$ (MHz)	8034.19879 (78)	8032.2175 (21)	8050.2480 (24)	8023.5200 (25)	7999.5626 (31)
$B_v^{(A)}$ (MHz)	5412.8321 (63)	5409.9369 (63)	5414.853 (35)	5410.445 (35)	5400.91201 (49)
$C_v^{(A)}$ (MHz)	3228.523 (37)	3236.30842 (24)	3230.266 (37)	3235.56729 (32)	3238.30917 (31)
Δ_J (kHz)	0.845501 (84)	0.82632 (11)	0.82659 (12)	0.83424 (15)	0.82394 (12)
Δ_{JK} (kHz)	-0.40184 (41)	-0.24169 (59)	-0.1098 (33)	-0.4162 (37)	-0.09689 (57)
Δ_K (kHz)	2.4491 (15)	2.3410 (28)	2.2087 (33)	2.2285 (50)	2.3723 (49)
δ_J (kHz)	0.317019 (40)	0.305890 (55)	0.306081 (70)	0.309322 (64)	0.303285 (61)
δ_K (kHz)	0.89511 (63)	0.90251 (45)	1.0165 (50)	0.8087 (50)	0.85759 (51)
Φ_J (Hz)	[0.000321][a]	[0.000321][a]	[0.000321][a]	[0.000321][a]	[0.000321][a]
Φ_{JK} (Hz)	[-0.00103][a]	[-0.00103][a]	[-0.00103][a]	[-0.00103][a]	[-0.00103][a]
Φ_{KJ} (Hz)	[-0.00172][a]	[-0.00172][a]	[-0.00172][a]	[-0.00172][a]	[-0.00172][a]
Φ_K (Hz)	[0.00448][a]	[0.00448][a]	[0.00448][a]	[0.00448][a]	[0.00448][a]
ϕ_J (Hz)	[0.000150][a]	[0.000150][a]	[0.000150][a]	[0.000150][a]	[0.000150][a]
ϕ_{JK} (Hz)	[-0.000107][a]	[-0.000107][a]	[-0.000107][a]	[-0.000107][a]	[-0.000107][a]
ϕ_K (Hz)	[0.00308][a]	[0.00308][a]	[0.00308][a]	[0.00308][a]	[0.00308][a]
$\nu_7 \leftrightarrow \nu_{12}$ G_b (MHz)	803.1 (3.0)				
$\nu_7 \leftrightarrow \nu_{20}$ G_c (MHz)	1857.0 (10.0)				
$\nu_7 \leftrightarrow \nu_9$ G_a (MHz)	[-1837][b]				
$\nu_7 \leftrightarrow 2\nu_{14}$ W (MHz)	[-8699][b]				
$\nu_{12} \leftrightarrow \nu_{20}$ G_a (MHz)		594.92 (32)			
$\nu_{12} \leftrightarrow \nu_{20}$ G_a^K (MHz)		-0.005178 (29)			
$\nu_{20} \leftrightarrow \nu_9$ G_b (MHz)			-662 (21)		
$\nu_{20} \leftrightarrow \nu_9$ G_b^K (MHz)			0.1347 (42)		
$\nu_9 \leftrightarrow 2\nu_{14}$ G_a^J (MHz)				-0.00319 (12)	
$\nu_9 \leftrightarrow 2\nu_{14}$ G_a^K (MHz)				-0.12550 (65)	
$\nu_9 \leftrightarrow 2\nu_{14}$ F_{bc} (MHz)				-0.2573 (39)	
$N_{lines\ MMW}$	841	500	633	401	415
N_{lines} IR	1947[c]				
σ_{MMW} (MHz)	0.062	0.082	0.073	0.218	0.304
σ_{IR} (cm^{-1})	0.000089				
κ	-0.0909	-0.0935	-0.0935	-0.0915	-0.0916
Δ_i (uÅ^2)	0.265	-0.177	0.341	-0.200	-0.686

[a] Held constant at the ground-state value, [b] Held constant at value calculated from B3LYP, [c] Transitions from reference [8]
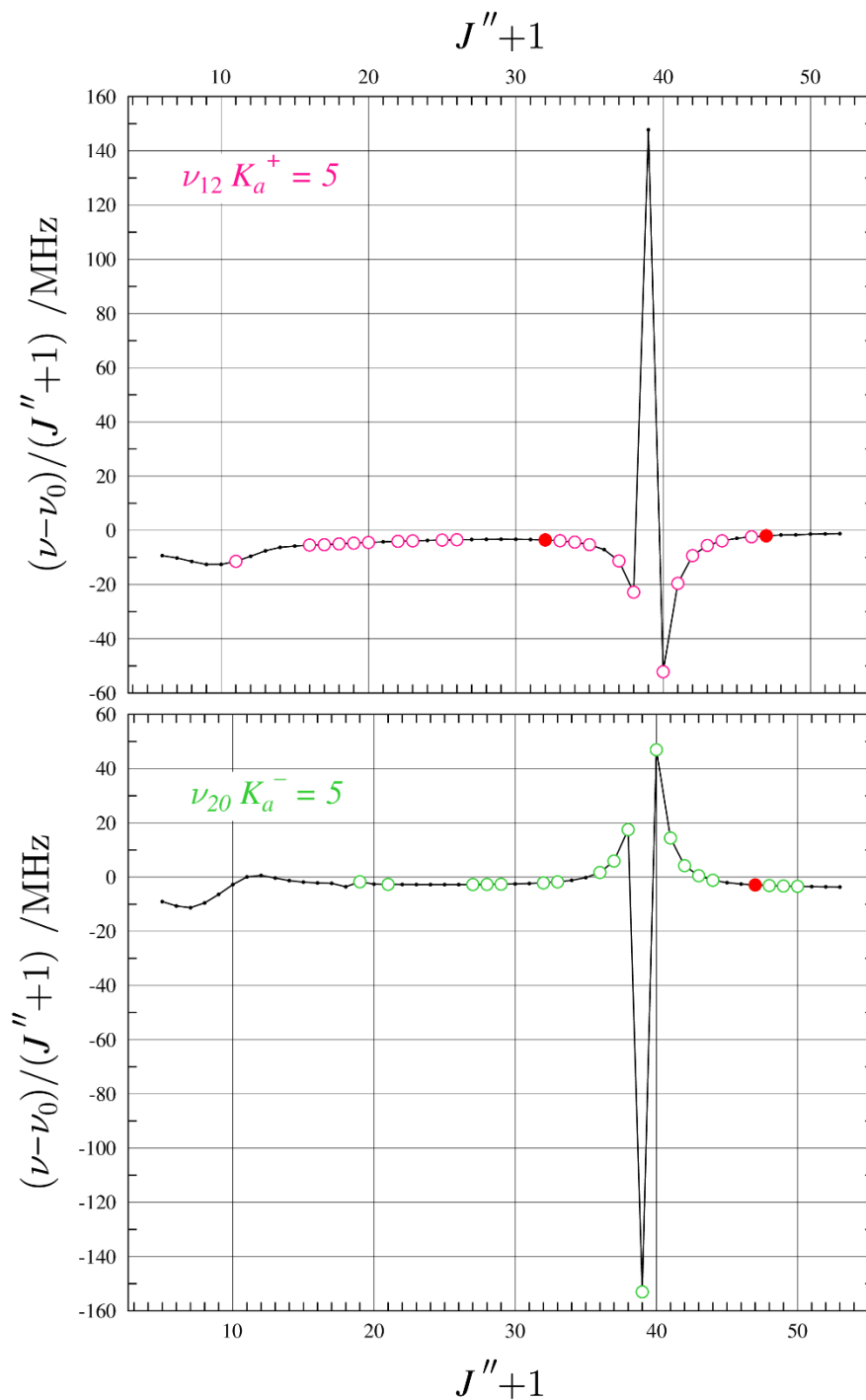
Figure 5.4. Resonance plots of thiophene vibrational states for $K_a^+ = 5$ of ν_{12} (above, pink), and $K_a^- = 5$ of ν_{20} (below, lime green) demonstrating the $\Delta K_a = 0$ coupling giving rise to the resonances. Open pink or lime green circles have $|(f_{obs.} - f_{calc.})/\delta f| < 3$ and filled, red circles have $|(f_{obs.} - f_{calc.})/\delta f| > 3$. The black dots/solid black line represent the predicted frequencies whose experimental frequencies have not been included in the least-squares fit.

The next two states in the pentad are ν_9 (A_2, 900 cm^{-1})[14] and $2\nu_{14}$ (A_1, 904 cm^{-1}),[14] which correspond to an asymmetric H−C2=C3−H torsion, and the second harmonic of the ν_{14} the symmetric ring-folding mode, respectively. The ν_9 vibrational state is coupled to ν_7 through a G_a term, which is currently held to its predicted value of −1837 MHz. It is further coupled to ν_{20} with a b-type Coriolis interaction. The coupling constant G_b is determined to be −662 (21) MHz and a higher-order term, G_b^K, is determined to be 0.1347 (42) MHz. State ν_9 is very close in energy to $2\nu_{14}$ (ΔE = 3.7551 (11) cm^{-1}), with which it has higher-order Coriolis interactions, which are discussed in the following paragraph. With all these Coriolis interactions, the frequency of ν_9 is established by the least-squares fit at 900.01243 (80) cm^{-1}, which is in excellent agreement with the previously reported value of 900 cm^{-1} for this IR inactive state.[14]

The first overtone of ν_{14}, $2\nu_{14}$, is the highest energy state involved in the pentad. This state was found using the linear extrapolation from the ground state and ν_{14}. Figure 5.5a shows the current experimentally determined rotational constants for v =1 and 2 of ν_{14} relative to the ground state (v = 0). Figure 5.5b shows the experimentally determined quartic distortion constants for v = 0, 1, and 2 of ν_{14} relative to the ground state and includes the extrapolated terms for comparison. Strong deviation from the predicted values is apparent for Δ_{JK} and Δ_K further indicating that some interactions between the states are not yet being well treated. Future work will involve fixing Δ_{JK} and Δ_K of $2\nu_{14}$ to extrapolated values and investigating if that allows other coupling terms to be incorporated into the fit and improvements to be made in the modeling of this state. Since $2\nu_{14}$ is an overtone, first-order Coriolis coupling terms (G_a, G_b, G_c) are not possible for the Coriolis interactions, and while the higher-order terms (G_a^J, G_a^K, F_{bc}, G_b^J etc.) are possible. So far, only the higher-order G_a terms between $2\nu_{14}$ and ν_9 have been utilized and determined. These higher-

order Coriolis terms are currently converging at values of $G_a{}^J = -0.00319$ (12), $G_a{}^K = -0.12550$ (65), $F_{bc} = -0.2573$ (39) all in MHz, with a frequency for $2\nu_{14}$ of 903.76750 (80) cm^{-1}. This frequency is also in satisfactory agreement with the reported experimental value of 904 cm^{-1}.[14] As $2\nu_{14}$ is an A_1 symmetry state, there is also a Fermi term (W) predicted with ν_7 which is held fixed in the current least-squares fit, as noted previously. There is also the possibility for higher-order G_b terms with ν_{12} (B_1 symmetry) and higher-order G_c terms with ν_{20} (B_2 symmetry).
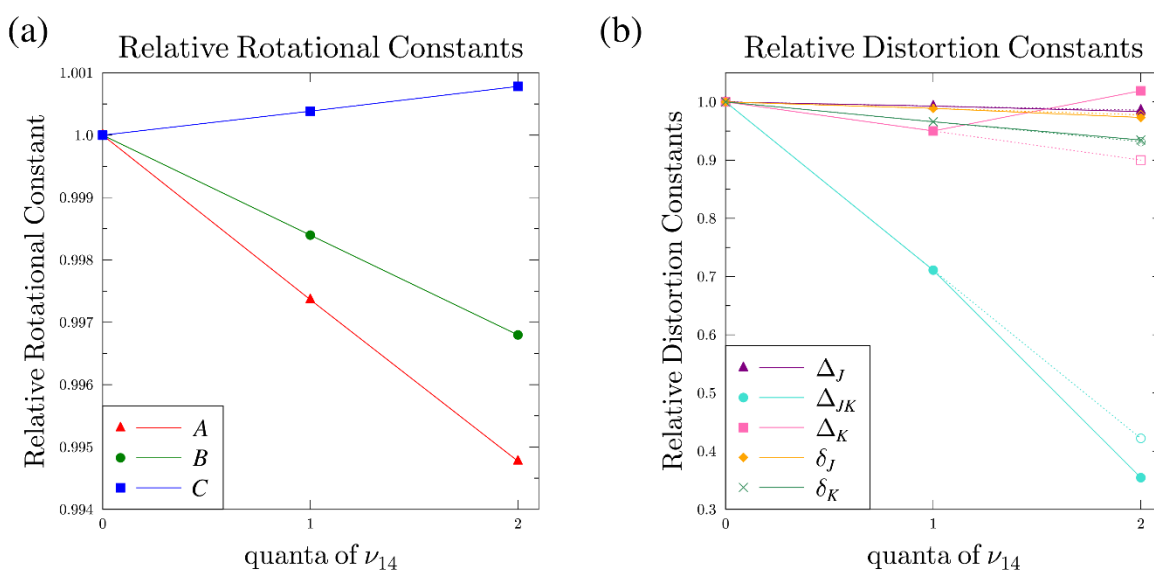
Figure 5.5. (a) Rotational constants and (b) quartic distortion terms for v = 0, 1, and 2 harmonics of ν_{14}, relative to the ground state (v = 0). The solid markers are experimentally determined values connected by solid lines. Linearly extrapolated values for the quartic distortion terms for v = 2 are displayed with unfilled markers connected to previous points with dashed lines.

The least-squares fit errors of ν_7, ν_{12}, ν_{20}, are outside the bounds of our standard measurement error (0.05 MHz) but within 2σ, which is promising for the early stages of this complex pentad fit. The higher errors on ν_9 and $2\nu_{14}$ ($\sigma > 0.2$ MHz) are not very large for this stage of the fitting process, but do indicate that the coupling interactions are not yet being

adequately treated. This is also confirmed in the Loomis-Wood plots, which exhibit strong curvature for many K_a's of these upper two states. There are local resonances predicted in ν_9 and $2\nu_{14}$, and some resonance transitions are currently measured and include in the least-squares fit, while many others are yet to be measured. Overall, this initial work on the pentad is very promising, especially the determination of all energies involved, and we anticipate that with additional transition assignment, the fixed or not-yet-determinable coupling interactions will be elucidated.

Vibrational States from 1000 cm^{-1} to 1163 cm^{-1}

There are many states above the pentad between 1000 and 1163 cm^{-1} for which transitions can be assigned. They include $\nu_{14}+\nu_{11}$, ν_6, and $\nu_{14}+\nu_8$, $2\nu_{11}$, $\nu_{14}+\nu_{10}$, and $\nu_{14}+\nu_{13}$. Their frequencies and spectroscopic constants are presented in Table 5.6. Though the ν_5 and ν_{19} vibrational states are in this energy region, they are separately discussed in the next section, since they are clearly a coupled dyad, as expected based on the previous IR work for these states.[10] The fundamentals ν_6, ν_5, and ν_{19} were initially predicted by using the previously published constants.[10] To utilize the previous constants, however, required conversion from III^r representation to I^r representation: (i) the rotational constants were converted from units of wavenumber into MHz, (ii) the rotational constants were converted to determinable constants, (iii) all quartic constants converted were from III^r into I^r, and (iv) the determinable constants were converted into their I^r representation values. The determinable constant equations and matrices for the conversion of the quartic distortion constant representation are from Chapter 8 of Gordy and Cooke's *Microwave Molecular Spectroscopy*.[42] The ν_6 mode is the C3–C4 stretching motion. The previous ro-vibrational study noted that ν_6 exhibited local resonances, indicated by large residuals at high J in

the K_c = 49-55 range.[10] The authors proposed a higher-order, c-type Coriolis perturbation with $\nu_{14}+\nu_{11}$. We attempted to include a G_c^K term which converged to a value of 0.0297 (13) MHz. As we resume assigning transitions for these states, we will continue to investigate the incorporation of additional higher-order coupling terms.

For the combination states and the $2\nu_{11}$ overtone, the rotational and quartic distortion constants from the ground state and respective vibrational states were utilized to extrapolate the constants for an initial prediction. With both rotational and quartic distortion constants predicted in this way, assigning transitions to the states was relatively straightforward. The quartic distortion terms for $2\nu_{11}$ and $\nu_{14}+\nu_{10}$ were predicted by extrapolation from fundamental state constants before coupling between the relevant lower energy states was employed, and the undeterminable quartic terms were held fixed to these values. As additional transitions are assigned for these states, hopefully these terms will become determinable. If they are not, the values will be re-predicted based on the current distortion terms for the lower energy states. The $\nu_{14}+\nu_{13}$ state was identified recently, and only 23 transitions have been assigned to this state thus far. Based on the energies of the next highest vibrational states above $\nu_{14}+\nu_{13}$, displayed with dashed grey lines in Figure 5.2, we fully expect that transitions for additional vibrational states will be measurable.

Table 5.6. Spectroscopic constants of thiophene vibrational states above 1000 cm^{-1} (A-reduction, I^r representation)

	$\nu_{14}+\nu_{11}$, B_2	ν_6, A_1	$\nu_{14}+\nu_8$, B_1	$2\nu_{11}$, A_1	$\nu_{14}+\nu_{10}$, B_2	$\nu_{14}+\nu_{13}$, A_1
Freq. (cm^{-1})	[1016.8][a]	1036.434222 (33)	[1061.082][a]	[1128.5][14,a]	[1135.9][a]	[1162.5][14,a]
$A_v^{(A)}$ (MHz)	7995.2024 (36)	8031.8158 (57)	8026.7782 (37)	7986.6 (11)	8015.7725 (25)	8011.8 (13)
$B_v^{(A)}$ (MHz)	5404.01261 (93)	5420.8611 (21)	5412.93741 (92)	5408.63 (52)	5396.9580 (16)	5401.19 (57)
$C_v^{(A)}$ (MHz)	3238.13330 (33)	3232.58195 (32)	3228.87331 (34)	3238.06175 (63)	3237.86486 (54)	3238.04330 (69)
Δ_J (kHz)	0.83160 (26)	0.84186 (84)	0.84150 (27)	0.8180 (42)	0.80826 (39)	0.82698 (14)
Δ_{JK} (kHz)	−0.15430 (86)	−0.2432 (25)	−0.24519 (93)	[−0.210][b*]	[−0.0527][b*]	[−0.223][b]
Δ_K (kHz)	1.9517 (61)	2.420 (11)	2.4680 (66)	[1.77][b*]	[2.097][b*]	[2.19][b]
δ_J (kHz)	0.30733 (13)	0.31360 (42)	0.31335 (14)	0.3012 (21)	0.29613 (21)	[0.305][b]
δ_K (kHz)	0.78359 (65)	0.9312 (10)	0.98803 (66)	0.609 (15)	0.8312 (14)	[0.802][b]
Φ_J (Hz)	[0.000321][c]	[0.000321][c]	[0.000321][c]	[0.000321][c]	[0.000321][c]	[0.000321][c]
Φ_{JK} (Hz)	[−0.00103][c]	[−0.00103][c]	[−0.00103][c]	[−0.00103][c]	[−0.00103][c]	[−0.00103][c]
Φ_{KJ} (Hz)	[−0.00172][c]	[−0.00172][c]	[−0.00172][c]	[−0.00172][c]	[−0.00172][c]	[−0.00172][c]
Φ_K (Hz)	[0.00448][c]	[0.00448][c]	[0.00448][c]	[0.00448][c]	[0.00448][c]	[0.00448][c]
ϕ_J (Hz)	[0.000150][c]	[0.000150][c]	[0.000150][c]	[0.000150][c]	[0.000150][c]	[0.000150][c]
ϕ_{JK} (Hz)	[−0.000107][c]	[−0.000107][c]	[−0.000107][c]	[−0.000107][c]	[−0.000107][c]	[−0.000107][c]
ϕ_K (Hz)	[0.00308][c]	[0.00308][c]	[0.00308][c]	[0.00308][c]	[0.00308][c]	[0.00308][c]
$\nu_{14}+\nu_{11} \leftrightarrow \nu_6\ G_c^K$ (MHz)	0.0297 (13)					
$N_{lines\ MMW}$	200	155	217	56	73	23
$N_{lines\ IR}$		1645[d]				
σ_{MMW} (MHz)	0.073	0.084	0.059	0.068	0.058	0.096
σ_{IR} (cm^{-1})		0.0010627				
κ	−0.0894	−0.0881	−0.0896	−0.0858	−0.0962	−0.0937
Δ_i (uÅ^2)	−0.658	0.188	0.192	−0.643	−0.605	−0.572

[a] Calculated from addition of the fundamental frequencies of the two states involved and held constant, or held constant to experimental value.[14]
[b] Extrapolated from the ground state and excited vibrational states involved and held constant
  [b*] indicates the values were predicted before coupling terms were incorporated into the involved lower-energy states
[c] Held constant to ground state value
[d] Transitions from reference 10

Dyad, ν_5 (A_1, 1081.5 cm^{-1}) and ν_{19} (B_2, 1083.97 cm^{-1})

The vibrational states of ν_5 (A_1) and ν_{19} (B_2) correspond to the symmetric and asymmetric H–C=C–H scissoring motion, respectively. These two states were previously analyzed both as single states and as a coupled dyad by Hegelund *et al.*[10] When treated as a dyad, frequencies of 1081.54328 (5) cm^{-1} for ν_5 and 1083.96911 (6) cm^{-1} for ν_{19} where determined when including a G_c term held fixed to a computationally predicted value of 772.6 MHz, and an F_{ab} term determined at -3.59 (2) MHz. The predicted spectra, generated from the previously published rotational constants and distortion terms, allowed for initial assignment of ν_5 and ν_{19} in the mm-wave region, and we have so far assigned over 160 distinct transitions to each state. We utilized the previously published transitions from Hegelund *et al.*[10] in combination with our mm-wave transitions to determine the following spectroscopic constants: G_c coefficient of 810.9 (6.0) MHz, F_{ab} term of -2.07 (22) MHz, ν_5 frequency of 1081.544113 (47) cm^{-1}, ν_{19} frequency of 1083.968984 (43) cm^{-1}, in addition to fitted values of the rotational constants and of the Δ_J, δ_J , and δ_K distortion terms. Unfit quartic and the sextic distortion terms are held fixed to ground-state values. These two states each have a relatively large error in the least-squares fit, especially ν_5 which has a σ_{MMW} of 0.159 MHz and a σ_{IR} of 0.0094 cm^{-1} (much greater than the 0.001 cm^{-1} estimated uncertainty for these transitions) indicating the interaction between the states is not yet being accurately modeled. Nonetheless, the values determined by our least-squares fit are similar enough to the values from the previous work to signal encouraging initial progress on this dyad.

Table 5.7. Spectroscopic constants of the ν_5 and ν_{19} dyad of thiophene vibrational states (A-reduction, I^r representation)

	ν_5, A_1	ν_{19}, B_2
Freq. (cm^{-1})	1081.544113 (47)	1083.968984 (43)
$A_v^{(A)}$ (MHz)	8049.186 (14)	8043.9501 (22)
$B_v^{(A)}$ (MHz)	5425.4571 (69)	5425.6910 (30)
$C_v^{(A)}$ (MHz)	3235.97 (13)	3235.52 (13)
Δ_J (kHz)	0.85125 (70)	0.84274 (63)
Δ_{JK} (kHz)	[−0.273][a]	[−0.273][a]
Δ_K (kHz)	[2.33][a]	[2.33][a]
δ_J (kHz)	0.32217 (38)	0.30919 (38)
δ_K (kHz)	0.9780 (32)	0.9492 (32)
Φ_J (Hz)	[0.000321][a]	[0.000321][a]
Φ_{JK} (Hz)	[−0.00103][a]	[−0.00103][a]
Φ_{KJ} (Hz)	[−0.00172][a]	[−0.00172][a]
Φ_K (Hz)	[0.00448][a]	[0.00448][a]
ϕ_J (Hz)	[0.000150][a]	[0.000150][a]
ϕ_{JK} (Hz)	[−0.000107][a]	[−0.000107][a]
ϕ_K (Hz)	[0.00308][a]	[0.00308][a]
G_c (MHz)	810.9 (6.0)	
F_{ab} (MHz)	−2.07 (22)	
$N_{lines\ MMW}$	164	160
$N_{lines\ IR}$	1204[b]	1507[b]
σ_{MMW} (MHz)	0.159	0.077
σ_{IR} (cm^{-1})	0.0094	0.0019
κ	−0.0902	−0.0890
Δ_i (uÅ^2)	0.240	0.224

[a] Held constant to ground state value
[b] Transitions from reference [10]

Coriolis-Coupling Terms

The Coriolis-coupling terms presented were initially predicted from the computed Coriolis zeta constants (B3LYP/6-311G+(2d,p)) using equation 5.1

$$G_x \approx 2 * \zeta_x * X_e \tag{5.1}$$

where G_x is the Coriolis-coupling constant, ζ_x is the computationally predicted Coriolis zeta value between the two states of interest, where x can be the a-, b-, or c-principal axis, and X_e is the predicted equilibrium rotational constant for the corresponding principal axis.[43] Table 5.8 shows the comparison between the predicted Coriolis-coupling constants and the values determined

experimentally. While some values are quite close to the predicted value, for example G_b between ν_7 and ν_{12}, other interactions are much smaller than the predicted value, such as G_a between ν_{12} and ν_{20}, which is expected to be relatively well determined by the fitting of nominal interstate transitions. At this current stage of the global least-squares fit analysis, it is not possible to draw conclusions about the accuracy of the computational predictions due to the incomplete assignment of transitions, combined with the high error of the global fit ($\sigma_{MMW} > 0.05$ MHz) and the known inaccurate modeling for a number of the vibrational states.

Table 5.8 Predicted and Experimental Coriolis coupling terms for vibrational states of thiophene

Coriolis-coupling Constant	B3LYP[a]	Experimental
$\nu_{11} \leftrightarrow \nu_8\ G_a$ (MHz)	−2967	−3150 (19)
$\nu_{10} \leftrightarrow \nu_{21}\ G_b$ (MHz)	2611	398 (28)
$\nu_{13} \leftrightarrow \nu_{21}\ G_a$ (MHz)	−2585	−2090 (54)
$\nu_7 \leftrightarrow \nu_{12}\ G_b$ (MHz)	797	803.1 (3.0)
$\nu_7 \leftrightarrow \nu_{20}\ G_c$ (MHz)	2052	1857.0 (10.0)
$\nu_7 \leftrightarrow \nu_9\ G_a$ (MHz)	−1837	[−1837][a]
$\nu_{12} \leftrightarrow \nu_{20}\ G_a$ (MHz)	1003	594.92 (32)
$\nu_{20} \leftrightarrow \nu_9\ G_b$ (MHz)	−400	−662 (21)
$\nu_5 \leftrightarrow \nu_{19}\ G_c$ (MHz)	756	810.9 (6.0)

[a] B3LYP/6-311G+(2d,p)
[b] Held constant to B3LYP/6-311 predicted value

FUTURE WORK

The future work of this project involves continuing to add transitions to the least-squares fit for all vibrational states, as has been noted throughout this Chapter. Based on the intensities of the lines already observed, we are optimistic that significant additional lines can be observed, measured, and assigned, even for the highest states that have been described here. The treatment of the couplings present in the pentad of thiophene is incomplete, and ongoing work will especially focus on this aspect of the project. The dyad fit of ν_5 and ν_{19} is also unsatisfactory at this time, and continued investigation into these states is planned. The extrapolated values for $2\nu_{11}$ and

$\nu_{14}+\nu_{10}$ may be determined with the addition of more transitions to the least-squares fit, or their fixed values will be re-extrapolated from the current fit values and held constant. Transitions for the $\nu_{14}+\nu_{13}$ state were assigned and least-squares fit, prompting investigation for the vibrational states even higher in energy, as noted previously. These additional states should be well predicted by extrapolation from the ground state and lower lying states of their component excited vibrations. The next currently unidentified fundamental is ν_{18} (B_2, 1255.8 cm^{-1}),[14] for which we also plan to search. While there remains a significant amount of analysis left to be done, the work thus far provides a strong foundation for the continued global analysis of the excited vibrational states of thiophene.

ACKNOWLEDGMENTS

REFERENCES

1. Ogata, T.; Kozima, K., Microwave spectrum, barrier height to internal rotation of methyl group of 3-methylthiophene, and dipole moments of 3-methylthiophene and thiophene. *J. Mol. Spectrosc.* **1972**, *42* (1), 38-46.

2. Bak, B.; Christensen, D.; Rastrup-Andersen, J.; Tannenbaum, E., Microwave Spectra of Thiophene, 2- and 3-Monodeutero, 3,3′-Dideutero, and Tetradeuterothiophene. Structure of the Thiophene Molecule. *J. Chem. Phys.* **1956**, *25* (5), 892-896.

3. Bak, B.; Christensen, D.; Hansen-Nygaard, L.; Rastrup-Andersen, J., The structure of thiophene. *J. Mol. Spectrosc.* **1961**, *7* (1), 58-63.

4. Pozdeev, N. M.; Gunderova, L. N., Microwave spectra of thiophane and thiophene. *Khim. Seraorg. Soedin., Soderzh. Neftyakh Nefteprod.* **1972**, *9*, 101-6.

5. Pozdeev, N. M.; Panikovskaya, L. I.; Lisovskaya, L. N.; Mamleev, A. K. Rotation constants and dipole moment of thiophene, *Primen. Mol. Spektrosk. Khim., Sb. Dokl. Sib. Soveshch., 3rd, Krasnoyarsk, USSR*, 1966; 26-7.

6. White, W. F. *Microwave Spectra of Some Sulfur and Nitrogen Compounds*; NASA: Hampton, VA, 1974; pp 99-100.

7. Kretschmer, U.; Stahl, W.; Dreizler, H., The Rotational Spectra of the ^{32}S-, ^{33}S-, and ^{34}S-Isotopomers of Thiophene. *Z. Naturforsch., A: Phys. Sci.* **1993**, *48* (5-6), 733-736.

8. van Wijngaarden, J.; Van Nest, S. J.; van Dijk, C. W.; Tokaryk, D. W., Rovibrational spectrum and analysis of the ν_8 band of thiophene using infrared synchrotron radiation. *J. Mol. Spectrosc.* **2010**, *259* (1), 56-59.

9. van Wijngaarden, J.; Tokaryk, D. W., High resolution synchrotron-based study and analysis of the ν_{14} band of thiophene. *J. Mol. Spectrosc.* **2008**, *251* (1), 365-368.

10. Hegelund, F.; Wugt Larsen, R.; Palmer, M. H., The high-resolution infrared spectrum of thiophene between 600 and 1200cm^{-1}: A spectroscopic and theoretical study of the fundamental bands ν_6, ν_7, ν_{13}, and the *c*-Coriolis interacting dyad ν_5, ν_{19}. *J. Mol. Spectrosc.* **2008**, *247* (1), 100-114.

11. Pankoke, B.; Yamada, K. M. T.; Winnewisser, G., High resolution IR-spectra of furan and thiophene. *Z. Naturforsch., A: Phys. Sci.* **1994**, *48* (12), 1193-202.

12. Coblentz, W. W., *Investigations of Infrared Spectra Part 1 - Infra-Red Absorption Spectra*. Carnegie Institution of Washington: 1905.

13. Bonino, G. B.; Manzoni-Ansidei, R., The Raman Spectra of Thiophenes and Furans and a few of their derivatives. *Z. Physik. Chem.* **1934**, *B25*, 327-347.

14. Klots, T. D.; Chirico, R. D.; Steele, W. V., Complete vapor phase assignment for the fundamental vibrations of furan, pyrrole and thiophene. *Spectrochim. Acta A* **1994**, *50* (4), 765-795.

15. Singh, D. K.; Srivastava, S. K.; Ojha, A. K.; Asthana, B. P., Vibrational study of thiophene and its solvation in two polar solvents, DMSO and methanol by Raman spectroscopy combined with ab initio and DFT calculations. *J. Mol. Struct.* **2008**, *892* (1), 384-391.

16. Wu, X.-F.; Zheng, X.; Wang, H.-G.; Zhao, Y.-Y.; Guan, X.; Phillips, D. L.; Chen, X.; Fang, W., A resonance Raman spectroscopic and CASSCF investigation of the Franck–Condon region structural dynamics and conical intersections of thiophene. *J. Chem. Phys.* **2010**, *133* (13), 134507.

17. Barnes, R.; Liddel, U.; Williams, V., Infrared Spectroscopy. Industrial Applications. *Ind. Eng. Chem. Anal. Ed.* **1943**, *15* (11), 659-709.

18. Thompson, H. W.; Temple, R. B., The infra-red spectra of furan and thiophen. *Trans. Faraday Soc.* **1945**, *41*, 27-34.

19. Hidalgo, A., Spectres d'absorption infrarouge du thiophène et de dérivés mono et disubstitués (attribution des modes de vibration aux bandes enregistrées). *J. Phys. Radium* **1955**, *16* (5), 366-372.

20. Rico, M.; Orza, J. M.; Morcillo, J., Fundamental vibrations of thiophene and its deuterated derivatives. *Spectrochim. Acta* **1965**, *21* (4), 689-719.

21. Loisel, J.; Pinan-Lucarre, J.-P.; Lorenzelli, V., Spectres infrarouges du furanne et du thiophéne aux basses températures. *J. Mol. Struct.* **1973**, *17* (2), 341-354.

22. Kobayashi, K.; Takamura, K.; Sakai, Y.; Tsunekawa, S.; Odashima, H.; Ohashi, N., The Microwave Spectroscopy of Methyl Formate in the Second Torsional Excited State. *Astrophys. J., Suppl. Ser.* **2013**, *205* (1), 9.

23. Fukuyama, Y.; Odashima, H.; Takagi, K.; Tsunekawa, S., The Microwave Spectrum of Propionitrile (C₂H₅CN) in the Frequency Range from 8 to 200 GHz. *Astrophys. J., Suppl. Ser.* **1996**, *104*, 329.

24. Zdanovskaia, M. A.; Esselman, B. J.; Woods, R. C.; McMahon, R. J., The 130–370 GHz Rotational Spectrum of Phenyl Isocyanide (C₆H₅NC). *J. Chem. Phys.* **2019**, *151* (2), 024301.

25. Esselman, B. J.; Amberger, B. K.; Shutter, J. D.; Daane, M. A.; Stanton, J. F.; Woods, R. C.; McMahon, R. J., Rotational spectroscopy of pyridazine and its isotopologs from 235–360 GHz: Equilibrium structure and vibrational satellites. *J. Chem. Phys.* **2013**, *139* (22), 224304.

26. Kisiel, Z.; Pszczółkowski, L.; Drouin, B. J.; Brauer, C. S.; Yu, S.; Pearson, J. C.; Medvedev, I. R.; Fortman, S.; Neese, C., Broadband rotational spectroscopy of acrylonitrile: Vibrational energies from perturbations. *J. Mol. Spectrosc.* **2012**, *280*, 134-144.

27. Kisiel, Z.; Pszczółkowski, L.; Medvedev, I. R.; Winnewisser, M.; De Lucia, F. C.; Herbst, E., Rotational spectrum of trans–trans diethyl ether in the ground and three excited vibrational states. *J. Mol. Spectrosc.* **2005**, *233* (2), 231-243.

28. Pickett, H. M., The fitting and prediction of vibration-rotation spectra with spin interactions. *J. Mol. Spectrosc.* **1991**, *148* (2), 371-377.

29.   Kisiel, Z. PROSPE - Programs for ROtational SPEctroscopy. http://info.ifpan.edu.pl/~kisiel/prospe.htm

30. Frisch, M. J.; Trucks, G. W.; Schlegel, H. B.; Scuseria, G. E.; Robb, M. A.; Cheeseman, J. R.; Scalmani, G.; Barone, V.; Petersson, G. A.; Nakatsuji, H.; Li, X.; Caricato, M.; Marenich, A. V.; Bloino, J.; Janesko, B. G.; Gomperts, R.; Mennucci, B.; Hratchian, H. P.; Ortiz, J. V.; Izmaylov, A. F.; Sonnenberg, J. L.; Williams-Young, D.; Ding, F.; Lipparini, F.; Egidi, F.; Goings, J.; Peng, B.; Petrone, A.; Henderson, T.; Ranasinghe, D.; Zakrzewski, V. G.; Gao, J.; Rega, N.; Zheng, G.; Liang, W.; Hada, M.; Ehara, M.; Toyota, K.; Fukuda, R.; Hasegawa, J.; Ishida, M.; Nakajima, T.; Honda, Y.; Kitao, O.; Nakai, H.; Vreven, T.; Throssell, K.; Montgomery, J. A., Jr.; Peralta, J. E.; Ogliaro, F.; Bearpark, M. J.; Heyd, J. J.; Brothers, E. N.; Kudin, K. N.; Staroverov, V. N.; Keith, T. A.; Kobayashi, R.; Normand, J.; Raghavachari, K.; Rendell, A. P.; Burant, J. C.; Iyengar, S. S.; Tomasi, J.; Cossi, M.; Millam, J. M.; Klene, M.; Adamo, C.; Cammi, R.; Ochterski, J. W.; Martin, R. L.; Morokuma, K.; Farkas, O.; Foresman, J. B.; Fox, D. J. Gaussian 16, Revision B.01, Gaussian, Inc., Wallingford CT, 2016.

31. Schmidt, J.; Polik, W., WebMO Enterprise. *WebMO LLC, Holland, MI USA* **2013**.

32. Pople, J. A.; Head-Gordon, M.; Raghavachari, K., Quadratic Configuration Interaction. A General Technique for Determining Electron Correlation Energies. *J. Chem. Phys.* **1987**, *87* (10), 5968-5975.

33. Woon, D. E.; Dunning, T. H., Gaussian basis sets for use in correlated molecular calculations. V. Core-valence basis sets for boron through neon. *J. Chem. Phys.* **1995**, *103* (11), 4572.

34. Woon, D. E.; Dunning, T. H., Gaussian basis sets for use in correlated molecular calculations. III. The atoms aluminum through argon. *J. Chem. Phys.* **1993**, *98* (2), 1358-1371.

35. Dunning, T. H., Gaussian basis sets for use in correlated molecular calculations. I. The atoms boron through neon and hydrogen. *J. Chem. Phys.* **1989**, *90* (2), 1007-1023.

36. Mills, I. M., Vibration-Rotation Structure in Asymmetric- and Symmetric-Top Molecules. In *Molecular Spectroscopy: Modern Research*, Rao, K. N.; Mathews, C. W., Eds. Academic Press: New York, 1972; Vol. 1, pp 115-140.

37. Schneider, W.; Thiel, W., Anharmonic Force Fields from Analytic Second Derivatives: Method and Application to Methyl Bromide. *Chem. Phys. Lett.* **1989**, *157* (4), 367-373.

38. Stanton, J. F.; Lopreore, C. L.; Gauss, J., The equilibrium structure and fundamental vibrational frequencies of dioxirane. *J. Chem. Phys.* **1998**, *108* (17), 7190-7196.

39. J. F. Stanton, J. Gauss, M. E. Harding, and P. G. Szalay, with contributions from A. A. Auer, R. J. Bartlett, U. Benedikt, C. Berger, D. E. Bernholdt, Y. J. Bomble, L. Cheng, O. Christiansen, M. Heckert, O. Heun, C. Huber, T.-C. Jagau, D. Jonsson, J. Jusélius, K. Klein, W. J. Lauderdale, F. Lipparini, D. A. Matthews, T. Metzroth, L. A. Mück, D. P. O'Neill, D. R. Price, E. Prochnow, C. Puzzarini, K. Ruud, F. Schiffmann, W. Schwalbach, C. Simmons, S. Stopkowicz, A. Tajti, J. Vázquez, F. Wang, J. D. Watts, and the integral packages MOLECULE (J. Almlöf and P. R. Taylor), PROPS (P. R. Taylor), ABACUS (T. Helgaker, H. J. Aa. Jensen, P. Jørgensen, and J. Olsen), and ECP routines by A. V. Mitin and C. van Wüllen, CFOUR, Coupled-Cluster Techniques for Computational Chemistry, v.2.0 (2014), http://www.cfour.de.

40. Zdanovskaia, M. A.; Esselman, B. J.; Lau, H. S.; Bates, D. M.; Woods, R. C.; McMahon, R. J.; Kisiel, Z., The 103 – 360 GHz Rotational Spectrum of Benzonitrile, the First Interstellar Benzene Derivative Detected by Radioastronomy. *J. Mol. Spectrosc.* **2018**, *351*, 39-48.

41. Dorman, P. M.; Esselman, B. J.; Woods, R. C.; McMahon, R. J., An analysis of the rotational ground state and lowest-energy vibrationally excited dyad of 3-cyanopyridine: Low

symmetry reveals rich complexity of perturbations, couplings, and interstate transitions. *J. Mol. Spectrosc.* **2020**, *373*, 111373.

42. Gordy, W.; Cook, R., *Microwave Molecular Spectra*. 3rd. ed.; Wiley Interscience: New York, 1984; Vol. XVIII.

43. Dorman, P. M.; Esselman, B. J.; Park, J. E.; Woods, R. C.; McMahon, R. J., Millimeter-wave spectrum of 4-cyanopyridine in its ground state and lowest-energy vibrationally excited states, ν_{20} and ν_{30}. *J. Mol. Spectrosc.* **2020**, *369*, 111274.

Appendix A:

Ro-vibrational Spectra from the Far-IR Beamline at the Canadian Light Source

Includes the work of several collaborators:

Brian J. Esselman, Samuel M. Kougias, Samuel A. Wood

R. Claude Woods, Robert J. McMahon

of the University of Wisconsin–Madison

and

Brant E. Billinghurst and Jianbao Zhao

of the Canadian Light Source

(a)

(b)

(c)
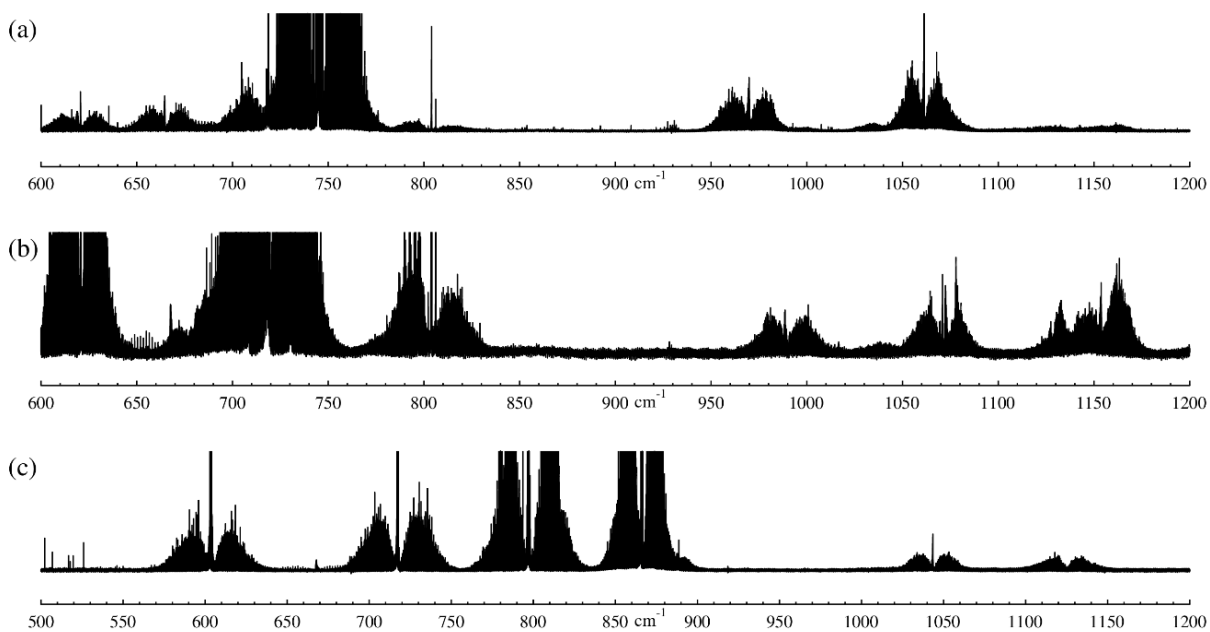
INTRODUCTION

As noted in Chapter 3 of this thesis, we learned about the Canadian Light Source (CLS), particularly their Far-IR beamline, while at the International Symposium on Molecular Spectroscopy.[1] The rotational spectroscopy of the vibrational states of 4-cyano-1,2-butadiene, hydrazoic acid (HN_3), and deuterio-hydrazoic acid (DN_3), were three projects that our group had already made significant progress on, but would benefit immensely from ro-vibrational data. The vibrational spectroscopy of these molecules was submitted as two proposals to the Canadian Light Source August 2019, and both proposals were awarded beamtime.[2-3] Due to the COVID-19 pandemic, we have not been able to travel to conduct our experiments, but we have been able to run experiments remotely with the beamline staff Brant Billinghurst and Jianbao Zhao in August and September 2020 and February 2021. In this appendix, we present the current work that has resulted from this collaboration. Spectrometer-specific experimental details for each experiment are contianed in the notes and raw data files. Visualization of the spectra and figure generation was performed with Kisiel's SVIEW_L.[4]

4-CYANO-1,2-BUTADIENE

The analysis of the rotational spectroscopy of 4-cyano-1,2-butadiene ($H_2C=C=CH-CH_2CN$) is presented in Chapter 3 of this thesis. That investigation indicated that the ro-vibrational spectrum of the torsional mode, ν_{27}, would be useful for the analysis of the coupling between the ground state and the torsional mode, as well as the couplings with other harmonics of the torsional mode.

August & September 2020 Beamtime

For our first remote experiments in 2020, Samuel Kougias worked to prepare three samples for shipping to CLS: Vial 1) a pure sample of 4-cyano-1,2-butadiene preserved for work on the synthesis of cyanobutadiene isomers[5] in May 2019 and redistilled in Feb. 2020, Vial 2) a new sample synthesized in July-Aug. 2020, Vial 3) a sample generated from multiple small-scale reactions (for screening) that had 4-cyano-1,2-butadiene present, which was purified by flash-chromatography and vacuum distillation to remove other isomers of cyanobutadiene. Due to the expediency needed to ship the samples to Canada, these samples were not checked for purity in our rotational spectrometer. Additionally, shipping complications did not allow our sample to arrive in a timely manner, which was problematic because the samples had been shipped on ice packs.

The spectra collected at the various experimental pressures we tested are shown from 40-400 cm^{-1} in Figure A.1, and from $40 - 150$ cm^{-1} in Figure A.2. The first sample we used was from vial 1 at 319 mTorr and about room temperature (Figure A.1,2 a). This sample showed some features, particularly around 320 cm^{-1}, but they did not appear well resolved. We suspected a lower pressure might help resolve this issue and make some of the features clearer since we expected the spectrum to be very dense from our initial predictions, so we tried 51 mTorr from Vial 1 and Vial 2 (Figure A.1,2 b), and then even lower at 15 mTorr from Vial 2 (Figure A.1/2 c). Neither of these tests revealed distinctive band structures. When we finished our August time, our next steps were to try cooling the cell to try and decrease the number of populated rotational levels that are populated and increase population in the lower energy vibrational states. Therefore, during our time in September, we initially tried to run the sample with the cell at −45 ºC, a value chosen based on the approximate cell temperature of our instrument from thermocouple readings, but

unfortunately the pressure was limited to 18 mTorr, and given our previous experience with the 15

mTorr sample we did not suspect that would be a useful spectrum. When the cell returned to room

temperature (294.45 – 294.85 K), it was filled to 600 mTorr (dropped to 575 mTorr by morning)

(Figure A.1,2 d) which does display more spectral features than the previous three spectra. The

spectral features were not well resolved, and no features were visible in the $40 - 60$ cm^{-1} region,

where the ν_{27} torsional mode band is predicted (and expected based on the coupling analysis

presented in Chapter 3). The data we obtained in August and September did not provide strong

indication that we collected a viable spectrum of 4-cyano-1,2-butadiene.
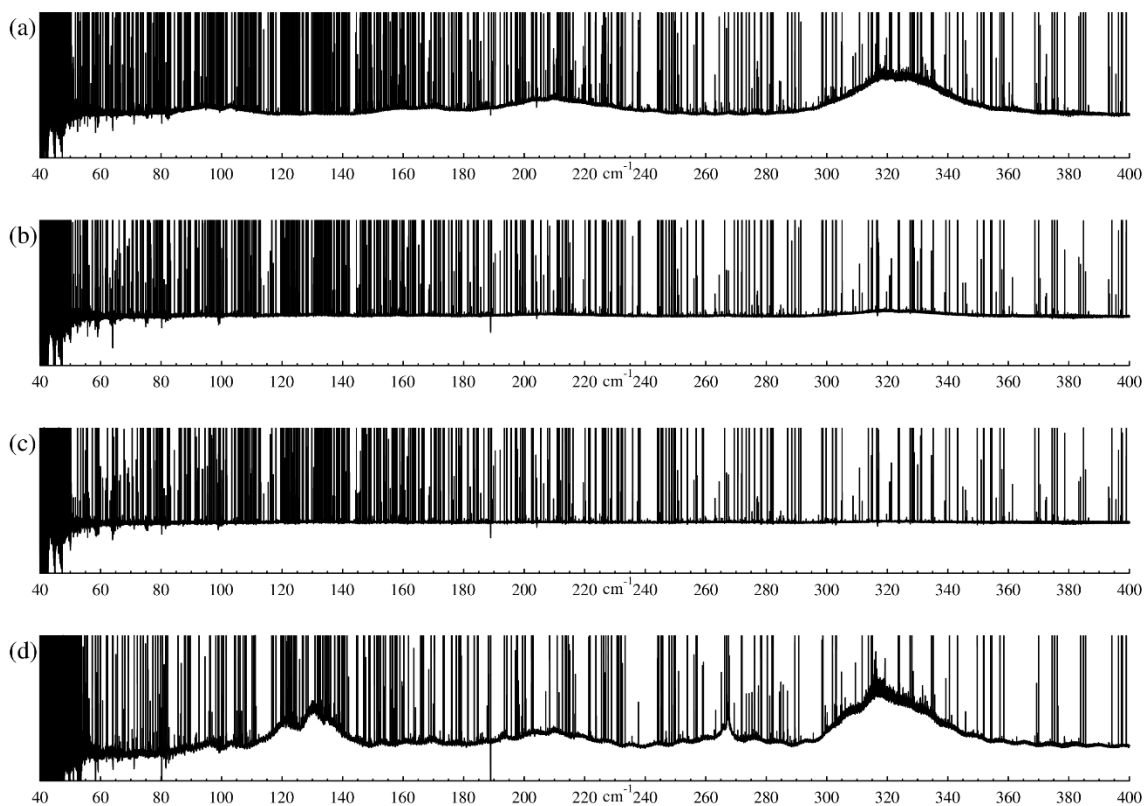
Figure A.1. Four infrared spectra displayed from $40 - 400$ cm^{-1} (a) 319 mTorr, 154 avg. scans (b) 51 mTorr, 160 avg. scans (c) 15 mTorr, 195 avg. scans (d) 600 mTorr, 225 avg. scans.
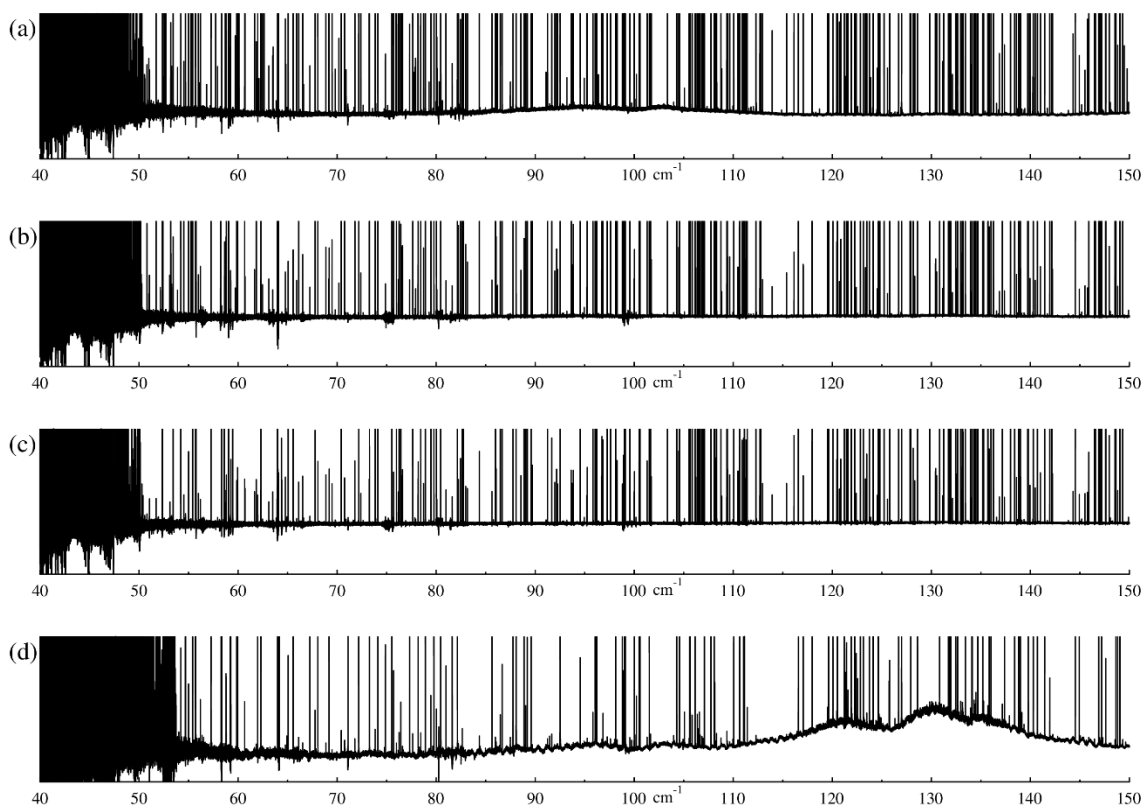
Figure A.2. Four infrared spectra displayed from $40 - 150$ cm^{-1} (a) 319 mTorr, 154 avg. scans (b) 51 mTorr, 160 avg. scans (c) 15 mTorr, 195 avg. scans (d) 600 mTorr , 225 avg. scans.

February 2021 Beamtime

In February 2021, beamtime was awarded from Feb 2 to Feb 8, 2021. Prior to the beamtime, samples of 4-cyano-1,2-butadiene were synthesized (Samuel M. Kougias) and shipped (Samuel A. Wood) to CLS in January 2021. The samples were tested in our rotational spectrometer by Brian J. Esselman and Samuel Kougias to verify them before they were sent to CLS. The ATR-IR spectra for 4-cyano-1,2-butadiene published in the supporting information of the synthetic work by Kougias *et al.*,[5] indicated a strong peak at 852.4 cm^{-1}, so our next experiments at CLS sought to confirm our sample arrived properly by scanning in a higher frequency range, $400 - 1200$ cm^{-1}, than used for this sample before. The first sample tested was, 2021 vial 1, and the first overnight scans revealed a strong, unresolved peak at 1140 cm^{-1} which was determined to be the diethyl

ether from the work-up of the reaction. To remove the diethyl ether from the sample, Brant and I monitored the peak at 1140 cm^{-1} and observed when the expected strong peak around 852 cm^{-1} became more prominent, though some diethyl ether was still present. The 186 scans of this more purified sample at 31 mTorr revealed a strong peak centered around 859 cm^{-1}, however the transitions were not clearly resolved. Therefore, for the remainder of the beamtime, we switched to the collection of thiazole in the 400 – 1200 cm^{-1} region.

Fortunately, additional time was granted to us the following week, Feb. 11 to Feb.16, 2021. Samples from 2021 vials 2 and 3 were combined and monitored in the 400 – 1200 cm^{-1} region in attempt removal of the majority of the diethyl ether before switching to scan at low frequency, the volume of sample, however, was too small to make complete removal of the impurity possible while still having any sample remain. Then, the spectrum of our more-pure sample from 2021 vial 1 was collected from 30 – 300 cm^{-1} with a new beam splitter to optimize the 30 – 150 cm^{-1} region. The initial scans were run at 0.107 Torr which used all of the remaining 2021 vial 1, and this pressure was insufficient, so the remainder of vials 2 and 3 were added, but this only increased the pressure to 0.148 Torr. After a scanning overnight with the higher pressure for 197 averaged scans some transitions started to become apparent, particularly around 80 cm^{-1}. Scanning for over 3 days (morning Feb. 12 to morning Feb. 16), for a total of 802 averaged scans and a final pressure of 0.142 mTorr reveals the spectrum in Figure A.3. For the next CLS beamtime, a larger quantity of sample needs to be synthesized and highly purified before it is sent CLS, so that a sufficiently high pressure (>150 mTorr), can be achieved in the 300 L vacuum chamber of the CLS spectrometer. Determining the vapor pressure and temperature relationship of 4-cyano-1,2-butadiene would also prove useful if cooling of the chamber will be required.
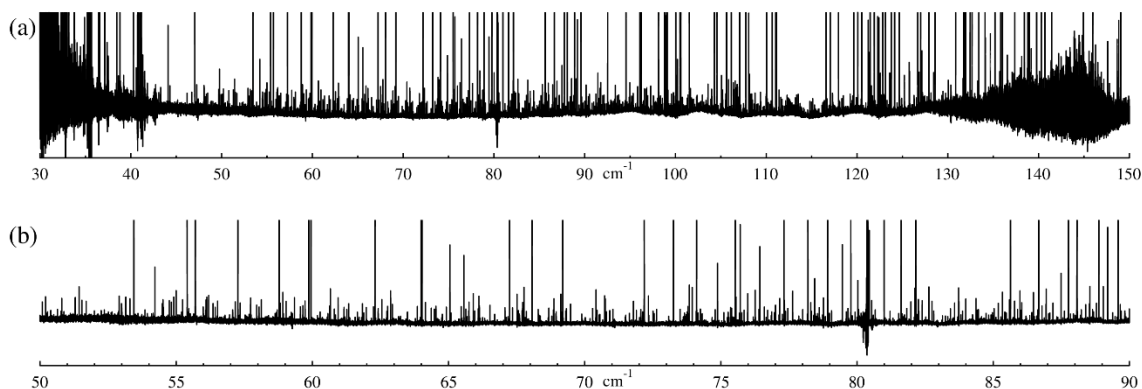
Figure A.3. Infrared spectra of 4-cyano-1,2-butadiene at 142 – 148 mTorr and 802 averaged scans from (a) 30-150 cm^{-1} and (b) 50-90 cm^{-1} collected in February 2021.

PYRIMIDINE, PYRIDAZINE, AND THIAZOLE

Without access to our labs during part of 2020 (Covid-19 pandemic), we made sure that other experiments would be possible if 4-cyano-1,2-butadiene could not be synthesized and shipped to CLS in time. These experiments were related to the heterocycles pyrimidine (*m*-$C_4H_4N_2$) and pyridazine (*o*-$C_4H_4N_2$), which were both were studied by the group previously.[6-7] Their r_e^{SE} structures were determined, and multiple vibrational states for these molecules have also been studied, and were published, or are part of on-going projects. Another heterocyclic molecule currently under investigation in the group is thiazole (*c*-C_3H_3NS). Each molecule has coupling between states, and the analysis of this coupling is benefited by the high-resolution FTIR obtainable from CLS. The pyrimidine spectrum was collected at room temperature (295 K) at 225 mTorr for 144 averaged scans, and at 49 mTorr for 195 averaged scans. Pyridazine was observed at room temperature with 71 mTorr for 171 averaged scans. The spectra of both molecules were collected from 400 – 1200 cm^{-1}. Pyridazine spectrum was also collected at 45 mTorr for 133 averaged scans from 35 – 600 cm^{-1}. The thiazole spectrum was collected at room temperature at 2 mTorr (134 avg. scans), 14 mTorr (176 avg. scans), 208 mTorr (209 avg. scans), and 418 mTorr

(198 avg. scans) from 400 – 1200 cm^{-1}. A spectrum for each molecule is shown in Figure A.4. Figure A.5 narrows the view on the thiazole spectrum to show the resolution achieved for the ν_{17} and ν_{13} bands. The work on these molecules with the new high-resolution FTIR spectra is ongoing and led by Brian J. Esselman.
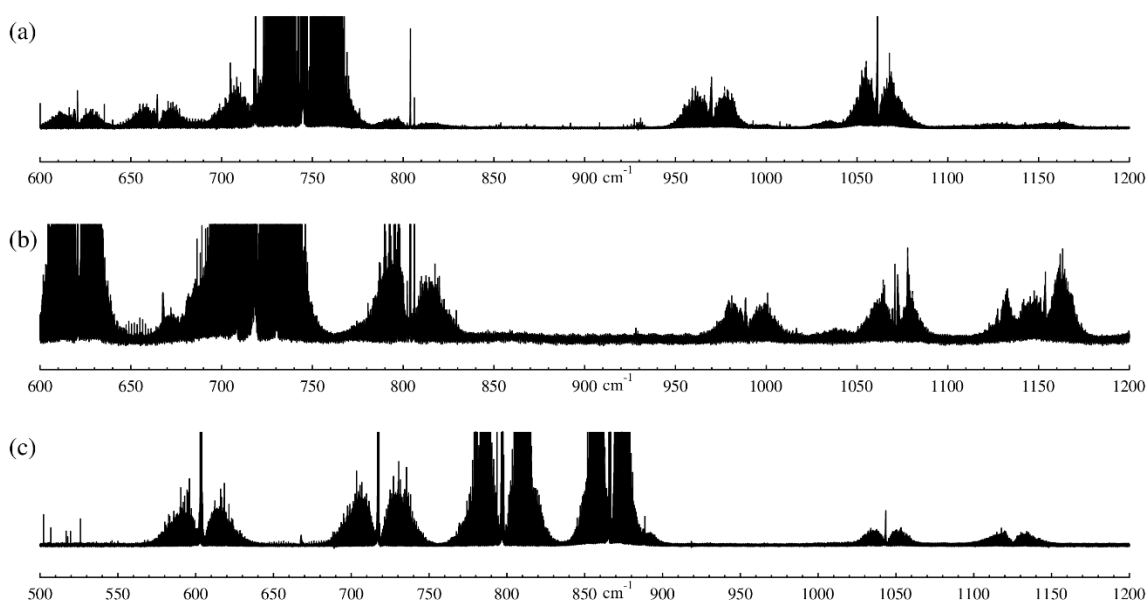
Figure A.4. High-resolution infrared spectra of (a) pyridazine at 71 mTorr, (b) pyrimidine at 14 mTorr from 600 – 1200 cm^{-1} and (c) thiazole at 14 mTorr from 500 – 1200 cm^{-1}.
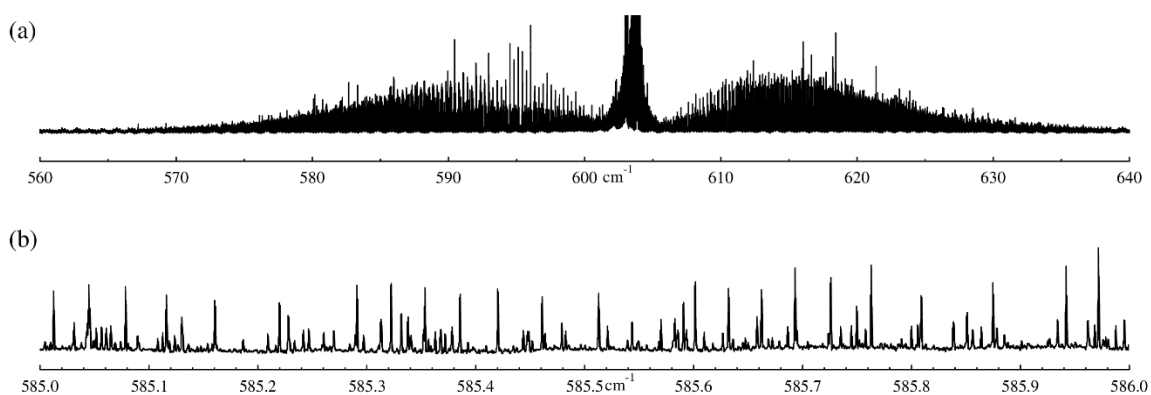
Figure A.5. High-resolution infrared spectrum of ν_{17} and ν_{13} of thiazole at 14 mTorr from (a) 560 – 640 cm^{-1} and (b) 585.0 – 586.0 cm^{-1}.

Note: for Figures A.1-A.5 a compression factor of 10 was necessary for making the images.

HN₃ and DN₃

Our second proposal to CLS was submitted for the collection of spectra on hydrazoic acid, HN₃, and its deuterio form, DN₃, from $35 - 1300$ cm^{-1}. Both isotopologues have a complex set of eight vibrational states that are interconnected and must be treated simultaneously in an eight-state global fit to accurately model the system. There is a strong foundation for this work from the original microwave and IR studies,[8-13] and the extensive high-resolution IR studies by Bendtsen and coworkers.[13-21] Our group, led by Brent K. Amberger, published the precise semi-experimental equilibrium structure of HN₃. In that study, the mm-wave spectrum of both isotopologues was analyzed between $235 - 450$ GHz.[22] Chapter 5 of Amberger's 2015 thesis details the extensive work done on the analysis of the eight lowest energy vibrational states of both HN₃ and DN₃, conducted at the point of his graduation, including initial 3-state coupled fits of the ground state, ν_5, and ν_6 for both molecules.[23] Subsequently, the work by Vávra, Urban, Kisiel and co-workers on a three-state, coupled fit of the ground state, ν_5, and ν_6 analyzed from $90 - 672$ GHz was published, after which we initiated a collaboration with them.[24] The combined rotational spectra of HN₃ currently cover the frequency range from around 100 to 720 GHz through this collaboration.

After completing his thesis,[23] Amberger continued to work on HN₃ and DN₃ and started 8-state fits for both molecules combining our data with published data in the literature. At the time of resuming this project, we were fortunate to have a ×12 Amplification-Multiplication Chain on loan from Michael McCarthy, so with Sam Wood and Claude Woods, we synthesized a new sample of DN₃ and collected the spectrum from $130 - 230$ GHz at pressures between $12 - 28$ mTorr in early August 2019. (The total pressure did increase throughout the scans due to the need to use a static system and the leak-rate of the vacuum system.). The number of transitions

measured and assigned for DN_3 was almost doubled in that effort. Claude and I revived Amberger's former work on the eight-state fit of DN_3, and we began to assign transitions from this new frequency region. While the fit did not achieve a low error, the prediction of vibrational states was improved, which improved our ability to continue to assign transitions.

Despite much rotational and high-resolution IR spectral analysis already done on these molecules, we noted in our proposal to CLS that "[t]he aforementioned published IR data has made possible the assignment and analysis progress achieved thus far, but the additional information that we need is simply not available in the old IR data. The published work includes the ν_5, ν_6, ν_4, and ν_3 bands for both molecules, the ground state far-IR pure rotational spectra for both, and a few sub-bands of the $2\nu_6$ overtone band of DN_3 only (generally at 0.03 cm^{-1} resolution). For many bands, line frequency lists were published in the papers, while for others the lists were deposited as supplementary materials, which have been subsequently lost, and only the effective B and D values of individual sub-bands remain."[3] The goal of our future beamtime at CLS is to collect high-resolution FTIR spectra from 35 – 400 cm^{-1} and 400 – 1300 cm^{-1}, specifically focusing on weak transitions, such as the overtones and combination bands. We were awarded time for this proposal in 2020, which has been delayed due to the Covid-19 pandemic and our need to travel to perform the synthesis on site. The work on the rotational spectrum has continued, however, and our collaborator K. Vávra was able to extend the spectrum of DN_3 up to 730 GHz, and the number of transitions assigned has consequently increased very greatly again. We look forward to conducting our planned experiments at the Canadian Light Source in the near future. This is currently scheduled at CLS in June 2021.

ACKNOWLEDGMENTS

REFERENCES

1. Orr, V. L.; Esselman, B. J.; Owen, A. N.; Kougias, S. M.; Woods, R. C.; McMahon, R. J. Rotational Spectroscopy of *syn* and *anti-clinal* Penta-3,4-dienenitrile from 130-375 GHz, *International Symposium on Molecular Spectroscopy*, Champaign-Urbana, Illinois, June 17-21, 2019; Champaign-Urbana, Illinois, 2019; RI07.

2. Orr, V. L.; Esselman, B. J.; Woods, R. C.; McMahon, R. J., Collection of the Far-Infrared Spectrum for the Analysis of the Internal Rotation in Penta-3,4-dienenitrile. *Canadian Light Source Proposal* **2019**, *Cycle 31*.

3. Orr, V. L.; Esselman, B. J.; Woods, R. C.; McMahon, R. J., Infrared Spectroscopy of HN_3 and DN_3 – pure rotational, vibrational satellite bands, hot-bands, ν_5 and ν_6 combination and overtone bands. *Canadian Light Source Proposal* **2019**, *Cycle 31*.

4. Kisiel, Z. PROSPE - Programs for ROtational SPEctroscopy. http://info.ifpan.edu.pl/~kisiel/prospe.htm

5. Kougias, S. M.; Knezz, S. N.; Owen, A. N.; Sanchez, R. A.; Hyland, G. E.; Lee, D. J.; Patel, A. R.; Esselman, B. J.; Woods, R. C.; McMahon, R. J., Synthesis and Characterization of Cyanobutadiene Isomers—Molecules of Astrochemical Significance. *J. Org. Chem.* **2020**, *85* (9), 5787-5798.

6. Esselman, B. J.; Amberger, B. K.; Shutter, J. D.; Daane, M. A.; Stanton, J. F.; Woods, R. C.; McMahon, R. J., Rotational spectroscopy of pyridazine and its isotopologs from 235–360 GHz: Equilibrium structure and vibrational satellites. *J. Chem. Phys.* **2013**, *139* (22), 224304.

7. Heim, Z. N.; Amberger, B. K.; Esselman, B. J.; Stanton, J. F.; Woods, R. C.; McMahon, R. J., Molecular structure determination: Equilibrium structure of pyrimidine (m-$C_4H_4N_2$) from rotational spectroscopy (r_e^{SE}) and high-level ab initio calculation (r_e) agree within the uncertainty of experimental measurement. *J. Chem. Phys.* **2020**, *152* (10), 104303.

8. Winnewisser, M.; Cook, R. L., Centrifugal Distortion Effects and Structure of Hydrazoic Acid from the Millimeter Wave Rotational Spectra. *J. Chem. Phys.* **1964**, *41* (4), 999-1004.

9. Kewley, R.; Sastry, K. V. L. N.; Winnewisser, M., Microwave and Millimeter Wave Spectra of Hydrazoic Acid. *J. Mol. Spectrosc.* **1964**, *12*, 387-401.

10. Levine, D. M.; Dows, D. A., Infrared Spectrum of HN3 and DN3: Assignment of the Coriolis-Coupled Bending Vibrations. *J. Chem. Phys.* **1967**, *46* (3), 1168-1172.

11. White, K. J.; Cook, R. L., Millimeter-Wave Rotational Stark Spectra of HNCO, DNCO, and HN$_3$: Dipole-Moment Changes with K. *J. Chem. Phys.* **1967**, *46* (1), 143-151.

12. Krakow, B.; Lord, R. C.; Neely, G. O., A high resolution far infrared study of rotation in HN$_3$, HNCO, HNCS, and their deuterium derivatives. *J. Mol. Spectrosc.* **1968**, *27* (1–4), 148-176.

13. Carlotti, M.; Di Lonardo, G.; Galloni, G.; Trombetti, A., Rotation-vibration spectrum of hydrazoic acid in the near infra-red and in the visible. *Trans. Faraday Soc.* **1971**, *67* (0), 2852-2861.

14. Bendtsen, J.; Winnewisser, M., Ground state spectroscopic constants and dipole moment of hydrazoic acid, $H^{14}N_3$. *Chem. Phys. Lett.* **1975**, *33* (1), 141-145.

15. Bendtsen, J., Pure rotational Raman spectra of hydrazoic acid HN$_3$ and DN$_3$. *J. Raman Spectrosc.* **1977**, *6* (6), 306-313.

16. Bendtsen, J.; Winnewisser, M., Absorption spectrum of deuterated hydrazoic acid, $D^{14}N_3$ in the microwave and millimeterwave region. *Chem. Phys.* **1979**, *40* (3), 359-365.

17. Bendtsen, J., Raman spectrum of the ν_2 band of $H^{14}N_3$. *J. Raman Spectrosc.* **1980**, *9* (3), 162-165.

18. Bendtsen, J., Raman and infrared rotation-vibration spectra of the ν_1 Band of $D^{14}N_3$. *J. Raman Spectrosc.* **1984**, *15* (2), 113-119.

19. Bendtsen, J.; Hegelund, F.; Nicolaisen, F. M., Infrared spectrum of the Coriolis coupled vibrations ν_5 and ν_6 of hydrazoic acid. *J. Mol. Spectrosc.* **1986**, *118* (1), 121-131.

20. Bendtsen, J.; Nicolaisen, F. M., The pure rotational absorption spectrum of hydrazoic acid in the far-infrared region. *J. Mol. Spectrosc.* **1986**, *119* (2), 456-466.

21. Hansen, C. S.; Bendtsen, J.; Nicolaisen, F. M., Analyses of the High-Resolution Infrared Absorption Spectra of the ν_2 and ν_3 Bands of Deuterated Hydrazoic Acid (DN_3). *J. Mol. Spectrosc.* **1996**, *175* (2), 239-245.

22. Amberger, B. K.; Esselman, B. J.; Stanton, J. F.; Woods, R. C.; McMahon, R. J., Precise Equilibrium Structure Determination of Hydrazoic Acid (HN_3) by Millimeter-wave Spectroscopy. *J. Chem. Phys.* **2015**, *143* (10), 104310.

23. Amberger, B. K. Millimeter-wave Spectroscopy of Highly Nitrogenous Molecules of Potential Astrochemical Interest. Ph.D. Thesis, University of Wisconsin-Madison, Madison, WI, 2015.

24. Vávra, K.; Kania, P.; Koucký, J.; Kisiel, Z.; Urban, Š., Rotational spectra of hydrazoic acid. *J. Mol. Spectrosc.* **2017**, *337*, 27-31.

Appendix B:

Millimeter-wave Spectrometer Modifications:
Updates and Maintenance of the Hardware and Software

Includes the work of several collaborators:

Brian J. Esselman, P. Matisha Dorman, Maria A. Zdanovskaia, Brent K. Amberger, Joshua D.

Shutter, Zachary N. Heim, R. Claude Woods, Robert J. McMahon

INTRODUCTION

The purpose of this chapter is to provide further information about the updates to the McMahon | Woods millimeter-wave spectrometer. The instrument's hardware and software has been described in great detail by Brian J. Esselman in Chapter 4 of his Ph.D. thesis[1] and further modifications were made and detailed by Brent K. Amberger in the third chapter of his Ph.D. thesis.[2] Esselman and Amberger's continued use of this instrument since writing their theses led to many additional ideas for its improvement. Upon joining the group, I too became involved with the maintenance and improvement of the mm-wave spectrometer. This appendix seeks to document many of the modifications to hardware and LabVIEW code made since Esselman and Amberger wrote their theses.

MM-WAVE SPECTROMETER LabVIEW CODE

At the time of Esselman's thesis, the mm-wave spectrometer code only allowed for the acquisition of Individual Scans, which at the time were on the front panel (the user facing view of the LabVIEW code) under the tab called "Acquire mm-wave data". These scans could only scan one segment of the spectral region at a time. Broadband scanning capability, the ability to collect our whole spectral window of 235 – 360 GHz into a single file, was developed shortly after. This collects the full spectrum in segments but stitches them together into a single file automatically as the scan progresses.

After I joined the group, Brian Esselman, with assistance from myself and Maria Zdanovskaia, modified the save routine for the spectrometer code to save into folders based on the user selected from the LabVIEW User Array on the front panel the front panel view of this is shown in Figure B.1. This array has four selection tabs that allow for up to four different LabVIEW

Users (Primary, Secondary, Tertiary, and Quaternary) to be selected. Once users are selected from the drop-down options, the data generated is saved simultaneously into each of their LabVIEW user folders, specifically into a further folder designated by the type of data collected, i.e. "Individual" for Individual scans and Queued Scans, and "BroadBand" for BroadBand Scans, and "Data Analysis" for saving data analysis spectra and figures analysis done in LabVIEW. This new routine makes it much easier for the user to find data generated by a past group member, or to find their own current data. To add new group members or remove old group members the name simply needs to be added/removed from the User array and their folder and sub-folders must be created.
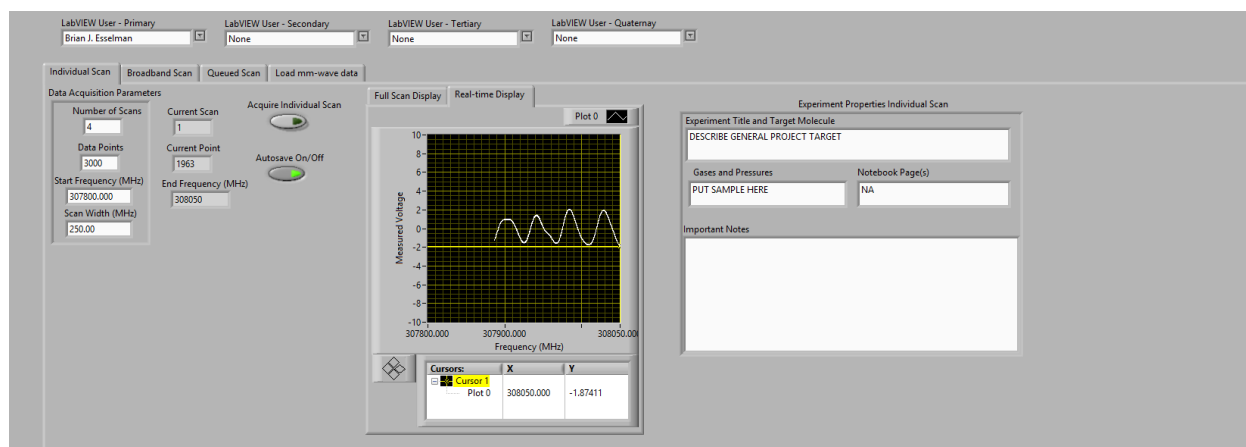
Figure B.1. The mm-wave spectrometer LabVIEW front panel view displaying the LabVIEW user array and the Individual Scan tab.

Broadband Scan

We further developed the Broadband Scan option so that the data can be collected across the full spectral range starting at the highest frequency and working in segments towards the lower frequency, "High to Low", or starting at the lowest frequency and working towards higher frequency, "Low to High". We also added a Reference Measurement option into the Broadband Scan tab. When this feature is turned on, the user can select a specific frequency region of the spectrum to collect after a user designated number of segments have been completed in the

Broadband Scan. These reference scans save into a folder called "Reference Scans" within the user's "Broadband" data folder. Some of the molecules that have been studied by the group will degrade overtime or are precious samples that are collected using a static chamber (not with a flow system). In cases like this, it is important to ensure that the signal from the reference transition(s) is staying fairly consistent in intensity (and width) throughout the scan. Both the "Broadband Scan Direction" option and the "Include Reference Measurement" option are visible in the Broadband Scan tab on the LabVIEW front panel shown in Figure B.2. Also visible in Figure B.2. is the "Time Remaining" feature which gives an approximate time the Broadband scan will be completed based on the number of segments remaining and the average time to complete a segment.
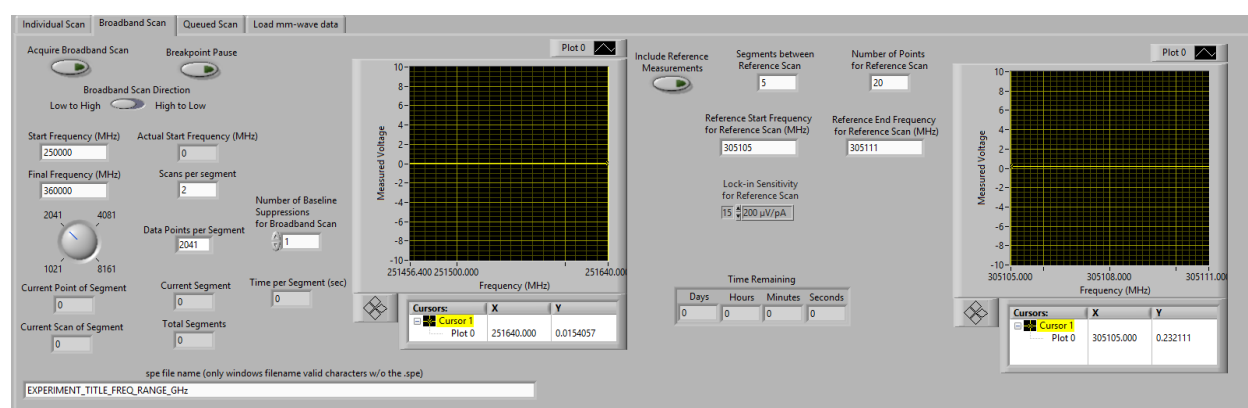
Figure B.2. The mm-wave spectrometer LabVIEW front panel view displaying the Broadband Scan tab which includes "Broadband Scan Direction" feature, the Reference Measurement feature, and the Time Remaining feature.

Queued Scan

The queued scan was developed to scan multiple, user-designated segments of the spectral region in succession, so that user input is only need once during the initial set-up, not for each segment as the "Individual Scan" function would require. This new feature is particularly useful if the user is looking for more than one molecule in the sample, e.g. searching for an impurity in a

synthesized sample. It would also be useful if the user desired to scan the same segments at various time points to monitor the chemistry occurring in the chamber. The LabVIEW front panel of the Queued Scan feature is show in Figure B.3.
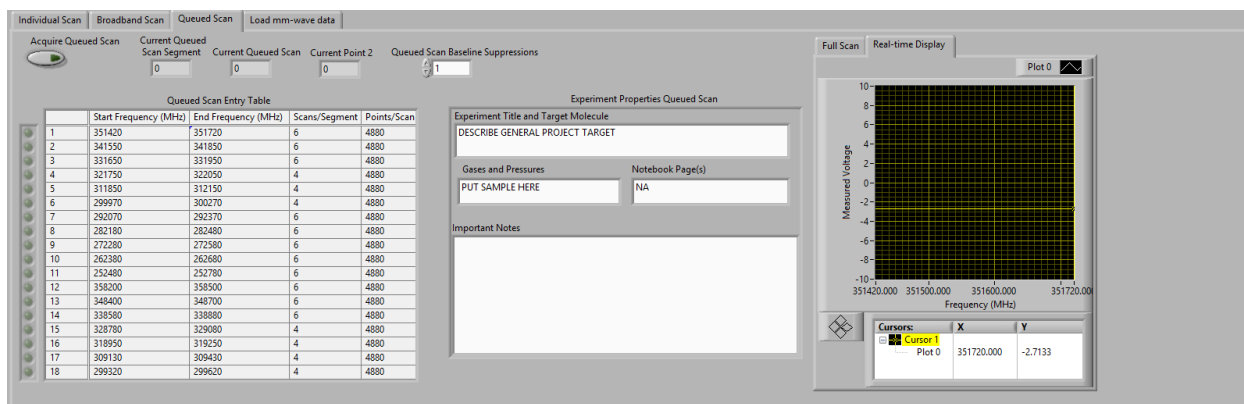
Figure B.3. The mm-wave spectrometer LabVIEW front panel view displaying the LabVIEW user array and the Queued Scan tab.

Additional Features

Another feature added is a "Tektronix Measurement" light which functions as an indicator for when the "Update Tektronix 494AP Setting and Obtain Modulation dbc" button is pressed. This process is not instantaneous, and the indicator light alerts the user that the code is carrying out the update process and the light turns off when the update is completed. Another addition is the "GPS Read" indicator which displays green when the signal GPS is locked by satellites.

Leak Detection

A Leybold-Heraeus helium leak detector (Figure B.4) was no longer functioning when we had substantial leaks in our vacuum system. Bill Goebel of the Department's electronics shop and Claude Woods dedicated a significant amount of time and effort to get it into proper working order. Once it was working, Matisha Dorman, Woods, and myself spent time running Helium around each of the fixtures of our vacuum chamber in search of leaks. A major leak was discovered to be an internal leak from tiny pin-prick size hole in the South electrode (not the tower electrode) where the Syltherm chiller fluid (used to chill the electrode when a discharge is running) was leaking into the vacuum chamber. The leak detector was also extremely useful for finding o-rings that were no longer sealing properly or welds that were not or no-longer vacuum tight.

Figure B.4. The Leybold-Heraeus Helium leak detector.

DC DISCHARGE, ION OPTICS, AND MASS SPECTROMETER

The quadrupole mass spectrometer in-sequence with the mm-wave spectrometer is capable of detecting ions from the DC discharge when the Tower Electrode is in use, and neutrals when the internal ionizer in the mass spectrometer is in use. These capabilities, especially the former, are useful when attempting to determine which species are being formed in the DC discharge. The ion optics, an arrangement of electrically charged cylinders, is used to focus the ions from the discharge into the mass spectrometer. To properly operate a discharge, the ion optics, the mass spectrometer, and the mm-wave spectrometer a step-by-step instruction guide was created and laminated for the lab. A version of this document, "Woods & McMahon Millimeter-wave Spectrometer Operating Instructions", created with assistance from Claude Woods and Matisha Dorman in 2017, is included in this Appendix after the References section.

Ion Optics pinhole covered

A pinhole between the chamber and the ion optics is how gases from the discharge, including ions created by the discharge, enter the ion optics and then into the mass spectrometer. (A schematic of the ion optics and mass spectrometer is included in the thesis of Rudolph Petrmichl and is included in the Operating Instructions document presented at the end of this appendix.[3]) This pinhole has a glass disk with a hole in the center that goes around the pinhole and insulates the ion optics chamber from the discharge. This disk had fallen down and was physically blocking the pinhole when we first began testing the mass spectrometer. The disc was replaced to its proper position with the assistance of Tracy Drier and we were then able to see ions from the discharge in the mass spectrometer.

Langmuir Probe Cover

During the use of the discharge, the Langmuir probe is used to measure the voltage of the discharge in the chamber. This probe is constructed of a long metal pin with a flat head that is insulated by glass rods. To bond the metal and glass together an epoxy resin is used, and this resin was burnt during the course of a discharge and therefore no longer vacuum tight. Therefore, new parts of the Langmuir probes were built by the machine shop and the glass shop. This probe extends out of the Teflon flange and is quite fragile, as well as being at very high voltage when a discharge is running. We therefore built a cover to protect the probe with the machine shop. The first model cracked, likely due to the band clamp used to prevent the electrical wire attached to the metal rod of the Langmuir probe from putting stress on the fragile glass. The next and current model constructed by the Machine shop out of PVC (Figure B.5). The holes on the side of the cover ensure that attachment of the alligator clip to the metal of the Langmuir probe does not attach at an angle that puts strain on the Langmuir probe or the electrical wire. The cover and cap deter accidental contact with the probe, which is especially important while a discharge is running.
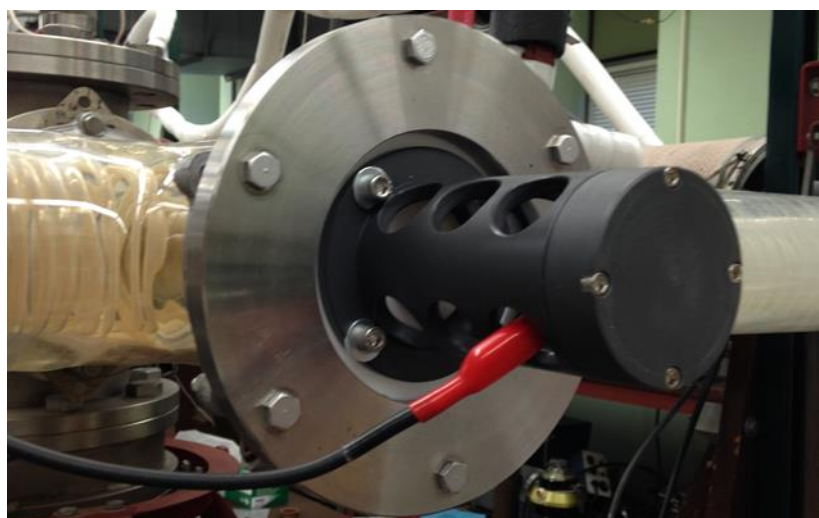
Figure B.5. Cover of the Langmuir probe in place on the instrument.

Glass Beads on Electrodes

The spectrometer has three electrodes: the North, the South, and the Tower. The North and South electrodes are cylinders with two arms curving off them which extend outside the vacuum chamber and allow for the electrical connection and chiller-fluid circulation. These arms must be insulated from the discharge inside the vacuum chamber and were formerly insulated with a thin Teflon sleeve. The sleeves burned on the North electrode and have been replaced by glass beads made by Tracy Drier. These glass beads are simply glass tubing cut into ~ 1-inch pieces to allow them to follow the curve of the electrode arm. The rough edges of the beads sparked initially during the first discharge but have worked well as a long-term insulation that will not burn.

Mass Spectrometer Hardware

A number of hardware changes have been made to the quadrupole mass spectrometer. A large leak valve has been attached to the East side of the mass spectrometer to facilitate a connection with the South glass manifold. The purpose of this connection is to allow the transfer of sample from the glass manifold directly into the mass spectrometer. A repair to the mass spectrometer involved replacement of a filament in the ionizer of the mass spectrometer which had burnt out. The tungsten wire specified by the manual was ordered, and Tracy Drier was able to affix this new wire to replace the burnt-out filament.

There are two diffusion pumps that create the vacuum in the ion optics and mass spectrometer. The heating element of one of the pumps burnt out, so supports were constructed by the machine shop to maintain the position of the ion optics and mass spectrometer while allowing for the removal these pumps. The inside of each pump was thoroughly cleaned, and new

heating elements were ordered. The machine shop team was able to install the new heating element and repair the copper water cooling line that was damaged during the removal of one of the pumps. The pumps were reinstalled, leak tested, and have been working well since.

Mass Spectrometer Code

The code for the mass spectrometer was not included in Chapter 4 of Esselman's thesis, though he mentions that the work is on-going.[1] Josh Shutter and Esselman worked on the original code that allowed the mass spectrometer to communicate with the computer through the LabVIEW software. When Esselman and I, with assistance from Matisha Dorman, resurrected the code in 2016/17, the former code had a non-functioning save routine. Having re-written the save routines for the mm-wave spectrometer code, we decided to do the same for the mass spectrometer save routine. This original save routine code was removed and replaced with the simpler LabVIEW User array and a *filename.txt* file saving system utilized in the mm-wave spectrometer save routines. This LabVIEW program for the mass spectrometer is separate from the mm-wave spectrometer LabVIEW program, and is called "Mass Spectrometer data acquisition and analysis v3.0.vi". Currently, when the "Save Data Analysis" button is pressed on the front panel the collected data saves to the user's "Mass Spec" folder (where the user is selected in the LabVIEW user array section).   The   raw   data   is   saved   in   a   text   file   with   a   name *Date_Time_Experiment_LowMass_HighMass*amu.txt with columns from left to right containing Mass (amu), Voltage Scan 1, Voltage Scan 2, Voltage Scan 3, etc. Experimental Properties are saved into a file ending in "_header.txt" as it is in the mm-wave spectrometer code. The Raw Data, Average Data and Baseline Corrected Data, is also saved to an Excel file. The "Save Graph Image" saves an image of the Baseline Gain Corrected Mass Spectrum graph panel.

The mass-to-charge ratio (*m/z*) of an ion is indicated in the mass spectra by a peak with a sharply rising right edge at the *m/z* of the ion. This large, positive first derivative value indicates that the presence of an ion at the *m/z* where the rising edge is steepest. Therefore, we added a first derivative of the collected mass spectrum to the Data Analysis graph displayed in LabVIEW. To facilitate visualization of both sets of data, a "Mass Spectrum Zoom" and a "Derivative Zoom" options were added. A threshold selection tool was implemented so that sharp peaks in the first derivative could be populated into a Mass and Amplitude table beneath the plotted data. The collected data can also be baseline adjusted using the Average of Scans graph baseline selection tool and polynomial smoothed following the method used for the mm-wave data.[1] An example the Baseline Gain Corrected Mass Spectrum graph on the front panel in use for a mass spectrum of N_2^+ from a N_2 discharge is shown in Figure B.6.
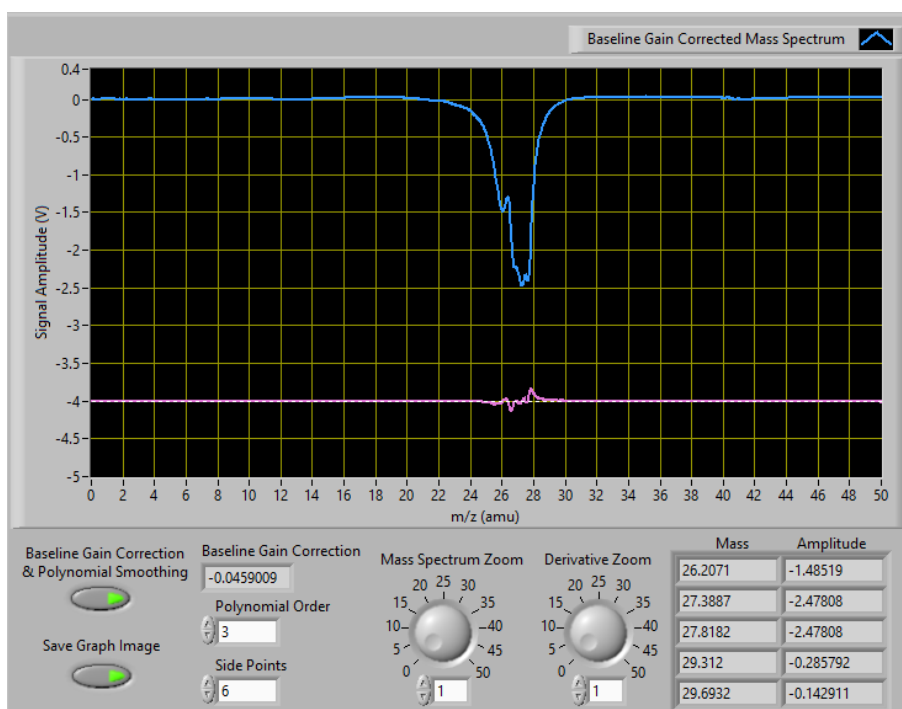
Figure B.6. Example of the LabView collection of data from the Mass Spectrometer for the isotopes of N_2^+. The mass spectrum is shown in blue and the first derivative of the mass spectrum is shown in pink. The white, dashed line is positioned by the user to select the threshold of peaks in the first derivative data, and peaks are populated in the Mass and Amplitude array in the bottom right of the panel.

NESLAB CHILLER SYSTEM: MODIFICATIONS

Compatible O-rings

The NesLab Chiller system and coolant lines have been problematic over the years. Amberger mentioned some of the challenges that the chiller has presented in the past, and how some of them were overcome. Specifically, he mentions on page 58 that "leaks were springing up at a great many points in our plumbing, likely the result of repeated cycling between −80 ºC and room temperature. We found by trial and error that Cajon fittings (now Swagelok UltraTorr) handled the temperature change better than regular Swagelok tube fittings."[2] During my first couple years the chiller had a series of leaks at various points with the Cajon fittings. It occurred to me that the Viton o-rings in the Cajon fittings may not be the proper temperature rating. We then acquired some silicone o-rings from the machine shop, which turned out to be just as incompatible as the Viton o-rings. The silicone o-rings are chemically incompatible with the Dow Syltherm XLT that is currently used as the coolant fluid and started to swell and fail when exposed to the fluid. The available o-ring materials were researched to ensure there was chemical and temperature compatibility. Fluorosilicone o-rings were determined to be best for the temperatures we are working at (−80 ºC to room temp) and would be more chemically compatible with the Syltherm XLT fluid than the silicone o-rings based on the product specifications. Upon ordering the –010 fluorosilicone o-rings and installing them in the Cajon fittings, the leaking of the system due to o-ring failure has decreased significantly.

Water Removal from the Chiller

After the replacement of the o-rings, the main continuing (and mostly unavoidable) issue with the chiller is the accumulation of water. When being frequently used, the chiller is kept at −20 ºC which results in water condensing on and in the unit as ice. Once defrosted, the main basin

has large bubbles of water that are very difficult to remove *via* the drain port at the back of the machine. The previous method of draining required three people: one to hold a bucket in place, one to remove the stopper, and one to tip the unit to get the water out (as the drain port is not completely at the bottom of the basin, and water is more dense than Syltherm). The new system only requires two people: one to position the plastic hose, and the other to use the syringe to suction the water bubbles out. The procedure can be done by one person if necessary. This method is much simpler, much less likely to result in solvent spills, and much more effective at removing water than the previous method. The thin plastic hose and disposable plastic syringe (60 mL) are both currently available and inexpensive to purchase from the Department of Chemistry 5th floor stockroom. The plastic hose is attached to a metal rod with electrical tape to facilitate its positioning within the basin, and a flashlight is very helpful to locate the water bubbles.

In his thesis, Amberger also mentions that, with the Dow Syltherm XLT that compared to the previously used solvent (R-123), the Slytherm evaporates less, but problems of the plumbing being blocked with ice have increased. He describes that "a canister filter [is being built] to attempt to remove ice particles from our loop."[2] The canister that was designed has now been installed in the loop thanks to the Machine shop and Zachary Heim, and has been fairly effective in extracting water ice from the system. When the syringe method is used extract water from the basin as described above, the canister filter also must be drained through a metal NPT fitting at the bottom of the canister. In order to perform both tasks the chiller must be put on by-pass for both the system and the canister filter (see full step-by-step instructions for putting the chiller on by-pass in the user manual included at the end of this Appendix). Additionally, separation of the Syltherm from the water was formerly performed with a separatory funnel, however, Matisha and myself discovered a simpler method with a funnel and filter paper. A paper filter is folded and placed in

a plastic funnel, and once the paper is coated in Syltherm it does not allow water to pass but will allow the Syltherm to pass into the receiving container. Since a very large funnel can be used, the process is significantly sped up. This also helps remove any dust or debris that may be present in the fluid.

ACKNOWLEDGMENTS

Thank you to Steven Meyers, Matt Martin, and Kendall Schneider in the machine shop, Bill Goebel in the electronics shop, and Tracy Drier in the glass shop. All have been immensely with helpful with repairs or taking our ideas from concept to reality and many of the hardware updates described would not have been possible without their expertise and skill.

REFERENCES

1. Esselman, B. J. Computational and Spectroscopic Investigations of Species of Astrochemical Relevance. Ph.D. Thesis, University of Wisconsin-Madison, Madison, WI, 2012.

2. Amberger, B. K. Millimeter-wave Spectroscopy of Highly Nitrogenous Molecules of Potential Astrochemical Interest. Ph.D. Thesis, University of Wisconsin-Madison, Madison, WI, 2015.

3. Petrmichl, R. H. Microwave Spectroscopy and Mass Spectrometry of Molecular Ions in Glow Discharges. Ph.D. Thesis, University of Wisconsin-Madison, Madison, WI, 1990.

A copy of the "**Woods & McMahon Millimeter-wave Spectrometer Operating Instructions**"

Woods & McMahon Millimeter-wave Spectrometer Operating Instructions

Turning On Spectrometer

1. Electrically ground yourself, and turn on the Virginia Diodes Multiplier (green light will turn on)
2. Turn on Agilent Signal Generator
3. Turn on the Tektronix and the FM Signal Modulator
4. Turn on the Lock-In Amplifier
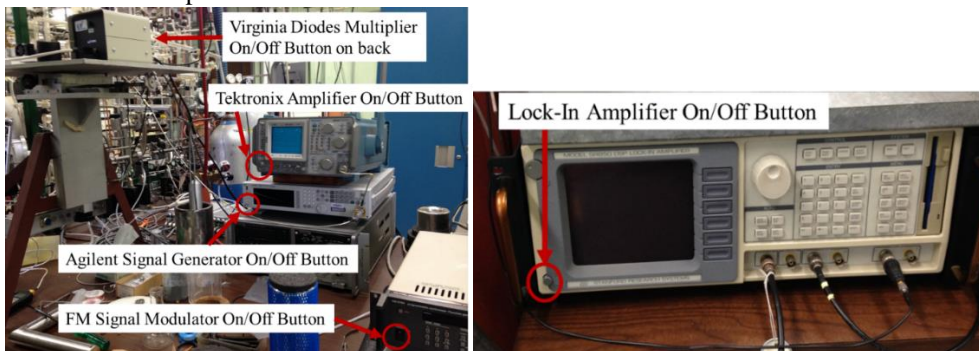
5. Start current LabVIEW program on computer
6. Close glass diffusion pump for the glass manifold, and open glass manifold to chamber
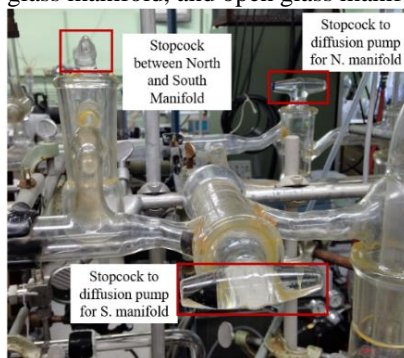
7. Open stopcock/valve on desired, freeze-pump-thawed sample or green valves for cylinder sample (see details on mass flow controller operation in the *Turning on a Discharge* section)
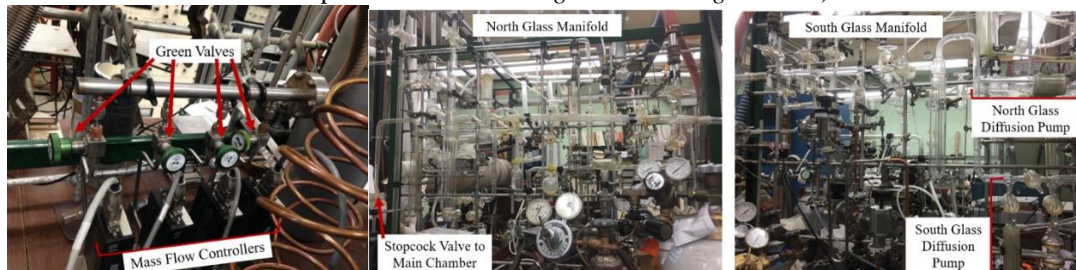
8. Put automatic gate valve in position mode to run a flow system of sample, or close gate valve to run a static sample

Turning On the Mass Spectrometer

1. Open up Mass-Spec. (MS) backing valve, watch the pressure decrease on thermocouple gauges (make sure the roughing valves are closed, can use them to pump out first, but must be closed after)
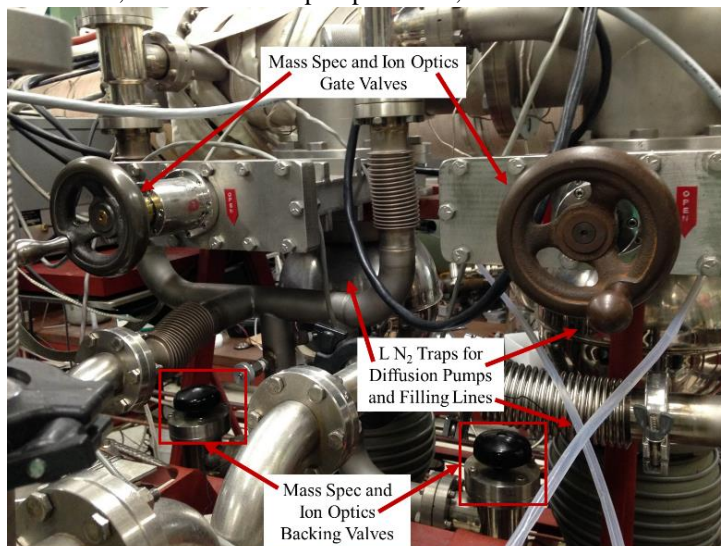
2. Open up Ion Optics (IO) backing valve, watch the pressure decrease on thermocouple gauges
3. Turn on water cooling lines for diffusion pumps (middle 2 levers, in set of 4, second set of water pipes from left from turbo pump) and all thin pipe water cooling return lines to right of water cooling lines.
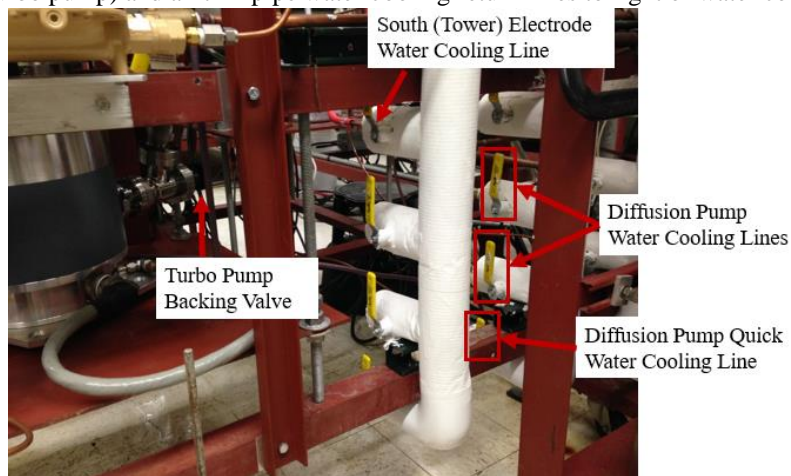
4. Turn on Diff 1 (MS) and Diff 2 (IO) using breaker switches on west wall breaker box L.
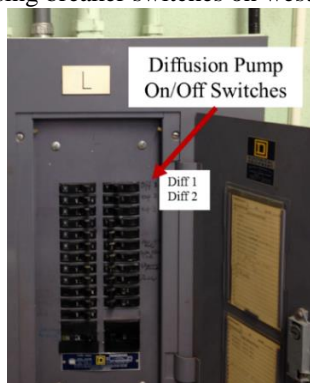
5. Open the gate valves for MS and IO (turn slowly until hear click, then turn the rest of the way until open – don't force)
6. Monitor diffusion pumps with contact pyrometer or IR thermometer (temp should settle around 310 °C)
7. After thermocouple gauges indicates ~0 mTorr in IO and MS, start attempting to turn on Bayard-Alpert Ion Gauges to monitor pressure. If ion gauge turns off when button is released, don't force it on, give it time to decrease pressure and test again (degas if continually have trouble turning on at low pressure)
8. Once Pressure is $< 10^{-6}$ for MS and IO fill liquid N_2 traps on the diffusion pumps, LN_2 will start flowing out (steady flow, not just drops) when the traps are full, stop and switch to other trap filling line
9. Turn on the MS and IO electronics (see *Turning on the Mass Spectrometer and Ion Optics Electronics* instructions on the following pages)
10. Open the diagonal valve to MS
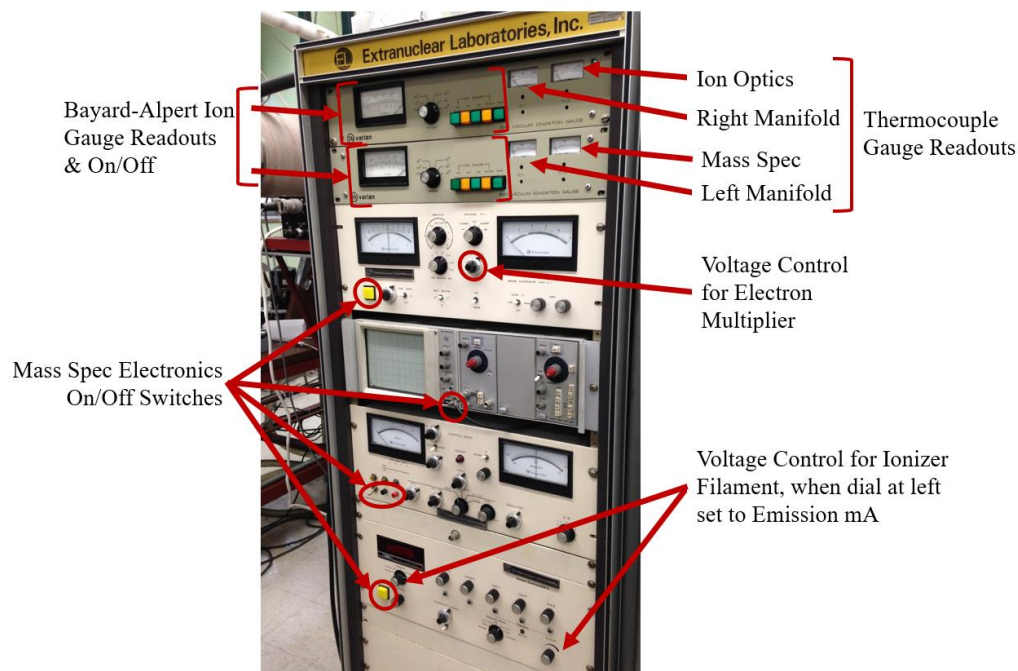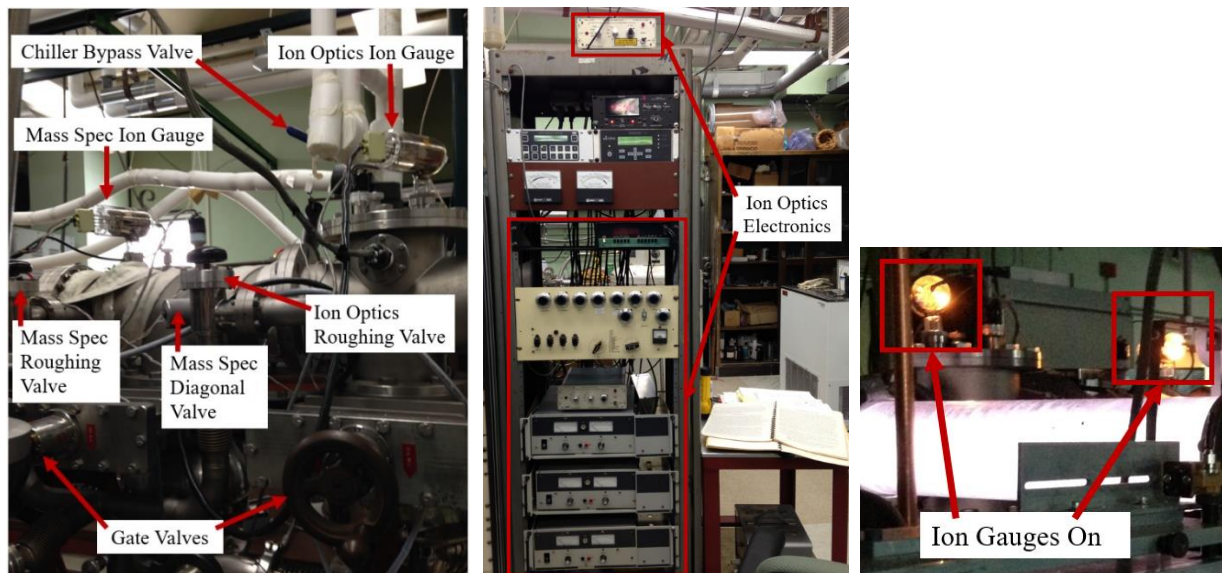
Turning on the Mass Spectrometer and Ion Optics Electronics

1. Make sure pressure in MS and IO is below 10^{-5} mTorr
2. Turn on the Mass Spec Detector Panel, set the electron multiplier to 3.5 kV with the voltage dial
3. Turn on the Mass Spec Monitor Oscilloscope, this will display a spectrum (usually 10 amu wide is set on the Quadrupole Control unit, so each line vertical line on the 'scope screen is one amu)
4. Turn on Quadrupole control power, let it warm up, then turn on power
5. Turn on the Ionizer Control Panel, turn on ionizer (if not running a discharge) with controls for ionizer filament. Set dial to Emission mA, then adjust with knob to 3.00 mA)
6. Turn mass selection dial to observe desired mass on oscilloscope (mass on dial will be left edge of the oscilloscope window)
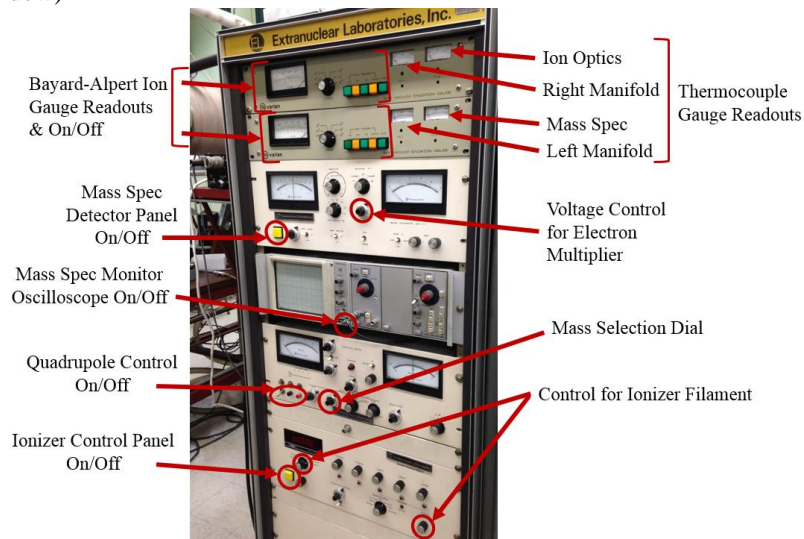
7. On IO control dials panel, turn on switches labeled "power", "PS", "HV+" and "HV-"
8. Turn on Power Supply Boxes for Ion Optics (IO) (lower should be ~ 1200 V, top ~ 500 V)
9. Turn on High Voltage Power Source for Langmuir probe emitter follower amplifier
10. Turn on Voltage Readout box, use selection knob on control dials panel to select what voltage is being displayed
11. Use dials on control dials panel to set voltages of IO parts
12. To use LabVIEW to collect MS data, must switch from *Sweep* to *EXT CMD* (external command) on the Quadrupole Control Panel
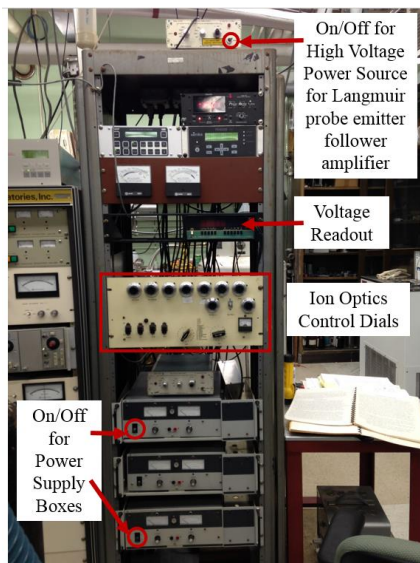
Turning Off the Mass Spectrometer and Ion Optics Electronics

1. On IO control dials panel, turn off switches labeled "power", "PS", "HV+" and "HV-"
2. Turn off High Voltage Power Source for Langmuir probe emitter follower amplifier
3. Turn off Power Supply Boxes for IO
4. Turn off Voltage Readout for IO
5. Turn off ionizer for MS on Ionizer Control Panel (if in use)
6. Turn voltage down to zero for electron multiplier on MS detector panel
7. Turn off MS detector panel
8. Turn off Oscilloscope for MS
9. Put quadrupole into standby, then turn it off

Schematic of IO and MS from pg 72 of the 1990 thesis of Rudolph Petrimichl
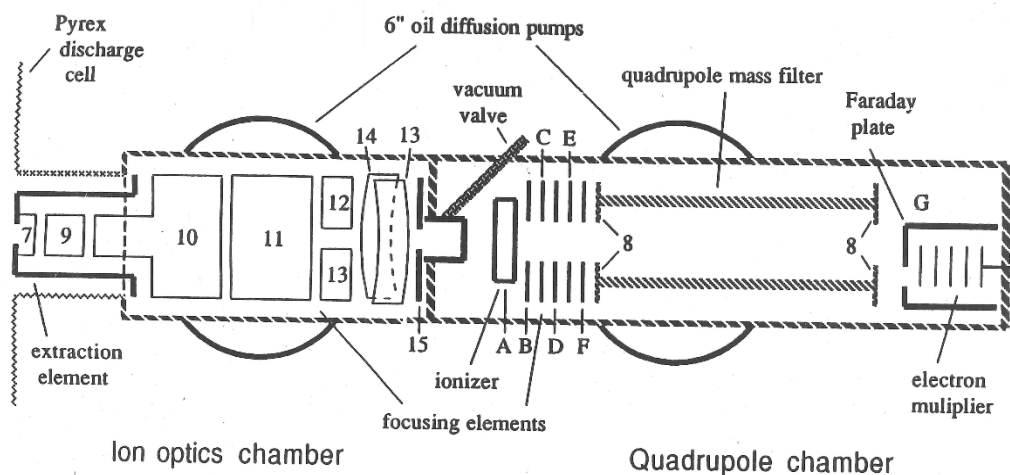
Figure 3.1 A cross sectional view of the mass spectrometer system. The focusing lenses controlled by the ion optics circuitry are labeled numerically (7 - extractor, 8 - quadrupole common, 9 - small, 10 - taper, 11 - long, 12 - door, 13 -up/window, 14 -down, 15 - partition), while the focusing elements controlled by the ionizer control are given alphabetic designations (A - electron energy, B - ion energy, C - ionizer extractor, D through F - lens 1, 2, and 3, respectively, G - Faraday plate).

Turning On a Discharge

1. Close Glass diffusion pump to vacuum manifold and open manifold to chamber
2. Open green valve(s) for desired gas(es) and let vacuum re-establish
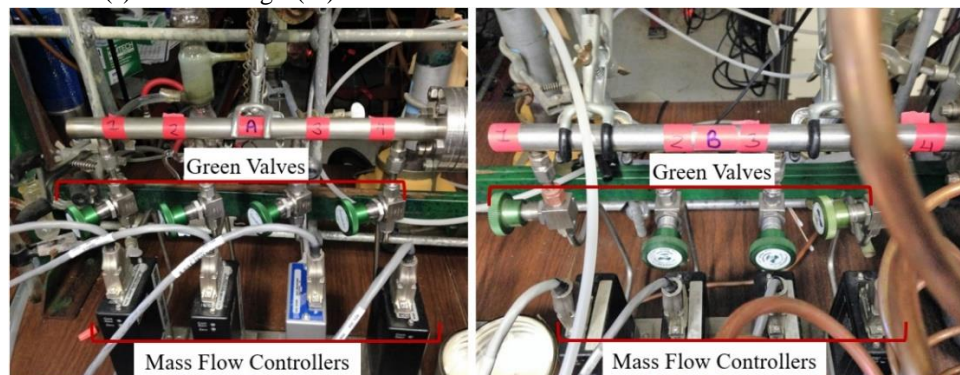
3. Start flow with mass flow controller (MFC) switch(es) for desired gas(es).
4. To achieve desired flow pressure:
   a. Set readout control dial to desired gas (#1-4). Set desired flow setpoint with small screwdriver and screw. The setpoint switch must be held up when turning the screw. The screw is inset from faceplate of the box, to the right of the setpoint switch.
   b. Set turbo pump gate valve to pressure/position mode

5. If putting a non-cylinder sample in discharge, use flow system with needle valve on glass manifold
6. If running a negative glow discharge, magnet must be turned on:
   a. Make sure cathode is north electrode, and anode is south electrode (not tower)
   b. Turn on water cooling for magnet
   c. Turn on magnet power
   d. Turn magnet dial to establish desired magnetic field (usually, ~250 - 300 G)
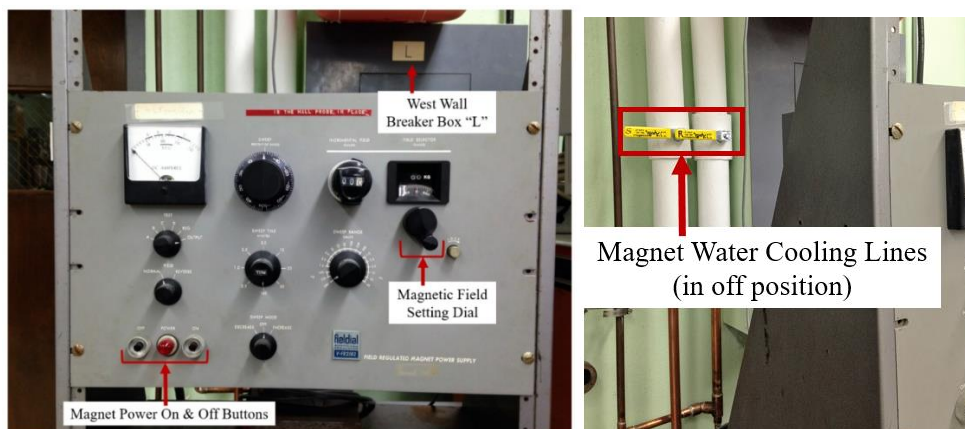
7. On green high voltage discharge box, turn on the main power supply
8. Turn on the control power (wait for fan for ballast resistor to run)
9. Press the high voltage "On" button
10. Turn black center knob until discharge is established, then turn down to desired voltage or amperage
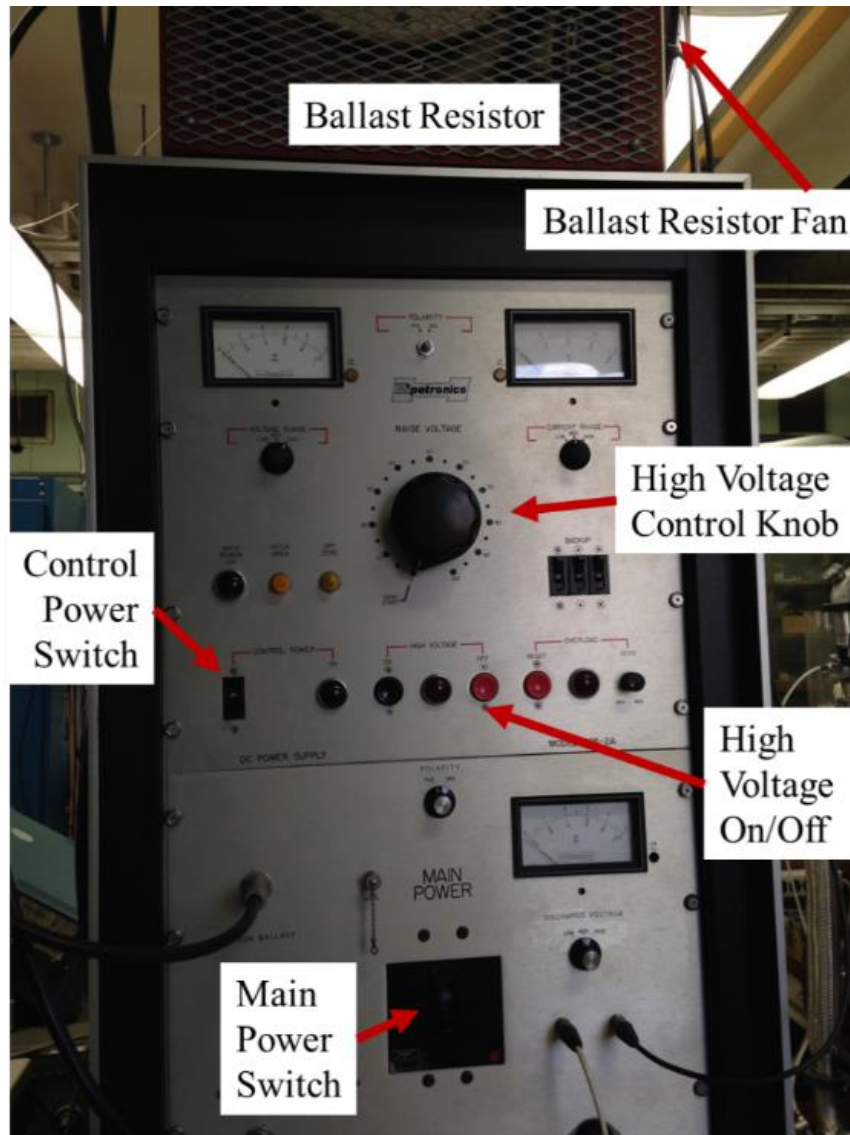
Turning on the NesLab Chiller System

1. Turn on chiller power and refrigeration
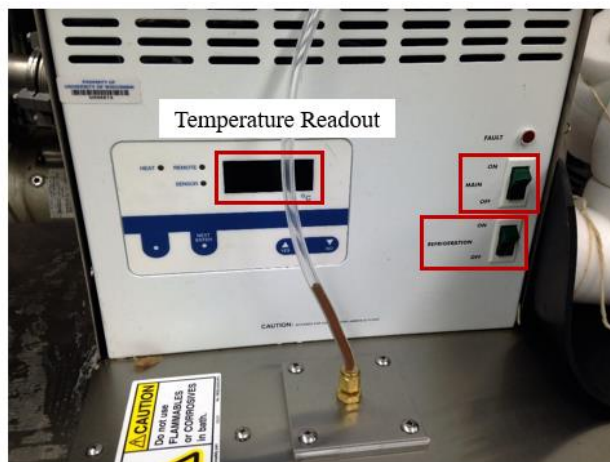
2. Make sure ice trap is open: valves 1 and 2 open, valve 3 closed.(To clean out: close 1 and 2, and open 3)
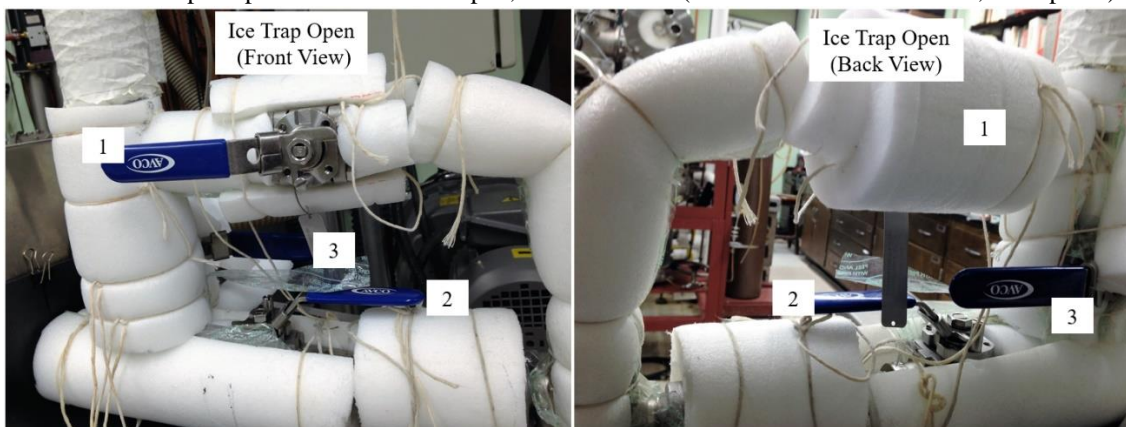
3. Set the temperature set point in the LabVIEW program
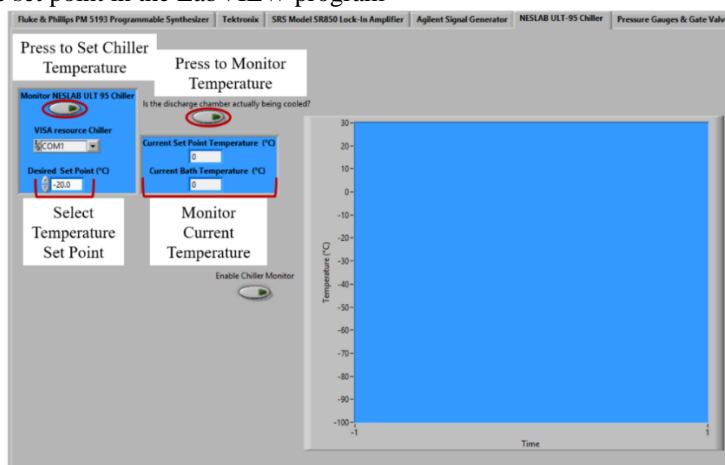
4. Take the chiller off by-pass mode (Close 4 and open 5 and 6)
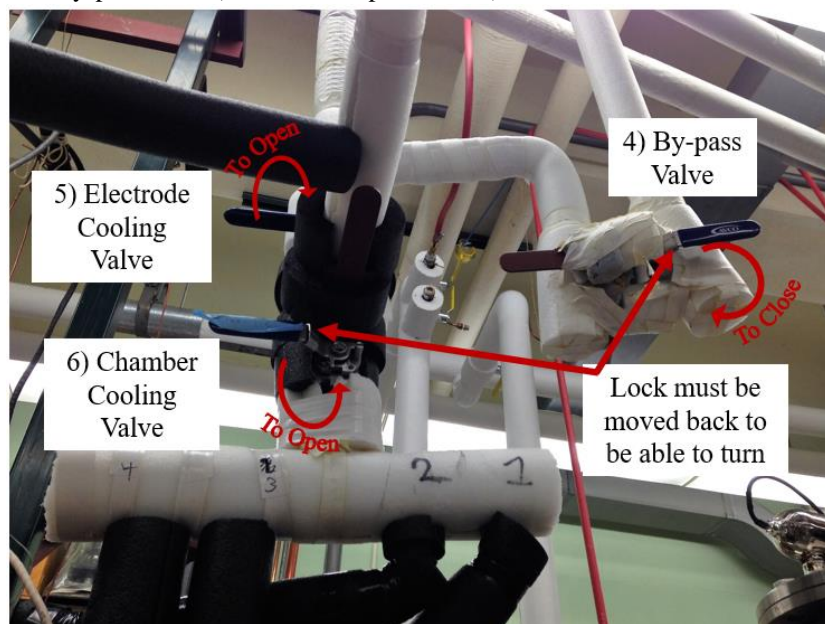
5. Return lines must be open (stay open at all times except for during maintenance of lines)
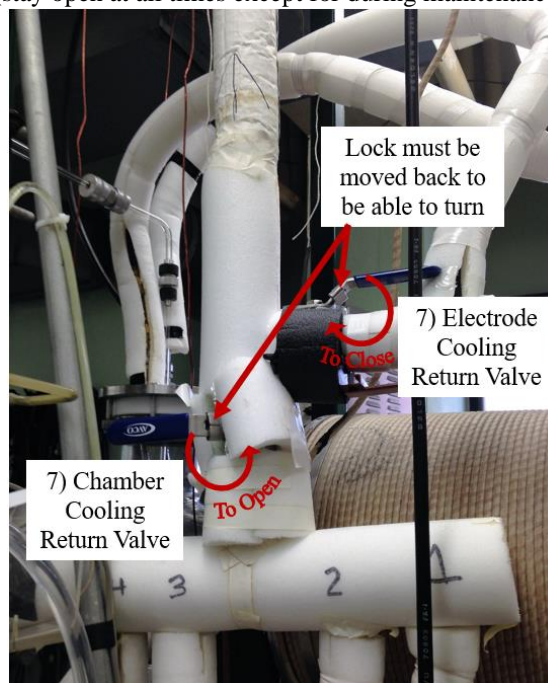
Turning Everything Off

1. Turn off MS and IO electronics (see *Turning Off the Mass Spectrometer and Ion Optics Electronics* on previous pages)
2. Turn off the Bayard-Alpert ion gauges
3. Turn off the MS and IO diffusion pumps using breaker switches on west wall in breaker box L
4. Turn on the quick cooling for the MS and IO diffusion pumps (bottom lever in the same set of four water lines second set to the left of the turbo pump)
5. Close the MS and IO gate valves (close slowly until a click is felt/heard, do not bear down on valve)
6. Close the diagonal valve to MS
7. Turn off the discharge power supply:
   a. Turn down black knob to zero, wait until gauge reaches zero (it is discharging the capacitors!)
   b. Turn off high voltage
   c. Turn off the control power
   d. Turn off main power
8. Turn off the magnet
   a. Turn down magnetic field
   b. Turn off magnet power
   c. Turn off cooling water lines once magnet is only warm (~ 50 °C), not hot
9. Turn off the mass-flow controller(s), let line pump down, then shut the green valve(s) for the MFC
10. Open the automatic gate valve
11. Close any sample valves/stopcocks on the glass manifold
12. Shut the stopcock from the glass manifold to the chamber
13. Open the stopcock to the glass diffusion pump for the vacuum manifold, make sure the stopcock between the North and South manifold is closed
14. Check MS and IO temperature with contact pyrometer or IR thermometer (wait for temp to get down to at least 100 °C)
15. Close the backing valves for the MS and IO
16. Turn off the water cooling for diffusion pumps (all 3 valves)
17. **Be sure** the liquid N_2 is reconnected to the trap (the auto-fill set-up)
18. Put the chiller system on by-pass at -20 °C (set temp. in LabVIEW and close valves 5 and 6, open 4)
19. Turn off the water cooling to the South electrode (if using the tower electrode)
20. Turn off all mm-wave spectrometer instruments with Virginia Diodes Multiplier last
21. Turn off lights and lock doors